



Advanced Drug Delivery Group
School of Pharmacy
Institute of Biophysics, Imaging and Optical Science (iBIOS)
The University of Nottingham

Total internal reflection microscopy studies on colloidal particle endocytosis by living cells

Gerard Byrne MPharm MRPharmS

**Thesis submitted to the University of Nottingham
for the degree of Doctor of Philosophy, December 2009**

*“We must take care not to make intellect our God. It has, of course, powerful muscles,
but has no personality. It cannot rule, only serve.”*

- Albert Einstein

Abstract

The purpose of this study was to develop novel optical microscopy techniques in order to investigate colloidal drug particle endocytosis by mammalian cells. A total internal reflection microscope (TIRM) was initially developed for high resolution cellular imaging. TIRM is a non-fluorescent imaging technique based on the principle of ‘scattering’ of the evanescent field created when a light beam undergoes total internal reflection at an interface between two media with different refractive indices, such as glass and air. The key design considerations with respect to development of a TIRM instrument are discussed. The technique is also compared and contrasted to the more commonly known non-fluorescent RICM (Reflection Interference Contrast Microscopy) technique using computer simulations. Time-lapse video TIRM is applied to imaging the interaction between A549 and 3T3 cells, and a polylysine coated substrate. Real-time *label-free* visualisation of 0.5 and 1 μm polystyrene particle endocytosis by living cells is then demonstrated. Modifications to the TIRM system to include a dual-colour fluorescent TIRF (Total Internal Reflection Fluorescence) microscope are described in detail. Results are shown which demonstrate the ability of a combined TIRM/TIRF instrument to selectively image the basal cell membrane both *label-free* and fluorescently. 3T3 fibroblast cells were genetically modified using standard molecular biology protocols to express the fluorescent fusion protein EGFP-Clathrin LCa (enhanced green fluorescent protein clathrin light chain a). Finally, colloidal particle endocytosis by the genetically modified cell was imaged using the TIRM/TIRF microscope. Direct visualisation of the internalisation of 500 nm particles *via* clathrin coated pits in 3T3 cells was shown for the first time.

Acknowledgements

I have been very lucky to be supervised by four truly inspirational academics, across three very diverse backgrounds, who have bestowed upon me but a fraction of their considerable knowledge. I would like to thank Prof. Mike Somekh and Dr. Mark Pitter from iBIOS for their show of faith (in a pharmacy student!), fantastic insight into the world of optical engineering and for all their help in general. I wish to also thank Dr. Snow Stolnik for teaching me the ways of colloidal drug delivery, our existential chats and her kindness. Finally, I would also like to thank Dr. Franco Falcone for introducing me to the intricate, sometimes frustrating, but overall fascinating ways of Molecular Biology. I wish to extend my appreciation to Ms Christine Grainger-Boulty and Mrs Teresa Marshall for their technical support and assistance.

I would like to thank everyone within the Advanced Drug Delivery group and the institute of Biophysics Imaging and Optical Sensors, especially Emilia, Driton, Alpesh, Anne, Lilia, Ibticiem, Graeme, Lin, Jo, Kevin, Noah, Roger, Jing, Shugang, Barry and Shailesh for all the helpful advice and making sure there were some fun times. Special thanks to Dr. Nick Johnston for design and manufacture of circuitry utilised in Chapter 4. I would also like to thank all the guys I've lived with over the years - Sean, Rose, JC, Greg, Andy and Ahmet. Thanks also to the lads from home, Peter, Aidy, Leo and Cormac for coming over to visit and fill me in on all the craic from home. Finally, a big thanks to Kieran and Helen for the much loved (and now missed) Sunday lunches.

I consider myself lucky to have also crossed paths with some truly wonderful and caring people and a big thanks to Mrs. Kelly Vere – only you know what you’ve done, and for that I’ll be eternally grateful.

Finally, I offer a sincere thank-you to my long-suffering parents, who have listened, encouraged, and supported me not only over the last three and a half years but throughout my life. This thesis is dedicated to you both.

Narcissus

Table of contents

Abstract	i
Acknowledgements	ii
Table of contents	iv
List of figures	xiii
List of tables	xviii
List of abbreviations and nomenclature	xix
Chapter 1 Introduction	0
1.1 Particulate drug delivery	1
1.1.1 Particulate endocytosis and intracellular fate in mammalian cells	4
1.1.2 Ideal properties of a particulate drug delivery imaging technique	9
1.2 Microscopy fundamentals	11
1.2.1 What is resolution?	11
1.2.2 Point spread function	14
1.2.3 The Abbe resolution limit	15
1.3 Brightfield microscopy	16

1.4	Confocal Microscopy	17
1.5	Evanescient wave techniques	19
1.5.1	Surface plasmon resonance	19
1.5.2	Total internal reflection fluorescence microscopy	24
1.6	Scanning Probe techniques	25
1.6.1	Atomic Force Microscopy	25
1.6.2	Scanning Ion Conductance Microscopy	26
1.6.3	NSOM	29
1.7	Far-field super-resolution techniques	31
1.7.1	Stimulated emission depletion	32
1.7.2	Pointillist microscopy	34
1.7.2.1	Photoactivated localisation microscopy	34
1.7.2.2	Stochastic optical reconstruction microscopy	36
1.7.3	Structured illumination microscopy	37
1.8	I5M and 4Pi microscopy	39
1.9	Summary	40
Chapter 2	Label-Free Total Internal Reflection Microscopy	44
2.1	Introduction	45
2.1.1	The surface contact microscope	45
2.1.2	The Reflection Interference Contrast Microscope	49
2.1.3	Principles of total internal reflection	49

2.1.4	Early applications of total internal reflection microscopy	53
2.1.4.1	TIRM for measuring colloidal separation distances	54
2.1.4.2	TIRM for measuring the interaction between model cells and biomaterials	59
2.1.4.3	Interference TIRM for measuring Kinesin motion	60
2.1.5	Evanescent wave illumination	61
2.2	Aims and objectives	63
2.3	Materials and methods	64
2.3.1	Microscopy	64
2.3.2	Cell Culture	65
2.3.3	Preparation of PLGA coated surfaces	66
2.3.4	Simulations of TIRM and RICM	67
2.4	Results and discussion	68
2.4.1	Comparison of RICM and TIRM contrast mechanisms using computer modelling	68
2.4.2	TIRM illumination strategies	75
2.4.3	TIRM temporal resolution	83
2.4.4	Combined TIRM and Brightfield imaging	84
2.4.5	Depth of field and focussing	86
2.4.6	Substrate selection	88
2.5	Conclusions	92

Chapter 3	Applications of TIRM for live cell imaging	93
3.1	Introduction	94
3.2	Aims and objectives	95
3.3	Materials and Methods	96
3.3.1	Total internal reflection microscopy	96
3.3.2	Surface plasmon resonance microscopy	96
3.3.3	Cell culture	97
3.4	Results and discussion	98
3.4.1	Label-free high resolution TIRM imaging of 3T3 fibroblast cells	98
3.4.2	Surface plasmon resonance microscopy	104
3.4.3	TIRM imaging of an epithelial cell line	106
3.5	Conclusions	112
Chapter 4	Combined Total Internal Reflection Microscopy and Total Internal Reflection Fluorescence Microscopy (TIRM/TIRF)	113
4.1	Overview of study	114
4.2	Introduction	115
4.2.1	Types of TIRF setups – Practical implications	120
4.2.1.1	Prism type setup	120
4.2.1.2	Objective type setup	121
4.2.2	High resolution TIRF imaging of living cells	123

4.3	Materials and methods	125
4.3.1	Cell Culture	125
4.3.2	Microscopy	125
4.3.3	Cell labelling	126
4.3.4	Transfection	127
4.4	Microscope alignment and operation	128
4.4.1	General considerations	128
4.4.1.1	Objective correction	128
4.4.1.2	Illumination methods	129
4.4.1.3	Field of view and light source	130
4.4.1.4	Imaging detector	131
4.4.1.5	Objective lens	132
4.4.2	Optics for illumination and imaging	132
4.4.2.1	Illumination optics – TIRF	132
4.4.2.2	Illumination optics – TIRM	135
4.4.2.3	Imaging optics – TIRM and TIRF	135
4.4.3	Optical alignment	136
4.4.3.1	TIRM alignment issues	138
4.4.3.2	TIRF alignment issues	139
4.4.3.3	General alignment issues	142
4.4.4	Choice of multi-band dichroic beamsplitter	144
4.4.5	Control of illumination pathways	147
4.5	Results and discussion	150
4.6	Conclusions	155

Chapter 5	Clathrin Mediated Endocytosis	156
5.1	Overview of study	157
5.2	Introduction	158
5.2.1	Endocytosis	158
5.2.2	Mechanisms of endocytosis	158
5.2.2.1	Phagocytosis	160
5.2.2.2	Macropinocytosis	161
5.2.2.3	Caveolae-mediated endocytosis	161
5.2.2.4	Clathrin and caveolin-mediated independent endocytosis	162
5.2.2.5	Clathrin-mediated endocytosis	163
5.3	Materials and methods	169
5.3.1	Plasmids	169
5.3.2	Oligonucleotide primers	169
5.3.3	Chemical reagents & media	170
5.3.3.1	General Chemicals	170
5.3.3.2	Antibiotics	170
5.3.4	Growth media	170
5.3.4.1	Luria Bertani medium	170
5.3.5	Growth & storage of bacteria	171
5.3.5.1	Bacterial growth conditions	171
5.3.6	DNA manipulation	171
5.3.6.1	Isolation of mRNA and production of cDNA	171
5.3.6.2	Isolation of plasmid DNA from electrocompetent <i>E. coli</i> cells	172
5.3.6.3	Polymerase chain reaction (PCR) amplification	172
5.3.6.4	DNA agarose gel electrophoresis	173
5.3.6.5	DNA molecular weight markers	173
5.3.6.6	DNA restriction enzymes	174

5.3.6.7	DNA ligation	174
5.3.7	Electroporation of electrocompetent <i>E. coli</i> cells	174
5.3.8	DNA sequence analysis	175
5.3.9	Transfection	175
5.4	Results and discussion	176
5.4.1	Development of EGFP-clathrin fusion protein	176
5.4.2	Clathrin expression in a mouse fibroblast cell line	185
5.4.2.1	Dynamics of clathrin coated pits and vesicles in live cells	189
5.4.3	Caveolae mediated endocytosis	191
5.5	Conclusions	192
Chapter 6	Clathrin mediated particle endocytosis	193
6.1	Overview	194
6.2	Introduction	195
6.3	Materials and methods	196
6.3.1	Cell labelling for confocal microscopy	196
6.3.2	Particle deposition for TIRM/TIRF uptake studies	196
6.3.3	Particle uptake for q(RT) ² -PCR studies	197
6.3.4	Quantitative real time reverse transcriptase polymerase chain reaction (q(RT) ² -PCR)	198
6.3.5	Microscopy	200
6.3.5.1	Confocal laser scanning microscopy (CLSM)	200
6.3.5.2	Scanning electron microscopy (SEM)	201
6.3.6	Image analysis	201

6.4	Results and discussion	202
6.4.1	Particle – cell interactions	202
6.4.2	TIRM imaging of particle endocytosis	210
6.4.3	Combined TIRM/TIRF microscopy of nanoparticle endocytosis	218
6.4.4	Clathrin gene expression after particle exposure	228
6.4.4.1	Method development for q(RT)2-PCR	229
6.4.5	q(RT)2-PCR results	231
6.5	Conclusions and future work	233
Chapter 7	Summary, Conclusions and Suggestions for Future Work	234
7.1	Overview of work undertaken in this study	235
7.2	Original goal	237
7.3	Output	237
7.4	Method development	238
7.4.1	Optical Engineering	238
7.4.1.1	TIRM system	238
7.4.1.2	TIRM/TIRF system	239
7.4.2	Molecular biology	242
7.5	Outcomes/Results	243
7.5.1	TIRM imaging of 3T3 and A549 cells	243
7.5.2	TIRM/TIRF imaging of clathrin mediated endocytosis	244

References	246
Appendix - Results from qRT²-PCR experiments	282

List of figures

Chapter 1

Figure 1.1	Multifunctional nanoparticle for drug delivery	3
Figure 1.2	Citation report for search term “nanoparticle cell interaction”	4
Figure 1.3	Nanoparticle-cell interactions	6
Figure 1.4	The point spread function	14
Figure 1.5	Schematic diagram showing the Kretschmann configuration for the excitation of surface plasmon’s	20
Figure 1.6	Comparison of the spatial and temporal resolutions of biological imaging techniques	42

Chapter 2

Figure 2.1	Schematic diagram of the surface contact microscope developed by Ambrose in 1956 in (a) darkfield arrangement and (b) brightfield arrangement.	47
Figure 2.2	Plot of reflected intensity versus incident angle for cell/media and cell/cytoplasm interface	51
Figure 2.3	Schematic diagram illustrating (a) Brownian fluctuations of a sphere (b) ‘frustrated’ total internal reflection	56

Figure 2.4	Schematic diagram of a typical flowcell used by many authors for TIRM experiments	59
Figure 2.5	Plot of simulated reflection coefficient versus cell/substrate separation for RICM	70
Figure 2.6	Plot of simulated reflection coefficient versus cell/substrate separation for TIRM with collimated illumination	71
Figure 2.7	Plot of simulated reflection coefficient versus cell/substrate separation for RICM with high NA illumination ($0 \leq NA \leq 1.3$)	73
Figure 2.8	Plot of simulated reflection coefficient versus cell/substrate separation for TIRM with high NA illumination ($1.3 \leq NA \leq 1.45$)	74
Figure 2.9	Prism based total internal reflection scattered light image of a 3T3 cell	76
Figure 2.10	(a) Schematic of TIRM illumination using a laser focused to a point on the back focal plane of the objective lens. (b) TIRM image of a 3T3 fibroblast cell using this illumination setup.	77
Figure 2.11	Schematic representation of annular mask used to for TIRM illumination.	79
Figure 2.12	(a) Schematic representation of TIRM illumination achieved using a diffuse laser beam imaged onto the back focal plane of the objective lens. (b) TIRM image of a 3T3 fibroblast cell using this illumination setup.	81
Figure 2.13	TIRM image of a 3T3 fibroblast cell captured using a LED illuminated setup.	83
Figure 2.14	Brightfield and TIRM images of A549 cells.	85
Figure 2.15	Schematic diagram illustrating the depth of field dependence on NA	87
Figure 2.16	TIRM images and line plot of a Human Osteoblast like cells (HOBs) adhering to PLGA coated surface	90

Chapter 3

Figure 3.1	Schematic diagram of the Kohler illuminated SPR microscope	97
Figure 3.2	TIRM image of a 3T3 fibroblast cell cultured on a PLL coated cover slip for 3 h	99
Figure 3.3	Series of images from a TIRM time-lapse sequence of unlabelled 3T3 fibroblast cells adherent to a poly-L-lysine coated coverslip	101
Figure 3.4	TIRM image of a 3T3 fibroblast cell cultured on a PLL coated cover slip for 3 h	102
Figure 3.5	Series of images from a TIRM time-lapse sequence of unlabelled 3T3 fibroblast cells adherent to a poly-L-lysine coated coverslip	103
Figure 3.6	SPRM image of a 3T3 fibroblast cell adhered to a PLL coated gold substrate	105
Figure 3.7	Bright-field image of a population of A549 cells adhered to a PLL coated coverslip	107
Figure 3.8	TIRM images of unlabelled A549 cells adherent to a PLL coated coverslip for 4 hours	108
Figure 3.9	TIRM images of unlabelled A549 cells adherent to a PLL coated coverslip for 24 hours	110

Chapter 4

Figure 4.1	Schematic diagram illustrating two types of setup for TIRF microscopy	122
Figure 4.2	Schematic illustration of TIRF imaging of a cell adhered to a glass coverslip	124
Figure 4.3	Schematic diagram illustrating the beam paths used in the TIRM/TIRF microscope	134
Figure 4.4	Schematic illustration of TIRF/TIRM illumination optics	137
Figure 4.5	Placement of the MDBS, focussing lens (lens 5), and translation stage	141

Figure 4.6	Placement of the emission filter and position of imaging beam path in the Meiji TC5400 inverted microscope	143
Figure 4.7	Typical transmission spectra for filters and mirrors used in the microscope	146
Figure 4.8	Andor break-out box and custom built LED control circuit	149
Figure 4.9	DiI-labelled 3T3 fibroblast cell on poly-L-lysine-coated glass slides	151
Figure 4.10	TIRM/TIRF images of 3T3 fibroblast cells	154

Chapter 5

Figure 5.1	Pathways of entry into mammalian cells	159
Figure 5.2	Schematic diagram for clathrin-mediated endocytosis	165
Figure 5.3	TIRF imaging of clathrin mediated endocytosis	167
Figure 5.4	Insertion of clathrin LCa into pEGFP-C1	177
Figure 5.5	Cloning PCR products by addition of restriction sites	180
Figure 5.6	Agarose gel showing the PCR amplification of murine clathrin light chain A	182
Figure 5.7	Agarose gel showing the digestion of EGFP plasmid	182
Figure 5.8	Schematic diagram outlining the cloning process	184
Figure 5.9	TIRM/TIRF analysis of clathrin distribution in a 3T3 fibroblast cell 24 hrs post transfection	188
Figure 5.10	TIRF analysis of clathrin coated pit dynamics in 3T3 fibroblast cells	190

Chapter 6

Figure 6.1	TIRM image of polystyrene particles undergoing Brownian motion and adhering to a PLL coated substrate	204
Figure 6.2	Schematic representation of the adherence of white carboxyl polystyrene spheres to a PLL coated coverslip	205

Figure 6.3	TIRM image showing the adherence of white carboxyl polystyrene spheres to a PLL coated coverslip	206
Figure 6.4	SEM images of 2 μm polystyrene beads undergoing internalisation by a 3T3 fibroblast cell	208
Figure 6.5	SEM images of 2 μm polystyrene beads undergoing internalisation by a 3T3 fibroblast cell	209
Figure 6.6	TIRM/TIRF images of 100 nm particles	211
Figure 6.7	TIRM image series depicting the uptake of colloidal particles	213
Figure 6.8	Z-stack confocal micrograph illustrating the uptake of 2 μm polystyrene spheres by 3T3 fibroblast cells	215
Figure 6.9	Low magnification TIRM/TIRF imaging of 0.5 μm particles undergoing endocytosis by EGFP-clathrin Lca labelled 3T3 cells	220
Figure 6.10	TIRM/TIRF images of polystyrene latex endocytosis by 3T3 cells expressing EGFP-Clathrin (n=3)	222

Chapter 7

Figure 7.1	Overview of experimental work undertaken in this study	236
------------	--	-----

Appendix 1

Figure A.1.1	PCR amplification/cycle graph for SYBR-490 and HPRT1, RPL32 and Clathrin genes	282
Figure A.1.2	Melt curve graph for SYBR-490 and HPRT1, RPL32 and Clathrin genes.	283

List of tables

Chapter 1

Table 1.1	Ideal properties of an imaging system for studying nanoparticle entry into cells	10
Table 1.2	Summary of imaging systems described in this chapter	43

Chapter 4

Table 4.1	Comparison of TIRF and confocal microscopy techniques. Adapted from Steyer and Almers (2001)	119
-----------	--	-----

Chapter 5

Table 5.1	Oligonucleotide primer sequences for RT-PCR experiments	169
-----------	---	-----

Chapter 6

Table 6.1	PCR primers for the reference genes HRPT1, RPL32 and the target gene clathrin, used in the qRT ² -PCR experiments	198
Table 6.2	Percent decrease in clathrin LCa mRNA expression in 3T3 cells exposed to 2 μm and 0.2 μm particles for 2 hrs (n=2, mean \pm SD)	232

List of abbreviations and nomenclature

%	Percentage
°	Degree
°C	Degrees Celsius
AFM	Atomic force microscope
CCD	Charged Coupled Device
CLSM	Confocal laser scanning microscopy
CO ₂	Carbon dioxide
DF	Darkfield
DiD	1,1'-dioctadecyl-3,3,3',3'-tetramethylindodicarbocyanine perchlorate
DiI	1,1'-dioctadecyl-3,3,3',3'-tetramethylindodicarbocyanine perchlorate
DLS	Dynamic Light Scattering
DMEM	Dulbecco's modified eagle's medium
DMSO	Dimethylsulphoxide
DPMG	Dimyristoyl phosphatidylglycerol

DPFC	Dipalmitoyl phosphatidylcholine
DsRed	<i>Discosoma</i> sp red fluorescent protein
EDTA	Ethylenediaminetetraacetic acid
EF	Evanescent field
EGF	Epidermal growth factor
EGFP	Enhanced green fluorescent protein
EMCCD	Electron multiplying charged coupled device
EW	Evanescent wave
FCS	Fetal calf serum
FCS	Fluorescent correlation spectroscopy
FLIM	Fluorescence lifetime imaging microscopy
FRAP	Fluorescence recovery after photobleaching
FRET	Fluorescence resonance energy transfer
FTIR	Frustrated total internal reflection
fN	Femto-Newton
He-Ne	Helium-Neon
HEPES	<i>N</i> -2-hydroxyethyl piperazine- <i>N'</i> -2-ethanesulfonic acid
HILO	Highly inclined laminated optical sheet microscopy
hOBs	Human osteoblast like cells
IRM	Interference reflection microscope

LAO	Low-angle oblique
LED	Light emitting diode
M	Molar
MDBS	Multiband dichroic beamsplitter
ml	Millilitre
mW	MilliWatt
MW	Molecular weight
NA	Numerical aperture
NBCS	New born calf serum
NCI	Nanoparticle-cell interaction
Nm	Nanometer
NSOM	Near-field scanning optical microscopy
PBS	Phosphate buffered saline
PE	Potential energy
PCR	Polymerase chain reaction
PSF	Point spread function
RT-PCR	Reverse transcriptase polymerase chain reaction
qRT ² -PCR	Quantitative real time reverse transcriptase polymerase chain reaction
PALM	Photoactivated localisation microscopy
PLGA	Poly(lactic- <i>co</i> -glycolic acid)

PLL	Poly-L-Lysine
RI	Refractive index
RICM	Reflection interference contrast microscopy
SICM	Scanning ion conductance microscopy
SCM	Surface contact microscope
SLM	Spatial light modulator
SPR	Surface plasmon resonance
SRIC	Surface reflection interference contrast
SSCM	Scanning surface confocal microscopy
SSIM	Saturated structured illumination microscopy
STED	Stimulated emission depletion
STORM	Stochastic optical reconstruction microscopy
TIR	Total internal reflection
TIRAF	Total internal reflection aqueous fluorescence
TIRF	Total internal reflection fluorescence
TIRM	Total internal reflection microscopy
μm	Micrometer
w/v	Weight per unit Volume
w/w	Weight per unit Weight

Chapter 1

Introduction

1.1 Particulate drug delivery

Advanced drug delivery is an area of research concerned with improving the pharmacological profile, toxicity and efficacy of ‘free’ drug in the body through the use of novel carrier systems. The carriers include different structures, such as polymer and/or lipid based particulates [1, 2], micellar-type systems [3], polymer-drug macromolecular conjugates [4], molecular assemblies [5] or complexes [6]. Advanced drug delivery systems can also include medical devices such as stents, implants and microneedles [7-9]. The aim of a drug delivery system is to improve the non-ideal properties associated with administration of ‘free’ drug into the body, such as their poor solubility (which lead to poor absorption and bioavailability), poor selectivity for target tissue (resulting in undesired toxicity), unfavourable pharmacokinetics (increases dosage required) and degradation (drug loses activity following administration) [10]. The ‘free drug’ in this context can be either small molecular weight molecules or biologicals; the later including peptides, proteins, antibodies and nucleic acids.

One way of ameliorating some of the issues associated with delivery of ‘free drugs’ is their incorporation into a colloidal particulate carrier such as a nanoparticle or microparticle. Nanoparticles may be defined as solid colloidal particles ranging from 1 to 100 nm in size [11]. They can be manufactured from biodegradable synthetic polymers such as poly(lactic acid) and poly(lactic-co-glycolic acid) or from biodegradable natural polymers such as chitosan, alginate and gelatin. Drug (including

small molecular weight drugs and biologicals) may be either dissolved, entrapped, encapsulated or attached to a nanoparticle matrix. Depending on the process used for their preparation, nanospheres, nanoparticles or nanocapsules may be obtained [12]. Nanospheres are defined as monolithic systems in which the drug is dissolved or entrapped throughout the particle matrix while the nanocapsules are reservoir-type systems comprising an oily liquid core, in which drug is usually dissolved, surrounded by a polymeric shell. In both these systems drug may also be adsorbed onto the surface of the particle [13]. Other examples of nanoparticles include liposomes [14], micelles [3] and dendrimers [15]. Several nanoparticulate drug formulations have made it onto the market including AmBiosome® (liposomal amphotericin B), Doxil® (PEG-stabilised liposomal doxorubicin) and Abraxane® (albumin-based nanoparticle containing paclitaxel). These products demonstrated an increased efficiency of drug in the body and a reduction of associated side-effects [16-18].

The applications and efficiency of nanoparticles as a drug delivery system can be enhanced through the addition of functional surface moieties. Whereas, monofunctional nanoparticles provide a single function—for example, a liposome transports incorporated drug around the body but does not have the inherent characteristics to enable it to distinguish between healthy and unhealthy cells or tissue—a multifunctional nanoparticle combines different functionalities in a single stable construct. For example, it is possible to engineer nanoparticles to contain not only the therapeutic agent(s) but also to have a specific targeting function that recognises unique surface receptors expressed on the target cells [19]. Other functional moieties that can be readily added to the nanoparticle include a biocompatible polymer such as poly(ethylene) glycol to

modify the biodistribution [20, 21], an imaging agent to afford recording of the systems efficiency [22, 23] and/or a cell-penetrating agent such as the TAT peptide [24, 25] to increase the efficiency of intracellular drug delivery (Fig. 1.1).

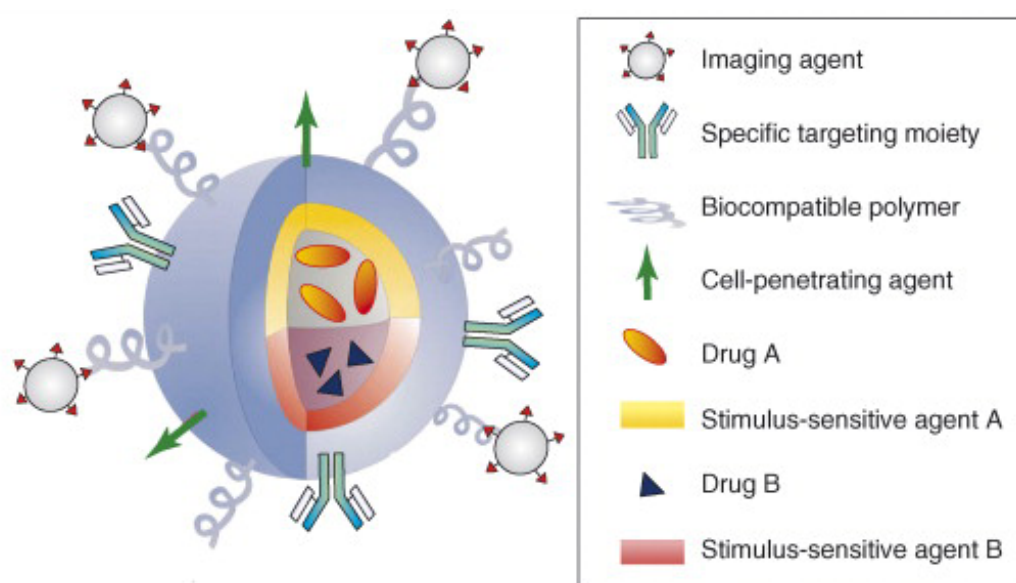


Figure 1.1 Multifunctional nanoparticle for drug delivery

Multifunctional nanocarriers can combine a specific targeting agent (usually an antibody or peptide) with nanoparticles for imaging (such as quantum dots or magnetic nanoparticles), a cell-penetrating agent (e.g. the polyArg peptide TAT), a stimulus-sensitive element for drug release, a stabilising polymer to ensure biocompatibility (most frequently polyethylene glycol) and the therapeutic compound. Development of novel strategies for controlled release of drugs will provide nanoparticles with the capability to deliver two or more therapeutic agents. Reprinted from [26], with permission from Elsevier.

1.1.1 Particulate endocytosis and intracellular fate in mammalian cells

The area of research regarding nanoparticle-cell interactions (NCIs) has been receiving significant interest over the last number of years as shown by the increasing number of published items and citations (Fig. 1.2) and emphasised at the 2007 European Science Foundation conference dealing specifically with this topic in relation to the toxicology and efficiency of the nanoparticulate system [27]. This conference dealt with many aspects of NCIs including the effect of particle design, particle size and surface charge on the internalisation, intracellular fate and toxicity of the particulate drug delivery system. One of the most important themes to arise at the conference was the need to determine the nature of the initial interaction of the particle with the cell, the entry mechanism of the particle and the translocation of the particle within the cell body.

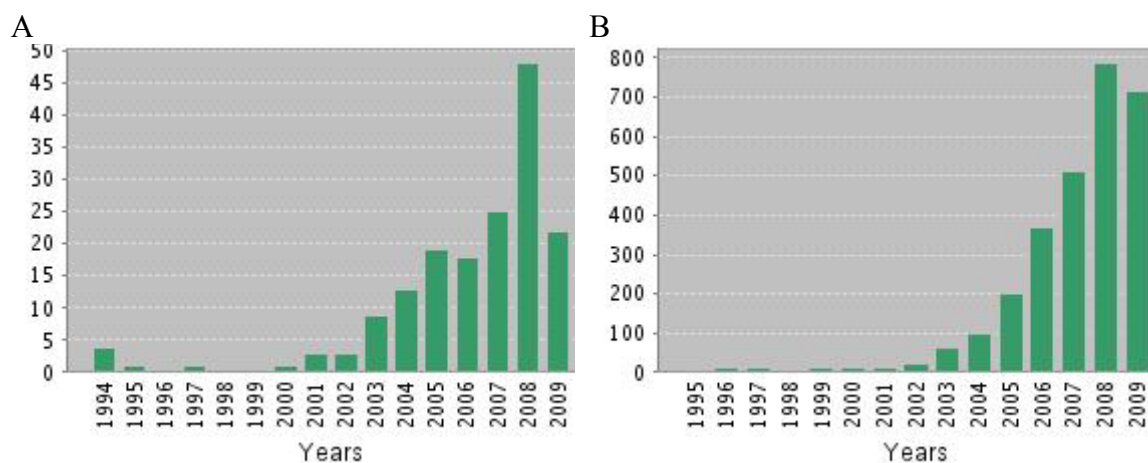


Figure 1.2 Citation report for search term “nanoparticle cell interaction”
(a) Published items over the last 15 years. (b) Citations made each year for the past 14 years. Data generated from Web of Knowledge citation report (www.isiknowledge.com. Website accessed on 20th August 2009).

Figure 1.3 is a schematic diagram representing the key areas associated with NCIs. The first area of interest is how the particle initially interacts with the cell (Fig. 1.3 (1)). The crucial questions for drug delivery researchers include; can particles be designed to have an exclusive interaction with the cell membrane through, for example, utilising surface ligands to target cell surface receptors, and hence reduce the interaction with non-targeted cells resulting in a decrease in side-effects, what are the dynamics of the particle on the cell surface i.e. how long does the particle reside on the surface, can the particle be rationally designed to maximise this residence time and is there an equilibrium for the number of particles that can remain on the surface at any given time? Answering these pertinent questions is vital in, for example, gene delivery, since the efficiency of the delivery system depends on the amount of DNA entering the cell. Therefore, by having a thorough understanding of how a DNA delivery device interacts with the cell it should enable us to increase the efficiency of gene transport into the cell. Indeed, this is the case for all drug delivery systems which deliver their therapeutic payload into the cell including; nanoparticles [28], dendrimers [29], polymer-drug conjugates [30], microparticles [31] and liposomes [32].

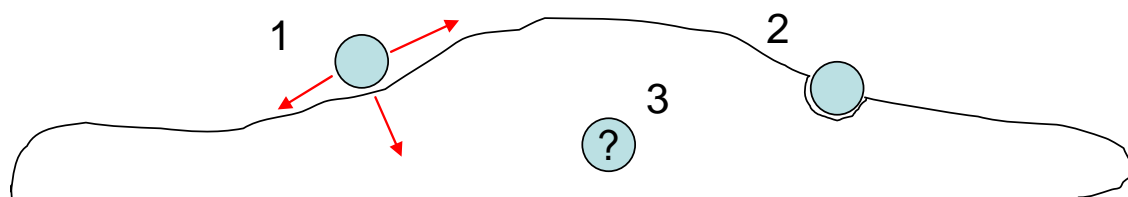


Figure 1.3 Nanoparticle-cell interactions

This schematic illustrates the key areas which need to be considered when investigating nanoparticle-cell interactions. 1) Initial ‘docking’ of particle onto the cell membrane. This can take place through receptor-ligand binding (e.g. targeting of transferrin receptor [33]) or electrostatic interactions with the cell membrane (e.g. through using cationic lipids [34] or polymers [35]). It is also important to know whether the particle is presented singularly or as an agglomerate [36]; 2) Movement of the particle from the cell membrane into the main cell body takes place through a process known as endocytosis. There are several different routes through which the particle may be endocytosed in mammalian cells. This includes clathrin mediated endocytosis, caveolae endocytosis, phagocytosis and clathrin-independent endocytosis; 3) Translocation of the particle within the cell occurs after the particle has been internalised. It is known that the mechanism of endocytosis, such as via clathrin or caveolae, greatly influences the final destination of the particle within the cell. The particle efficiency and/or toxicity may be dependent upon where the particle ends up within the cell.

The second question regards how the particle traverse's the cell membrane and what impact this has upon its subsequent sub-cellular localisation. Generally, for a therapeutic nanoparticle to exert its effect, it must interact with cells in some way, either by docking onto the cell and releasing its therapeutic payload, or by being internalised into the cell and subsequently exerting its effect. There are several ways in which a particle can be internalised by the cell including; clathrin mediated endocytosis (CME), caveolae endocytosis, phagocytosis, pinocytosis (fluid phase internalisation) and clathrin/caveolin independent endocytosis. The most widely studied endocytic mechanism—not necessarily with reference to drug delivery—is that of the clathrin mediated route. Currently, the understanding of the entry route is limited, with most research focusing on the final localisation of the particle in the cell [37]. The limited body of studies performed to date have utilised biochemical blockers which prevent cellular processes involved in particle internalisation. However, this approach suffers from specificity problems, as these inhibitors inherently cause other mechanisms to be affected in addition to the one under analysis, making clear distinctions difficult [38].

The route of entry into the cell is very important for determining the final intracellular location of the particle and its resultant efficacy and/or toxicity. For example, 60 nm NH₂-labeled polystyrene (PS) nanospheres are internalised via caveolae in human epithelial (BEAS-2B) cells and an unspecified mechanism in pheochromocytoma (PC-12), resulting in a significantly higher toxicity in the epithelial cell line [39]. Another important consideration is that clathrin mediated endocytosis is often reported to result in the delivery of the nanoparticle to a lysosome, resulting in degradation, if the device is pH sensitive. This can be advantageous if using a pH sensitive delivery device, where

upon a drop in pH it releases its therapeutic payload. Conversely, if delivering DNA, it will ultimately lead to its destruction due its inherent instability at acidic pH. Additionally, Lysosome's contain digestive enzymes, known as acid hydrolases, which can also lead to degradation of sensitive material such as DNA and RNA.

Therefore, for the delivery of, particularly, biologicals, it is essential to control the mechanism of entry into the cell, and consequently their intracellular trafficking, through rational design of the delivery system. For example, when designing a gene delivery device it is important to make sure it is not internalised via CME (clathrin mediated endocytosis) as this typically results in translocation to acidic lysosome's resulting in degradation [40, 41]. However, precise data regarding the key attributes needed to target a particular pathway, and the relationship between the particles biophysical properties and its intracellular fate is currently limited. The resulting situation is that in many cases the device is not internalised, and if it is it tends to be less efficient than administering 'free' drug or the currently marketed formulation. Currently, it is known that changing the shape [42], size [43] and surface charge [44] can affect the endocytosis of particulates. Conjugating particles with surface ligands such as transferrin, folate and peptide molecules can also affect their endocytosis [45-48].

The aims of this thesis are to provide an insight and further understanding into particle endocytosis in living cells through development of novel optical microscopy techniques.

1.1.2 Ideal properties of a particulate drug delivery imaging technique

Cell-based assays are an important part of the drug discovery process allowing for interrogation of targets and pathways in a more physiological setting compared to biochemical assays. One of the main hurdles in the cell-based assay field is to design sufficiently robust assays with adequate signal to noise parameters while maintaining the inherent physiology of the pathway or target being investigated. Conventional label and reporter-based cell assays may be more prone to artefacts due to considerable manipulation of the cell either by the label or over-expression of targets or reporter proteins. Cell-based label-free technologies preclude the need for cellular labelling or over-expression of reporter proteins, utilising the inherent morphological and adhesive characteristics of the cell as a physiologically relevant and quantitative readout for various cellular assays. When considering the development of a microscopy system for imaging of colloidal drug particle endocytosis, one needs to consider the characteristics needed to give reliable and robust information.

Table 1.1 outlines the ideal characteristics of a NCI imaging technique. In addition to the physiological arguments outlined above for having a *label-free* system, it is also beneficial due to its relative simplicity, low cost and low levels of light toxicity introduced to the cell. The major drawback associated with a *label-free* optical microscopy system is that it is difficult to image specific cellular components and/or small particles (<200 nm). Generally, it is difficult to image specific routes of endocytosis without utilising fluorescence, either through green fluorescent protein

(GFP) technology in living cells or fluorescently tagged antibodies in fixed cells. Therefore, a trade-off exists between having a completely *label-free* imaging system and the need for labelling specific cellular components for detection of individual endocytic mechanisms.

Another beneficial characteristic of a NCI imaging system is to have high spatial and temporal resolutions, which enables precise localisation of particles and cellular components with the temporal resolution required to follow the dynamic process of endocytosis. Ideally, the technique should also minimise potential toxicity to the cell. This may be achieved through, for example, the use of high-end electron multiplying charged coupled device (EMCCD) cameras, which allows the user to reduce the photon load experienced by the cell and hence help to decrease phototoxicity. Finally, the technique should be suitably sensitive to image the particle/molecule/protein of interest.

Table 1.1 Ideal properties of an imaging system for studying nanoparticle entry into living cells

Property	Description
Label-free	To image cell and/or colloidal drug delivery system without the need for a marker, such as a fluorescent molecule.
Temporal resolution	Sufficient resolution to record dynamic cellular events such as membrane invagination.
Spatial resolution	Sufficient resolution to detect single particle endocytosis.
Cell perturbation/toxicity	Technique should not introduce unnecessary toxicity to cell. This could be caused by over-exposure to illumination light or through free radical generation by fluorescent molecules.
Sensitivity	Technique should be suitably sensitive to detect different nanoparticle formulations and sizes.

1.2 Microscopy fundamentals

Before discussing the various microscopy techniques that have been utilised to study the interaction of drug delivery systems with cells, it is important to discuss the fundamental principles of microscopy. These principles which include resolution, point spread function and the Abbe limit, are outlined below.

1.2.1 What is resolution?

It is important to understand the meaning of the word resolution when applied to optical imaging and to distinguish it from other terms such as sensitivity, sampling and precision. For example, it is possible to have a very sensitive light microscope which makes it possible to see a 50 nm polymeric particle or even a single fluorescent molecule. However, this means we only have single molecule sensitivity, even though the size of such a molecule could still correspond to 500 nm in the sample coordinate system, meaning the system has relatively poor optical resolution.

Another important difference which can sometimes become confused is that between resolution and sampling (in relation to magnification). It is simple to magnify an object by optical means, however, the process of magnification does not increase the optical resolution; at best it preserves it. In the case of a sample being imaged onto a CCD camera, it gets sampled into a discrete set of measured intensity values, one for each detector element, i.e. a pixel. Magnification needs to be adjusted such that the finest level of detail present in the sample is still measured (sampled) by at least two detector

elements, but greater sampling will not yield any new information about the sample. A process known as empty magnification occurs where there is magnification significantly beyond this limit.

Specific questions in cell biology which may be addressed by microscopic methods could be for example, determining the distance between two molecules of interest in a sample. In this case, there is no need for resolution in the order of this distance, but the error of localisation (reciprocal of localisation precision) needs to be below this expected distance. Localisation precision can be far higher than the optical resolution, for example, the localisation error of single molecules can be smaller than 10 nm on a system of 200 nm optical resolution. The higher the resolution the better the localisation precision, but how much better than the optical resolution, has a strong square root dependence on the number of photons collected from the target.

When the term high-resolution is used within this chapter, it is the ability to see a structure at a high level of detail that is meant. The Rayleigh resolution limit uses the example of two point-like objects and defines the resolution as the distance, where the maximum in each of these objects occurs at the position where the image of the other object has its first intensity minimum, i.e. two patterns will be distinguished when the central maximum of one pattern lies over the first minimum of the other. The diffraction limit as given by the Rayleigh criterion is:

$$d_{\min} = 0.61 \frac{\lambda}{NA} \quad (1.1)$$

where λ is the wavelength of light being used and NA is the numerical aperture of a microscope objective. Numerical aperture is defined as the sine of the angular semi-aperture in the object space multiplied by the refractive index of the objective space. Two identical diffraction limited spots cannot be distinguished if their separation distance is less than d_{\min} . To increase the lateral resolution of the system, one needs to decrease the value of d_{\min} , which can be realised by reducing the illumination wavelength (λ) or increasing the NA of the objective lens. For example, at $\lambda = 0.6328 \mu\text{m}$ using 0.4 NA and 1.45 NA objectives, the obtainable lateral resolution is $0.97 \mu\text{m}$ and $0.28 \mu\text{m}$ respectively.

1.2.2 Point spread function

The point spread function (PSF) shown in Fig. 1.4, is the response of an imaging system to a point source (in theory an infinitely small emitter). As a sample can be thought of consisting of many points each with its own intensity, the image can be described as an equivalent sum of corresponding PSFs. Since the PSF is determined entirely by the microscope, the whole image can be described by knowing the optical properties of the system. This process is usually formulated by a mathematical operation called convolution.

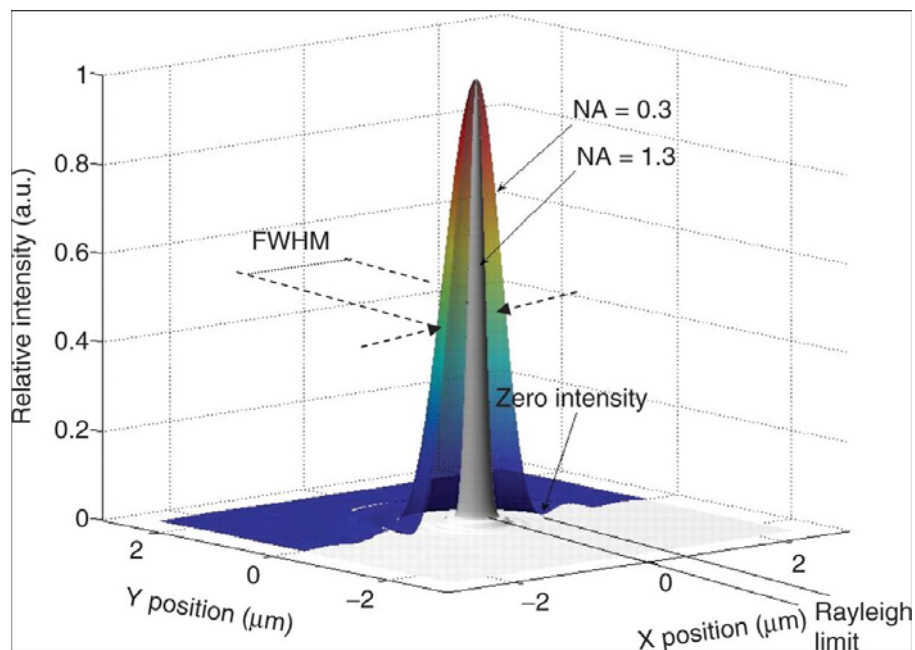


Figure 1.4 The point spread function

Two PSFs are shown, one for high numerical aperture ($NA = 1.3$ in grey) and one for $NA = 0.3$ (coloured). At low NA the PSF is wide and has well-defined positions of zero intensity, leading to the definition of the Rayleigh limit. The high NA PSF (uniformly grey peak in the middle) is much finer. FWHM – Full width half maximum. Reprinted from [49], with the kind permission of Oxford University Press.

1.2.3 The Abbe resolution limit

The Abbe limit corresponds to the distance of the finest periodical structure which can be imaged by a diffraction limited optical microscope. According to Abbe, for brightfield microscopy, a detail with a particular spacing in the specimen is resolved when the numerical aperture (NA) of the objective lens is large enough to capture the first-order diffraction pattern produced by the detail, at the wavelength employed. The NA of the system, along with the illumination angles and the wavelength, thus define the Abbe resolution limit:

$$d = \frac{\lambda}{NA_{\text{illumination}} + NA_{\text{detection}}} \quad (1.2)$$

In the case of fluorescence microscopy, the image of a fluorescent molecule will be formed by the waves leaving this molecule and by their coherent interference for each wavelength in the image plane. For the detection of a widefield fluorescence image the corresponding Abbe limit becomes:

$$d = \frac{\lambda}{2NA_{\text{detection}}} \quad (1.3)$$

The factor of two in Eq. 1.3, when compared with $NA_{\text{detection}}$ in Eq. 1.2, stems from the fact that in an incoherent fluorescence PSF, the finest detail stems from mutual interference of the highest angled rays (e.g. left with right side), whereas in brightfield transmission, the finest scattering structure would be defined by the difference of the incident illuminating ray (e.g. in the middle of the aperture) and the highest angled rays that are captured (e.g. at the side of the aperture).

1.3 Brightfield microscopy

Imaging living cells with transmitted light is often used in conjunction with fluorescence microscopy in order to provide information on cell shape, position, and motility [50]. Techniques such as phase contrast [51] and differential interference contrast (DIC) [52] are the most common examples of brightfield microscopy and are used in most bio-research labs for routine cell analysis. Phase contrast works by converting the otherwise invisible small phase changes—generated as light passes through a sample—into amplitude or contrast changes in the image. These phase changes can be easily observed when they are interfered with a reference beam. One of the problems suffered by the phase contrast microscope is the production of a halo around the image, this can, however, be overcome through the use of DIC microscopy.

In DIC, a polarized light source is split into two spatially offset beams with a Wollaston prism and these beams pass through the sample. The optical path lengths of the two beams differ as a result of changes in optical density (RI-refractive index) experienced by each path. After the beams have been recombined and interfered, the phase differences (introduced as a direct result of the changes in optical density) cause the generation of image contrast. The main limitations of brightfield microscopy for live cell biology include the fact that it cannot be used to identify specific organelles and its inability to image thick biological samples. For the study of nanoparticle-cell interactions, one of the main limitations is its limited axial resolution, i.e. it would be difficult to determine whether a particle is either inside or outside the cell membrane. However, its main advantage is that it affords *label-free* detection.

1.4 Confocal Microscopy

The confocal laser scanning microscope (CLSM) came on the market in the late 1980's and soon caused a rapid increase in publications on cell biology and drug delivery applications. The CLSM utilises fixed-line laser illumination for excitation of a fluorescently labelled specimen and detects the emitted fluorescence through photomultiplier tubes. Through careful positioning of a pinhole in a plane conjugate to that of the image, and the scanning of a focussed laser beam across the sample, it is possible to restrict fluorescent collection to that of the image plane. This means that the axial resolution is significantly improved over that attainable in the standard wide-field fluorescent microscope. Spinning disc confocal microscopes work by illuminating the sample with >1000 mini-beams of light, passing through a spinning disc containing a number of mini-lenses. Emitted light is then collected with a CCD, instead of raster scanning a single point across the sample. The Spinning disc confocal is generally considered to be better for imaging living samples since the method of illumination affords faster imaging and less photobleaching than scanning microscopes. Their key disadvantage is that they are less easily configured than laser scanning systems (particularly in terms of imaging multiple fluorophores) and cannot be used for photobleaching and photoactivation experiments [53]. Additionally, the spinning disc confocal microscope is not known to have the same optical sectioning capability, in thick samples, as the CLSM.

There are numerous examples of the use of CLSM for imaging drug delivery in living cells [53-57]. It is possible to speculate on a number of possible reasons for this.

Firstly, confocal microscopes can be found in most pharmaceutical research departments, making them widely accessible. Secondly, the technique allows one to determine the precise location (in x , y and z space) of the particle in the cell. For example, consider a particle that is interacting with a cell membrane, under widefield fluorescence microscopy it would be difficult to determine the precise axial location of the particle whereas the ability to optical section with CLSM allows one to determine if it is within the cell membrane or not. It is important to remember however, that the imaged location of the particle is determined by the resolution of the system. Thirdly, the application of two-photon confocal microscopy affords particle detection in thick biological samples such as tissue [58].

The major drawback of CLSM in the study of nanoparticle-cell interactions is its inability to accurately co-localise two or more different points, since the maximum axial resolution of CLSM is approximately 500 nm and 800 nm for one- and two-photon systems respectively. These points could, for example be a nanoparticle and a fluorescently tagged marker of endocytosis, such as clathrin. In this case it is difficult to be exactly sure of the precise position of the particle in relation to the marker of interest. This is true of all fluorescent microscopy techniques, however, techniques such as total internal reflection fluorescence microscopy (TIRF) afford greater resolution in the axial direction. Other limitations of CLSM include poor frame rate when compared with widefield techniques (spinning disk confocal systems somewhat increase the temporal resolution but with a trade-off in sensitivity), potential for photobleaching and phototoxicity and that they are not well suited to long-term live cell imaging.

1.5 Evanescent wave techniques

1.5.1 Surface plasmon resonance microscopy

Surface plasmon's (SPs) are electromagnetic radiation that propagate along the interface between dielectrics and a conducting layer [59]. Typically, the conductor is a thin metal film—with a thickness of approximately 50 nm for optimum excitation—such as gold, silver and more recently aluminium [60]. One of the principal properties of this conducting film is its inherent negative charge. Several of the most important properties of SPs are illustrated with reference to the Kretschmann configuration illustrated in Fig. 1.5.

The incident beam in the case of surface plasmon resonance microscopy (SPRM) must be *p*-polarized (plane polarized) in order to ensure that the carriers oscillate parallel to the direction of propagation along the interface; a necessary condition for SP excitation. In the Kretschmann configuration, the reflection coefficient for *p*-polarized light will suffer a minimum when the incident angle (θ_i) is approximately 40° for gold on glass in air. This minimum corresponds to the excitation of SP's propagating along the film-dielectric interface and being absorbed in the film. In this configuration, the \mathbf{k} vector—also known as the wave-vector—of the SP is greater than light in free space so that excitation on to a planar interface requires that the refractive index of the medium from which the wave is excited (i.e. the prism) is greater than that of air [59, 60].

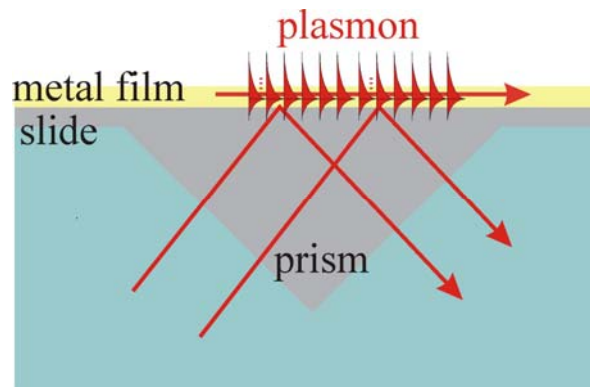


Figure 1.5 Schematic diagram showing the Kretschmann configuration for the excitation of surface plasmon's

A laser beam is introduced into the side of the prism and undergoes total internal reflection resulting in evanescent wave generation. When the beam is introduced at a specific angle, known as the plasmon angle, it results in the excitation of surface plasmons in the thin gold layer.

Since the \mathbf{k} vector of the surface wave in the direction of the propagation is greater than that of a plane wave in the upper dielectric, the wave is evanescent here, decaying exponentially away from the surface over distances of the order of 100 nm. It is the large field enhancement which occurs at the interface between the metal film and upper dielectric that makes SPs so useful from the point of view of sensors. The presence of a dielectric in contact with the conducting layer will affect the \mathbf{k} vector for SP propagation so that the value of θ , where the reflection coefficient is at a minimum will change. This θ change can be detected by surface plasmons for layers of atomic thickness and fractions of monolayers.

The technique of SPRM harnesses the great sensitivity of surface plasmons and couples it with the spatial capabilities of traditional imaging devices. The principle of SPR imaging was first introduced by Yeatman and Ash [61]. The authors based their imaging system on a modification of the Kretschmann configuration. Others were also

successful in developing SPRM instruments in this period [62, 63], with both scanning and widefield instruments having been reported.

The major drawback of SPRM based on the Kretschmann configuration is its poor lateral resolution—in the order of several μm —compared with conventional microscopy. This can be attributed to the fact that lateral resolution is determined by the propagation length of the SP, which in gold at 633 nm wavelength is approximately 7 μm [59]. Researchers have applied various methods to try and improve upon this limited lateral resolution. Giebel *et al.*, utilised aluminium as the thin conducting layer since it has a higher absorptivity than gold at the illuminating wavelength, with the resultant effect of reducing SP propagation length [64]. Others have operated at a shorter illuminating wavelength, for example 530 nm, where the propagation length will be approximately 2 μm . The problem with these two approaches is that the improvement in resolution is at the expense of the very sensitivity that makes the technique so appealing.

Kano and co-workers demonstrated that SPs may be excited using an oil immersion objective [65]. Here the objective lens generates a range of angles, some of which excite SPs. The SPs scattered out into propagating light can be subsequently collected by a dry objective on the other side of the sample in a transmission configuration. However, this instrument is limited by the need for two objective lenses. Recently, developments in scanning SP microscopy have allowed the same objective to be used for both the collection and detection of the light. In a method developed by Somekh *et al.* (2000), the authors used a heterodyne interferometer arrangement, in which the interference

signal is determined principally by two contributions: one due to normally reflected light and the other due to light that is converted to SPs. The system resulted in excellent contrast and sub-micrometer resolution when the sample was moved above the focal plane towards the objective i.e. it was defocused. This confirms that SP image resolution could in essence be diffraction limited rather than propagation limited, as is the case with the Kretschmann configuration. The spatial resolution can be attributed to the self-focusing SPs, which result in an intensity peak on the optical axis of the microscope [60].

In another method developed by Kano and Knoll [66], the principle involved examining the back focal plane of the light reflected from the objective lens. In the back focal plane there is a noticeable dip corresponding to excitation of SPs. By analysing the movement of the dip as the sample was scanned it was possible to form an image of the structure under investigation. Lateral resolution of approximately 1.5 μm was achieved by the authors but this method is limited by difficulty in data processing and elimination of background signals. Recently, Stabler *et al.* have developed a Kohler illuminated high-resolution microscope using surface plasmons to provide the image contrast[59].

Toyama and co-workers used SPR imaging in conjunction with a SPR sensing system to observe the process of adsorption and desorption of polymers [67]. Here, the SPR imaging system was used qualitatively to confirm that electrochemical potential application caused the desorption of poly-l-lysine from a gold surface. Steiner and co-workers [68] developed a SPR imaging system in order to characterise patterned organic

monolayers, which are a basic commodity for the development of biochemical sensor arrays. In this paper the authors claim a lateral resolution of 2 μm using a HeNe laser source ($\lambda = 633 \text{ nm}$) and a Kretschmann prism coupler. Other applications where SPR imaging has been used include; the detection and identification of DNA and RNA by hybridization adsorption onto DNA or RNA microarrays [69, 70], protein-DNA binding using DNA arrays [71-73], kinetic studies of enzymatic reactions of peptide microarrays [72], protein interactions using protein arrays [74], and studies of DNA-DNA and DNA-drug binding kinetics [75].

1.5.2 Total internal reflection fluorescence microscopy

Total internal reflection microscopy (TIRM) and total internal reflection fluorescence (TIRF) microscopy are discussed in detail in Chapters 2 & 3 and therefore are only briefly introduced here. TIRM is a technique which generates contrast from the scattering or ‘frustration’ of a totally internally reflected light beam. If an object, of refractive index (RI) n_1 , is placed within the evanescent field of a light beam undergoing total internal reflection, at the interface between a dense (n_2) and less dense (n_3) e.g. glass and air, and n_1 is greater than n_3 , then the object will tend to scatter the evanescent light, resulting in linearly propagating light. By studying either the totally internally reflected light beam or the scattered evanescent light, it is possible to build up an image of the object under examination.

TIRF is an evanescent wave (EW) technique, where the sample is illuminated at an angle greater than the critical angle formed by the sample and its substrate. This allows selective illumination of a very thin region directly above the substrate and therefore can offer views of the basal membrane of adherent cells. The TIRF technique has been used extensively in the imaging of different systems including single molecule detection [76-78] imaging endocytic and exocytotic events [79] and analysis of cell-substrate interactions [80, 81].

1.6 Scanning Probe techniques

1.6.1 Atomic Force Microscopy

The atomic force microscope (AFM) was invented in 1986 by Binnig, Quate and Gerber [82], and its main features include the ability to image non-conductive samples—therefore a range of biological and drug particles can be studied—and the ability to measure the surface topography of samples with subnanometer resolution. During the process of AFM imaging a sharp probe tip located on the underside of a flexible cantilever, raster scans across the sample surface. The bend and twist of the cantilever due to the forces of interaction between the tip and sample are monitored via a laser beam that is reflected from the back of the cantilever onto a position sensitive, quadrant photodiode detector. A relay to a feedback loop from the photodiode and the piezoelectric position scanner helps to maintain a set deflection, amplitude, frequency or phase of the lever, dependent on the imaging mode being used [83].

AFM imaging of cells was first performed in the early 1990's [84-86]. However, there proved to be many difficulties when it came to imaging living cells with the AFM [87]. This originates from the fact that the sharp probe tip can damage the cell membrane when raster scanning the sample. Notwithstanding this problem, it is still possible to image soft samples such as cells, albeit without achieving molecular resolution. This is due to both the softness of the sample, high lateral mobility and in some cases motility of the cells [84]. Dynamic events such as cellular protrusion, filopodia and lamella extension have been successfully imaged in living rat liver macrophages (kupfer

cells) [88]. Müller *et al.*, (2003) have used AFM to image, at sub-nanometer resolution, single sodium-driven rotors from a bacterial (adenosine triphosphate) ATP synthase embedded into a lipid membrane. Using time lapse AFM imaging they were able to follow the movement of single proteins within the membrane [89].

1.6.2 Scanning Ion Conductance Microscopy

The aforementioned problems of membrane damage and ‘stickiness’, which occur when the AFM is used for bio-imaging can somewhat be overcome through the use of an alternative scanning probe technique known as the scanning ion conductance microscope (SICM). SICM was developed specifically for biology and electrophysiology because of its ability to image soft non-conductors, such as a cell membrane, covered in an electrolyte solution [90]. The principle of SICM imaging evolves from scanning conductance measurements between an electrode in an electrolyte filled micropipette and an electrode within the sample reservoir. As the pipette is scanned across the surface, the conductance varies accordingly with the ion flow between the two electrodes. If the pipette encounters an object in the reservoir, the ion conductance will decrease as the space through which ions can flow is decreased. By scanning the probe laterally across the surface and using a feedback loop to keep the conductance constant, it is possible to build up a topographical image of the surface as the tip will raise and lower in order to maintain a constant ion current between tip and sample [91].

Korchev and colleagues at Imperial College London have recently published several papers using SICM for high resolution cellular imaging, including studies on the dynamics of individual microvilli in living epithelial cells [92], cell volume measurements at 10^{-19} litre resolution [93], imaging single active ion channels in cardiac myocytes and imaging spatial distribution of maxi-anion channels in rat cardiomyocytes [94]. Shin and Gillis (2006) have recently used SICM to measure the changes in membrane surface morphology associated with exocytosis in adrenal chromaffin cells [95].

A combination of SICM and confocal microscopy, also known as scanning surface confocal microscopy (SSCM) has recently been utilised to image common endocytic pathways, including clathrin coated pits (CCPs) and caveolae [96]. The advantage of this system, over a single instrument such as TIRF or confocal, is that not only can the molecular nature of the endocytic pathway be identified but also its size and location. This is advantageous because with all fluorescent techniques it is difficult to determine the exact location of the endocytic pit relative to the cell membrane since the membrane position is hard to define. SSCM affords gathering of high resolution structural information on the pit of interest, previously only achievable using electron microscopy techniques.

A similar cell sample as described above was imaged using a combination of AFM and fluorescence microscopy. However, for this technique, the membrane has to be stripped from the cell and re-adhered to a suitable substrate prior to imaging [97]. AFM can also result in unwanted deformation of the plasma membrane resulting in skewing of the

image and also the pits and valleys associated with endocytosis are poorly visualised [98]. The major advantage of SSCM is the fact that it can also be applied to imaging endocytic pits in living cells [96]. Compared with fluorescent microscopy, the main advantage of SICM arises from the fact that the position of fluorescently labelled particles can be accurately related directly to the topography of the cell surface, without the need for additional fluorescent markers. Also, since only the sample surface is scanned, intracellular autofluorescence is reduced. This makes it possible to count single virus labelled particles on an undulating cell surface as accurately as if they were spread on a flat surface. SSCM has recently been used to show the distribution of 50 nm latex particles on the surface of immortalised alveolar type II cells [99].

Both the SICM and SSCM techniques offer much potential for future studies of nanoparticle-cellular interactions. For example, it may allow a greater insight into the initial stages of particle internalisation. When particulate drug delivery systems are delivered to cells, little is known about their lateral movements on the cellular surface. For example, do they simply move around the surface until they reach a preformed endocytic pit or do they adhere to the surface immediately, causing the cell to recruit endocytic machinery to the area? Answering these questions may allow more rational design of drug delivery systems. For example, if it is found that the particle rolls around on the surface until reaching a preformed pit, then it may be possible to design particles which will afford greater movement on the surface.

Another significant advantage of SICM is that it does not require either the cell or the particle to be labelled, however for identification of specific cellular components,

labelling is required. The current drawback for studying NCIs is the poor temporal resolution of the technique. This has been reported to be on the order of 18 minutes for a virus internalisation study. The authors believe that this can be reduced to 30 – 50 seconds by using a faster piezo and by scanning a smaller area, making it possible to study many uptake events [100]. Another useful feature of SICM is that materials such as particles or ions may be deposited in a controlled manner through the pipette onto cells. It may be possible to use this controlled deposition to place particles directly onto endocytic pits on cell surface. Additionally, multiple tips can be used with the SICM system, affording concomitant imaging and deposition.

1.6.3 Near-field scanning optical microscopy (NSOM)

As previously discussed in Section 1.2, the diffraction limit of light has proved a considerable obstacle in achieving higher resolution cellular imaging. However, several techniques have recently been developed to break through this barrier. When high resolution is mentioned, it is assumed that the spatial resolution is equal to or better than 200 nm. High resolution microscopy is traditionally thought of as almost exclusively electron based. Techniques such as the scanning electron microscopy (SEM) and transmission electron microscopy (TEM) offer superb resolution but lack the advantages associated with optical and fluorescence microscopy, such as the ability to image living cells and closely follow the dynamics of multiple proteins through tagging with green fluorescent protein (GFP) or one of its variants.

One of the first suggestions for breaking the diffraction limit was made by E. H. Synge in 1928 [101]. Synge contemplated what would occur if light passing through an aperture, of diameter smaller than the wavelength of incident light, were to be placed so close to a sample surface that the separation distance was smaller than the incident light wavelength. He concluded that the light passing through the aperture would not have sufficient distance to diffract before hitting the sample and passing back through the aperture. In this case, the resolution is dependent only on the probe size and the probe to sample distance. The validity of Synge's concept was first demonstrated in 1972 by E. A. Ash and G. Nicholls, who attained $\lambda/60$ resolution by using $\lambda = 3$ cm microwaves [102]. It was a further 12 years before the technique was successfully applied at optical wavelengths [103, 104], and it became known as NSOM. Resolutions as low as 25 nm have been achieved ($\lambda/20$), which is an order of magnitude better than that of conventional optical microscopy. Although NSOM has been used to study the nanoscale organisation of some proteins [105, 106], imaging in the near-field is technically challenging. The aperture probe is difficult to manufacture, and the need for feedback to maintain a constant distance from an irregular sample limits the speed of image acquisition. Additionally, NSOM is exclusively a surface imaging technique and has rarely been applied to living cells. These technical challenges and imaging limitations have prevented the widespread use of NSOM in cell biology.

1.7 Far-field super-resolution techniques

The NSOM technique is an example of near-field super resolution imaging. The near-field can be considered as a region close to the source within a radius (r) much smaller than the wavelength of the illumination source. The limitations associated with NSOM, such as difficulty with sample manipulation, fixed cell imaging and lack of 3D imaging can be overcome by using far-field super resolution imaging. The fundamental difference between NSOM and far-field microscopy is that lenses are used in the latter technique. In far-field super-resolution imaging the key to overcoming the diffraction limit is to spatially and/or temporally modulate the transition between two molecular states of a fluorophore, e.g. a dark or bright state. Several techniques achieve super-resolution by sharpening the axial and lateral width of the PSF of an ensemble image of many fluorophores. Such techniques include stimulated emission depletion (STED) [107], ground-state depletion (GSD) [108], saturated structured illumination microscopy (SIM) [109-111] and its recent combination with I⁵M, known as I⁵S [112]. Other super-resolution imaging techniques detect single molecules and rely on the principle that a single emitter can be localised with high accuracy if sufficient numbers of photons are collected [113]. Techniques include photoactivated localisation microscopy (PALM) [114], fluorescence photoactivation localisation microscopy (fPALM) [115] and stochastic optical reconstruction microscopy (STORM) [116]. Of these techniques, only those with applications in cell biology and potential applications in nanoparticle-cell interactions are discussed below.

1.7.1 Stimulated emission depletion

STED was the first far-field super-resolution imaging technique to be applied to cell (*S. cerevisiae* yeast cell) imaging [117]. The basic principle of STED is to deactivate excited fluorophores surrounding the centre of the scanning spot by a process known as stimulated emission (process whereby excited fluorophores exposed to the STED beam are transferred back to their ground state). This can be achieved using two laser beams for illumination. Firstly, the sample is illuminated by an excitation laser pulse, which is immediately followed by a red-shifted pulse called the STED beam. The non-linearity associated with the de-excitation of the excited state is the basis of breaking the diffraction limit in STED imaging. Even though both the beams used in the system are inherently diffraction limited, the STED beam is modified to feature a zero intensity point at its centre and strong intensities in the surrounding peripheral area, resulting in a doughnut shaped pattern. Illuminating the sample with the two beams superimposed causes only those molecules present within the zero intensity area (i.e. the centre of the doughnut) to fluoresce. STED effectively narrows the PSF, and ultimately the resolution is beyond the diffraction limit. A complete image is obtained by scanning a zero intensity spot across the sample. The technique has recently achieved 20 nm lateral resolution [118] and 45 nm in three dimensions [119].

STED has been applied to several biological problems including the resolution of synaptotagmin-1 in individual synaptic vesicles (~ 40 nm in size) [120], determining the size and density of syntaxin-1 clusters in PC12 cells [121] and visualisation of the nicotinic acetylcholine receptor [122]. Two-colour STED has also been achieved

enabling co-localisation studies of two mitochondrial proteins [123]. This is impressive since the entire mitochondrion is only ~200 – 500 nm. Video-rate imaging of synaptic vesicles has also been achieved in live hippocampal neurons with a lateral resolution of 62 nm [124]. An important recent development has been the ability to acquire time-lapse images in live mammalian cells with <50 nm resolution [124]. The use of fluorescent proteins in this study as opposed to an antibody label has greatly improved the functionality of this system by opening it up to live cell imaging.

At the moment STED remains a highly complicated system to implement and has been mainly consigned to the labs of Stefan Hell who invented the technique. The demonstration of STED using continuous wave beams has been recently reported [125]. This has the potential to be implemented in any conventional confocal setup which should greatly improve the availability of the instrument. Leica offer a STED module for attachment to their TCS confocal microscope which has a lateral resolution of 70 nm, however the high cost does remain a barrier to widespread use [126]. The application of STED to studying nanoparticle-cell interactions has many advantages. 3D multi-colour STED has the potential to follow single nanoparticles (<100 nm) from the moment they interact with the cell to their final destination. This should give an unparalleled view of the dynamics and interactions of nanoparticle within in the cell and greatly enhance our understanding of how nanoparticle drug delivery systems work in living cells.

1.7.2 Pointillist microscopy

Both PALM and STORM can be thought of as forms of pointillist microscopy. Pointillism is more commonly known as a style of painting where small distinct points of primary colors create the impression of a wide selection of secondary and intermediate colors. One of the most recognisable paintings in the pointillism style is Seurat's masterpiece *A Sunday Afternoon on the Island of La Grande Jatte* (1884-1886). From a distance the picture represents a scene of people resting by the Seine. However, upon closer inspection it is revealed that the painting is made up of thousands of millimeter sized dots that, through optical unification, form a single hue in the viewer's eye. Even though it is the thousands of dots that make up the picture, it must be viewed as a whole to fully appreciate the context and meaning of the dots [127]. In pointillist microscopy, the basic principle is to build up an image over several frames, of precise single molecule localisations by means of either photo-switchable fluorophores (STORM) or through photobleaching of activated fluorophores (PALM). These techniques are discussed in more detail below.

1.7.2.1. Photoactivated localisation microscopy

Whereas STED involves the imaging of an ensemble of molecules i.e. a number of molecules close together are excited, PALM is truly a single molecule technique. Rather than modify the excitation light pattern to yield a smaller PSF, as in STED and SSIM, image resolution below the diffraction limit is achieved by precisely determining the positions of the fluorophores labelling the sample. The precise position of a single molecule can be determined to 1 nm accuracy or better if enough photons are collected

and there are no similarly emitting molecules within ~ 200 nm [128]. Localisation accuracy does not, however, directly translate into super-resolution images since overlapping images of these fluorophores would prevent their accurate localisation. In PALM this may be overcome by serial activation, localisation and bleaching of numerous sparse subsets of photoactivatable fluorescent molecules. The aggregate position information from many such molecular subsets is then assembled into a super-resolution image [114, 129]. Imaging of single molecules is made possible through the use of fluorescent photoactivatable labels. Generally, they start out in a dark state and can be activated with weak excitation light causing a few molecules to fluoresce. These are then subsequently imaged and deactivated (photobleached), before the process is repeated for many cycles. Through reconstruction of each image it is possible to build a super-resolved image.

PALM has been used for two colour imaging of actin and adhesion complexes in fixed cells [130]. PALM has also been extended to 3D imaging, achieving 30 nm resolution in the xy plane and 75 nm resolution in the axial dimension [131]. Another group have used a combination of PALM and two-photon temporal focussing to enable 50 nm lateral resolution over an axial range of ~ 10 μm in both mitochondrially labelled fixed cells and in the membranes of living *S2 Drosophila* cells [132]. Perhaps the most significant advancement in PALM microscopy has been its extension to live cell imaging [129, 132-134]. An example of this is where Shroff and colleagues have imaged adhesion-complex dynamics in live CHO cells with 60 nm resolution at an imaging speed of 25-60 seconds per frame. Vesicle transport, however, occurs at speeds up to 400 times faster than the previously reported adhesion dynamics [135]. This

means it would be difficult to follow dynamics of nanoparticle transport inside cellular vesicles, assuming they travel at the same speed as the vesicles. Currently only a small number of photoactivatable fluorescent molecules are available, making widespread use of the technique limited.

1.7.2.2 Stochastic optical reconstruction microscopy

In essence, STORM is very similar to the PALM technique, with the major distinction being that a photoswitchable fluorophore is used as opposed to a photoactivatable molecule. In STORM the molecules are reversibly switched between the light and dark states, whereas in PALM they are irreversibly bleached. STORM was developed by Zhuang and co-workers who demonstrated an imaging resolution of 20 nm using a cyanine switch (Cy3-Cy5) [116]. The same group have used two-colour STORM to reveal the organisation of microtubule networks and clathrin coated pits in fixed mammalian cells with a resolution of ~ 20 nm [136]. Three-dimensional super-resolution imaging has also been achieved with STORM. Huang and colleagues have performed STORM imaging with 20 – 30 nm lateral resolution and 50 nm axial resolution [137]. The drawback, however, is that only relatively thin samples can be imaged. This has recently been improved through the use of focal plane scanning to image substantially thicker samples and to achieve multi-colour high-resolution whole cell imaging [138]. In this work, spatial resolution of 20-30 nm and 70 nm in the lateral and axial dimensions respectively have been achieved. The 3D-STORM images revealed mitochondrial morphologies as well as mitochondria-microtubule contacts that were obscured in conventional fluorescence images. At present, live cell STORM

imaging has not been performed. This may be accounted for by the fact that many imaging cycles are currently needed to build up one super-resolution image and that the resultant high photon load is harmful to the cell. 3D-STORM has recently given truly astounding images of clathrin coated pits in BS-C-1 cells including the circular ring-like structure of the pit periphery, previously only resolvable using EM techniques [137].

1.7.3 Structured illumination microscopy

Structured illumination microscopy (SIM) is a technique which overcomes the classical diffraction limit by means of spatially structured illumination in a standard widefield fluorescence microscope setup. If a pattern with features too fine to be imaged by a conventional microscope, for example fluorescent proteins in a cell, is illuminated with a series of excitation light patterns, then the normally inaccessible high resolution information will be encoded in the observed image. This image will be a set of low-resolution Moiré fringes which contain information about the original fine pattern. Following the collection of a series of images under different excitation patterns (position and orientations), a high resolution image can be reconstructed using linear processing mathematical techniques [109, 139]. In comparison to confocal microscopy, structured illumination captures high spatial frequencies of the sample much more efficiently, and thus allows for a factor of two resolution improvement, albeit at the expense of requiring extensive computational reconstruction. The speed of imaging, afforded by the widefield nature of the systems makes this an attractive option for studying dynamic process within the cell e.g. endocytosis.

3D structured illumination microscopy (3D-SIM) is a technique that builds upon the successful lateral resolution enhancement achieved with 2D-SIM. By using three beams of interfering light, compared with two in the 2D system, it is possible to achieve resolution enhancement in both the lateral and axial directions. 3D-SIM is currently the only sub-diffraction resolution imaging technique that allows detection of three or more wavelengths in the same sample, using standard fluorescent dyes, with 3D optical sectioning and enhancement of resolution in both lateral and axial directions [140]. The authors have demonstrated a resolution of 100 nm, thus affording the detection of novel cytological features. For example, they were able to image nuclear invaginations which were previously only detectable by TEM. The level of resolution afforded by 3D-SIM is less favourable when compared to the aforementioned PALM, STED and STORM techniques. However, 3D-SIM is the only technique to offer both multicolour 3D images of whole cells with enhancement of resolution in both lateral and axial directions [111]. The major drawback with this type of microscopy is that it is currently only applicable to fixed cell lines, thus making the imaging of dynamic cellular processes beyond reach. Also, the light load experienced by the cell is potentially large.

1.8 I₅M and 4Pi microscopy

I₅M and 4Pi are techniques which have been developed by Gustafsson [141-143] and Hell [144-150] respectively that have resulted in a 3-fold improvement in the axial resolution compared with confocal fluorescence microscopy. As the name 4Pi suggests (a full sphere has a solid angle of 4π), the idea is to get as close as possible to illumination and detection from all sides of the sample. In practical terms this can be achieved by focusing excitation light through two opposing high numerical aperture objective lenses in a coherent manner onto the same spot and/or by coherently detecting the emerging fluorescence light through both lenses. An *xy*-image is produced by either scanning the beams or the laser source. Axial resolution on the order of 100 nm has been achieved using 4Pi microscopy. The main difference in I₅M microscopy is that the laser source is replaced by a spatially incoherent illumination source such as an arc lamp, thus making *xy*-scanning redundant. There is practically no *xy*-resolution improvement in either of the techniques as compared to a standard confocal microscope.

1.9 Summary

The super-resolution techniques described above all offer superb potential for the imaging of NCIs but currently they are restricted to but a few labs world-wide. Also, although the resolution of techniques such as STED and PALM are unparalleled for far-field optical techniques, there is an issue surrounding the trade-off between signal-to-noise and sensitivity. Generally, if a technique increases the resolution beyond the diffraction limit it will result in a decrease in the signal-to-noise thus meaning a larger photon load is needed to image the sample [151, 152]. In the case of a small particle (<50 nm) the number of photons emitted may be insufficient to enable it to be imaged using these techniques. The scanning probe techniques such as AFM and SICM have also not been considered since, the temporal resolution of the techniques are still too low to record dynamic events such as endocytosis. In the future, SICM may prove useful if the scan time can be reduced. The light microscopy techniques such as DIC and phase contrast are useful to give a *label free* image of the whole cell however, they do not offer any depth discrimination and have diffraction limited lateral resolution. An overview of the spatial and temporal resolution of various microscopy techniques can be seen in Fig. 1.6.

Having discussed some of the main techniques which have been used or have potential for imaging NCIs, it is important to come to a conclusion as to which method(s) potentially offer the chance to garner the appropriate information on particle endocytosis. This thesis is concerned with the development of a microscopy system and model cellular assay which is capable of imaging the initial interaction of colloidal

particles with the cell membrane, and its subsequent internalisation (endocytosis). As discussed earlier, one would like the system to be able to detect the drug delivery system without any prior labelling.

TIRF provides extremely high axial resolution when imaging regions in close proximity to the coverslip. For the example of a cell on a coverslip, this means it will provide a very detailed view of the cell membrane, free from background ‘noise’ originating from the cytosol. This thesis will concentrate on the development of a TIRF instrument, since it affords an excellent view of the cell membrane and endocytic events which occur here [153]. Also, it is highly amenable to live cell imaging due to its low levels of phototoxicity and photobleaching. Additionally, since it is a widefield technique the temporal resolution is excellent and depends on camera sensitivity, optical setup, illumination intensity and exposure time. Also, a large part of this thesis is concentrated on developing a *label-free* variation of the TIRF microscope called total internal reflection microscopy (TIRM). The technique was developed as a result of the criterion outlined in Table 1.1. TIRM will be introduced and discussed in more detail in Chapter 2 and 3. A summary of all the microscopy techniques discussed in this thesis introduction is presented in Table 1.2.

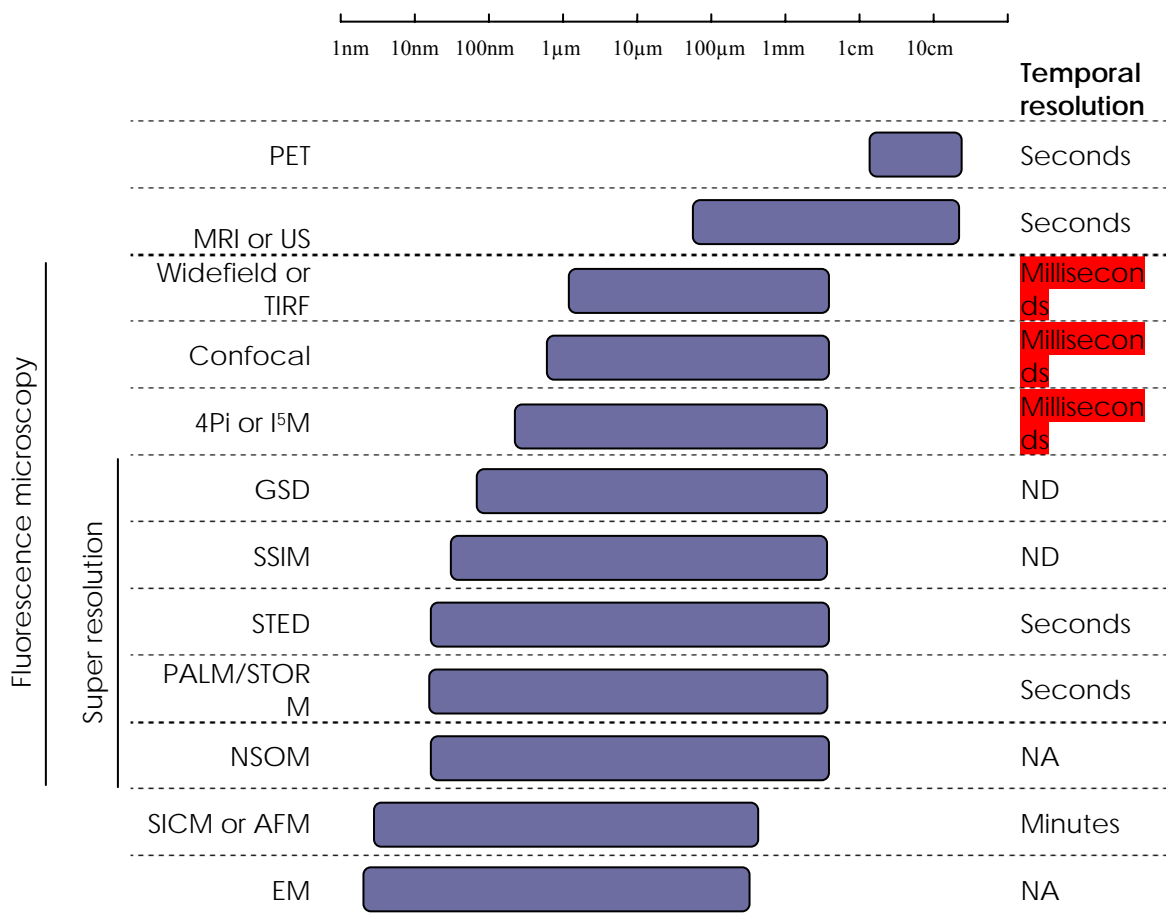


Figure 1.6 Comparison of the spatial and temporal resolutions of biological imaging techniques

The size scale is logarithmic. The spatial resolution is given for the focal plane. The temporal resolution is not applicable (NA) for electron microscopy or near-field scanning optical microscopy (NSOM) because they image static samples. Ground-state depletion (GSD) and saturated structured illumination microscopy (SSIM) have not been shown on biological samples thus their temporal resolution are not determined (ND). MRI, magnetic resonance imaging; PET, positron emission tomography; STED stimulated emission depletion; STORM, stochastic optical reconstruction microscopy; TIRF, total internal reflection fluorescence; US, ultrasound; WF, widefield microscopy.

Table 1.1 Summary of imaging systems described in this chapter

Technique	Label-free?	Live cells	Temporal resolution	Spatial resolution	Particle endocytosis
Transmitted light (DIC, phase contrast etc)	Yes	Yes	Excellent	Poor	No
Fluorescence (widefield, confocal)	No	Yes	Good	Good	Yes
Electron (SEM, TEM)	Yes	No	NA	Excellent	No
Far-field super resolution (STED, PALM & STORM)	No	No	Poor	Excellent	No
Scanning probe (AFM, NSOM & SICM)	Yes	AFM – Problematic SICM – Yes NSOM - No	Poor	Excellent	No
4Pi & I ₅ M	No	Yes		Axial – Very Good Lateral - Good	No
<i>Evanescent wave (TIRF, SPR)</i>	<i>TIRF – No SPR - Yes</i>	<i>Yes</i>	<i>Good</i>	<i>Good</i>	<i>Yes</i>

Chapter 2

Label Free Total Internal Reflection Microscopy

2.1 Introduction

2.1.1 The surface contact microscope

One of the first references to a microscopy system based on the principle of total reflection of light between a dense and a less dense medium was made by Stoney (1896). However, it wasn't until 1956 that the first demonstration of a microscopy technique based on the principle of total internal reflection (TIR) was made [154]. In this seminal work, Ambrose conceived the surface contact microscope (SCM) and applied it to studying how contact formation by moving cells influenced their subsequent behaviour. By utilising the phenomena that light will penetrate slightly into a less dense medium when undergoing total internal reflection at a glass/water interface, it afforded the ability to selectively probe the contacts formed by a moving cell [154].

Two alternate setups for SCM, as described by Ambrose (1961), are illustrated schematically in Fig. 2.1. In the darkfield version (Fig. 2.1a) light from an intense source, such as a mercury arc lamp, passes through the slit and strikes the upper surface of the 60 degree prism. A cell sample is mounted between a coverslip and a glass slide and optically coupled to the prism using immersion oil. As described in detail in Section 2.1.2, when light hits the prism at an angle greater than the critical angle for a glass/water interface it will be totally internally reflected, resulting in the formation of an evanescent field in the less dense medium.

When a cell of greater refractive index than water is moving on the surface, areas in close contact with the glass surface will enter the evanescent field and scatter the light, owing to the presence of small inhomogeneities in their structure. This is the fundamental principle of TIR microscopy. When viewed from above, the field appears completely dark, but for the regions in close contact with the glass which appear bright due to light scattering. Ambrose also noted that contours of the cell surface could be explored by changing the angle of the incident beam. When the incident angle is increased the resulting evanescent field penetration depth is reduced. This means the cell area illuminated is reduced and eventually only those regions in molecular contact with the surface may be viewed [154].

Ambrose also introduced a brightfield version of his surface contact microscope (Fig. 2.1b). Here, the object is viewed in the reflected beam. As the name suggests, the field of view appears uniformly bright when the critical angle is exceeded and objects in contact with the glass appear dark on a bright background. It is claimed that a brightfield arrangement is most satisfactory for a general view of the nature of the contacts formed by cells lying on a glass surface. For studying cell movements which involve minute but rapid changes in contact, Ambrose considered the darkfield arrangement more appropriate [155]. However, no evidence was presented to justify these claims.

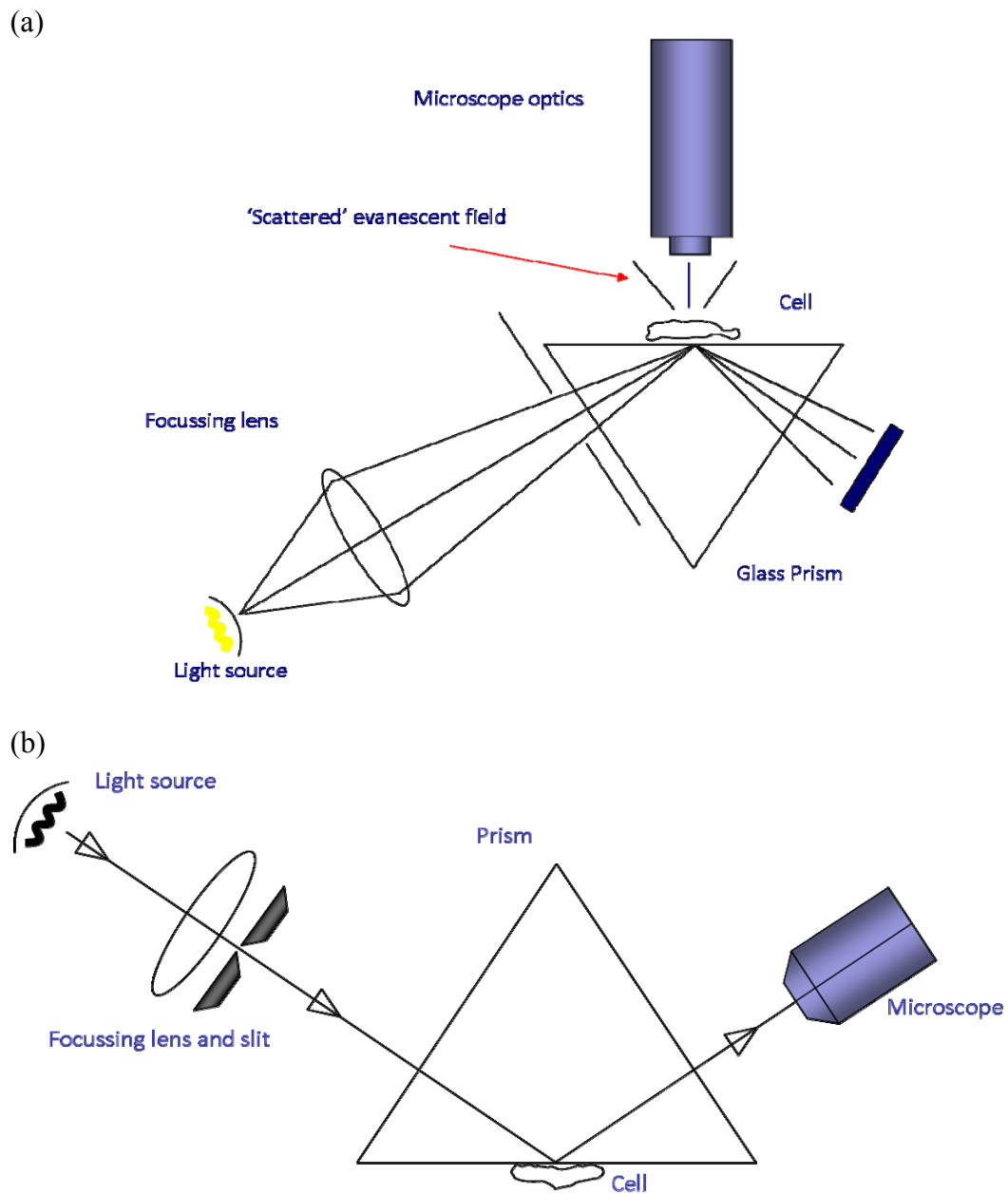


Figure 2.1 Schematic diagram of the surface contact microscope developed by Ambrose in 1956 in (a) darkfield arrangement and (b) brightfield arrangement.

(a) In the darkfield setup, a light source (mercury arc lamp) is focussed by an external lens through a slit onto the prism at an angle greater than the critical angle. An evanescent light path is formed in the area above the prism and is coupled out by the presence of cells in the beam. Frustrated (scattered) light can be detected by a microscope placed above the prism. (b) In the brightfield setup, the field of view appears uniformly bright when the critical angle is exceeded and objects in contact with the glass appear dark on a bright background

Even though the principle of using evanescent fields for studying cell movements was an adroit effort on Ambrose's behalf—due to the selective illumination of the basal cell membrane region—the surface contact microscopy technique did not become routinely used. There are a number of reasons which may have contributed to the lack of utilisation of the SCM. Firstly, few if any pictures were actually published in the scientific literature, thus making it difficult for others to judge the quality of the instrument. Most of the images in Ambrose's work were schematic illustrations of his observations.

Around the same time as the development of the surface contact microscope some authors were developing a form of interference microscopy. This technique, commonly known as interference reflection microscopy, reflection contrast microscopy or reflection interference contrast microscopy (RICM) became extremely popular during the 1960's and 70's for studying contact formation by cells during locomotion [156, 157]. So much so that it superseded the surface contact microscope and no further use of this technique for live cell imaging was made until recently [153]. The early work by Ambrose was performed using a prism type setup, whereas the later study was performed using an objective lens. The key differences between the two setups are discussed in detail later in this chapter.

2.1.2 The Reflection Interference Contrast Microscope

Currently, RICM is probably the most widely used non-fluorescent technique for imaging cell/substrate contacts. RICM derives its contrast by interfering light reflected from the sample with a reference reflection from the sample coverslip or substrate. The amplitude and phase of the sample reflection contain information about the sample refractive index and substrate separation respectively and by interfering the sample reflection with a reference, it is possible to measure the phase.

Initially, RICM suffered from some serious limitations, namely low contrast images caused by stray reflections, unwanted interference with reflections from the cell dorsal membrane and ambiguity between refractive index and substrate separation. These were later addressed by using polarisation to eliminate unwanted reflections [158], employing a high illumination numerical aperture (NA) to defocus dorsal membrane reflections [159] and by illuminating with two different wavelengths [160] respectively. The approach suggested by Ploem (1975) [158] has been widely adopted, and antireflective objective lenses based on his technique are commercially available.

2.1.3 Principles of total internal reflection

When a light beam propagating through a transparent medium of high refractive index (e.g. glass prism) encounters an interface with a medium of lower refractive index (e.g. aqueous solution), it undergoes TIR for incidence angles greater than the critical angle.

The principle of TIR is based on Snell's law, which is described by the following equation:

$$n_1 \sin \theta_1 = n_2 \sin \theta_2 \quad (2.1)$$

where n_2 and n_1 are the refractive indices of the liquid and the solid respectively.

If the incidence angle is equal to the critical angle θ_c (Eq. 2.2), the propagating light beam moves parallel to the interface:

$$\theta_c = \sin^{-1}(n_2/n_1) \quad (2.2)$$

For the example model of a glass/cell media interface—which is the case for cells on a microscope slide—the n_2/n_1 ratio is equal to 1.34/1.518, with a resultant critical angle of 62° . A simulation using Fresnel reflection coefficient versus angle of incidence is shown for a glass/media and a glass/cell cytoplasm interface in Fig. 2.2. The Fresnel reflection coefficient is equivalent to the normalised reflected intensity, thus under conditions of TIR, the reflected intensity equals one. It can be seen for all illumination angles above the critical angle, the light is totally reflected. Whereas, at the critical angle there is an interesting phenomenon where the light will propagate parallel to the interface. Below the critical angle the intensity begins to decrease rapidly.

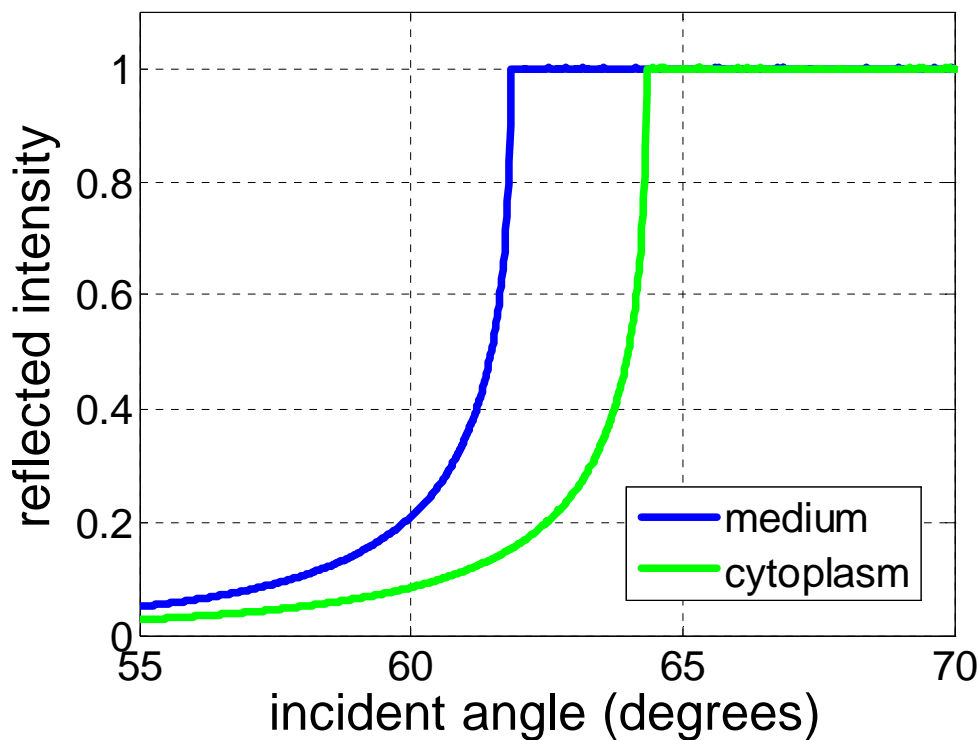


Figure 2.2 Plot of reflected intensity versus incident angle for cell/media and cell/cytoplasm interface

The presence of cell cytoplasm in the cell culture medium causes a shift in the critical angle from 62° to 64° . The glass, cell culture medium and cell cytoplasm have refractive indices of 1.52 and 1.34 and 1.37 respectively. Image reproduced with the kind permission of Dr. Mark Pitter.

Although the incident propagating light beam is totally internally reflected at the interface, an electromagnetic field known as the evanescent wave (EW) penetrates a small distance into the medium and propagates a short distance parallel to the surface in the plane of incidence [161, 162]. The EW is capable of exciting fluorescent molecules that might be present near the interface. This effect has been regarded as experimental proof of the existence of the EW [163].

For an infinitely wide beam the intensity $I(z)$ of the evanescent electric field (measured in units of energy/area/s) decays exponentially with perpendicular distance z from the interface:

$$I(z) = I_0 e^{-z/d} \quad (2.3)$$

Where

$$d = \frac{\lambda_0}{4\pi} [n_1^2 \sin^2 \theta - n_2^2]^{-1/2} \quad (2.4)$$

for angles of incidence $\theta > \theta_c$ and light wavelength in vacuum λ_0 . Depth d is independent of the polarisation of the incident light and decreases with increasing θ . Except for $\theta \approx \theta_c$ (where $d \rightarrow \infty$), d is on the order of λ_0 or smaller.

The beam can emerge from the immersion oil (refractive index n_{oil}) at a maximum possible angle θ_m given by:

$$NA = n_{oil} \sin \theta_m \quad (2.5)$$

Since $n \sin \theta$ is conserved—in accordance with Snell's law—as the beam traverses through planar interfaces from one material to the next, the right side of Eq. 2.5 is equal to $n_2 \sin \theta_2$ (where n_2 refers to the coverslip substrate upon which cells grow). For total internal reflection to occur at the interface with an aqueous medium of refractive index n_1 , θ_2 must be greater than the critical angle θ_c given by:

$$n_1 = n_2 \sin \theta_c \quad (2.6)$$

From Eq. 2.5 and 2.6, it is clear that NA must be greater than n_1 for TIR to occur. The inside of cells have a refractive index reaching 1.38 [162], and therefore require an objective lens with an NA sufficiently larger than this. Fortunately, a range of objective lenses are currently available with NA = 1.45, 1.49 and 1.65 [164, 165].

2.1.4 Early applications of total internal reflection microscopy

Since the development of the surface contact microscope by Ambrose in 1956 [154], which uses evanescent waves for contrast generation, there have been few examples of its use as an imaging technique published in the scientific literature. Azzam (1979) [166] claimed to use a bright-field prism arrangement and a polarised light source to monitor cell malignancy, through intensity and ellipse of polarisation variations of the reflected wave. However, no results from this technique were ever published.

TIRM has been utilised for measuring colloidal interactions between a glass plate and particle [167]. Other techniques, such as SPRM [61, 63], TIRF [163], standing wave fluorescence microscopy [168, 169] and NSOM [170] have since been developed which also utilise evanescent fields for the purpose of imaging. These techniques have proved popular in their own right and indeed TIRF is now available as a commercial instrument through all the major manufacturers.

2.1.4.1 TIRM for measuring colloidal separation distances

During the late 1980's, Prieve and colleagues began developing a prism based total internal reflection microscopy technique for measuring colloidal interactions between a single microscopic particle and a flat plate in an aqueous environment [167]. More generally, they used TIRM for monitoring the instantaneous separation distance between a sphere and a plate [171]. TIRM is a highly sensitive method of determining particle-wall interactions, with forces as small as 10 fN detectable. The technique has been applied to measure various types of interactions such as depletion forces, electrostatic and magnetic interactions and steric repulsion by adsorbed polymer layers [172-176].

For the example of a sphere on a glass surface, both similarly coated, the sphere experiences double layer repulsion, which increases in strength as it approaches the surface. There is one particular separation distance, corresponding to mechanical equilibrium, where double layer repulsion and gravitational attraction are exactly balanced. Here, the particle will not remain stationary, but instead will undergo axial movement due to Brownian motion (Fig. 2.3a). The probability of finding it at any particular axial position depends on the potential energy (PE) at that location. Positions of high PE will be sampled less frequently and vice versa. The quantitative relationship between PE and the sampling frequency of different elevations is given by Boltzmann's equation:

$$p(h) = A \exp\left[-\frac{\phi(h)}{kT}\right] \quad (2.7)$$

where $p(h)dh$ is the probability of finding the sphere between h and $h + dh$, $\Phi(h)$ is the PE of the sphere at elevation h , kT is the thermal energy and A is a normalisation constant whose value is chosen such that $\int p(h)dh = 1$.

To measure the instantaneous separation distance, h , a statistically large number of measurements (typically 50,000) are taken at 10 ms intervals. If all elevations have been sampled accordingly, then a histogram of the measurements will converge to the probability function $p(h)$ appearing in Boltzmann's equation. In essence, TIRM is then capable of measuring this probability density function. Knowing $p(h)$, Boltzmann's equation can be turned 'inside-out' to deduce the PE profile $\Phi(h)$: To eliminate A , we divide $p(h)$ by $p(h_m)$ evaluated at some reference position denoted h_m before solving for the PE. According to Eq. 2.1, this leaves:

$$\frac{\phi(h) - \phi(h_m)}{kT} = \ln \frac{p(h_m)}{p(h)} \quad (2.8)$$

Usually h_m is chosen as the elevation corresponding to the minimum in $\Phi(h)$. Since Boltzmann's equation defines the mean potential in statistical mechanics, it is claimed that TIRM directly measures the PE profile.

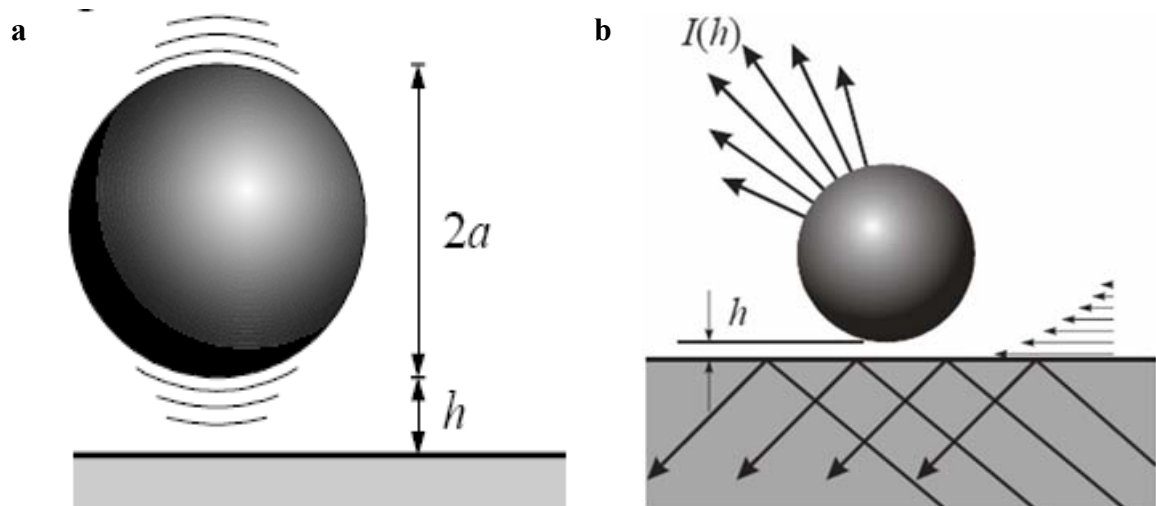


Figure 2.3 Schematic diagram illustrating (a) Brownian fluctuations of a sphere (b) ‘frustrated’ total internal reflection

(a) TIRM determines the interaction between a single microscopic sphere and a flat plate by measuring the Brownian fluctuations in separation distance, h . (b) When illuminated by an evanescent wave (horizontal arrows), the sphere scatters light which is exponentially sensitive to its elevation (h). The presence of a sphere, with a different refractive index from that of the water, near an interface at which total internal reflection occurs causes some of the evanescent wave to become scattered. This situation is also known as ‘frustrated’ total internal reflection. Horizontal arrows of different length indicate a decay of evanescent wave intensity with distance from the surface. Reproduced with permission from [171].

In order to determine the instantaneous separation distance, the intensity of light scattered by a sphere when it is illuminated by an evanescent wave is measured. Evanescent wave formation is discussed in detail in Section 2.1.4. When a sphere of refractive index different from that of the dispersion media settles near an interface where TIR occurs, some of the evanescent wave is scattered as shown in Fig. 2.3b. This situation is called ‘frustrated’ TIR. Since the EW decays exponentially with distance from the surface, the amount of light scattered by the sphere is exquisitely sensitive to its proximity to the interface.

The Mie scattering problem for a 1 μm sphere illuminated by an EW was solved by Chew *et al.* (1979). The solution revealed that the intensity of scattering is a complicated function of direction, involving multiple peaks and valleys. TIRM integrates the scattering intensity over a cone of solid angles corresponding to the numerical aperture of the microscope objective lens. Also, the intensity of scattering in any direction decays exponentially with elevation of the sphere above the plate. Ray optics have been used to calculate the distribution of scattering of the EW from spheres which are large compared to the wavelength of illuminating light [177]. Simulations showed that for spheres 30 μm or smaller, rays scattered towards the plate do not again encounter the sphere. Essentially, it was concluded that multiple scattering for objects below this size could be largely ignored. Experimentation has also been used to show that scattering intensity I decays with the same dependence on distance from the wall as the intensity of the EW itself, which is given by Eq. 2.3.

The penetration depth of the EW in the experiments carried out by Prieve is typically in the region of 100 nm. A consequence of the exponential sensitivity is that a very small change in h produces a measurable change in intensity. Photomultiplier tubes (PMT) can be used to quantify a 1 % change in light intensity. According to Eq. 2.3 with $d = 100$ nm, a 1 % change in I corresponds to a 1 nm change in h . The spatial resolution of the technique is thus on the order of 1 nm [171].

Apparatus

A schematic of a typical setup for performing TIRM force measurements is illustrated in Fig. 2.4. A flowcell is constructed using two glass slides and an O-ring, resulting in a separation distance of approximately 1 mm between the slides. The flowcell is then optically coupled to a dove tailed prism. Particles are injected into the flow cell, via a syringe, and viewed through the objective lens until one single levitated particle is focused upon. At this point, the particle appears in the microscope as a bright spot on a dark field with intensity fluctuations due to Brownian motion. Data is acquired using a single photon counting method to reduce instrument noise.

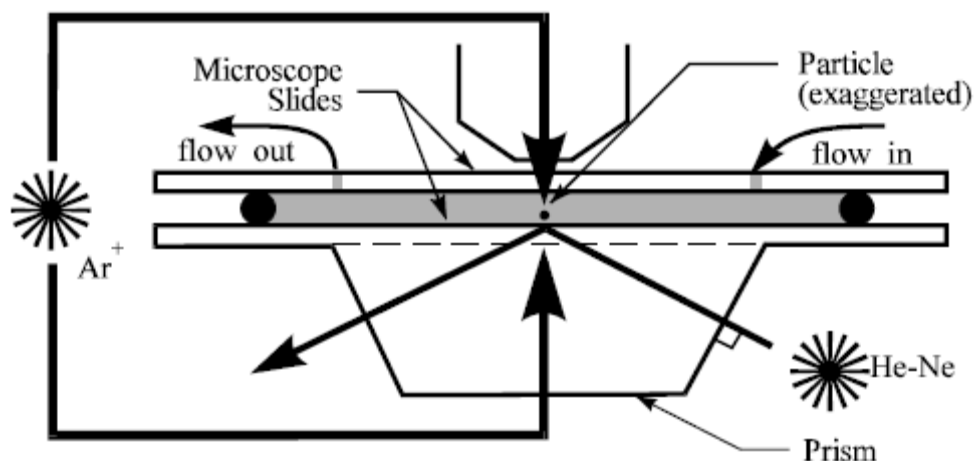


Figure 2.4 Schematic diagram of a typical flowcell used by many authors for TIRM experiments

A Helium-Neon laser is introduced to the prism at an angle greater than the critical angle, resulting in the formation of an evanescent wave localised to the bottom slide. Placement of a particle within the evanescent field results in scattering of the evanescent light. This change in intensity is used to monitor the elevation of the particle. The Argon (Ar^+) laser line is coupled through both the microscope objective and the bottom of the prism in order to create a two-dimensional optical trap in the horizontal plane and to exert an axial force on the particle. Reproduced with permission from [171].

2.1.4.2 TIRM for measuring the interaction between model cells and biomaterials

TIRM has been utilised to probe interactions between model cells and surfaces in the development of improved drug delivery systems and biomimetic materials [178]. In this work, the authors aim to quantify for the first time non-specific forces, such as electrostatic, van der Waals, and steric forces, that control the initial approach of the cell to the surface, as opposed to specific adhesive forces. Model cells were used since the

low refractive index associated with living cell membranes are experimentally challenging for TIRM. The model cell consisted of a polystyrene sphere coated with varying ratios of the zwitterionic lipid dipalmitoyl phosphatidylcholine (DPPC) and the negatively charged lipid dimyristoyl phosphatidylglycerol (DPMG). Surface potentials of the model cells are affected by the variation of the zwitterionic and negative lipid components.

2.1.4.3 Interference TIRM for measuring Kinesin motion

In 2003, Cappello and co-workers developed a novel interference total internal reflection microscope for measuring kinesin motion along a microtubule [179]. This method is based on the detection of light scattered from a single particle moving through an interference pattern generated by two identical laser beams undergoing TIR at the glass/water interface. By measuring the temporal variations of the total scattered light it is possible to estimate the position of an object moving in the fringes. The authors achieved a spatial resolution of a few nanometers using this setup, which equates to approximately 1% of the fringe periodicity. The fringe periodicity is dependant upon wavelength and incident angle of the two beams, as well as the refractive indices of the two media that form the planar interface where total internal reflection occurs [180]. The major advantage of this technique for studying single bio-molecules over current nanomanipulation techniques such as AFM and optical tweezers (OT) is that it can potentially afford microsecond time resolution, a requisite for the analysis of motor stepping dynamics of molecules such as kinesin. However the aforementioned OT method is currently the most widely used tool for studying kinesin

motion as the tweezers can be used to control molecules with extremely high resolution and precision [181, 182].

2.1.5 Evanescent wave illumination

There are two main methods for achieving evanescent illumination, namely through a high NA objective lens or through a prism. Ambrose (1956) [154] and Prieve (1999) [171] both utilised a prism-type setup to achieve evanescent wave generation. As discussed earlier, this can be accomplished by focussing a light source onto a prism at an angle greater than the critical angle (Fig. 2.1a, b). Prism based systems offer some advantages over the more modern objective based systems. The angle of incidence can be carefully defined by use of a mirror placed on a rotating micrometer stage. This is of importance since the penetration depth of the EW is dependent on the angle of incidence (Eq. 2.4). Careful adjustment of the illumination angle affords the ability to selectively illuminate different regions of the cell membrane.

The disadvantages of this type of setup include difficulty of sample manipulation due to the presence of the objective lens above the sample and the fact that a water immersion lens is used as opposed to an oil immersion lens, which is associated with a slight decrease in obtainable resolution. Also, since it is a darkfield technique, low scattering objects may be difficult to observe without sophisticated cameras or photo-multiplier tubes (PMT). Another drawback of the prism type setup stems from the unidirectional illumination inherent in this type of system. The visualisation of long, thin objects such as microtubules or flagellar axonemes depends very strongly on the polarization and

direction of the incident light. Thus, when using unidirectional laser illumination or a mercury lamp polarised prior to reaching the sample, it is possible to view only those objects in one particular orientation. Intensity and polarisation of evanescent light scattered by these objects is strongly dependent on their orientation relative to the direction of illumination. In summary, visualisation of long, thin objects will be orientation dependant when illuminated with polarised light directed through a totally internally reflecting prism [183]. Objective type systems will not be subject to this phenomenon as the sample is illuminated by light waves from all angles.

An optical system for observing surface topography by frustrated TIR using a through the objective setup was developed by McCutchen (1964) [184]. In this work, light is coupled through an objective lens with $NA > 1$ in an episcopic arrangement. When a glass/air interface is used as a sample, all illumination light at $NA > 1$ will be totally internally reflected, resulting in the formation of an evanescent field in a region localised to the glass surface. Evanescent illumination through a high NA objective lens for a glass/medium interface is discussed at length later in this chapter, thus I will not go into further detail at this point.

In the early 90's, a clever form of evanescent illumination was achieved using a darkfield (DF) condenser [185]. When a cardioid DF condenser with NA 1.4 is illuminated under normal conditions, a region of light rays corresponding to NA 1.33 – 1.4 will be totally internally reflected at the glass-water interface. By defocusing the condenser, the specimen illumination becomes annular, corresponding to a cross-section of the beam above or below the focal point. If the defocused condenser is placed to one

side of the optical axis, the field of view of the objective lens may encompass a region of sample illuminated by evanescent waves only.

2.2 Aims and objectives

The purpose of this chapter is to introduce a novel objective based total internal reflection microscopy system. It is compared and contrasted to another high resolution label free technique, reflection interference contrast microscopy (RICM), and results of simulations are presented. The apparatus needed for developing a total internal reflection microscope are described and key design considerations are discussed. Some intrinsic properties of TIR microscopy are discussed in relation to other high resolution techniques. Finally, high resolution TIRM images of live cells are presented.

2.3 Materials and methods

2.3.1 Microscopy

The components used in the development of the through the objective TIRM system are described in detail later in this chapter. Briefly, TIRM was achieved utilising illumination through the microscope objective (PlanFluor 100x NA 1.45, Zeiss). All studies were performed using a standard inverted biological microscope (TC 5400, Meiji, Japan) with custom built illumination optics. TIRM imaging of living cells was achieved with a light emitting diode (LED) source with a centre wavelength of 580 nm (LXHL-ML1D Luxeon Star, Lumileds, CA) reflected off a polychroic mirror (z488/532, Chroma, Rockingham, VT, USA). After total internal reflection from the sample the illumination light is transmitted through both the polychroic mirror and emission filter (z488/532m, Chroma, Rockingham, VT, USA) with 85% efficiency, resulting in approximately 11% of the initial illumination reaching the camera.

The camera utilised to acquire images was a 14-bit cooled electron multiplying CCD (EMCCD) (iXon DV-885 KCS-VP, Andor Technology, Belfast UK). The resolution of the camera was 1004 x 1002 pixels, with each pixel 8 μm x 8 μm in size. TIRM images were acquired by the camera under the control of iQ version 1.5 (Andor Technologies, Belfast UK). For video imaging, frames were streamed to a kinetic image disc on a PC and then saved to hard disc. Analysis of still images and video sequences was performed with iQ, ImageJ and Excel (Microsoft, Redmond, WA). Digital brightness and contrast was adjusted in Photoshop CS2 (Adobe Systems, San Jose, CA).

A prism based total internal reflection microscope was constructed as follows. A Helium-Neon (HeNe) laser (CVI Melles Griot, USA) was used to generate coherent linearly polarised light at a wavelength of 633 nm. The laser light was directed by a highly reflecting mirror (4-6 wave mirror, Edmund Optics, UK) onto an inverted prism (BK7 commercial quality right angle prism, Edmund Optics, UK) at an angle above the critical angle of total internal reflection. Scattered light from the sample was collected from above the prism using a high NA water immersion lens (AchroPlan 100x NA 1.0 (W), Zeiss). The light was then directed through a tube lens with a focal length of 200 mm (Edmund Optics, UK) onto a charged-coupled device (CCD) camera (SXFV-H5, Starlight-Xpress, UK).

2.3.2 Cell Culture

A549 cells and murine fibroblast (3T3) cells were obtained from the European Collection of Cell Cultures (ECACC). The cells were cultured in Dulbecco's Modified Eagle's Medium (DMEM), supplemented with 10% new born calf serum (NBCS), 1 unit/ml penicillin, 1 mg/ml streptomycin, 2.5 µg/ml amphotericin B (antibiotic/antimycotic solution) and 1% L-glutamine, in a humidified incubator at 37 °C and 5% CO₂. Every 6-7 days the cells were removed from the tissue culture flasks, using 0.25% trypsin and 1 mM Ethylenediaminetetraacetic acid (EDTA) in Phosphate Buffered Saline (PBS), and reseeded. Purified 18.2 mΩ water was obtained from Maxima water purification system (Elga, USA) and was used in the preparations of all solutions. Chemicals were obtained from Sigma Aldrich unless otherwise stated.

A suspension of 3T3 cells was obtained by detaching and removing the cells from tissue culture flasks using 0.25% trypsin/1 mM EDTA in PBS and placing in 10 ml DMEM. A cell suspension (1.5 ml) with a final concentration of 1×10^5 cells/ml was then added to each chamber of a Lab-Tek II chambered coverglass system coated with 0.01% poly-L-lysine (PLL) solution (MW 70,000 – 150,000, Sigma-Aldrich, UK).

Primary human osteoblast cells (HOBs) were cultured in Dulbecco's Modified Eagle's Medium (DMEM), supplemented with 10% new born calf serum (NBCS), 1 unit/ml penicillin, 1 mg/ml streptomycin, 2.5 μ g/ml amphotericin B (antibiotic/antimycotic solution) 1% L-glutamine, 50 μ g/ml ascorbyl-2-phosphate and 10 mM beta-glycerol-phosphate, in a humidified incubator at 37 °C and 5% CO₂. Cells were used after passage number 5. Cells were seeded onto poly(DL-Lactide/Glycolide) (PLGA) coated 35 mm glass based dishes (Iwaki, Japan) at a concentration of 2×10^5 cells per plate.

2.3.3 Preparation of PLGA coated surfaces

Uniform thin polymers were generated by spin-casting polymer solutions onto a 35 mm glass based dish (Iwaki, Japan) diameter glass. For spin casting, a solution of 0.015 g/ml of PLGA 85:15 (MW 117,000) (Lakeshore Biomaterials, USA) was made by dissolving it in dichloromethane (Sigma-Aldrich, U.K.). The glass based dishes were spun at approximately 500 RPM while approximately 0.5 ml of the polymer solutions was dispensed onto the centre of the spinning dish in a fume hood. Following solvent evaporation, the polymer-coated dishes (hereinafter referred to as polymer films) were placed under 25 in. Hg of vacuum overnight to remove any remaining solvent. Presence

of the polymer film was confirmed by an etched pattern created when parallel samples of the clear film were scraped with forceps. The polymer film was pre-wet with 70% ethanol and placed under UV light for 30 min to sterilize. The ethanol was removed and the substrates were rinsed twice with PBS. The substrates were then soaked in growth medium (DMEM) with 10% fetal bovine serum and 25 $\mu\text{g/ml}$ gentamicin sulfate overnight, prior to cell seeding.

2.3.4 Simulations of TIRM and RICM

Simulations were performed using custom made MatLab (The Mathworks Inc., MA, USA) programs. Briefly, the cell was modelled as a semi-infinite region of index 1.37, an approximate value for the cytoplasm [186], the cell medium had an index of 1.34, and the glass substrate was a semi-infinite region of index 1.52. A Fresnel model was used to calculate the reflection coefficients for a range of cell/substrate separations from 0 to 1.2 μm . All simulations were kindly performed by Dr. Mark Pitter.

2.4 Results and discussion

The contrast mechanism in TIRM is frustrated total internal reflection. In common with TIRF, the sample is illuminated at greater than the critical angle, but in TIRM it is reflected light, rather than fluorescent emission, that is used to form an image. TIR occurs in regions of the substrate that are free of cells, particles or structure, giving an even, bright background. Imaged samples (e.g. cells or colloidal particles) generally possess a higher refractive index than the surrounding medium which causes a frustration of the TIR, that is, they scatter or couple light out of the illumination beam, reducing the intensity of the reflection. Hence, similar to transmitted light microscopy, features of interest appear in the image as darker regions against a bright field.

2.4.1 Comparison of RICM and TIRM contrast mechanisms using computer modelling

The aim of this section is to demonstrate the distinction between the TIRM and RICM techniques as both have been misinterpreted as one and the same during discussions with journal editors and external academics.

The simulated response of RICM and TIRM to a simplified model of a cell approaching and touching a substrate is presented in Fig. 2.5 and 2.6 respectively. The cell was modelled as a semi-infinite layer of index 1.37, an approximate value for the cytoplasm (Verschueren, 1985) [186], the cell medium had an index of 1.34, and the glass substrate was a semi-infinite layer of index 1.52. A Fresnel model was used to calculate

the reflection coefficients for a range of cell/substrate separations from 0 to 1.2 μm . The illumination is unpolarised, wavelength is monochromatic at 590 nm, and the incident beam is collimated and at normal incidence for RICM and 63° for TIRM. The value of 63° was chosen as it is the midpoint between the critical angles for the substrate/cell medium and substrate/cytoplasm.

It can be seen from Fig. 2.5 that the RICM response has a low amplitude, with a reflection coefficient between 0.275 % and 0.55 % and is oscillatory in nature. Indeed, the response is periodic, with a period of half the incident wavelength when in the cell medium. In contrast, TIRM has a much greater response, with a reflection coefficient between 25 % and 100 %. Also, compared with the oscillatory nature of the RICM response, TIRM is monotonic.

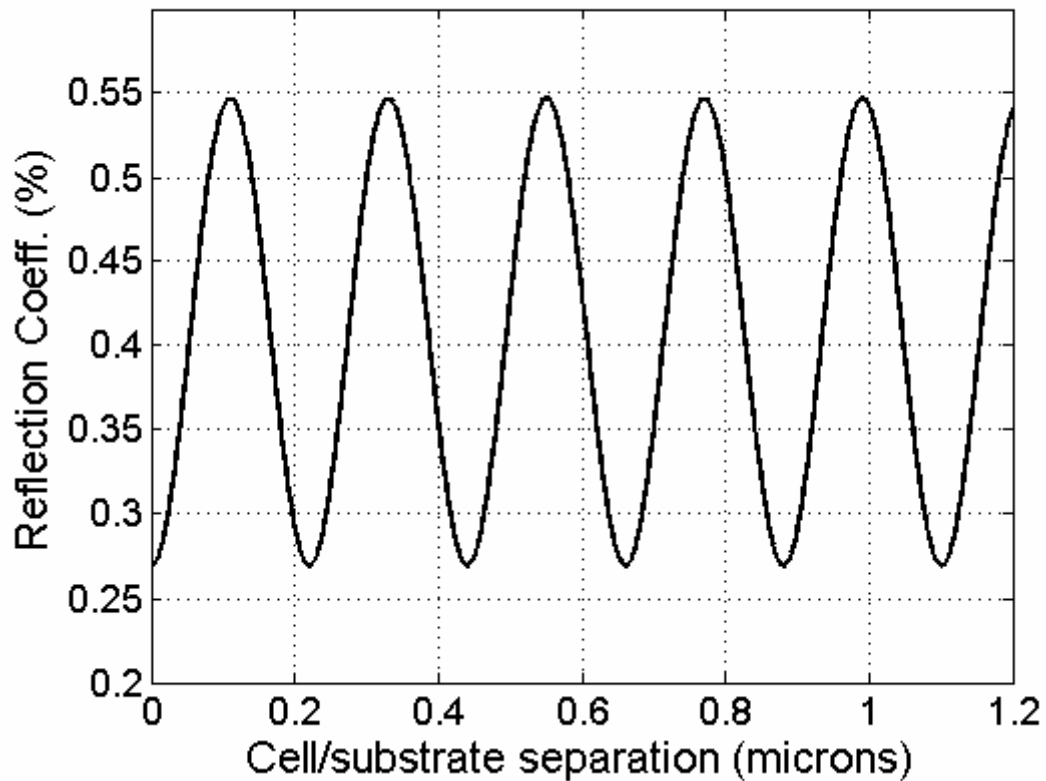


Figure 2.5 Plot of simulated reflection coefficient versus cell/substrate separation for RICM

RICM is characterised by a very low reflection intensity and the oscillatory nature of the response. The substrate, cell cytoplasm and cell medium have refractive indices 1.52, 1.37 and 1.34 respectively. Light is incident along the optical axis. Reproduced with the kind permission of Dr. Mark Pitter.

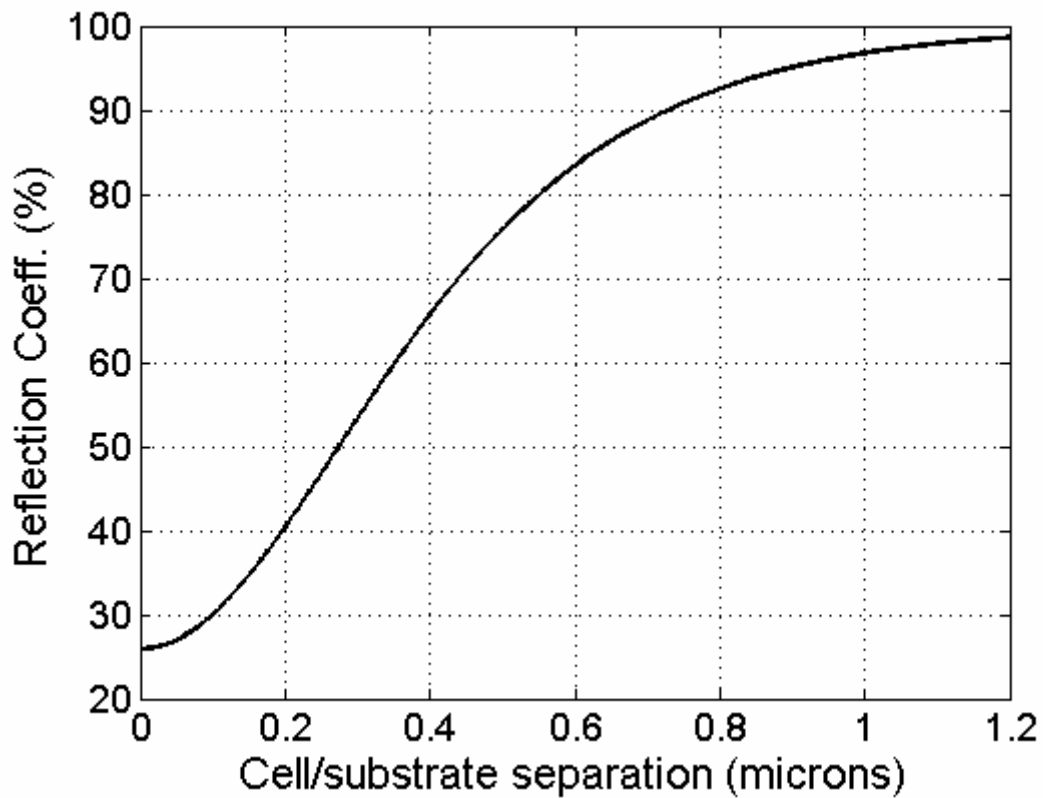


Figure 2.6 Plot of simulated reflection coefficient versus cell/substrate separation for TIRM with collimated illumination

TIRM has a much higher reflection coefficient than RICM and the response to cell/substrate separation is monotonic. The substrate, cell cytoplasm and cell medium have refractive indices 1.52, 1.37 and 1.34 respectively. The angle of incidence is 63° . Reproduced with the kind permission of Dr. Mark Pitter.

Several ambiguities could potentially arise when using collimated monochromatic light due to the low amplitude and oscillatory nature of the RICM response. This response illustrates that an interference pattern will be generated when the cell/substrate distance is increased. If, for example, a cell which has regions both approximately 0.2 μm and 0.4 μm from the surface, the resultant response from the microscope may be similar. Interestingly, as the cell/substrate distance approaches zero, there is no abrupt fall in reflection coefficient. This is in agreement with previous work [186, 187].

However, by illuminating with white light and/or a high numerical aperture in RICM it is possible to damp the oscillations. This is illustrated in Fig. 2.7, where the response of RICM with an illumination NA of 1.3 is simulated. As above, unpolarised light at 590 nm was simulated. It can be seen that the oscillatory nature of the response has been dampened, however, it is still not monotonic. Nevertheless, only the zero-order fringe is clearly visible meaning that it can be assumed that dark regions in the image can be expected to originate from regions of close cell contact.

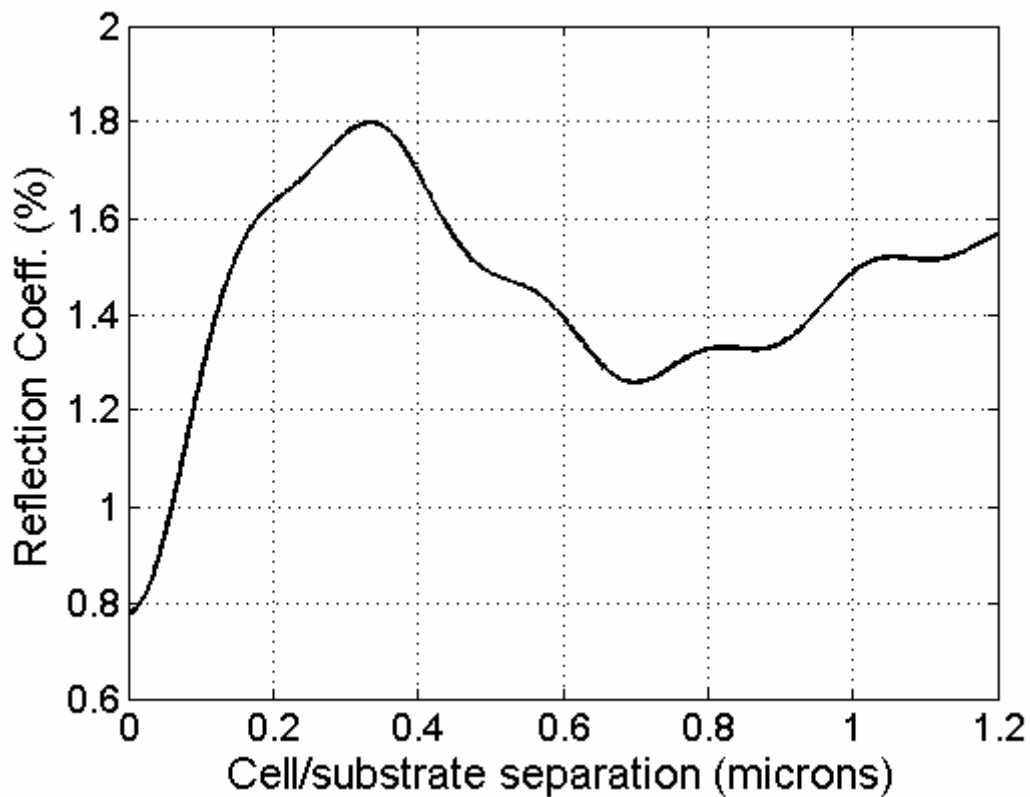


Figure 2.7 Plot of simulated reflection coefficient versus cell/substrate separation for RICM with high NA illumination ($0 \leq NA \leq 1.3$)

The use of high NA illumination suppresses the oscillatory nature of the response as compared with , but the reflection coefficient is still low. The substrate, cell cytoplasm and cell medium have refractive indices 1.52, 1.37 and 1.34 respectively. Reproduced with the kind permission of Dr. Mark Pitter.

Figure 2.8 shows the TIRM response using a very high NA objective suitable for TIRF with central block to remove most of the illumination from sub-critical angles. The contrast is reduced from Fig. 2.6 due to TIR of the higher incident angles, even in the presence of the cell, and the gradient of the curve is increased by the illumination at angles very near to the critical angle where evanescent penetration is reduced. The contrast can be enhanced by decreasing the size of the aperture diaphragm to remove light incident at higher than the critical angle formed by the cytoplasm and the substrate.

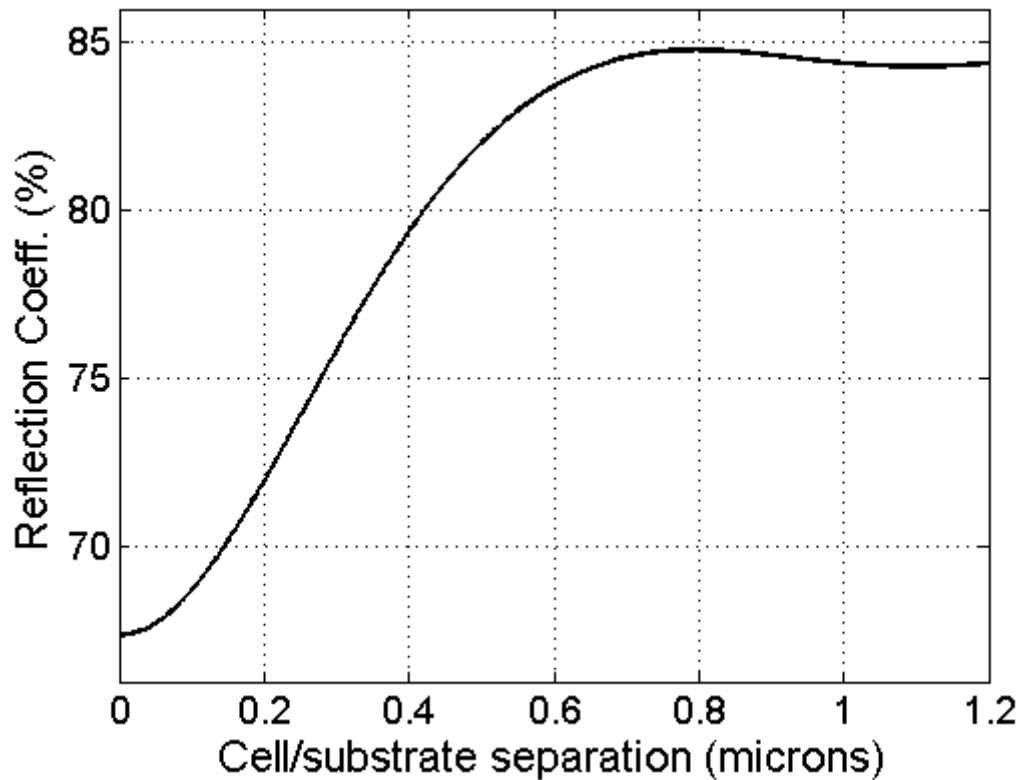


Figure 2.8 Plot of simulated reflection coefficient versus cell/substrate separation for TIRM with high NA illumination ($1.3 \leq NA \leq 1.45$)

The use of an annulus reduces the contrast of TIRM, but the monotonic response is largely maintained. The substrate, cell cytoplasm and cell medium have refractive indices 1.52, 1.37 and 1.34 respectively. The angle of incidence is 63° . Reproduced with the kind permission of Dr. Mark Pitter.

The results presented in Figs. 2.5 – 2.8 clearly demonstrate the difference in contrast generation between RICM and TIRM. Even though the two techniques have similarities in that they are both used for high resolution imaging of cell substrate contacts, they should never be misinterpreted as the same technique, which from experience has occurred frequently.

2.4.2 TIRM illumination strategies

As discussed previously and illustrated in Fig. 2.1a, a simple way to achieve evanescent illumination is to focus a laser beam on to the surface of a prism at greater than the critical angle for the glass/substrate interface. Figure 2.9 shows a scattered light image of a fibroblast cell produced using a prism type setup similar to Ambrose (1956) [154] but illumination was achieved via a Helium-Neon (HeNe, $\lambda = 633 \text{ nm}$) laser source (Section 2.3.1). The other difference was that the objective used to capture the scattered light was a high NA water immersion lens (AchroPlan 100x NA 1.0 (W), Zeiss). This lens has the ability to collect higher orders of diffracted light than those that were available in the 1950's. It can be seen that the image quality is extremely poor, indeed, it is difficult to view anything that even resembles an adhering cell. This can be explained by the use of a coherent illumination source. When scattered light from the sample is collected, individual waves will interfere constructively and destructively, resulting in the speckle pattern or coherence noise visible in Fig. 2.9. Clearly, illumination of this kind is unsuitable for high resolution TIR imaging.

Using a non-coherent source such as a light emitting diode (LED) or a mercury arc lamp will result in a decrease of coherent noise found on the image. Reverting to a brightfield system such as that shown in Fig. 2.1b will improve the quality of the image. However, long working distances, the associated low NA and the oblique viewing angle, mean that in practice the image resolution and image quality will be poor using a prism type setup. Clearly high resolution brightfield TIRM is not feasible using a prism arrangement for these reasons.

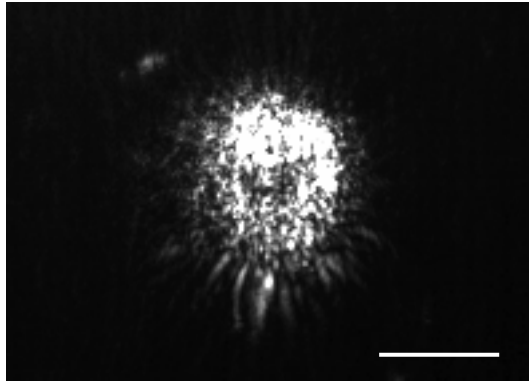


Figure 2.9 Prism based total internal reflection scattered light image of a 3T3 cell

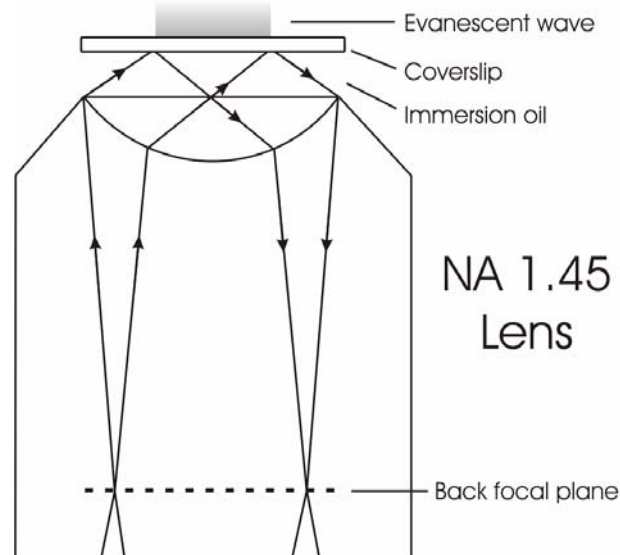
It can be seen that the image obtained is speckly in nature, a common feature of coherent illumination. As a result, evanescent wave illumination through a prism is unsuitable for high resolution TIR imaging.

Scale bar represents 20 μm .

An alternative means of achieving evanescent wave generation is to illuminate through a high NA objective lens [188]. The most elementary way to achieve through the objective evanescent illumination is to focus (using an external focussing lens) a laser beam to a point at the back focal plane of the objective lens. The point of focus in the back focal plane is then adjusted to be off-axis at a suitable radial distance to ensure total internal reflection, as illustrated in Fig. 2.10a [165]. This method is employed in most TIRF microscopes as it affords a well controlled incident angle and bright illumination. However, it is not an ideal illumination strategy for TIRM (Fig. 2.10b). In TIRM, the same laser beam is used for both illumination and image generation. Therefore, any coherence present in the illumination source will also be present on the image. Using a focussed laser beam in TIRM results in a large amount of coherence noise (laser speckle), which is clearly visible on the resulting image (Fig. 2.10b). These problems can be minimised by ensuring that optical components are very clean and stable, but in a practical microscope, the required level of cleanliness and stability can

be difficult to achieve. In contrast, in TIRF, the coherent laser beam is only used to excite the fluorescent molecules after which their red-shifted emission forms the basis for image contrast.

A



B

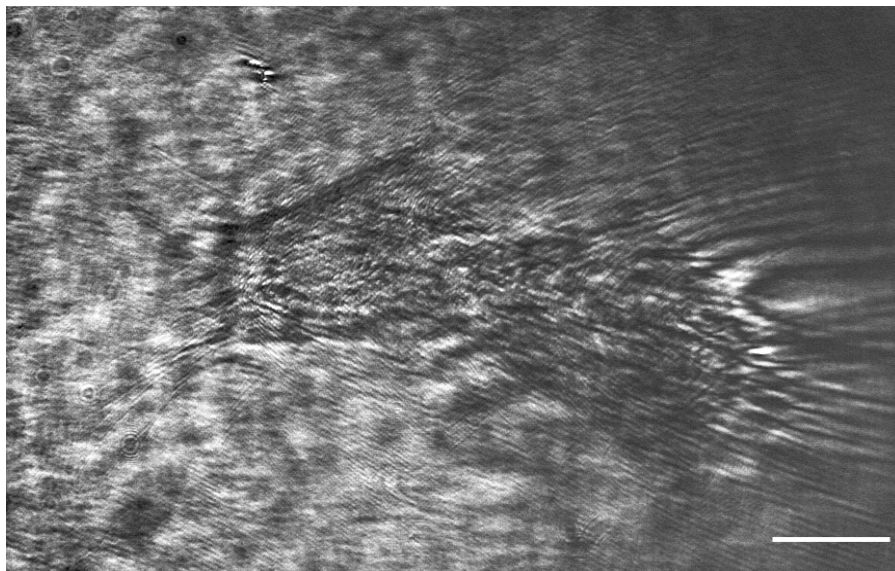


Figure 2.10 (a) Schematic of TIRM illumination using a laser focused to a point on the back focal plane of the objective lens. (b) TIRM image of a 3T3 fibroblast cell using this illumination setup.

(a) Total internal reflection is achieved by focussing a laser beam to a point on the back focal plane—via an external focussing lens—and adjusting the point of focus to be off-axis at a suitable radial position. (b) A high level of coherent noise (laser speckle) renders this illumination strategy unsuitable for TIR microscopy. Scale bar represents 20 μm

TIRM can also be accomplished using two alternative illumination arrangements. In the first, an expanded laser beam is passed through a rotating ground glass diffuser (Fig. 2.12a). The illuminated patch of diffuser acts as a temporally coherent, but spatially incoherent source. In order to exclude illumination from incident angles below the critical angle, this source is imaged onto an annular mask conjugate with the back focal plane of the microscope objective to block angles below the critical angle, and subsequently re-imaged into the back focal plane of the microscope objective. In the objective back focal plane, the distance from the optical axis corresponds to incident angle, so the annulus is designed to block light from the central, on-axis region, and allow light from the periphery only to illuminate the sample. The exact dimensions of the annulus depend on the specific objective lens in use. The annular dimensions can be calculated in the following way:

$$\theta_{edge} = \sin^{-1}(NA/n_{objective}) \quad (2.9)$$

For NA of 1.45 and $n_{objective}$ of 1.515, the maximum achievable illumination angle through the objective lens (Zeiss 1.45 NA 100x Plan-Fluar oil immersion - 000000-1084-514) is equivalent to 73° .

Since the critical angle for TIR to occur at a glass/water interface is 62° (Eq. 2.2) then it is reasonable to assume that TIR will occur across the angles ranging from 62° to 73° . The back aperture of the Zeiss 1.45 NA lens has a diameter of 6 mm. If it is assumed that the maximum illumination angle of 73° is equivalent to a diameter of 6 mm, then it means that the critical angle corresponds to a diameter of 5.05 mm. A schematic diagram illustrating the design of the central block is shown in Fig. 2.11. The placement

of a central block of 5.05 mm diameter in the illumination light path will result in pure evanescent field illumination of the sample since all sub critical angles are blocked.



Figure 2.11 Schematic representation of annular mask used to for TIRM illumination.

The mask is placed conjugate with the back focal plane (BFP) of the microscope objective. The annulus is designed to block light from the central, on-axis region, and allow light from the periphery only to illuminate the sample. The diameter of the central block (CB) is 5.05 mm and the full annulus is 6 mm (equivalent diameter of the back aperture of NA 1.45 Zeiss Plan-Fluar objective lens).

In practice, I have found that the inclusion of the central block does not result in an improvement of image quality. One might expect to be confused by spurious information from the central cone of light with $NA < 1.33$. This light will be partially reflected at the front surface of the coverglass and also at the surface of the specimen. The intensity that this cone of light contributes to the image will depend upon how these two reflections interfere. Fortunately, this contribution is weak enough to be effectively swamped by the light from $NA > 1.33$. Thus, it is not necessary to stop out this central zone. This is an agreement with previous work by McCutchen (1964) [184].

When the diffuser is stationary, this form of illumination produces an image which is deeply modulated by laser speckle. However, by rotating the diffuser to randomise the speckle pattern, and integrating over sufficient independent patterns with a CCD camera to render speckle noise negligible [60], relatively speckle free, evenly illuminated images are obtained (Fig. 2.12b). Although this illumination setup produces a vastly superior image to that formed without the use of a diffuser (Fig. 2.10b), unwanted effects due to the use of a temporally coherent source are still evident.

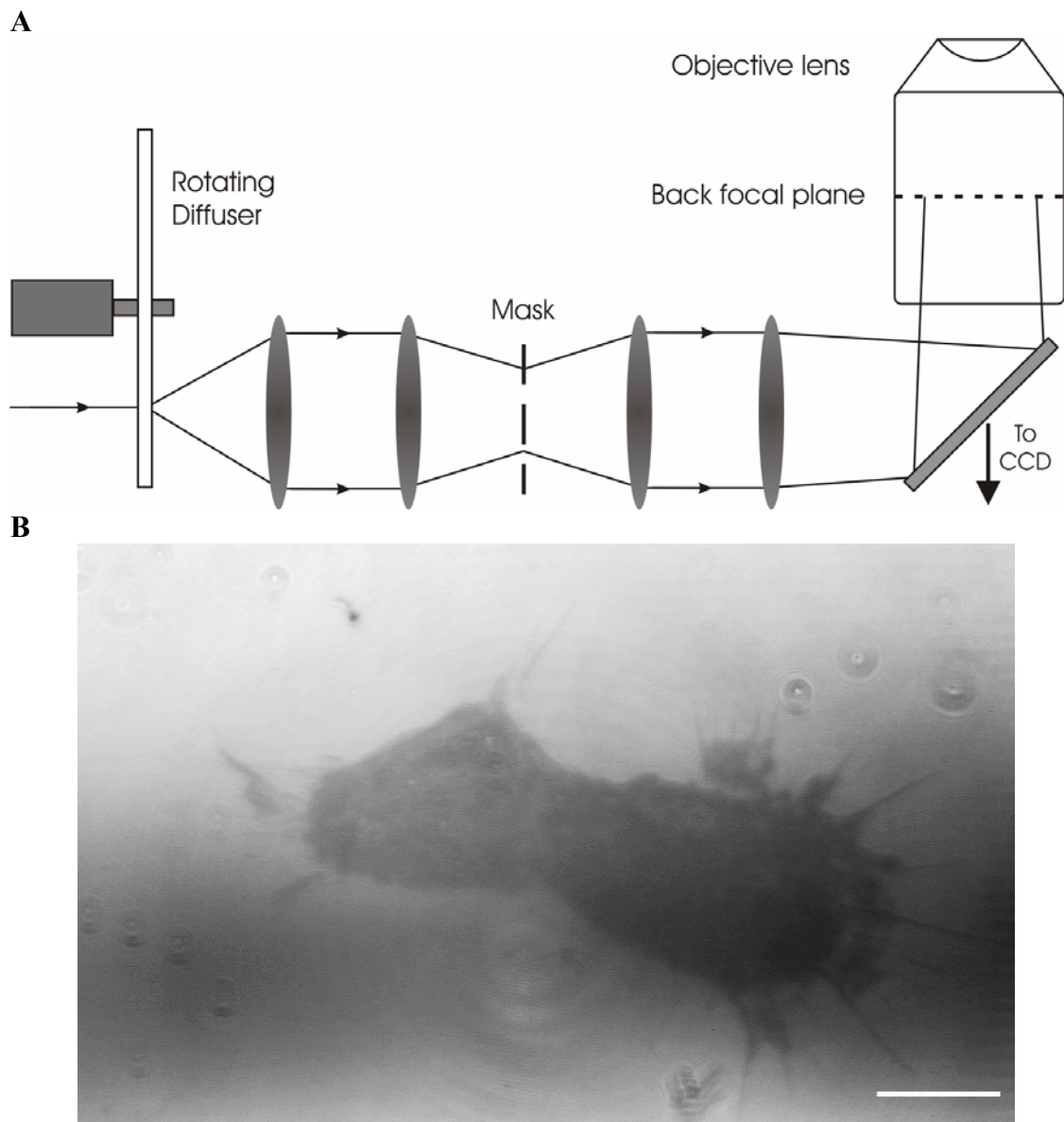


Figure 2.12 (a) Schematic representation of TIRM illumination achieved using a diffuse laser beam imaged onto the back focal plane of the objective lens. (b) TIRM image of a 3T3 fibroblast cell using this illumination setup.

(a) In this setup an expanded laser beam is passed through a rotating ground glass diffuser which produces a temporally coherent but spatially incoherent source. This incoherent source is subsequently imaged onto a mask and re-imaged into the back focal plane of the objective lens. (b) Using a diffuser in the illumination path results in a dramatic increase in the quality of the TIRM image. However, the resolution is not what is expected and the cell adherence regions are lacking in contrast. Scale bar represents 20 μm

Another suitable illumination scheme is to use an incoherent illumination source such as a halogen bulb, arc lamp or a LED. As with diffuse laser illumination, sub-critical illumination angles are removed by imaging the source onto an annular mask and then re-imaging into the back focal plane of the microscope objective. LED illumination was used to produce the image in Fig. 2.13. This setup results in sharp images, free from the effects of coherent noise found when using the previous two illumination strategies. LEDs also have several other advantages over laser sources, including their low cost and power requirements, relative level of eye safety, ease of alignment and range of available wavelengths. This is not only the first reported use of LEDs for TIR microscopy but also the first successful high resolution images of living cells obtained using TIRM [153].

Aside from the lack of fluorescent label, there is another major distinction between TIRM and TIRF which arises from the difference in the contrast mechanisms. Experience has indicated that the optimum image contrast for TIRM is obtained when the illumination is incident at an angle which is only marginally greater than the critical angle defined by the sample substrate (coverslip) and the sample medium (usually aqueous). In this case, when a cell or colloidal particle of refractive index greater than the medium is proximal to the substrate, the critical angle of the glass/cell interface is greater than the illumination angle and light is coupled out of the evanescent field into a propagating wave. Consequently, the reflected intensity reduces and a brightfield image of the cell is obtained. For TIRF however, illuminating at slightly above the substrate/medium critical angle produces poor quality images. The propagating light that couples out of the evanescent field can excite fluorophores away from the substrate

surface, and many of the advantages of TIRF are lost. Hence, a larger angle is required, preferably greater than the critical angle formed by the substrate and the cell body. This requires the use of very high NA objectives as compared to TIRM, where NA 1.4 is usually adequate for most cell media.

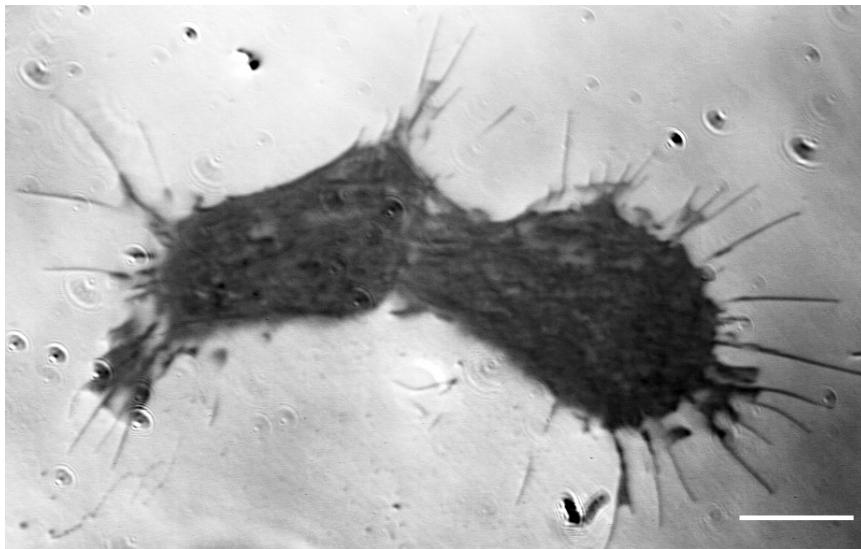


Figure 2.13 TIRM image of a 3T3 fibroblast cell captured using a LED illuminated setup.

This high quality image makes it possible to view the presence of two fibroblast cells in the field. Due to the high resolution achieved, it is possible to observe fine features such as the lamella and filopodia and also to study the adhesion profile of the cells to their substrate. Scale bar represents 20 μm .

2.4.3 TIRM temporal resolution

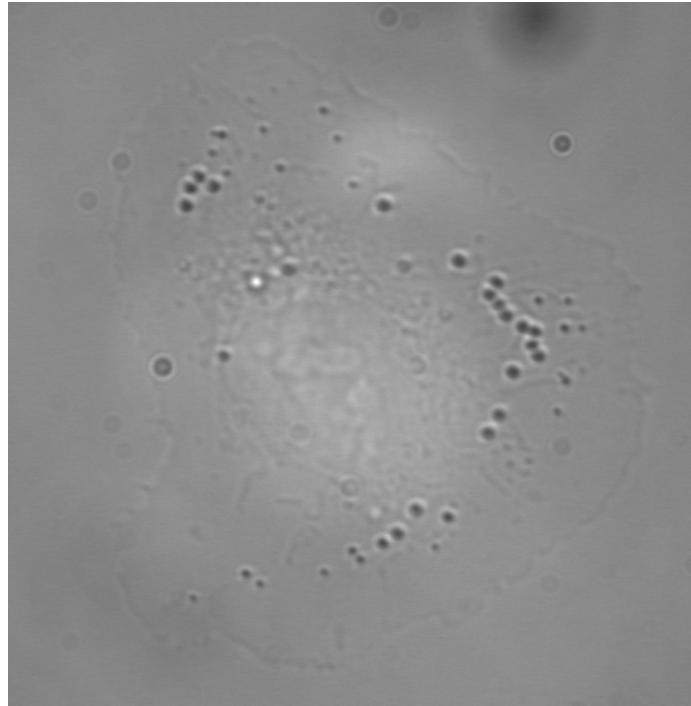
High speed time-lapse imaging can also be achieved using TIRM to obtain high resolution dynamic information on the interaction between cells and the surrounding extracellular environment. Cell membrane reorganisation and lamella protrusion and retraction play a key role in fibroblast locomotion [189]. Video-rate imaging is possible with TIRM due to the widefield nature of the system, as opposed to scanning, and the

fact that it is a brightfield technique thus affording very short exposure times. High temporal resolution imaging of living cells will be discussed in detail in Chapter 3.

2.4.4 Combined TIRM and Brightfield imaging

Combining TIRM with other complementary imaging modalities is clearly beneficial over TIRM alone, since it increases the power and range of applications of the system. Basing the TIRM system around a standard inverted biological microscope has meant that standard trans-illuminated BF microscopy can be performed through the same objective lens as that used for TIRM. Thus a combination of TIRM and BF imaging can be performed using the same system and captured on the same camera thus minimising problems associated with image registration. Figure 2.14 shows an image of an A549 lung alveolar like type II cell captured using BF microscopy (Fig. 2.14a) and TIRM (Fig. 2.14b). It can be seen that TIRM offers more depth discrimination over BF due to the nature of evanescent illumination. Also, areas in closer contact with the substrate, for example the nucleus, appear darker in the TIRM image. Discrimination of these regions is difficult in BF imaging. However, the benefit BF offers over TIRM is when a sample is not fully adhered to the substrate it can still produce an image of the cell outline. Thus, for cells that are not completely adherent to the surface BF would allow measurement of the cell outline whereas TIRM would give detailed information on cellular attachment sites. This is similar to an instrument developed by Weber *et al.* (1995) [190] which combined the power of RICM with brightfield microscopy.

A



B

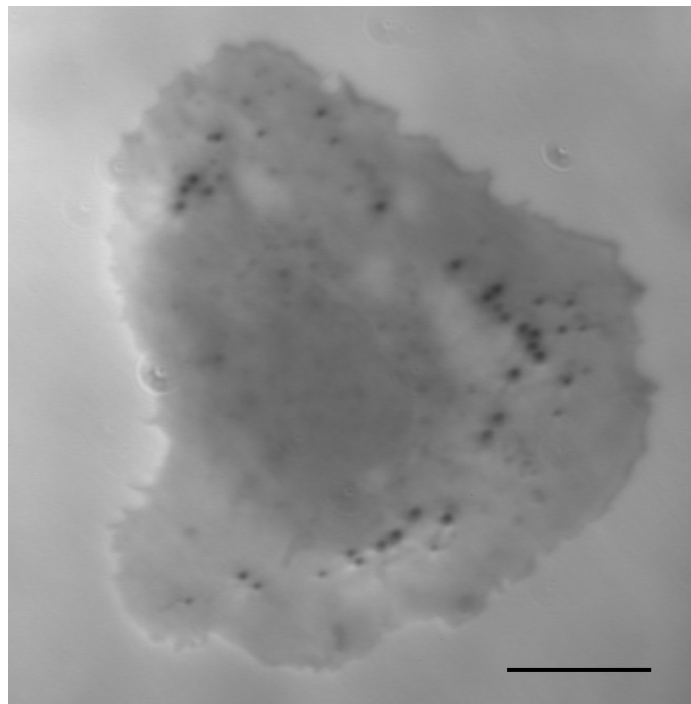


Figure 2.14 Brightfield and TIRM images of A549 cells.

(a) Bright field image of A549 lung alveolar type II like cell obtained using transmitted light function of the Meiji TC5400 and Zeiss 1.45 NA 100x Plan-Fluar objective lens. (b) Corresponding TIRM image of the same cell obtained using brightfield TIRM. Scale bar represents 15 μm .

2.4.5 Depth of field and focussing

High numerical aperture objectives generally have a very low depth of field where only a very thin section of the specimen falls into focus in the acquired image. The depth of field decreases proportionally with NA^2 (Eq. 2.10). This is illustrated schematically in Fig 2.15. When imaging using TIRM, the small depth of fields associated with the 1.45 NA objective lens make it extremely difficult to maintain focus in lengthy time-lapse studies.

$$D_f = \frac{\lambda_0 n}{NA^2} \quad (2.10)$$

Where λ_0 = wavelength of illumination, NA = Numerical aperture of objective lens and n = refractive index of the imaging medium.

Indeed, focal drift is further compounded when performing lengthy time-lapse studies where temperature fluctuations can affect focus. Another potential source of focus fluctuations within the sample is that the substrate supporting the specimen is not flat. For example, the height of a 9 x 15 mm² glass coverslip can vary 6 μ m across the diagonal [191]. Thus, when working with high NA objectives, where the depth of focus is small, it is possible to experience multiple focal spots on the same image plane. Also, when working with custom built microscope systems correct x, y and z alignment of the sample stage can be difficult to achieve, resulting in an image plane with multi focal points. Indeed, our experience with this problem led us to build our system around the body of an inverted biological microscope (Meiji TC5400), where the sample stage is

correctly aligned in all dimensions. Thermal variations are another potential source of focal fluctuations which cause the distance between the sample and the optical elements to drift over time. This can be as much as 1 μm per degree Celsius [192].

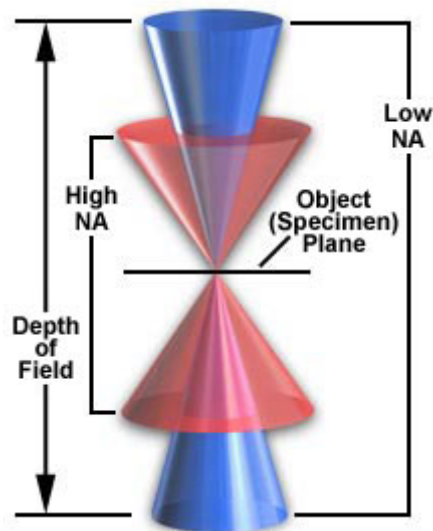


Figure 2.15 Schematic diagram illustrating the depth of field dependence on NA

For low NA objectives it can be seen that the cone of light produced is larger in the axial direction when compared to that for high NA objectives, thus resulting in a larger depth of field for the low NA lens. Depth of field is also an indication of the axial resolving power of the lens (Figure reproduced with the kind permission of Nikon MicroscopyU).

Auto-focusing is commonly used to overcome the problems associated with focal drift. There are several commercially available options for autofocus. However, these solutions can be difficult to adapt into individual user requirements [192]. Recently, a technique based on digital filtering of high frequency information has proved useful for focal drift associated with DIC images obtained with a 1.45 NA lens [193]. There are several drawbacks with autofocus systems; they are not trivial to implement and the temporal resolution of the microscopy system is generally reduced since typically

computation must take place prior to the adjustment in focus. In our system, focus was maintained manually by the user which, albeit being a soporific task, resulted in generation of suitable high quality images. Future modifications to the TIRM setup should see the implementation of an auto-focus module.

2.4.6 Substrate selection

The high resolution imaging obtainable by TIRM is limited to a region localised to the glass coverslip (typically 500 nm) due to the evanescent nature of illumination. The evanescent nature of the wave also means that the sensitivity of the instrument will decrease with distance from the surface i.e. the instrument is most sensitive at the total internal reflection interface. It follows that if a cell or a part of a cell is outside the evanescent field it will not be visible by TIRM. This situation may arise when for example a biomaterial is coated on top of the glass coverslip to promote cell adhesion and growth. If the biomaterial is sufficiently thick the EW may not penetrate it thus preventing TIR imaging. Also, if the surface of this biomaterial is rough, scattering of the evanescent field will occur at the interface. Figure 2.16a shows a TIRM image of a human osteoblast like cell growing on an uncoated glass coverslip. The cell is clearly visible in the image and certain contact points are easily discernible. Figure 2.16b is a TIRM image of the PLGA polymer film which has been coated onto a glass based dish. It can be seen there are heterogeneous light and dark regions, thus indicating the surface roughness is high. The dark regions represent areas where the PLGA has adhered to the glass substrate and is thus ‘frustrating’ TIR. The lighter regions are likely to represent areas where PLGA has not been coated and where it may not have adhered due to

surface tension effects. Figure 2.16c shows a coverslip which has an interface (yellow line) between an area of PLGA coating and an uncoated area. The cell is only visible on the area of the coverslip which is uncoated. Figure 2.16d is a line intensity profile of the dashed red line in Fig. 2.16c. Three distinct regions are visible from the line profile; the PLGA film on the glass coverslip, a region of the cell on glass and finally the glass substrate itself.

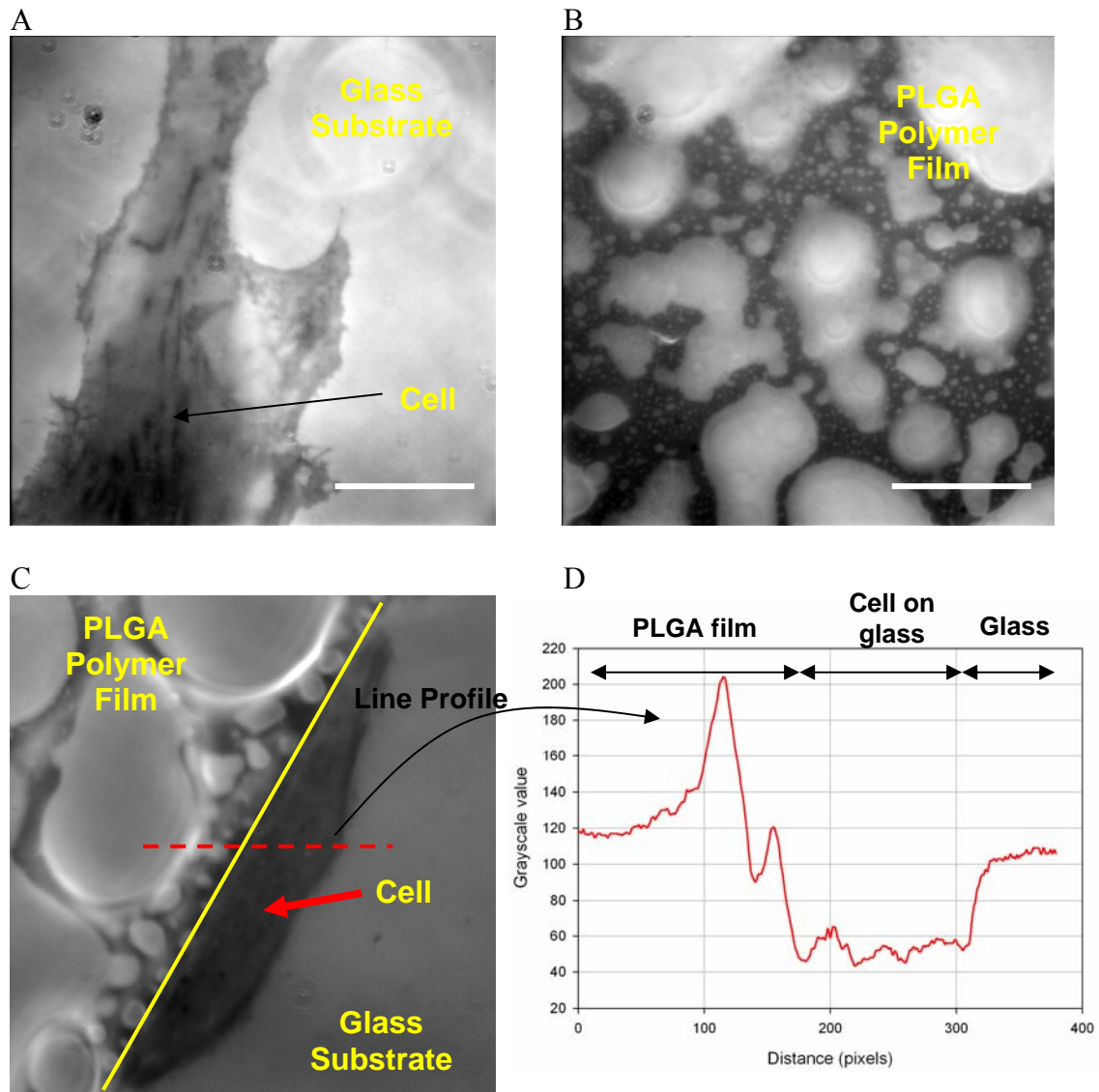


Figure 2.16 TIRM images and line plot of a Human Osteoblast like cells (HOBs) adhering to PLGA polymer film and glass

TIRM images of (a) HOB cell adhering to a glass coverslip, (b) PLGA polymer film and (c) HOB cell adhering to both polymer film and glass coverslip. This image shows a view of the interface between the polymer film and the glass coverslip. It can be seen that the cell is only in view on the glass region of the image, indicating the cell is outside the field of view when adhered to the PLGA polymer film. (d) Line plot of dashed red line in (c). The low grayscale value for the region between pixel 120 and 300 indicate the region of close cell attachment to the glass coverslip. Scale bar represents 20 μm .

These results highlight the fact that TIRM is not suitable for imaging through thickly coated and uneven coated substrates/biomaterial. For example, PLL of molecular weight 75,000 – 100,000 is homogeneously distributed on glass with a coating thickness of a few nanometers and exhibits a low surface roughness (rms = 0.35 nm) [194]. Clearly, this is an order of magnitude smaller than evanescent wave penetration depth, which is normally in the region of 100 – 200 nm. However, PLGA tends to form a much thicker coat when spun coat onto the surface and has a higher surface roughness. This is likely to be due to the relative viscosities of the two polymers. Therefore, it is unlikely that the evanescent wave will penetrate far enough into the sample in order to visualise the cells on top. Recently, Zhu and co-workers (2006) [195] imaged 3T3 fibroblast cells growing on PLGA using a confocal RICM technique without the aforementioned problem associated with sample thickness. RICM, being an interference technique and not associated with evanescent fields (Section 2.4.1), thus has the ability to illuminate through thickly coated substrates and produce an image.

2.5 Conclusions

A novel total internal reflection microscope has been developed enabling high resolution label free imaging of living cells. Contrast in TIRM is generated through ‘scattering’ of evanescent light and has shown to be different from other techniques used to study cell adhesion such as RICM. There are several methods distinct ways of achieving evanescent illumination in TIR microscopy, such as introducing the source through a prism, cardiod dark-filed condenser or through a high NA objective lens. We have utilised a high NA objective lens for TIRM due to the ease of setup and quality of images compared with the prism technique. Light emitting diodes are a simple and effective illumination source for TIRM. They are cheap, available in a range of wavelengths, relatively safe on the eyes and are free from the coherent artefacts associated with laser illumination. The major drawbacks of TIRM are associated with the method of illumination and the use of high NA objective lens. Evanescent illumination only affords the imaging of a defined region localised to the glass substrate and thus the microscope has no ability to section through the cell. However, this drawback is outweighed favourably by the very high resolution images produced without the need for a fluorophore. The use of a high NA objective lens means that the DOF is small resulting in the tendency for focus fluctuations. This can potentially overcome by the use of autofocus systems.

Chapter 3

Applications of TIRM for live cell imaging

3.1 Introduction

Over the past couple of decades tissue engineering has emerged as a major field of research which aims to provide new ways of preparing cost-effective and functional substitutes for damaged tissue [196-198]. Generally, the engineering of new tissue requires preformed substrates which allow control over growth, proliferation and function of cells and thus the final shape and function of the tissue. The cellular response to the substrate is known to be dependant on both the surface chemistry and surface topography of the substrate material [199-202]. Thus by modifying the material surface it is possible to control adhesion and proliferation of cells through a precise spatial distribution of adhesion factors.

Researchers in the fields of biomaterials and tissue engineering are interested in knowing to what extent and how a materials surface chemistry affects the interaction between the cell and its substrate. There are several ways of studying this interaction but probably the simplest way is to directly visualise it using microscopy techniques [203]. Indeed, it is preferable to image living cells, as opposed to fixed cells, as it affords one to build up a map of the cell-substrate interactions over time. There are a number of optical microscopy techniques which have been utilised over the years to look at this interaction between the cell and its substrate. Non-fluorescent techniques include RICM [186], surface plasmon resonance microscopy (SPRM) [64, 204] and DIC [50, 205]. Techniques such as DIC are useful for looking at a cell population, however they do not provide high resolution information on contact points made between a single cell and

the surface. In addition to high-resolution imaging, RICM also enables quantification of the cell-substrate separation distance [160]. It has also been used to identify focal and close contacts, which are normally only visible through immunostaining for proteins such as vinculin [206, 207] and paxillin [208], or through tagging of such proteins with green fluorescent protein (GFP) [209]. SPRM is a highly sensitive technique, and has been used to detect the binding of streptavidin to photopatterned biotinylated alkanethiol self-assembled monolayers [210], but is still lacking in terms of its spatial (xy) resolution [64, 204]. The commonly used fluorescent techniques such as CLSM [211] and TIRF [80] are also very useful but require a fluorescent label therefore making the study more complicated, and time-consuming and there is the increased risk of phototoxicity to the cell.

3.2 Aims and objectives

The aim of this chapter is to demonstrate the use of TIRM for label-free high resolution imaging of cell-substrate interactions on two different cell types, namely human Type II lung alveolar epithelial cells and murine 3T3 fibroblast cells. In addition, TIRM is compared and contrasted to another evanescent wave technique, SPRM.

3.3 Materials and methods

3.3.1 Total internal reflection microscopy

TIRM was performed as described previously [153] and in Chapter 2. Exposure times and frame rates used for imaging are discussed within the text.

3.3.2 Surface plasmon resonance microscopy

A schematic of the microscope system is shown in Fig. 3.1. The HeNe laser (CVI Melles Griot, USA) was used to generate coherent linearly polarised light at a wavelength of 633 nm. The laser illuminates a diffuser (Ground glass disc, custom made, University of Nottingham Electronic Engineering workshop), which is imaged on to an intermediate plane between F2 and F3 (TechSpec MgF2 coated achromatic lenses), which is, in turn, imaged on to the back focal plane of an oil-immersion objective (PlanFluor 100x NA 1.45, Zeiss). The sample is thus Köhler illuminated. Two CCD cameras connected to a personal computer (Dell, UK) are used in the system: one images the back focal plane distribution (SXFV-H5, Starlight-Xpress, UK) and the other (iXon DV-885 KCS-VP, Andor Technology, Belfast UK) a reflected image of the sample. The surface plasmon's are excited around the plasmon angle (48 for a bare gold coverslip [59]) and excitation at other angles does not contribute to the contrast and just adds background, an aperture is placed in a plane conjugate with the back focal plane of the objective as depicted in Fig. 3.1. This was achieved using a moveable slit (mask). The mask was adjusted so that the mean angle of incidence surface was just below the

surface plasmon resonance dip so that interfacial interactions between a cell and the substrate result in an increase in the magnitude of the reflected signal.

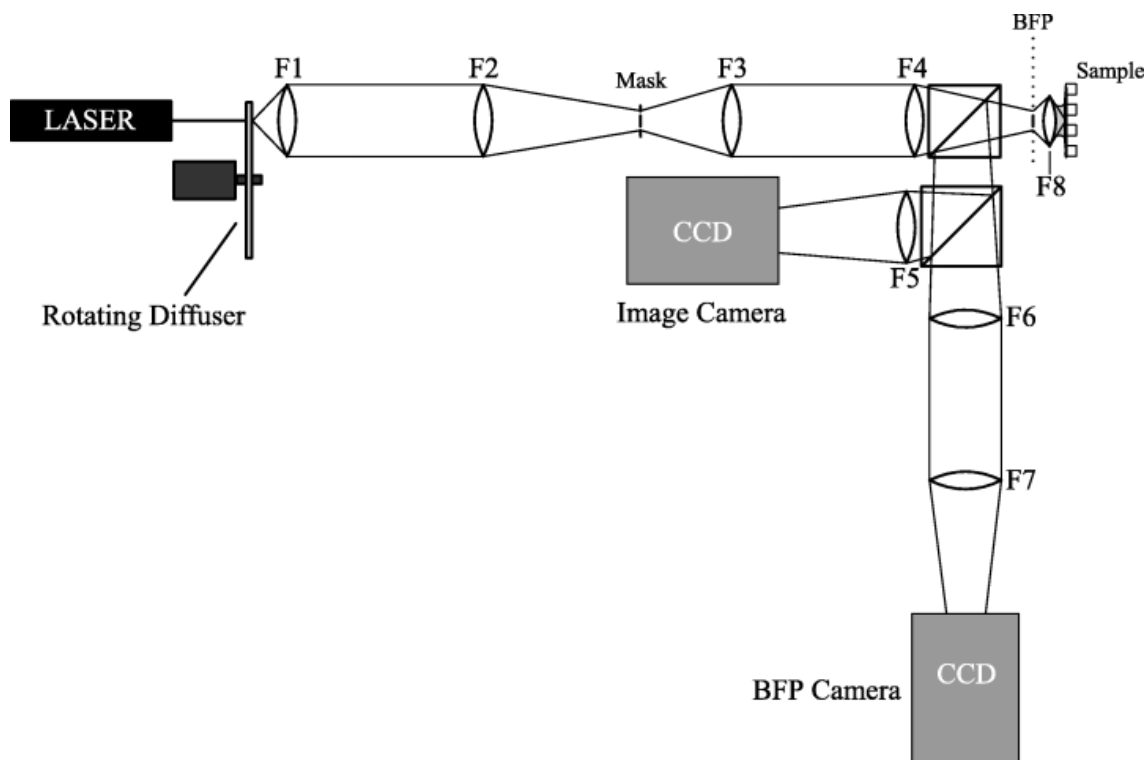


Figure 3.1 Schematic diagram of the Kohler illuminated SPR microscope configuration

F1 (focal length = 30 mm) and F2 (160 mm) function as a beam expander, F3 (80 mm) and F4 (80 mm) function as image relay, F5 (160 mm) is a tube lens and F6 (60 mm) and F7 (40 mm) function as BFP image relay and de-magnification. Reprinted from [59], with the kind permission of Blackwell Scientific.

3.3.3 Cell culture

Cell culture was performed as described in Section 2.3.2

3.4 Results and discussion

3.4.1 Label-free high resolution TIRM imaging of 3T3 fibroblast cells

The 3T3 cell line has become the standard fibroblast cell line used in cell culture and originally came from Swiss mouse embryonic tissue [212]. 3T3 cells have been successfully imaged using a plethora of microscopy techniques including; DIC, phase contrast, RICM, TIRF and CLSM. However, until recently [153] these cells had not been imaged using TIRM. A typical TIRM image of a fibroblast cell cultured for 3 h on PLL-coated cover slip can be seen in Fig. 3.2. PLL is routinely used in cell culture to aid adherence of cells to a substrate. Figure 3.2 demonstrates the high level of surface topographical detail achievable with TIRM. It can be seen that there is a large area of the cell which is not in contact with the coverslip, for example the region marked by the red asterisk. These areas of bright intensity indicate that little of the illumination light is being scattered by the cell and thus there is minimum contact of the cell with the substrate in this region. More homogeneous adhesions, represented by dark patches (arrows), can be seen towards the left and bottom of the image. The image intensity gives an indication of how closely the cell is attached, with these dark areas being close to the cell substrate. Currently, TIRM imaging remains qualitative in nature and can only be used as an indication of how close an object is to the substrate. However, with further work the quantification of cell-substrate separation distances should be achievable with TIRM. Presently this is achievable with the RICM technique [160, 186]. A more detailed discussion about the possibility of obtaining quantitative

information from TIRM imaging is contained within the future work section (Section 7.4.1.2).

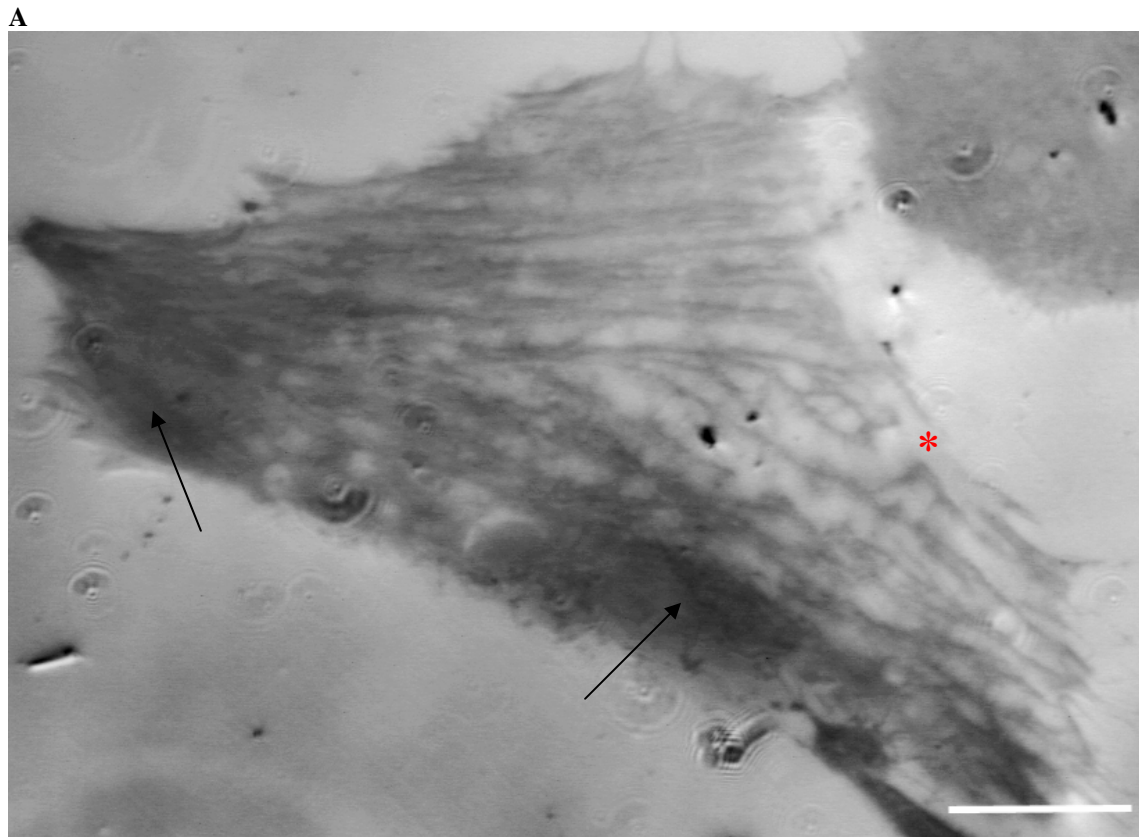


Figure 3.2 TIRM image of a 3T3 fibroblast cell cultured on a PLL coated cover slip for 3 h.

This image highlights the capability of TIRM to obtain high-resolution topographical information of the adhesion of fibroblasts to PLL substrates. Arrows represent areas forming a close and fairly homogenous contact with the substrate. The red asterisk represents a region of the cell which is scattering little of the illumination light and hence is lying far-away from the coverslip. Scale bar represents 30 μm .

High-speed time-lapse imaging can also be achieved using this technique to obtain high-resolution dynamic information on the interaction between cells and the surrounding extra-cellular environment. Figure 3.3 shows a series of TIRM images from a time-lapse sequence of a 3T3 cell on a PLL-coated cover slip. The arrows at $t=0$ indicate areas where cell contacts are visible. After 250 and 500 seconds, it can be seen that the contacts are no longer observable. Cell membrane reorganization and lamella protrusion and retraction are highlighted by the asterisks. It is known that these processes play a key role in fibroblast locomotion [189]. Although the time lapse illustrated in Fig. 3.3 is relatively long (500 sec), it is possible to follow the dynamics of cell contact movement on the basal cell membrane at frames rates up to 30 frames per second, since TIRM is a bright-field technique.

Figure 3.4 shows a different 3T3 fibroblast cell cultured on a PLL coated coverslip for 3 hours. Twelve sequential images from a TIRM time-lapse video of the cell shown in Fig. 3.4 are shown in Fig. 3.5a. These images show lamella movement (red arrows) and the membrane ruffling found at the leading edge of the cell (green arrows) in exquisite detail and provide a view of the basal cell membrane which is unrivalled for label-free optical microscopy. It is also possible to image filopodia structures which can be seen to flash in and out of the image (Fig. 3.5b). This flashing occurs when the filopodia are sensing the extracellular environment and therefore move in and out of the evanescent field.

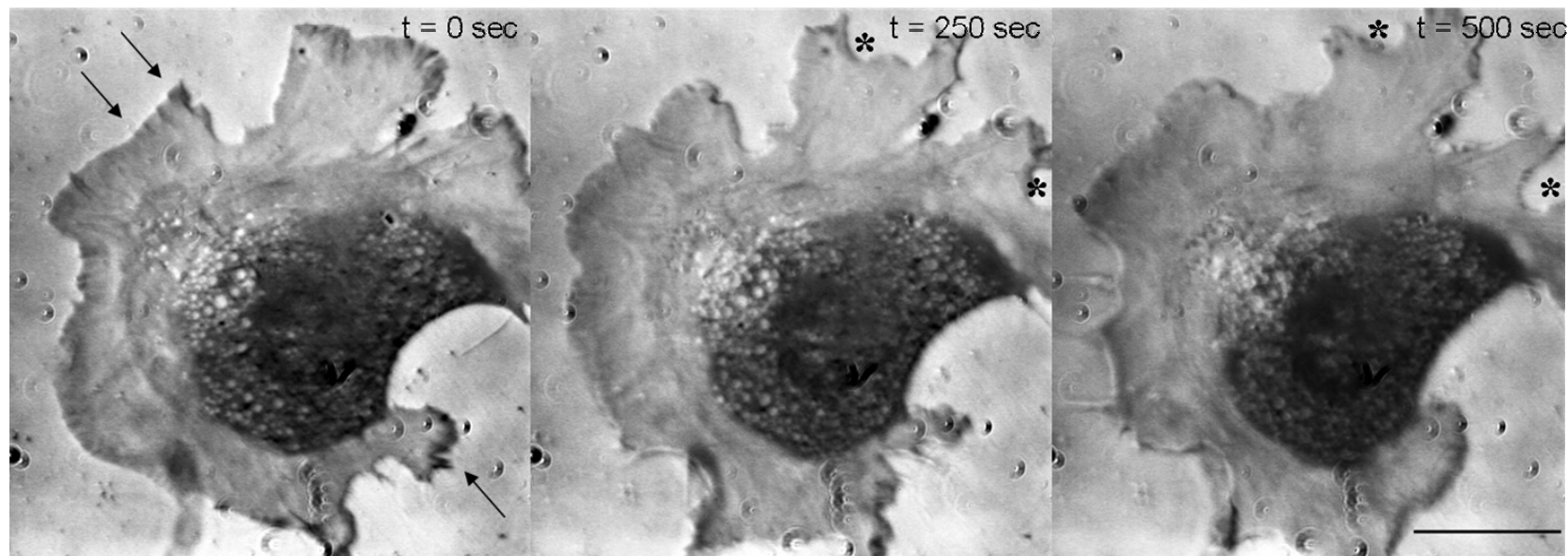


Figure 3.3 Series of images from a TIRM time-lapse sequence of unlabelled 3T3 fibroblast cells adherent to a poly-L-lysine coated coverslip.

At $t = 0$ several areas of close contact are highlighted with arrows. These areas of contact are not visible after 250 and 500 seconds. Cell membrane reorganisation is also seen to take place after 250 and 500 seconds, as seen highlighted by the asterisks. Cells were imaged after 24 hour incubation at 37°C and $5\% \text{CO}_2$. Scale bar represents $40 \mu\text{m}$. The video that this image sequence was extracted from can be found in the accompanied CD, named Figure 3.2.

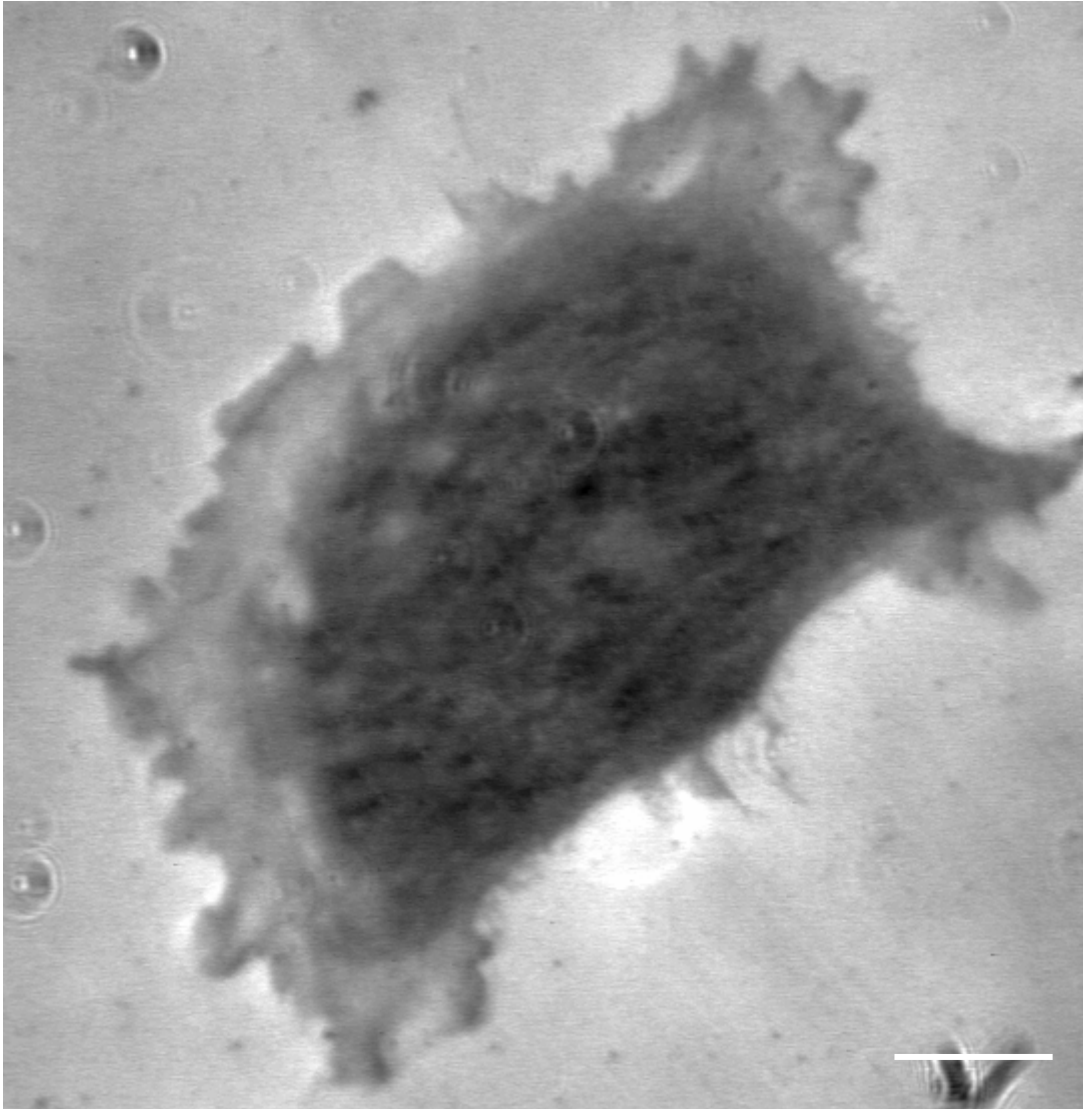


Figure 3.4 TIRM image of a 3T3 fibroblast cell cultured on a PLL coated cover slip for 3 h.

This image highlights the capability of TIRM to obtain high-resolution topographical information of the adhesion of fibroblasts to PLL substrates. Scale bar represents 20 μm . The image sequence that this image was extracted from is represented in Figure 3.5.

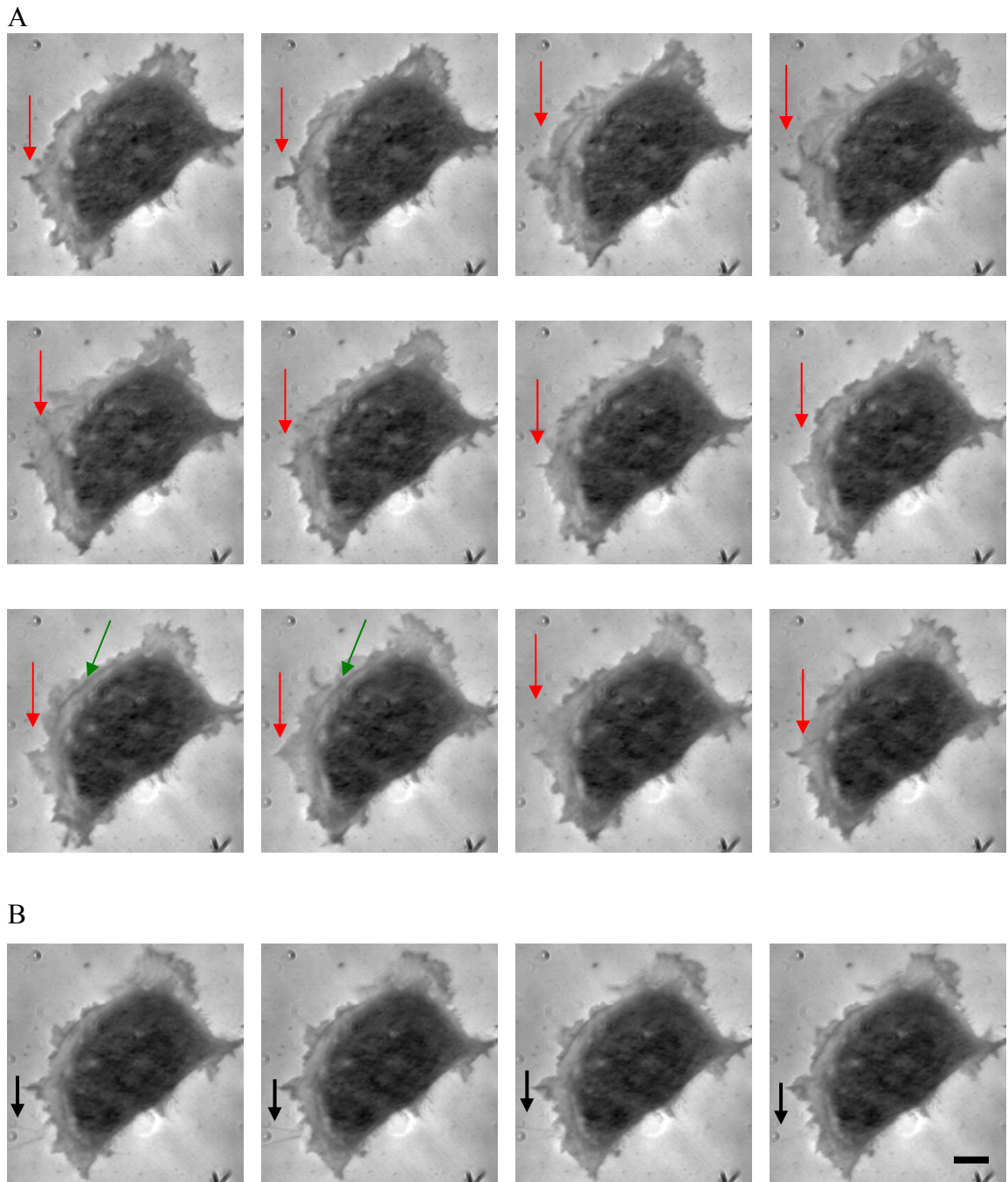


Figure 3.5 Series of images from a TIRM time-lapse sequence of unlabelled 3T3 fibroblast cells adherent to a poly-L-lysine coated coverslip.

A) 12 sequential TIRM images taken from a sequence of 200, at 10 seconds per frame. Red arrows represent an area where the lamella is observed to moving. The green arrow is representative of a membrane ruffle

B) 4 sequential TIRM images taken from a sequence of 200, at 1 second per frame. The black arrows represent filopodia touching the surface of the coverslip and subsequently disappearing from the image. Scale bar represents 20 μm .

3.1.1 Surface plasmon resonance microscopy

A similar technique to TIRM, known as surface plasmon resonance microscopy (SPRM), has also been utilized for label-free imaging (Fig. 3.6). The major drawback of SPRM is its limited lateral resolution, as is shown in Fig. 3.6, where it is difficult to discern any cellular features such as the lamella and filopodia. In SPRM, the lateral resolution is limited to approximately $1\ \mu\text{m}$ due to the propagation length of the surface plasmons, as opposed to being diffraction limited in conventional optical microscopy and limited by the scattering ability of the sample in TIRM. Surface plasmons propagate along the metal/dielectric interface until they finally decay back into photons or dissipate into heat [63]. Consequently, surface plasmons cannot resolve features below their propagation length. These low resolution images are similar to those produced by Giebel *et al* (1999) who imaged a goldfish glial cell using a prism based SPRM [64].

The lateral resolution of SPRM has been improved through the use of a 1.65 NA objective lens type setup [204]. In this work the author's imaged HaCaT cells in both air and cell media. Use of the objective lens to excite surface plasmons considerably improved the image resolution however, it is still not as good as that observed with TIRM. For example, Jamil *et al* (2008) claim they can see filopodia structures in their images however, it is unlikely that this is the case. Filopodia are normally seen to wave in and out of the evanescent field as seen in Fig 3.5b. The filopodia like structure seen in the SPRM images are more likely to be stress fibers which are made when the cell is under physiological stress. Additionally, SPRM is more complicated than TIRM to implement.

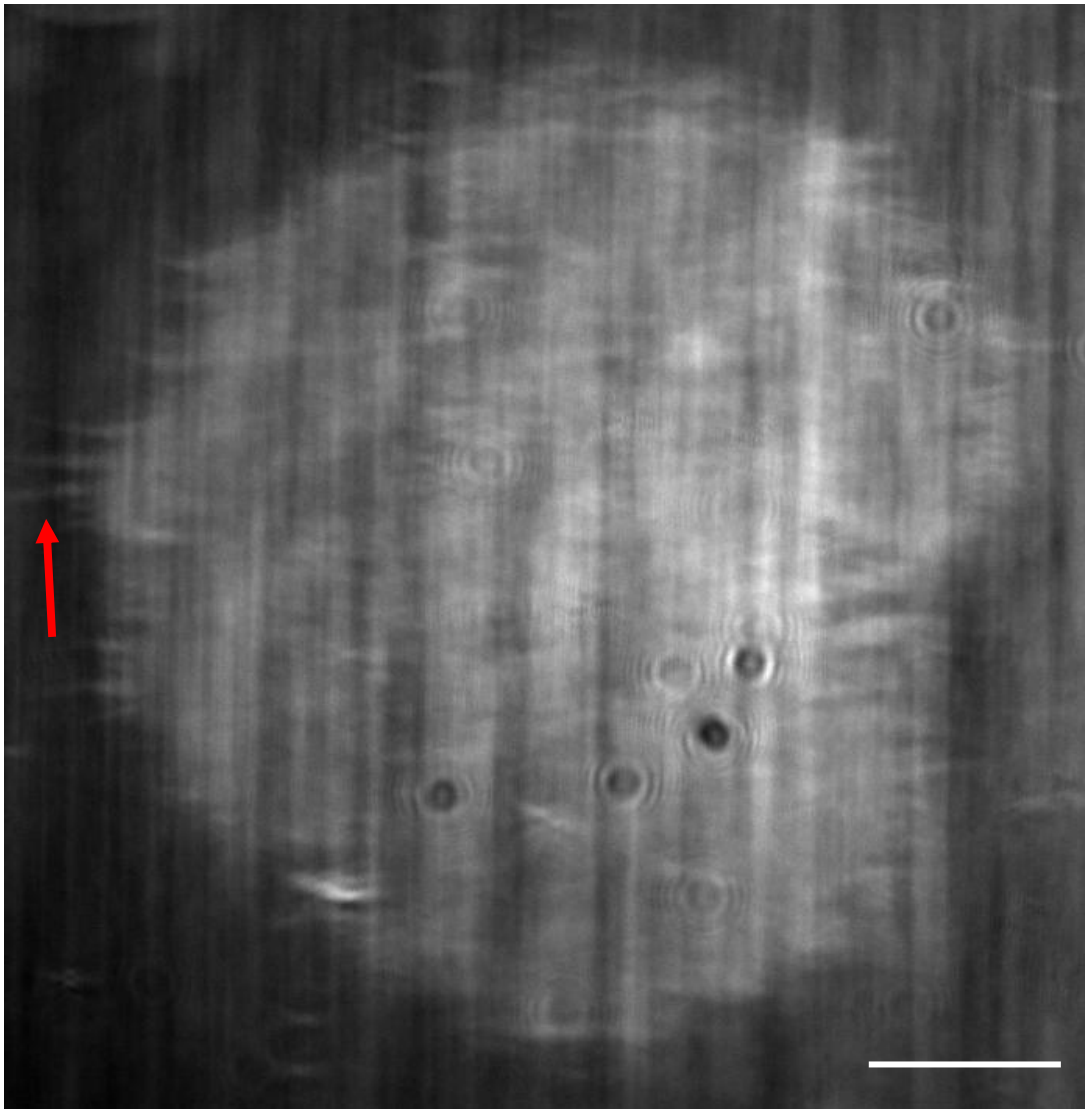


Figure 3.6 SPRM image of a 3T3 fibroblast cell adhered to a PLL coated gold substrate.

It can be seen that the resolution of the cell is much poorer in comparison to those imaged by the TIRM system. This is due to the inherently long decay length of the surface plasmon. However, it is possible to discern some features close to the edge of the image (red arrow) and these are likely to be stress fibres or filopodia. Scale bar represents 20 μm .

3.1.2 TIRM imaging of an epithelial cell line

TIRM has also been used to image A549 cells, a cell line derived from a human lung alveolar basal epithelial carcinoma [213] (Fig. 3.8-3.9). A549 cells are alveolar epithelial type II (AE2) cells and have been termed ‘defenders’ of the alveolus [214]. AE2 cells synthesise, secrete, and recycle all components of the surfactant that regulates alveolar surface tension in mammalian lungs. Figure 3.8a shows a single frame from a typical time-lapse video of A549 cells cultured on a PLL coated coverslip for 4 hours. It can be seen that cell is rounded in nature and is unpolarised. Also, the central region of the cell is darker than the outer regions of the cell. This is postulated to be because this area contains the nucleus directly above it which causes the membrane to be in close contact with the surface. For reference, a brightfield image of A549 cells is shown in Fig. 3.7.

One observation which is markedly different from that of the TIRM images of fibroblast cells is the presence of very dark puncta on the basal membrane of the A549 cell. One of these puncta, a punctum, is seen in more detail in the series of magnified images in Fig. 3.8b. In the series of images, the punctum, follows the path highlighted in yellow in the first frame of the image sequence. In frames 9 & 10 it can be seen that the punctum is beginning to fade away, with the intensity beginning to equal the background intensity. This motion represents firstly the lateral movement of the punctum and secondly its axial movement and eventual internalisation by the cell. Also, the yellow line in the first frame of the image sequence represents a tubular like structure which can be seen in the image.

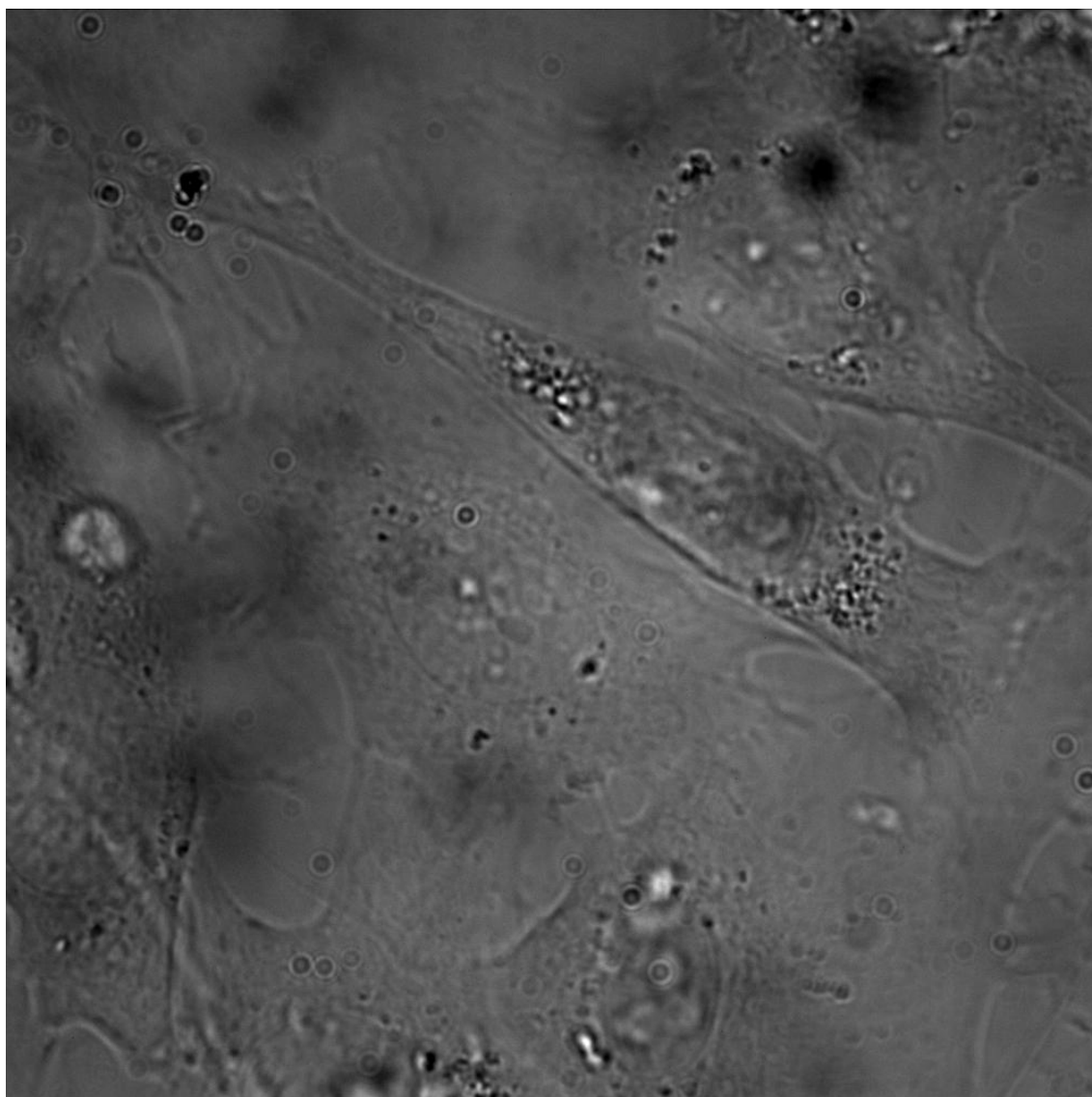


Figure 3.7 Bright-field image of a population of A549 cells adhered to a PLL coated coverslip

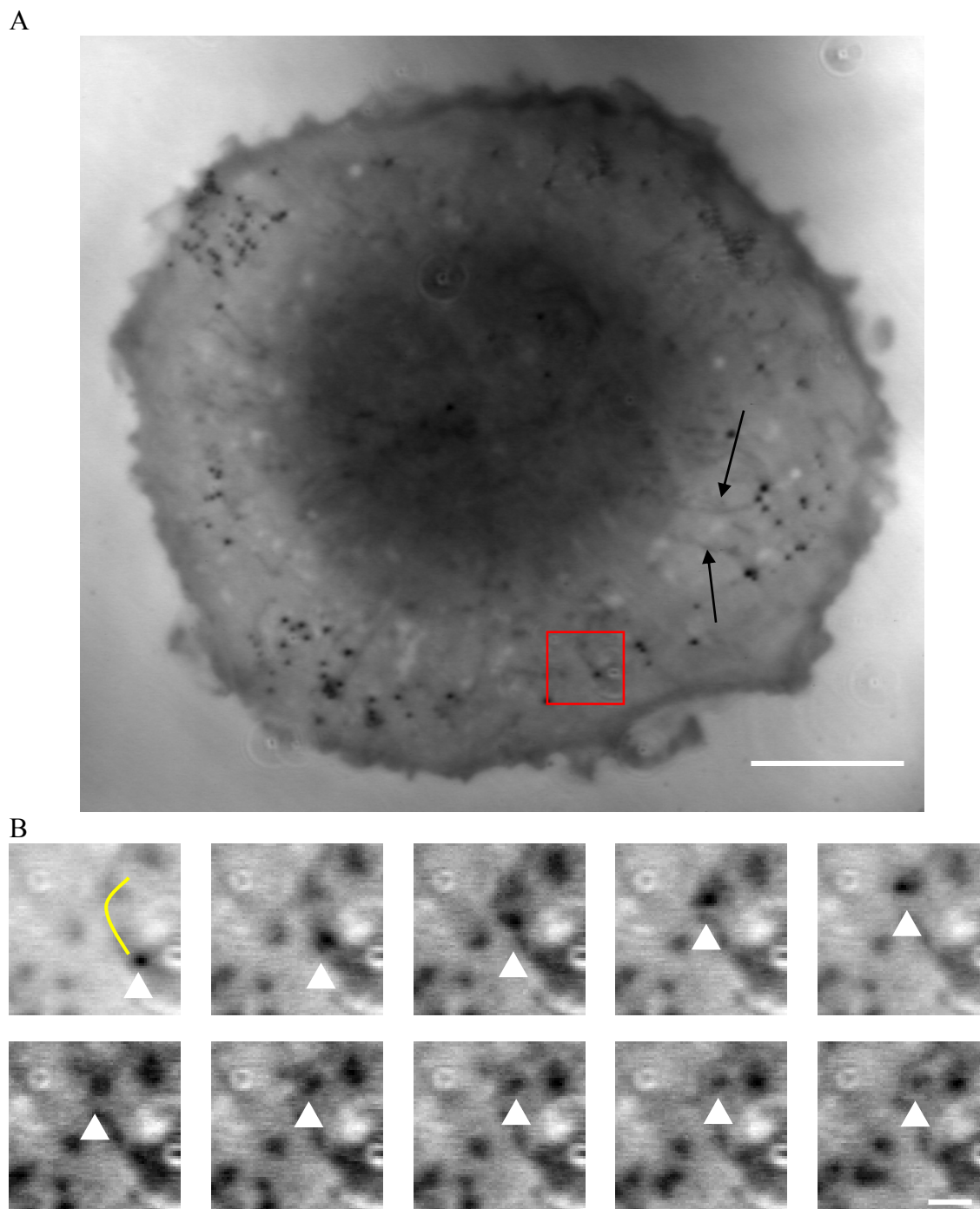


Figure 3.8 TIRM images of unlabelled A549 cells adherent to a PLL coated coverslip for 4 hours.

A) Typical image taken from a TIRM time-lapse sequence of A549 cells adherent to a PLL coated coverslip the arrows indicate tubular like structures. The red box represents the area magnified in B. Scale bar represents 20 μm . B) Series of images magnified from the TIRM sequence in A (area magnified is represented by the red box). The white triangle represents a vesicular body which is seen to move following the direction of the yellow line in frame 1. It can then be seen to gradually fade away indicating that it is moving out of the evanescent field and thus into the cell. There is a lapse of 5 seconds between each frame in the image sequence. Scale bar represents 4 μm .

Figure 3.9a shows a single frame from a typical time-lapse video of A549 cells cultured on a PLL coated coverslip for 24 hours. Similar to the cell cultured for 4 hours (Fig. 3.8a) it is rounded in nature however, the membrane is not as homogeneously adhered to the substrate. Here the cell membrane is characterised by many concave shaped cavities. These concavity-shaped patterns are randomly distributed over the cell membrane and are of varying size. This pattern has also been observed in fibroblast cells [215] and chick heart explant cells [216]. Polylysine is known to exert an attractive force on the cell membrane due to an electrostatic interaction. It is believed that the concavity features observed on the membrane result as a consequence of competition between the electrostatic interactions formed between PLL and the cell membrane, and the mechanical stiffness of the membrane inferred by the actin cytoskeleton [215]. This causes the actin cytoskeleton to bend in certain areas, giving rise to cavities. Lateral movement of a punctum can be seen in Fig. 3.9b. The speed of this movement has been recorded to be approximately 5 $\mu\text{m}/\text{min}$.

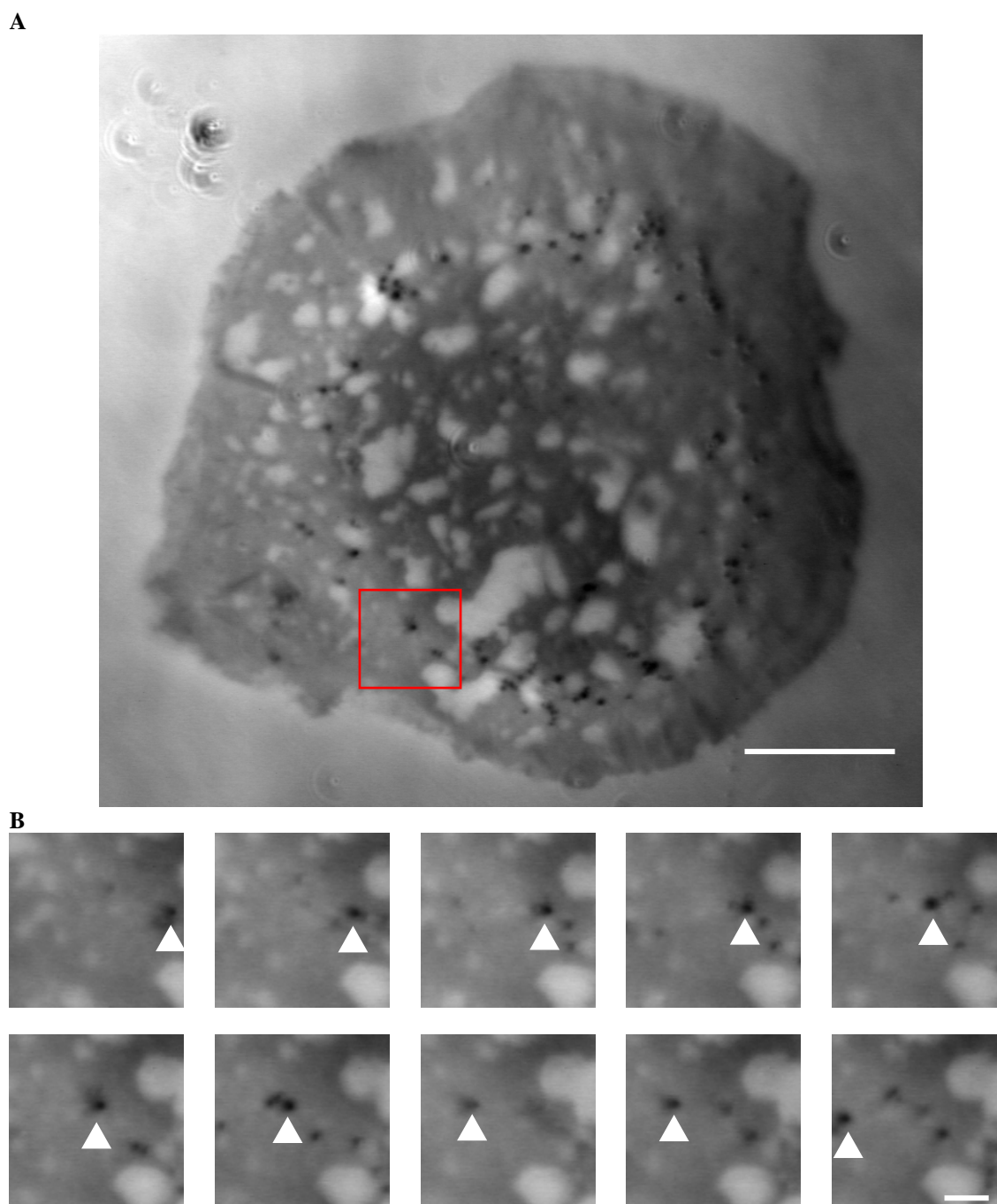


Figure 3.9 TIRM images of unlabelled A549 cells adherent to a PLL coated coverslip for 24 hours.

A) Typical image taken from a TIRM time-lapse sequence of A549 cells adherent to a PLL coated coverslip. Scale bar represents 20 μm . B) Series of images magnified from the TIRM sequence in A (area magnified is represented by the red box in A). The white triangle represents a vesicular body which is seen to move laterally. The spot moves at a speed of $\sim 5 \mu\text{m}/\text{min}$. There is a lapse of 25 seconds between each frame in the image sequence. Scale bar represents 5 μm .

Although the identity of the punctum and tubule like structures remains unclear and cannot be inferred directly from the TIRM images, it is still possible to speculate as to their function. As mentioned previously, AE2 cells are known to regulate the secretion of surfactant onto the lung epithelium. The surfactant is secreted from special intracellular storage organelles termed lamellar bodies. The biochemical composition of the storage organelles is similar to that of broncoalveolar lavage (BAL) which is composed of ~90% lipids and ~10% proteins [217].

Previously the lamellar bodies have been observed with transmission electron microscopy (TEM) as large densely packed structures which range in size from 0.5-2 μ m [217, 218]. It is possible and most likely that the puncta observed in the images of the A549 cells are lamellar bodies. The size of the structures in the TIRM images (Fig. 3.8b-3.9b) match that observed with TEM. Additionally, the structures are densely packed with lipids and proteins which would lead to a high degree of scattering in the TIRM image. It can be seen in the TIRM images that the puncta are very dark in contrast to the rest of the cell. This indicates that they are much closer to the surface and/or very densely packed, hence scattering more light. Another reason to believe that they are lamellar bodies is that they are known to originate from the cell, release their payload to the extracellular environment before recycling back into the cell. Time-lapse TIRM has shown a vesicle which has been recycled back into the cell (Fig. 3.8a) and also other vesicles which are seen to originate from within the cell.

3.2 Conclusions

Total internal reflection microscopy can be used for qualitative label-free high resolution imaging of the cell surface. High-speed time lapse video microscopy enables the study of dynamic cellular processes such as filopodia extension and retraction, membrane ruffling and lamellipodial movement. This technique has a plethora of potential application in studying cell-substrate interactions.

Chapter 4

Combined Total Internal Reflection Microscopy and Total Internal Reflection Fluorescence Microscopy (TIRM/TIRF)

4.1 Overview of study

The aim of this chapter is to introduce an instrument which combines the high resolution label-free imaging of TIRM with the specificity afforded by the fluorescence based TIRF technique. The key design considerations regarding the development of this instrument are discussed in detail. Results are presented which show how TIRM and TIRF images can be recorded sequentially. Other novel uses for the instrument are also discussed.

4.2 Introduction

Since Sir George G Stokes first described the term fluorescence in 1852 [219] and the subsequent development of fluorescent probes for biological imaging in the 1930's, there have been several paradigm shifts in fluorescence microscopy development. However, the fundamental principle remains the same. Generally, the biological molecule or material of interest is tagged with a fluorophore. This is subsequently excited using a specific excitation wavelength and according to the Stokes shift the excited molecule will then emit a photon of lower energy and hence longer wavelength. The longer wavelength emitted photon is then collected by means of a suitable detector. This affords rapid specific detection of the molecule or material of interest, free from 'noise' of all the other molecules within the sample. Fluorescence microscopy is now an essential tool in biology, biomedical science, drug delivery and materials science research due to the highly specific nature of contrast, which has enabled molecular imaging.

There are a plethora of microscopy techniques which are based on the fundamental principle of fluorescence. These include epi-fluorescence microscopy, confocal laser scanning microscopy (CLSM) and total internal reflection fluorescence (TIRF) microscopy. Each technique has its inherent advantages and disadvantages and generally one technique will be more suitable to a given application, depending on the nature of that application. Epi-fluorescence microscopy works in a way whereby a sample is illuminated through an objective lens, in a widefield manner, and the emitted photons are collected through the same objective lens. In this microscopy the collected

fluorescence comes from the whole sample and thus the image tends to contain a lot of out of focus fluorescence when observing a densely populated molecule such as actin. This is a major drawback of epi-fluorescence microscopy since it is difficult to discern individual molecules of interest.

Through careful positioning of a pinhole in a plane conjugate to that of the image and the scanning of a focussed laser beam across the sample it is possible to restrict fluorescent collection to that of the image plane. This is the principle behind the confocal microscope. The thickness of the image plane tends to be in the region of 500 – 800 nm, for 1 and 2-photon confocal systems respectively; thus the system offers an axial resolution of the same dimensions. Lateral resolution is typically slightly better than that of a widefield system since the pinhole nature of collection reduces the PSF of the microscope. However, as it is a scanning technique compared with the widefield nature of epi-fluorescence microscopy, the time taken for image generation tends to be higher. A great advantage of confocal microscopy is that it affords the ability to section through a sample of interest, however the thickness of this ‘slice’ is in the region of 500 nm thus making colocalisation studies difficult. Also, when focussed on the plasma membrane, confocal microscopy will show a large background signal from the cytosol that obscures the weaker fluorescence from small structures or molecular assemblies near the membrane [220].

The ability to restrict the illumination to a thinner region of the sample has many associated benefits. Since the illumination is only in a thin plane, background fluorescence will be eliminated, resulting in high contrast images with a high signal to

noise ratio. TIRF microscopy is a technique which works on the principle of restricting the illumination to a single thin plane and thus offers the potential for extremely high axial resolution imaging of biological samples. It's a widefield technique and thus temporal resolution does not suffer as it does with scanning techniques. However, the technique does not have the ability to 'optically section' throughout the whole sample. This is due to fact that TIRF microscopy is based on evanescent fields.

The theory of evanescent field (EF) generation has been extensively described earlier in this thesis (Chapter 2). Briefly, an EF can form when a beam of light travelling in a medium of high refractive index, such as glass, encounters one of lower refractive index such as the adjoining water or an adherent cell. If the angle of incidence is greater than the critical angle for the glass/medium interface, then the light will undergo total internal reflection at the interface. Classical electrodynamics does not allow an electromagnetic wave to vanish discontinuously at an interface, therefore total internal reflection sets up a thin layer of light in the water or cell, called the EF. An important property of the evanescent wave is that it decays exponentially with distance from the surface, z . The theoretical penetration depth, d , depends on the angle of incidence, wavelength and polarization of light, and the refractive index of the coverslip and medium. In practice, penetration depths of <100 nm are achievable.

It is the ability of TIRF to selectively illuminate a thin region of the sample that makes it so appealing. For the example of a cell adhering to a glass coverslip, the EF will only reach from the plasma membrane into the cytoplasm for little more than 100 nm, a distance comparable to ultrathin sections cut for electron microscopy. TIRF

microscopes are extremely sensitive to the movement of fluorescent objects which are moving perpendicularly to the glass, since structures will brighten when they approach the glass and dim when they retreat. For depth discrimination, TIRF is up to tenfold better than confocal microscopy, the only other fluorescent microscopy developed for this purpose. An overview and comparison of confocal and TIRF microscopy is shown in Table 4.1. Using intensified charge-coupled device (CCD) or electron multiplying CCD (EMCCD) cameras affords higher sensitivity and faster imaging. It is important not to think of TIRF as the panacea of fluorescent imaging techniques. Rather, it is a complementary technique which can be combined with other microscopy techniques such as brightfield, epifluorescence, CLSM, fluorescence correlation spectroscopy (FCS) [221], AFM [222] and fluorescence lifetime imaging microscopy (FLIM) [223] to name but a few. It has also been combined with fluorescence recovery after photobleaching (FRAP) [224], fluorescence resonance energy transfer (FRET) and surface reflection interference contrast microscopy [225].

Table 4.1 Comparison of TIRF and confocal microscopy techniques. Adapted from Steyer and Almers (2001)

Confocal	TIRF
Illuminates entire cell with excitation light, but rejects most fluorescence via confocal pinhole.	Illuminates only the plane of interest. No out-of-focus fluorescence. All fluorescence is usable for imaging
Potential for extensive bleaching and photodamage throughout the cell.	Less bleaching and photodamage per photon
Limited axial resolution of approximately 500 nm	Illumination declines exponentially over distances to 40-50 nm when high refractive index glass is used.
Pixels imaged sequentially in laser scanning microscopes. Temporal resolution relatively poor	Widefield technique therefore all pixels are imaged simultaneously. Rate determined by speed of camera and photon collection
Can image the whole cell with ability to section through it	No optical sectioning capability. Images only the basal cell surface

4.2.1 Types of TIRF setups – Practical implications

There are two methods commonly employed for achieving TIRF microscopy, namely prism-type TIRF and objective-type TIRF. Axelrod developed the prism setup in 1981 and the objective setup in 1989. Both strategies have different characteristics making them application dependent. Within each type of setup there are several possible illumination methods for evanescent field generation and collection of fluorescence [161, 165].

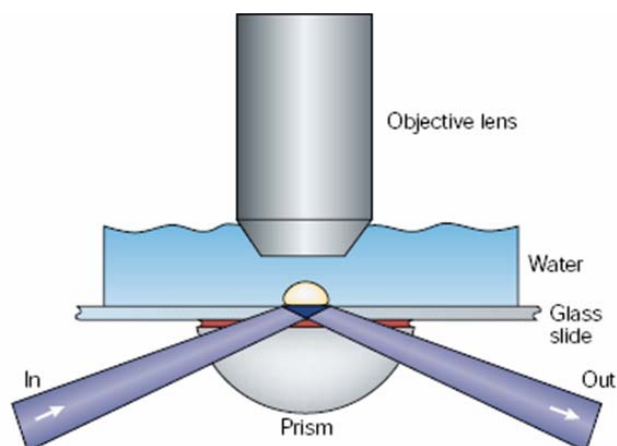
4.2.1.1 Prism type setup

The prism-type setup depicted in Fig. 4.1a is the most commonly used setup due to its relative ease of use, ease of setup and that it is inexpensive. It is also possible to achieve a ‘cleaner’ evanescent-excited fluorescence than through the objective TIRF, since it does not suffer from unwanted internal reflections that occur when introduced through the objective. The great advantage of using a prism is that it is possible to scan a large range of angles above the critical angle, whereas with the objective setup, the maximum achievable angle is 73° when using a NA 1.45 lens and the sample is aqueous in nature. This is useful when determining quantitative measurements of cell-substrate contacts [226]. The main drawback associated with the prism setup is that sample manipulation is restricted by the presence of the objective lens dipping into the sample. Also, the image quality can be slight degraded since the fluorescent emission firstly has to pass through the cell before being collected, unlike through the objective TIRF, where emitted fluorescence passes straight into the objective lens.

4.2.1.2 Objective type setup

The objective-type setup illustrated in Fig. 4.1b offers some key advantages over the aforementioned prism system. Firstly, since it is setup in an episcopic configuration, it means there is no restriction to manipulation of the sample. This is useful, for example, when adding chemicals during experimentation or if TIRF is being combined with another imaging technique such as AFM [222]. Lateral resolution is also slightly improved due to the large NA of the objective lens. Through the objective TIRF systems are now readily available from all the major microscope manufacturers such as Zeiss, Nikon, Olympus and Leica.

A



B

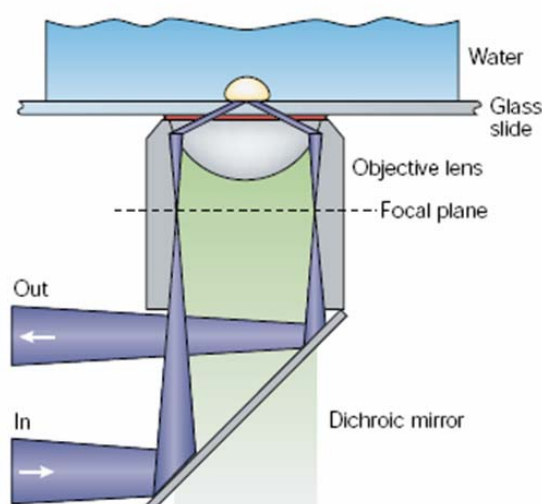


Figure 4.1 Schematic diagram illustrating two types of setup for TIRF microscopy

(a) Prism-type setup. Illuminating at an angle greater than the critical angle through the side of a hemispherical prism coupled optically to a glass coverslip with the use of an appropriate immersion oil results in the generation of an evanescent field. Fluorescent molecules present in this field will be excited if the appropriate excitation wavelength is used and the resulting emission can be collected by means of a high NA water immersion lens. The drawback of this system is the fluorescent emission has to first pass through the sample before being collected resulting in some distortion of the image. (b) Through the objective type setup. Focussing a laser beam at a lateral position on the BFP corresponding to an angle greater than the critical angle causes the generation of an evanescent field in a region just above the coverslip. As in the prism-type setup, fluorescent molecules in the field will be excited if the correct illumination wavelength is used. Fluorescent emission is collected through the same high NA objective lens and passes through a dichroic mirror prior to being collected by an appropriate camera.

4.2.2 High resolution TIRF imaging of living cells

TIRF is an extremely useful tool available to cell biologists for the study of cell membrane events due to its extremely high resolution imaging in this region. Figure 4.2 is a schematic representation of how TIRF affords high sensitivity in the cell membrane region. The evanescent field is localised to the coverslip, hence only those fluorescent molecules present in this area will be excited. Other molecules not present in the field will not be excited and therefore decrease the background signal when imaging. This increases the signal to noise ratio and results in images with better contrast. The evanescent nature of the excitation results in another interesting phenomenon when imaging. The intensity of an evanescent field drops off with distance from the surface. If a cell is attached to a substrate within the field, then those fluorescent molecules which are closer to the surface will have a greater intensity than those which are further away. Using an angle scanning TIRF system, it is possible to build up a quantitative map of cell-substrate adhesion [81, 226-230].

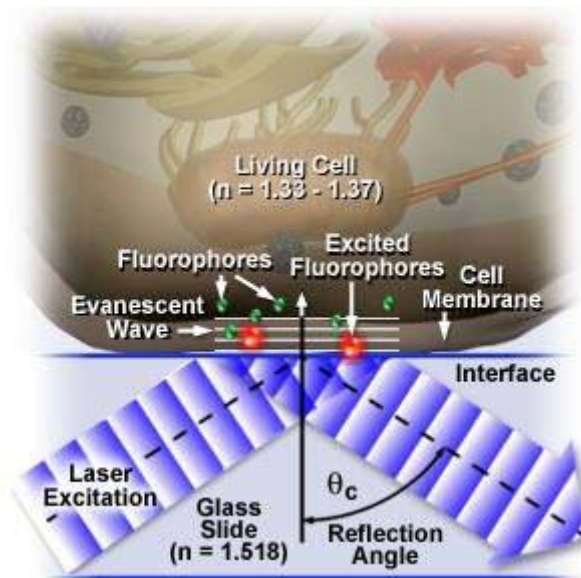


Figure 4.2 Schematic illustration of TIRF imaging of a cell adhered to a glass coverslip

This diagram illustrates the region of excitation when TIRF is applied to a living cell. TIRF selectively illuminates a thin region above the coverslip via an evanescent wave. This results in only those fluorophores present within the EF being excited. Since this region is typically on the order of 100 nm or less, it affords extremely high axial resolution of this region. In the example of a cell adhering to a coverslip, typically only the cell membrane region and a thin region of the cytoplasm will be excited, thus making TIRF invaluable for studying occurring at the cell membrane. Reproduced with permission from Nikon MicroscopyU website (www.microscopyu.com)

4.3 Materials and methods

4.3.1 Cell Culture

Murine fibroblast (3T3) cells were cultured and seeded as described in Section 2.3.2.

4.3.2 Microscopy

TIRM/TIRF microscopy was performed as described later in this chapter. Briefly, a combination of TIRM and TIRF was performed in the same instrument as previously described (Byrne *et al*, 2008) utilising illumination through the microscope objective (PlanFluor 100x NA 1.45, Zeiss). All studies were performed using a standard inverted biological microscope (TC 5400, Meiji) with custom built illumination optics. The optical configuration used for TIRF imaging included excitation with a 488 nm solid state laser (Protera 488-15, Novalux, Sunnyvale, CA) reflected off a polychroic mirror (z488/532). Emitted light was collected through a suitable emission filter (z488/532m). All filters and polychroic and dichroic mirrors were obtained from Chroma Technologies (Brattleboro, VT). TIRM imaging of 3T3 cells was achieved with illumination using a light emitting diode (LED) with a centre wavelength of 580 nm (LXHL-ML1D Luxeon Star, Lumileds, CA) reflected off the same polychroic mirror.

The camera utilised to acquire images was a 14-bit cooled EMCCD (iXon DV-885 KCS-VP, Andor Technology, Belfast UK). The resolution of the camera was 1004 x 1002 pixels, with each pixel 8 μm x 8 μm in size. Sequential TIRM and TIRF images

were acquired by the camera under the control of iQ version 1.5 (Andor Technologies, Belfast UK). Mechanical shutters, also under the control of iQ via a break-out box (Andor Technologies, Belfast UK), were placed in the beam path to minimise photobleaching and to switch between TIRM and TIRF illumination. TIRM and TIRF images were acquired with exposure times of 90 and 400 ms respectively. For video imaging, frames were streamed to a kinetic image disc on a PC and then saved to hard disc. Analysis of still images and video sequences was performed with iQ, ImageJ and Excel (Microsoft, Redmond, WA). Digital brightness and contrast was adjusted in Photoshop (Adobe Systems, San Jose, CA).

4.3.3 Cell labelling

Membrane labelling with 1,1'-dioctadecyl-3,3,3',3'-tetramethylindocarbocyanine-perchlorate (DiIC₁₈) (Molecular Probes, Invitrogen, Eugene, OR) was carried out as previously described (Axelrod, 1981). 1 mL of a 0.0001% (w/v) DiIC₁₈ in Hank's balanced salt solution (HBSS) was added to each chamber. The cover glass was then placed in a humidified incubator at 37°C and 5% CO₂ for 5 min. Following this step, the labelling solution was removed and the cells rinsed many times with HBSS. Finally, the cells were incubated with fresh DMEM for 20 min and rinsed with HBSS prior to imaging.

4.3.4 Transfection

For transient transfection, cells were grown to 80% confluence and transfected with 5 µg pDsRed-N1 plasmid DNA (Clontech, BD Bioscience, Palo Alto, CA) (at a DNA to lipid ratio of 1:1) using TransFast Transfection Reagent (Promega, UK) in accordance with the manufacturer's instructions. Firstly, cells were washed with PBS and detached from a T150 tissue culture flask (Nunc, Roskilde, Denmark) using Trypsin-EDTA solution 1X (Sigma-Aldrich, UK). Following inactivation of the trypsin with DMEM containing 10 % NBCS, cells were reseeded on a 6-well plate (Corning, Sigma-Aldrich, UK) at a concentration of 2.5×10^5 cells per well, for transfection the following day. Add the TransFast reagent and plasmid to 2 ml of prewarmed (37 °C) serum-free DMEM and incubate for 15 minutes at room temperature. The culture medium was removed from the cells grown O/N and the TransFast reagent/DNA mixture was added to the cells. The cells were immediately placed in the incubator for 1 hour at 37 °C and 5 % CO₂. Following the incubation period the cells were gently overlaid with prewarmed DMEM containing 10 % NBCS. Cells were incubated O/N at 37 °C and 5 % CO₂. Cells were then ready to be used for TIRF imaging.

4.4 Microscope alignment and operation

4.4.1 General considerations

In this section I will discuss some of the fundamental factors that influence the design and development of the optical TIRM/TIRF microscope. I will then discuss the development of the TIRM/TIRF microscope with regard to these fundamental principles.

4.4.1.1 Objective correction

The mechanical tube length of an optical microscope is defined as the distance from the nosepiece opening, where the objective is mounted, to the top edge of the observation tubes where the eyepieces (oculars) are inserted. For many years, almost all prominent microscope manufacturers designed their objectives for a finite tube length. The tube length was fixed by the Royal Microscopical Society (RMS) at a value of 160 mm for finite-corrected transmitted light microscopes. The main drawback associated with a finite tube length microscope system is that whenever an accessory such as a polarizing intermediate piece, a DIC Wollaston prism, or a fluorescence illuminator, is placed in the light path between the back of the objective and the eyepiece, the mechanical tube length becomes greater than 160 mm. This may result in aberration when the sample is refocused and means that additional optical elements need to be introduced into the system to bring the focal length back to 160 mm.

Since the late 1980's, almost all major microscope manufacturers have been designing their microscopes to support infinity-corrected objectives. Such objectives project an image of the specimen to infinity and incorporate an additional lens—known as a tube lens—to bring the image to focus at an intermediate image plane. This type of setup provides parallel optical beams between the objective and the tube lens and thus affords the introduction of auxiliary components, such as beam splitters, apertures, polarisers and prisms without the aberration associated with the finite-conjugate system. Generally, infinity corrected systems are also easier to design due to the presence of the parallel rays. For these reasons, it was decided to use an infinity-corrected objective lens in the development of the widefield TIRM/TIRF microscope.

4.4.1.2 Illumination methods

Controlled illumination of the sample is essential in microscopy for providing an even lighting in the specimen plane and for determining the area which is lit. Illuminating more than the visible portion of the specimen plane results in glare due to scattered light and this degrades the quality of the final image. Additionally, it is important to control the angle of the cone of light entering the objective lens. For non-fluorescent microscopy systems, if a significantly smaller cone of light is used, then the maximum attainable resolution is reduced whilst the use of a larger cone of light causes glare and image degradation. However, this is not the case for a fluorescent microscope.

There are two principal illumination arrangements used in optical microscopy, namely critical and Kohler illumination. In critical illumination a light source is imaged directly

into the specimen plane. This means a homogeneous source such as an electric bulb with a frosted opal surface must be used. Otherwise, the intensity of illumination will vary over the specimen plane resulting in intensity artefacts on the image. Critical illumination has been almost entirely superseded by Kohler illumination in modern microscopes. In Kohler illumination, the source is imaged to the back focal plane of the objective lens and therefore results in bright and even illumination over the entire sample [231]. For these reasons, Kohler illumination is used in our TIRM system.

4.4.1.3 Field of view and light source

Choice of a suitable light source for TIRM imaging was discussed in detail in Chapter 2. Briefly, a light emitting diode was chosen as the illumination source since it resulted in negligible coherence noise on the image. Also, LEDs are relatively cheap and are available in a range of spectral wavelengths. For TIRF illumination it is possible to use either a mercury arc lamp or a laser source. An arc lamp can be used for TIRF illumination by directing the light onto the objective BFP via an opaque disc to block out all sub-critical light. Arc lamp sources are advantageous due to the range of excitation wavelengths available through the use of narrow band filters and they are free from coherent light interference fringes associated with laser illumination. However, the drawback of using an arc-lamp source is that much of the power is wasted due to the necessary blockage of subcritical angles. In this system TIRF illumination was achieved using a laser source. The laser beam can be easily focussed to the objective BFP using custom built optics. Also, all the laser power is directed to the sample.

4.4.1.4 Imaging detector

In this microscope, an electron multiplying charged coupled device (EMCCD) was used as the image recording device. The term EMCCD was first coined by Andor Technology Plc. in early 2000. As the name suggests the technology is defined by a process which involves electron multiplying of a standard CCD readout signal. With a conventional CCD, readout noise of the output amplifier can present a serious problem especially when imaging at low light levels and high readout speeds. By adding a solid state EM register to the normal serial register it allows weak signals to be multiplied prior to any readout noise being added by the output amplifier. Thus it is possible to render the readout noise negligible.

EMCCD technology is particularly useful for imaging objects with low light signals. Since the work presented in this thesis utilises TIRF imaging to detect fluorescent proteins it was decided that EMCCD technology was required to provide optimum sensitivity. The EMCCD camera used in this thesis (iXon DV-885 KCS-VP, Andor Technology, Belfast UK) boasts single photon sensitivity, excellent resolution, high quantum efficiency, low dark current and high frame rates (31 frames per second). An additional advantage is that if more light is available from the sample, the EMCCD gain can be completely switched off and the camera operated as a 'traditional' CCD camera. Capturing both TIRM and TIRF images on the same camera greatly simplifies the optical system, and additionally the registered images obtained make subsequent image processing straightforward.

4.4.1.5 Objective lens

For TIRF imaging, an objective with NA greater than 1.4 is typically required. In this work the objective lens utilised was a Zeiss PlanFluor 100x NA 1.45. This affords a maximum illumination angle of 73° . Having a large NA is important when imaging samples with dense heterogeneities (such as cellular organelles) since they will otherwise convert some of the evanescent field into scattered propagating light. The objective lens is also infinity corrected, as previously discussed.

4.4.2 Optics for illumination and imaging

In this section I will discuss in detail the optical components used for both TIRM and TIRF illumination. I will also briefly discuss the imaging optics.

4.4.2.1 Illumination optics – TIRF

The optical system has the following general features:

- The laser beam used for excitation is focussed, using an external focussing lens, to a point on the objective back focal plane (BFP) so that the light emerges from the objective in a collimated form, i.e. the rays are parallel to each other. This ensures that all the rays are incident on the sample at the same angle θ with respect to the optical axis.

- The point of focus in the back focal plane is adjusted to be off-axis. There is a one-to-one correspondence between the off-axis radial distance ρ and the angle θ . At a sufficiently high ρ , the critical angle for TIR can be exceeded. Further increases in ρ serve to reduce the characteristic evanescent field depth d in a smooth and reproducible manner.

Illumination beam expanding ratio

In order to fill the entire array of the EMCCD camera, at the required imaging magnification, a field of approximately $200 \mu\text{m}^2$ must be illuminated on the object plane. This was achieved by expanding the laser beams prior to being focussed on the BFP of the objective lens. The illumination magnification used was approximately 21x. L1 – L2 and L3 – L4 (Figs. 4.3 and 4.4) are used to expand the beams and L1 equals L3 and L2 equals L4. To calculate the magnification of the lens pairs the following calculation is used:

$$M_{be} = \frac{f_2}{f_1} \quad (4.1)$$

Where M_{be} is the beam expander magnification, f_2 and f_1 are the focal lengths of lens one and two respectively. If we chose lens 1 with $f_1 = 12 \text{ mm}$ and lens 2 with $f_2 = 250 \text{ mm}$, the beam will be expanded from $\sim 1 \text{ mm}$ to $\sim 21\text{mm}$, which is suitable for illuminating a $200 \mu\text{m}$ field of view on the sample plane after divergence from the BFP.

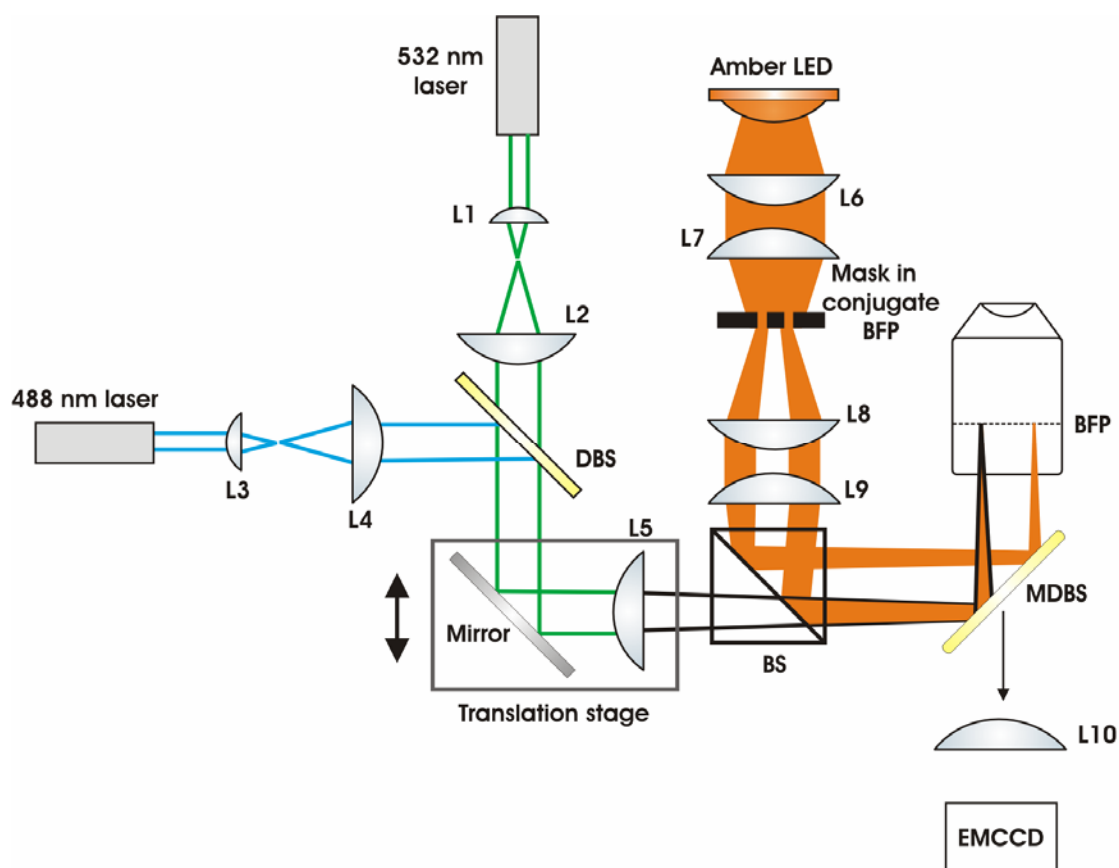


Figure 4.3 Schematic diagram illustrating the beam paths used in the TIRM/TIRF microscope

For the two colour TIRF illumination, the laser beams are expanded by lenses L1-4 and combined at a dichroic beamsplitter (DBS). To control the incident illumination angle, the mirror and focusing lens L5 can be translated by the stage to allow positioning of the focal point in the back focal plane (BFP) of the microscope objective lens. For TIRM illumination, the amber LED is imaged by condenser lenses L6 and L7 onto an annular mask that is conjugate to the BFP of the microscope objective. Lenses L8 and L9 image the mask into the BFP to provide illumination above the critical angle. Fluorescent emission and reflected LED illumination pass through the multiband dichroic beamsplitter MDBS, and tube lens L10 forms an image on the EMCCD.

4.4.2.2 Illumination optics – TIRM

In non-fluorescent optics, the lateral resolution of a microscope is defined by both the illumination and imaging NA. Since the NA of the imaging is fixed in our case then the NA of the illumination should be adjusted in order to achieve maximal lateral resolution. In order to gain the highest lateral resolution it is important to completely fill the aperture of the objective lens. However, it is important not to overfill the objective lens since it will waste optical power and may cause unwanted stray light in the illumination path. Also, the aperture should not be under-filled since it will decrease the lateral resolution of the microscope. Hence, it is important to take these considerations into account and control the size of the beam so that it just fills the objective aperture.

4.4.2.3 Imaging optics – TIRM and TIRF

As discussed in Section 4.4.1.5, the objective lens utilised in the TIRM/TIRF microscope is infinity corrected, thus necessitating infinite conjugate imaging optics. The TIRF/TIRM microscope in this work is built around the body of a Meiji TC5400 inverted biological microscope. The TC5400 microscope uses infinite-conjugate optics in the imaging path, thus there was no modification of the imaging optics (Fig. 4.6). Indeed, the imaging path is concealed within the main body of the microscope, which makes any modification difficult.

4.4.3 Optical alignment

Clearly, the development of a TIRM/TIRF system capable of high resolution imaging requires not only careful consideration of key optical design aspects but also the need for precise alignment of the system. There are a number of ways in which to achieve good optical alignment, however of fundamental importance is the practical experience of the user. In this system, alignment is complicated by the need for a dual-colour TIRF system coupled with a TIRM system, and the fact that the illumination optics for both the TIRM and TIRF need to take place through the same high NA objective lens. Also, the need for three separate wavelengths for illumination increases the chances of chromatic aberration, due to the fact that each wavelength will focus to a different axial position.

Figure 4.4 shows the illumination optics for the TIRM/TIRF system with beam paths illustrated for clarity. It can be seen that there are a large number of optical components which make up the system and each of these must be correctly aligned to achieve optimal contrast and resolution. In the following section alignment issues associated with each of these components will be discussed in detail.

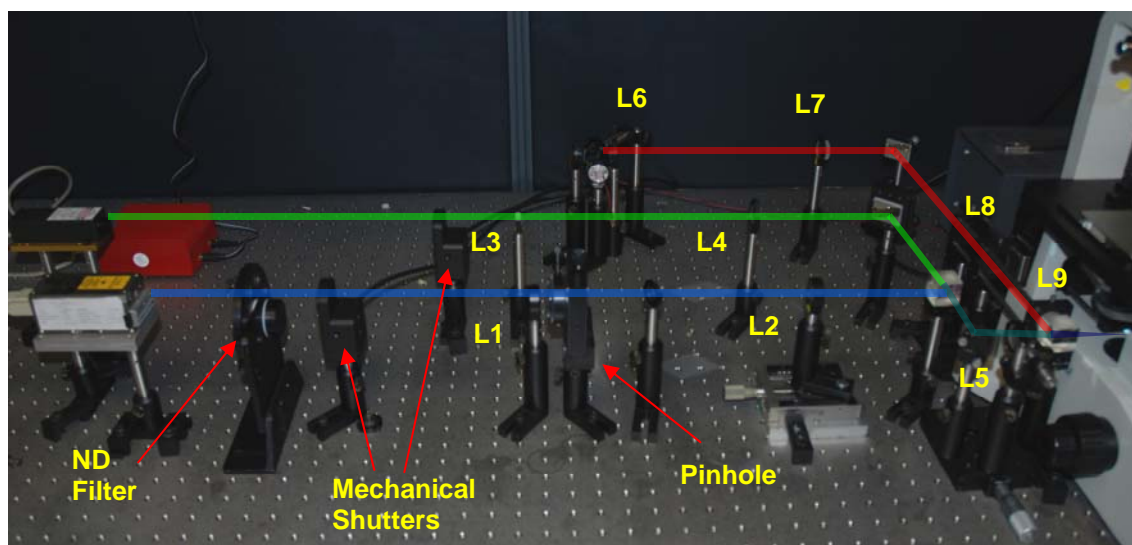


Figure 4.4 Schematic illustration of TIRF/TIRM illumination optics

The beam paths for the TIRF lasers are illustrated in blue and green, representing 488 nm and 532 nm excitation wavelengths respectively. The red beam illustrates the TIRM beam path. For the two colour TIRF illumination, the laser beams are expanded by lenses L1-4 and combined at a beamsplitter. To control the incident illumination angle, the mirror and focusing lens L5 can be translated by the stage to allow positioning of the focal point in the back focal plane (BFP) of the microscope objective lens. For TIRM illumination, the amber LED is imaged by condenser lenses L6 and L7 onto an annular mask that is conjugate to the BFP of the microscope objective. Lenses L8 and L9 image the mask into the BFP to provide illumination above the critical angle. Mechanical shutters are placed in the TIRF illumination pathway and are used to minimise photobleaching of the sample. Control of the shutters is by Andor iQ via a break-out box. The imaging pathway is not shown.

4.4.3.1 TIRM alignment issues

- *LED*

The LED is aligned parallel to the optical bench. The beam can be correctly aligned by using two apertures adjusted to the same height and placing one close to the source and much further away. If the source meets both apertures at the same point then the beam will be correctly aligned. To achieve imaging of the mask into the BFP of the objective lens, it is placed at the front focal plane of lens 6.

- *Image mask/central block*

The mask should be imaged to the back focal plane of the objective lens to produce uniform Kohler illumination. Since lenses 6 – 9 are aligned with the separations being equal to the sum of their focal lengths, i.e. are conjugate planes, then for correct alignment with the BFP, the mask can be placed at the front focal plane of lens 8. Alternatively, by using a transmitted light source it is possible to create an image of the BFP at the front focal point of lens 6, affording correct placement of the mask.

4.4.3.2 TIRF alignment issues

- *Laser*

The lasers are set as the reference and define the optical axis of the system. The lasers are aligned parallel to the optical bench. By using two mounted apertures it is possible to obtain a correctly aligned beam.

- *Lenses 1 & 2 and 3 & 4*

These lens pairs are used to magnify the illumination source and are more commonly known as beam expanders. The lens should be aligned with the beam traversing its centre to minimise aberrations. Also, the lens itself needs to be mounted with the correct orientation, i.e. with the curved surface focussing light coming from infinity. To ensure suitable collimation of the beam, i.e. little or no beam convergence or divergence, a collimation tester can be used. The collimator works on the principle of shearing interferometry. Basically, when a collimated beam is introduced into the cube, interference fringes are generated which will be straight and aligned to a predefined line. Any deviation from straight fringes is indicative of aberrations in the system. A 20 μm diameter pinhole accurately positioned at the intermediate focus of the beam expander produced spatial filtering by removing higher-order scattered light. This pinhole was placed between lens 1 and 2 to improve the quality of the 488 nm laser beam (Fig. 4.4).

- *Lens 5*

This lens is used to focus laser illumination onto the BFP of the objective lens. Correct alignment of this lens is important in order to afford angle scanning and to illuminate the full field of view. This can be achieved by adjusting the lens to give a diffraction limited spot on the BFP. A simple way of determining whether this is the case is to direct the beam through the objective onto the ceiling and adjust the focussing lens accordingly to result in the most highly collimated beam.

- *Dichroic beamsplitter (DBS)*

The purpose of the DBS is to make the blue and green lasers collinear. The mirror is positioned and adjusted to direct the beams along the optical axis.

- *Mirror on translation stage*

The purpose of this mirror is to direct the expanded laser beam through the focussing lens as illustrated in Fig. 4.5. Positioning of the mirror on the same stage as the focussing lens means that the beam is constantly positioned in the centre of this lens during translation of the stage. This mirror can also afford fast switching between epi and TIRF illumination.

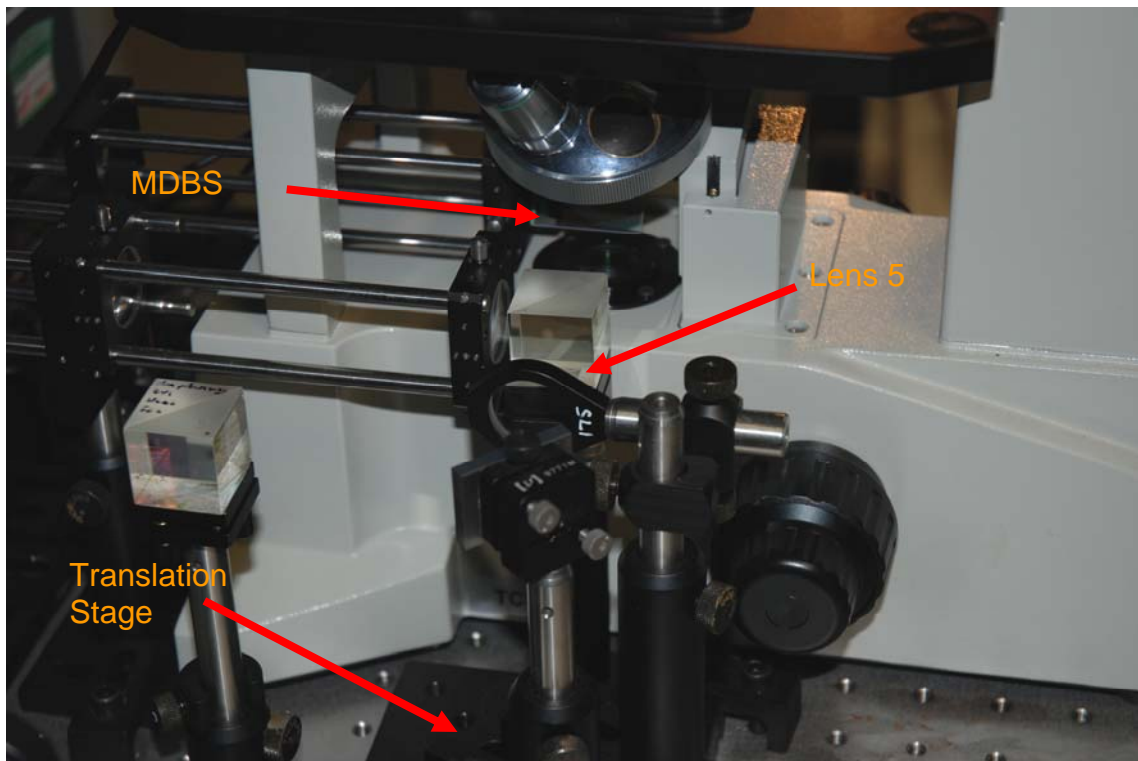


Figure 4.5 Placement of the MDBS, focussing lens (lens 5), and translation stage

Placement of the MDBS is prior to the objective turret in order to reflect illumination light onto the sample (not shown) and transmit fluorescent emission through the imaging path. Expanded light from the lasers is reflected through lens 5 ($f_5 = 175$), which focuses it to a point on the BFP of the objective lens. The translation stage is used to move the beam laterally across the BFP, and thus change the angle of illumination. Placement of both the mirror and focussing lens on the translation stage means that the expanded laser beam remains parallel to the optical axis while maintaining its shape.

4.4.3.3 General alignment issues

- *Multiband dichroic beamsplitter (MDBS)*

The purpose of the MDBS is to reflect illumination light into the objective lens and to transmit emitted light from the sample. Correct alignment was achieved by making light transmitted from the objective lens parallel to the optical axis.

- *Emission filter*

The purpose of the emission filter is to prevent laser illumination reaching the camera and thus contributing to background noise. Also, since we are using a trinocular head as part of the imaging optics, laser illumination needs to be prevented from reaching the user. The emission filter was placed prior to the trinocular head as shown in Fig. 4.6. This meant that laser power reaching the eyepiece and camera was significantly reduced to less than 0.01%.

- *Beamsplitter*

The beamsplitter is used to combine the laser and LED illumination and allow it to pass through to the BFP of the objective lens. Correct alignment is achieved by assessing whether transmitted light passes down the same optical axis as that of the reference laser beam.

- *1.45 NA objective lens*

The objective lens is inserted into the turret of the Meiji TC5400 inverted microscope affording correct alignment.

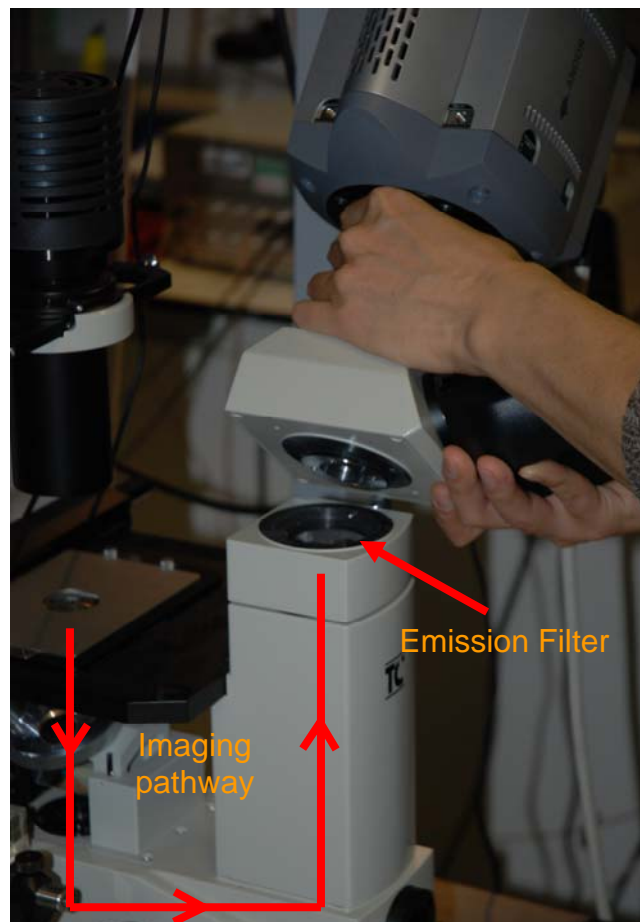


Figure 4.6 Placement of the emission filter and position of imaging beam path in the Meiji TC5400 inverted microscope

The emission filter is placed in the imaging optical axis prior to the trinocular head. This can be achieved by removing the top part of the microscope and placing the filter as shown. This prevents unnecessary laser exposure onto the camera and eyepiece which is crucial for both eye safety and to prevent damage to the camera.

- *EMCCD*

The camera is mounted on the trinocular head of the Meiji TC5400 inverted microscope. The following viewing can be achieved; 100 % eyepiece or 50 % eyepiece and 50 % camera. The bottom camera port of the microscope is not utilised due to the dimensions of the camera.

4.4.4 Choice of multi-band dichroic beamsplitter

In order to achieve dual colour TIRF, a polychroic beam splitter is required, which reflects the selected excitation laser wavelengths (488 and 532 nm) while transmitting the associated fluorescent emission. Such beam splitters are readily available (Fig. 4.7), however, a difficulty arises when wishing to perform TIRM and TIRF in the same instrument. The polychroic beam splitter is designed to reflect excitation wavelengths onto the sample and transmit maximum fluorescence emission. Therefore, if an attempt is made to perform TIR microscopy at 488 or 532 nm, it would lead to several problems. Firstly, only approximately 5% of the reflected beam will be transmitted through the microscope optics to the camera. This should not be a serious problem as TIRM is a brightfield technique and as such only requires relatively low optical power levels. However, in order to perform fluorescence microscopy an emission filter is required to block any stray illumination entering the camera and therefore a TIRM image at either 488 or 532 nm would be blocked.

Equally importantly, illumination at 488 or 532 nm could result in unwanted excitation of any fluorescent sample being imaged, leading to unnecessary levels of photobleaching and phototoxicity. Therefore, TIRM is best performed at wavelengths which do not cause fluorescent excitation, can pass through the emission filter and will be both reflected and transmitted by the polychroic beam splitter. It is possible to perform TIR microscopy at 690 nm, where the beam splitter will reflect and transmit ~50% of the laser beam. Also, it can be seen from the transmission spectra in Fig. 4.7 that this wavelength will pass through the emission filter, a fundamental requirement in this set-up.

As described in Chapter 2, and illustrated in Fig. 2.12b, a drawback of diffuse laser TIRM is that it can lead to unwanted artifacts on the image due to interference arising from the use of a temporally coherent laser beam. Firstly, the rotating diffuser does not always allow sufficient speckle averaging and some residual coherence noise often remains. Secondly, the temporal coherence of the illumination can cause fringe patterns from double reflections off optical components. A further problem with using illumination at 690 nm was chromatic aberration. The correct focal position at 690 nm caused noticeable defocus at the fluorescent emission wavelengths.

These problems were overcome by using a LED with a centre wavelength of 580 nm. It can be observed that the reflection of the polychroic mirror is reduced to around 15% at this wavelength (Fig. 4.7); consequently most of the illumination beam never reaches the sample. Although only 15% of the illumination light reaches the sample, it is interesting to note that this is sufficient to produce a sharp, bright image that is well

focused at the same focal position as the fluorescent emissions. This can be explained because 85% of the 15% illumination light passes through to the camera unhindered, which is enough light to give good contrast in TIRM.

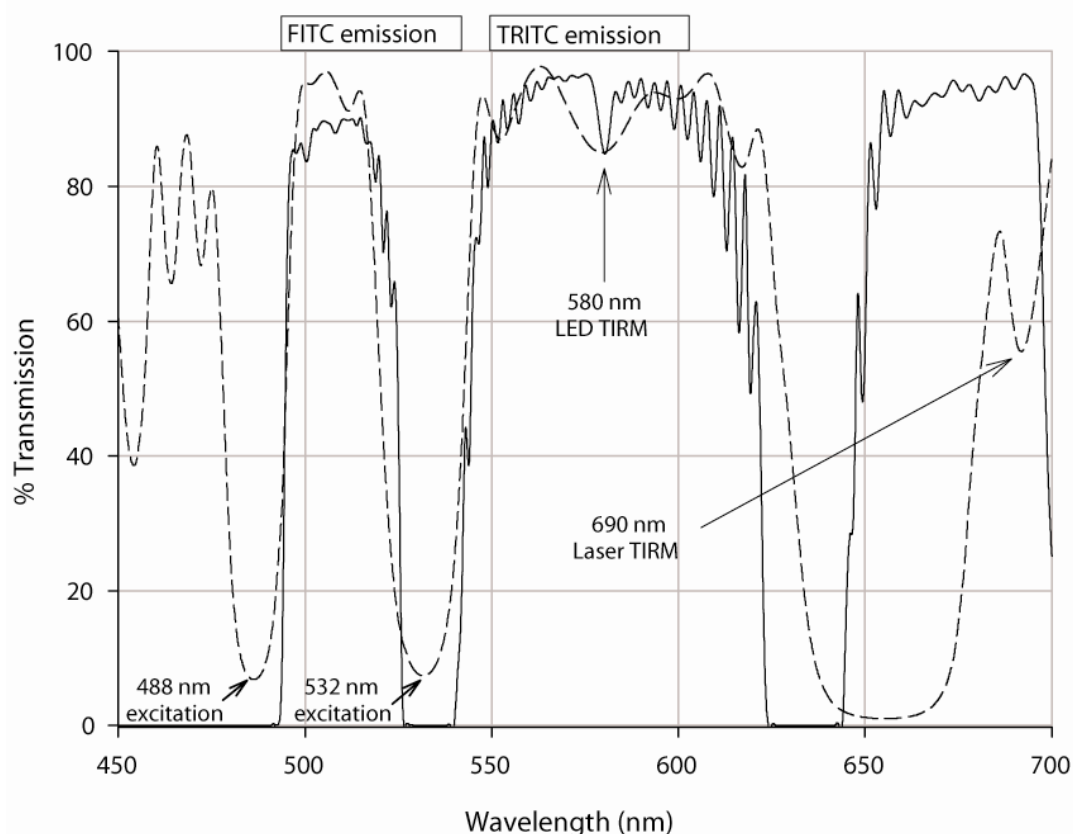


Figure 4.7 Typical transmission spectra for filters and mirrors used in the microscope

Transmission spectra for the z488/532 polychroic mirror (dotted line) and z488/532m emission filter (solid line) utilised in the combined TIRM/TIRF microscope. This filter combination efficiently reflects 488 and 532 nm laser illumination, transmits resulting fluorescent emission for fluorophores excited at this wavelength (e.g. FITC and TRITC) and blocks any residual illumination arriving at the camera. Additionally, non-fluorescent TIRM can be performed using this filter set at a wavelength where both reflection and transmission by the polychroic mirror occurs and transmission by the emission filter takes place, e.g. 580 and 690 nm. For TIRM using a LED with a centre wavelength of 580 nm it can be seen that the reflection of the polychroic mirror is approximately 15% at this wavelength. After reflection from the sample the illumination light is transmitted through both the polychroic mirror and emission filter with 85% efficiency, resulting in approximately 11% of the initial illumination reaching the camera. Chart plotted from ASCII data obtained from Chroma Technologies (Brattleboro, VT, USA)

4.4.5 Control of illumination pathways

To achieve dual-colour TIRF and TIRM illumination in one system, it is important to have a level of control over when each illumination source is switched on and off. Without this, it would be difficult to separate emission from dual-labelled samples as there may be secondary excitation from other sources. Additionally, the camera exposure times used for capturing TIRM images is much lower than that for TIRF imaging (in our experience, typical images could be captured with exposure times of 30 ms and 300 ms for TIRM and TIRF respectively). Obviously, controlling the illumination to coincide with image capture would also greatly simplify the system and reduce the effects of photobleaching.

Andor iQ imaging software affords the opportunity to send digital I/O signals from the PC (Dell, Dublin, Ireland) to a break-out box (ER-PCUA, Andor, Belfast, UK) (Fig. 4.8). The break-out box can then be used to drive various devices such as mechanical shutters, filter wheels and positioning stages placed within the system. In this system it was used to control two mechanical shutters (SH05 beam shutter, ThorLabs Ltd., Cambridgeshire, UK) via TTL (Transistor-Transistor Logic) signals sent to a T-cube shutter controller (SC10, ThorLabs, Cambridgeshire, UK). The shutters were placed in the optical axis of the blue and green lasers prior to beam expansion (Fig. 4.4). The location of the shutters was in front of the source as their aperture would not have accommodated the expanded beam and it also acted as an adequate beam stop for safety requirements. Another function of iQ is that it will synchronise the opening of the mechanical shutter with image capture. This is very important since it will mean that

the sample is only illuminated for a short period of time during image capture, hence reducing the effects of photobleaching.

The imaging software (Andor iQ) was also used to send digital signals to a custom built circuit for the control of the LEDs in the system. Use of a shutter in the optical axis of the TIRM illumination was difficult due to their highly divergent nature and also their cost. By designing our own circuit it was possible to control both the intensity and timing of the TIRM illumination. The circuit contained capacitors to control LED intensity and switches to switch between ON/OFF states and between two different colour LEDs. As with the mechanical shutters, switching on or off of the LEDs was synchronised with image capture through iQ. In summary, by utilising iQ with the Andor break-out box it was possible to have complete control over the illumination optics and clearly define when they were ON and OFF during imaging.



Figure 4.8 Andor break-out box and custom built LED control circuit.

Digital signals from the iQ imaging software were sent to the break-out box to trigger it to operate the mechanical shutters or LEDs (which were controlled via the custom designed circuit shown sitting on the break-out box). BNC cables connected directly to the LED circuit and to the mechanical shutters to trigger the devices. Both LEDs and shutters had their own external power supplies and were not powered via the break-out box.

4.5 Results and discussion

Although the TIRM system described in Chapter 2 offers several advantages over conventional fluorescent techniques including decreased phototoxicity and negligible photobleaching, it suffers from the loss of specificity of particular structure afforded by fluorescent labeling. A system which combines the label-free high resolution imaging afforded by TIRM and the potential of single molecule imaging afforded by TIRF using fluorescently labelled structures is potentially very useful in many areas of research. For example, morphological changes of the cell could be captured with high resolution using TIRM when they were deadhered using trypsin. At the same time, dynamic analysis of proteins involved in this process could be captured using the TIRF optics. Having control over image capture, illumination and the choice of technique from stand alone PC software (Andor iQ) is also extremely advantageous as it makes the system user-friendly.

The fluorescence photomicrographs in Fig. 4.9 highlight the advantages of EW illumination (TIRF image, Fig. 4.9b) over conventional fluorescence techniques (widefield epi-fluorescence image, Fig. 4.9a). The TIRF method produces images with much higher contrast, virtually no out-of-focus fluorescence and background fluorescence compared with the normal epi-fluorescence image. This allows high contrast imaging of fine cellular processes in the TIRF image that are not clearly visible in the conventional epi-fluorescence image. The very bright areas of the cell seen in Fig. 4.9b are thought to be areas of the cell membrane which are in closer contact with the coverslip. However, it may be argued that these areas have resulted from

inhomogeneous labelling of the cell membrane. If this were the case though, the increased fluorescence would also be seen in the epi-fluorescent image. Simply normalising the TIRF to the epi-fluorescent image would indicate the degree of labelling.

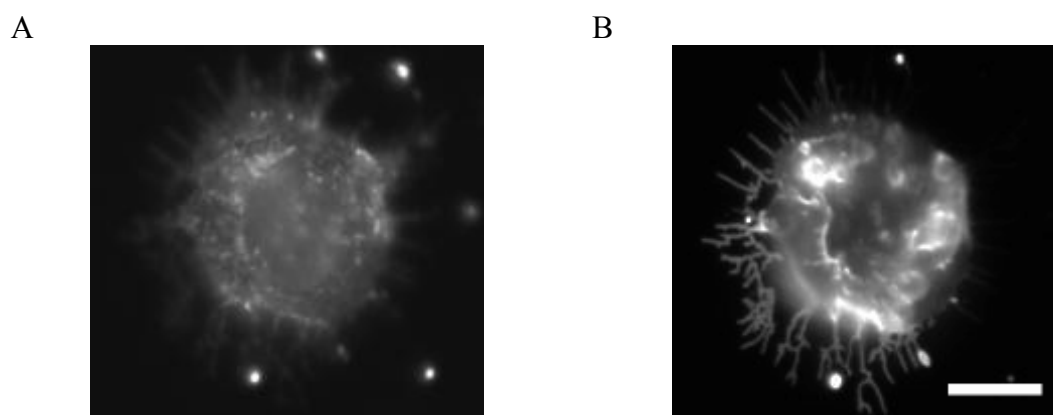


Figure 4.9 DiI-labelled 3T3 fibroblast cell on poly-L-lysine-coated glass slides.

Imaged by (a) conventional epifluorescence and (b) TIRF using a prism based system. The TIRF method produces images with much higher contrast, virtually no out-of-focus fluorescence and background fluorescence compared with the normal epifluorescence image. Cells were incubated at 37°C and 5% CO₂ for 3 hr prior to fluorescent labelling. Imaging was performed immediately following labelling. Scale bar represents 30 μm.

Sections 4.3 – 4.4 have described in detail the design and development of a combined TIRM and TIRF microscope. All the fundamental aspects and problems encountered during the development process have also been discussed. I will now comment on some other ‘label-free’ techniques which have been combined with TIRF and discuss their relevance to this work. Finally, I will show some images which illustrate the exact nature of TIRM/TIRF microscopy.

Hashido *et al* (2006) [225] published a paper describing the changes of intracellular calcium signalling during cell to cell adhesion and repulsion. In this work, the authors

have used a combination of surface reflection interference contrast (SRIC) and TIRF microscopy to measure changes in intracellular calcium (Ca^{2+}) signalling during cell-cell adhesion. SRIC is similar to the RICM technique outlined in detail in Chapter 2. However, the combination of the two techniques is to my best knowledge the first of its kind. In this paper, the authors use SRIC microscopy to analyse cell adhesion dynamics while simultaneously studying intracellular Ca^{2+} using TIRF microscopy. Although the combination of SRIC and TIRF has proved useful for this study, ultimately, it would not be overly useful for general use. The SRIC images obtained have extremely poor resolution and they can only be used to look at the cell periphery due to the presence of higher order fringes when imaging thicker regions of the cell. Additionally stray reflections will seriously degrade the weak RICM image. These problems can be addressed by using an antireflective lens, however lens with sufficient NA to achieve TIRF are not currently available. Clearly, the higher resolution achievable with our TIRM/TIRF system is advantageous for these types of studies.

Other authors have used a combination of differential interference contrast (DIC) and TIRF to study actin and myosin activity within lamellipodial adhesion sites [232]. This is a very powerful combination and provided very good results in the aforementioned paper. However, the authors did acknowledge that the temporal and spatial resolution of DIC was limited when used in combination with TIRF. DIC/TIRF is comparable to our TIRM/TIRF technique, however, for studying membrane events where extremely high spatial, especially in the axial direction, and temporal resolution is needed then TIRM/TIRF would be more suitable.

Finally, images of 3T3 cells obtained using the combined TIRM/TIRF system, described above, are illustrated in Fig. 4.10. The cells were transfected with a plasmid encoding the *Discosoma* sp red fluorescent protein (DsRed), which is then synthesised in the cytosol. After the protein has been synthesised, it will diffuse homogeneously throughout the cell [233]. Using TIRF it is possible to detect DsRed which has diffused close to the basal cell membrane. There are a number of cells present in the TIRM image (Fig. 4.10a) however, only one of the cells is visible in the TIRF image (Fig. 4.10b), indicating that only this cell has been transfected. TIRF microscopy is useful for highlighting features such as the filopodia, contact regions and basal cell membrane cavities. A comparison of Figs. 4.10a and 4.10b illustrates that a similar level of topographical information can be obtained using the fluorescent free TIRM as with the TIRF channel of the combined microscope. Regions where the cell does not make contact with the coverslip are shown as dark patches on the TIRF image and appear as bright patches on the TIRM image. Indeed the intensity within these regions is similar to the background intensity, indicating that the membrane in this region lies outside the evanescent field. These images also show that high resolution imaging of the cell membrane can be obtained with TIRM without the need for a fluorescent label.

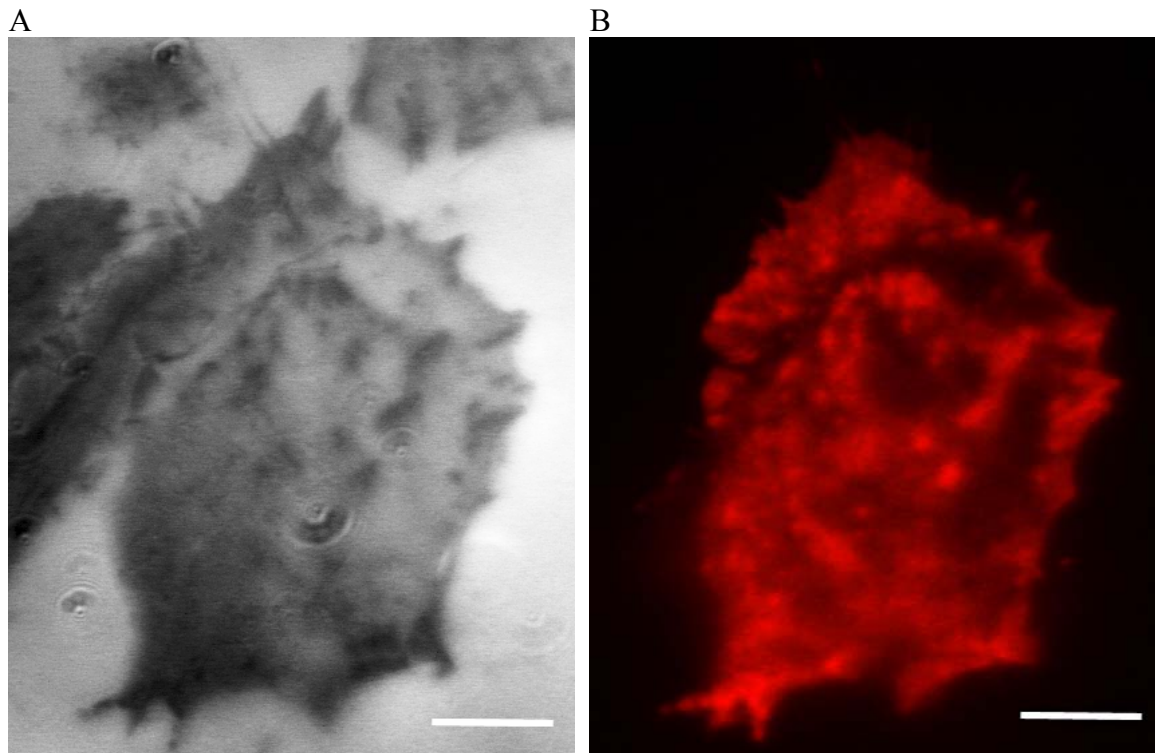


Figure 4.10 TIRM/TIRF images of 3T3 fibroblast cells

DsRed expressing 3T3 fibroblast cells imaged using (a) TIRM microscopy and (b) TIRF microscopy. The regions of cell attachment appear bright in the TIRF image and dark in the TIRM. Only the large cell in the centre of the image has been transfected with DsRed. Scale bar represents 20 μm .

4.6 Conclusions

The ability to combine TIRM with TIRF has been demonstrated in this chapter. All the key design considerations including components used, optical alignment and positioning have been discussed at length. Finally, results from the instrument show for the first time the similarities between TIRM and TIRF imaging and indeed that similar features can be imaged without the need for a fluorescent label. This combination has the capability to provide a powerful approach for investigating many biological questions where high resolution, both temporal and spatial, is required.

Chapter 5

Clathrin Mediated Endocytosis

5.1 Overview of study

The aim of this chapter is to introduce the field of endocytosis with particular reference to one common endocytic protein, clathrin. Standard molecular biology protocols have been used to develop an N-terminally tagged EGFP-clathrin fusion protein. The protein is then transiently expressed in murine 3T3 fibroblasts and analysed using the TIRF/TIRM microscope developed in previous chapters.

5.2 Introduction

5.2.1 Endocytosis

Endocytosis is a basic cellular process that is used by cells to internalise a variety of macromolecules. Since the nature of these molecules can be quite diverse e.g. receptor ligands, membrane proteins and drug delivery systems, understanding the different pathways that mediate their internalisation and how these pathways are regulated is important to many areas of cell biology and drug delivery. Endocytic pathways that mediate the transport of a specific cargo will first require mechanisms for selection at the cell surface. Next, the plasma membrane must be induced to bud and pinch off before finally, mechanisms are required for tethering these vesicles to the next stop on their itinerary and for inducing their subsequent fusion to this target [234].

5.2.2 Mechanisms of endocytosis

Many entry pathways into mammalian cells have been identified, which vary in the cargoes they transport and in the protein machinery that facilitates the endocytic process. The mechanisms fall into two broad categories, ‘phagocytosis’ or cell eating (the uptake of large particles) and ‘pinocytosis’ or cell drinking (the uptake of fluid and solutes). Generally, phagocytosis is restricted to specialised mammalian cells such as macrophages, dendritic cells or neutrophils, whereas pinocytosis occurs in all cells by at least four different mechanisms: macropinocytosis, clathrin-mediated endocytosis (CME), caveolae-mediated endocytosis and clathrin and caveolae independent

endocytosis (Fig. 5.1). These mechanistically diverse and highly regulated endocytic pathways function to control complex physiological processes such as hormone related signal transduction, immune surveillance, antigen presentation, and cellular and organismal homeostasis [235].

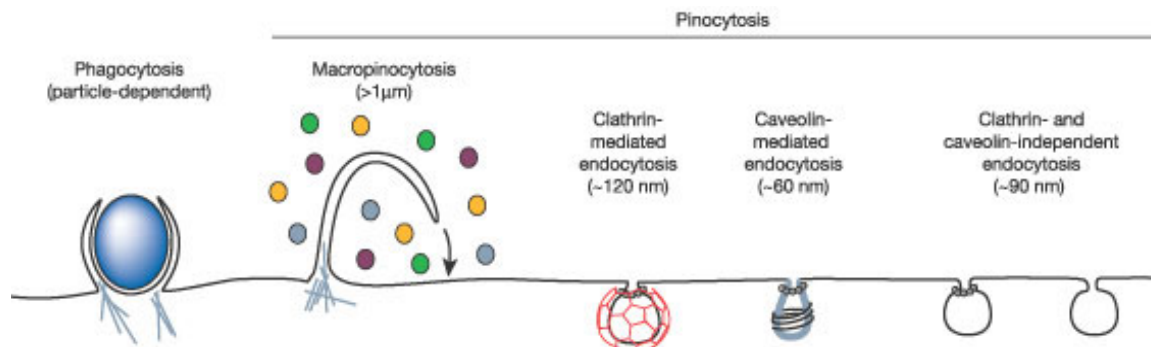


Figure 5.1 Pathways of entry into mammalian cells

The endocytic pathways differ with regard to the size of the endocytic vesicle, the nature of the cargo (ligands, receptors, lipids and nanoparticles) and the mechanism of vesicle formation. Large particles can be taken up by phagocytosis, whereas fluid uptake occurs by macropinocytosis. Both processes appear to be triggered by and are dependent on actin-mediated remodelling of the plasma membrane at a large scale. Compared with the other endocytic pathways, the size of the vesicles formed by phagocytosis and macropinocytosis is much larger. Numerous cargoes can be endocytosed by mechanisms that are independent of the coat protein clathrin and the fission GTPase, dynamin. Adapted by permission from Macmillan Publishers Ltd: [Nature] [235], copyright (2003).

5.2.2.1 Phagocytosis

In mammalian cells, phagocytosis is conducted primarily by specialised cells, including macrophages, monocytes, dendritic cells and neutrophils that function to clear large pathogens such as bacteria or yeast, or large debris such as remnants of dead cells, and/or play a key role in antigen presentation. It is an active and highly regulated process involving specific cell-surface receptors and signalling cascades. There are multiple modes of phagocytosis, which are determined by the particle to be ingested and the receptor(s) which recognise that particle.

Phagocytosis can play a detrimental role in the delivery of colloidal particles. As the function of phagocytic cells is to clear large debris, it means they can also recognise and clear different types of particulates used in drug delivery, before they reach their intended site of action. This poses a significant barrier to drug delivery researchers. For example, when nanoparticles are administered intravenously they are easily recognised by the body's immune system, which are then cleared from the circulation [1]. Typically, the particles best recognised by the immune system are hydrophobic in nature. In cases such as this it is important to design long circulating nanoparticles through surface modification with hydrophilic polymers such as poly(ethylene glycol) (PEG) [236].

5.2.2.2 Macropinocytosis

Macropinocytosis accompanies the membrane ruffling that is induced in many cell types upon stimulation by growth factors or other signals. The process of macropinocytosis involves the actin driven formation of membrane protrusions. These protrusions collapse onto and fuse with the plasma membrane to generate large endocytic vesicles (Fig. 5.1), called macropinosomes, which can sample large volumes of the extracellular milieu. Current knowledge about this process is limited, however, it is likely to be highly controlled and regulated even though it accompanies seemingly chaotic membrane ruffling.

5.2.2.3 Caveolae-mediated endocytosis

Caveolae are flask-shaped invaginations of the plasma membrane involved in endocytosis, transcytosis and signal transduction in mammalian cells. They were first identified by electron microscopy and are known to be 60-80 nm in diameter (Fig. 5.1) [237]. Caveolae are present on many cells, and demarcate cholesterol and sphingolipid-rich microdomains of the plasma membrane, in which many diverse signalling molecules and membrane transporters are concentrated. The shape and structural organisation of caveolae are conferred by caveolin, a dimeric protein that binds cholesterol and has its COOH and NH₂ termini located in the cytosol and a hydrophobic loop inserted into the membrane [238]. Caveolin-1 (Cav1), the major and essential structural protein in caveolae, exists in small vesicles in the cytoplasm that can undergo directed movement, in the Golgi complex, and as part of soluble lipoprotein complexes.

Cav1 and Cav2 are abundant in caveolae-rich non-muscle cells, whereas Cav3 is found in skeletal muscle and in some smooth muscle cells.

Experiments to track caveolae endocytosis in cultured cells with green fluorescent protein (GFP)-tagged caveolin show that caveolae are static structures at the plasma membrane. However, their internalisation can be triggered through a signalling cascade that results in tyrosine-phosphorylation of caveolae constituents. The simian virus 40 (SV40) acts as an opportunistic ligand and can activate the signalling cascade in order to get itself internalised [235]. Caveolar endocytosis is an inducible process and can be stimulated by the presence of cargo [234].

5.2.2.4 Clathrin and caveolin-mediated independent endocytosis

Currently, the mechanisms governing clathrin and caveolin independent (CCI) pathways are poorly understood. However, it is likely that each of these pathways fulfils unique functions in the cell and vary mechanistically not only in how the vesicles are formed, but in terms of which cargo molecules they transport, to what intracellular destination their cargo is delivered, and how their entry is regulated [235]. The integral membrane proteins flotillin-1 and flotillin-2 may have a role in CCI pathways including a role in selecting lipid cargo [96, 234].

5.2.2.5 Clathrin-mediated endocytosis

Clathrin-mediated endocytosis (CME) is the most studied internalisation route for membrane proteins and extracellular ligands in higher eukaryotic cells [239, 240]. Indeed, CME constitutes the major route for selective receptor internalisation in these cells [241]. CME carries out the continuous uptake of essential nutrients, such as the cholesterol laden low-density lipoprotein (LDL) particles that bind to the LDL receptor, and iron-laden transferrin (Tfn) that binds to Tfn receptors. CME has been previously referred to as ‘receptor mediated’ endocytosis, but it is now clear that this is a mistake since most pinocytic pathways involve specific receptor-ligand interactions. In fibroblasts the clathrin-dependent highly efficient endocytosis machinery has been estimated to internalise nearly the equivalent of the cell’s total plasma membrane within one hour [242]. The life of an endocytic coated vesicle begins with the recruitment of clathrin, adaptors and endocytic accessory proteins to the plasma membrane where they form patches ranging in diameter from 10 to more than 500 nm [243].

Clathrin is a spiderlike molecule, with three legs radiating from a central hub, called a triskelion. An antiparallel interaction of the legs from triskelions centered on adjacent vertices of the lattice allows assembly of the cage. As isolated from coated vesicles, clathrin is a trimer of 190-kDa heavy chains each with an associated \approx 25-kDa light chain (Lca). There are also other protein components in coated vesicles, the most important of which are the members of the so-called clathrin adaptor protein complexes (AP complexes) that mediate selective inclusion of membrane-anchored proteins into budding coated pits [244].

The classical model of endocytosis was postulated several decades ago mainly on the basis of electron microscopy studies and numerous biochemical assays. Figure 5.2 is a schematic diagram representing the process of CME. The first step in the CME pathway is the binding of extracellular cargo molecules to specific cell surface receptors. These receptors and other membrane proteins that are destined for endocytosis are then bound by intracellular adaptor proteins, such as the heterotetrameric adapter protein-2 (AP-2) complex [245], to sites of endocytosis. The adaptors, along with clathrin, form an endocytic coat at the cytoplasmic side of the plasma membrane. The coated membrane bends to form an invagination, also known as a clathrin coated pit (CCP) that subsequently pinches off to form a cargo-filled vesicle. The nascent coated vesicle is severed from the plasma membrane through a fission reaction thought to be mediated by dynamin (GTPase accessory protein) [246]. The protein coat that surrounds the newly formed endocytic vesicle is rapidly disassembled. The vesicles, known as clathrin coated vesicles (CCVs), then deliver their cargoes to early endosomes by fusing with the endosomal membrane. From early endosomes, the cargo molecules can be recycled back to the plasma membrane or trafficked further to late endosomes and, finally, to lysosomal organelles for degradation [239].

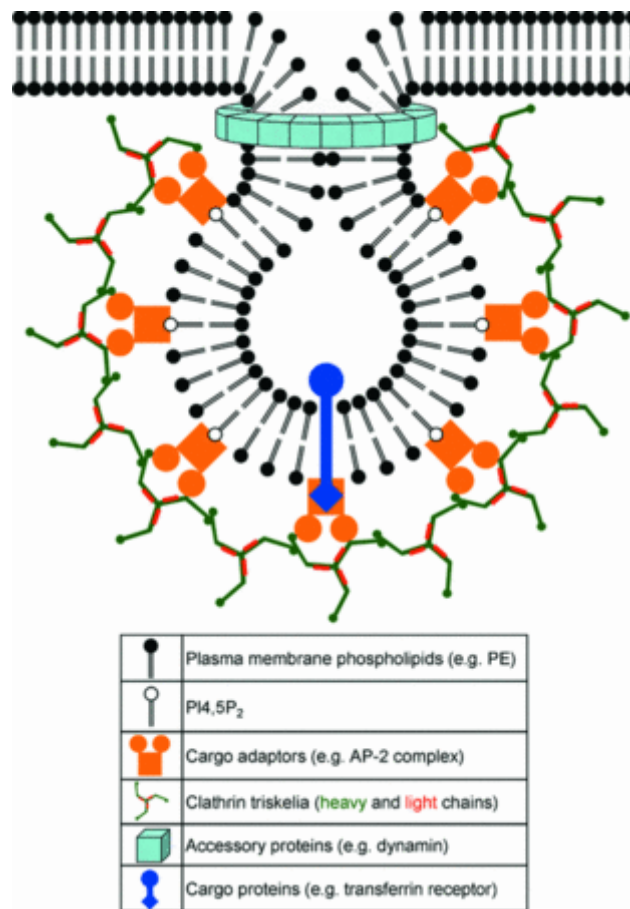


Figure 5.2 Schematic diagram for clathrin-mediated endocytosis

The endocytic pathways differ with regard to the size of the endocytic vesicle, the nature of the cargo (ligands, receptors, lipids and nanoparticles) and the mechanism of vesicle formation. Large particles can be taken up by phagocytosis, whereas fluid uptake occurs by macropinocytosis. Both processes appear to be triggered by and are dependent on actin-mediated remodelling of the plasma membrane at a large scale. Compared with the other endocytic pathways, the size of the vesicles formed by phagocytosis and macropinocytosis is much larger. Numerous cargoes can be endocytosed by mechanisms that are independent of the coat protein clathrin and the fission GTPase, dynamin. Adapted by permission from Macmillan Publishers Ltd: [Nature] [235], copyright (2003).

As mentioned, the model of CME described above was based on electron microscopy studies and biochemical assays in fixed cells. The recent availability of fluorescent derivatives of clathrin, such as GFP-clathrin LCa, have afforded the opportunity to test this model in living cells [247]. Many new findings have been garnered through the use of high resolution fluorescence microscopy studies of fluorescently tagged clathrin molecules in living cells. The first visualisation of fluorescent clathrin generated several surprising findings, among which was the perception that CCVs were produced recurrently from the specific sites within the plasma membrane. In addition, many of these sites displayed a gradual loss of fluorescence, not a sudden catastrophic disappearance, suggesting that individual coated pits could form from within an expansive clathrin patch [248].

One imaging modality that is particularly appropriate for studying endocytosis is TIRF [249]. A schematic representation of a typical TIRF setup for imaging cellular endocytosis is shown in Fig. 5.3. TIRF imaging of endocytosis can be performed on a system like the one described in Chapter 4. Images derived from TIRF imaging of clathrin are consistent among many groups using either DsRed-clathrin or enhanced green fluorescent protein (EGFP)-clathrin, in stable or transiently transfected cells [248]. The major findings from these studies include; 1) the vast majority (80%) of the clathrin signal on the plasma membrane is present as a population that is static during the average period of observation, typically 60 seconds, 2) Only a small population of clathrin (10-20%) is present as small, rapidly disappearing structures, which would be the ones expected to predominate if the classical model of CME were occurring in live cells [79, 240, 250-254]. Although these observations occur repeatedly, their

significance remains unclear, and there is a possibility that they may represent an artefact of cell adherence in culture [255].

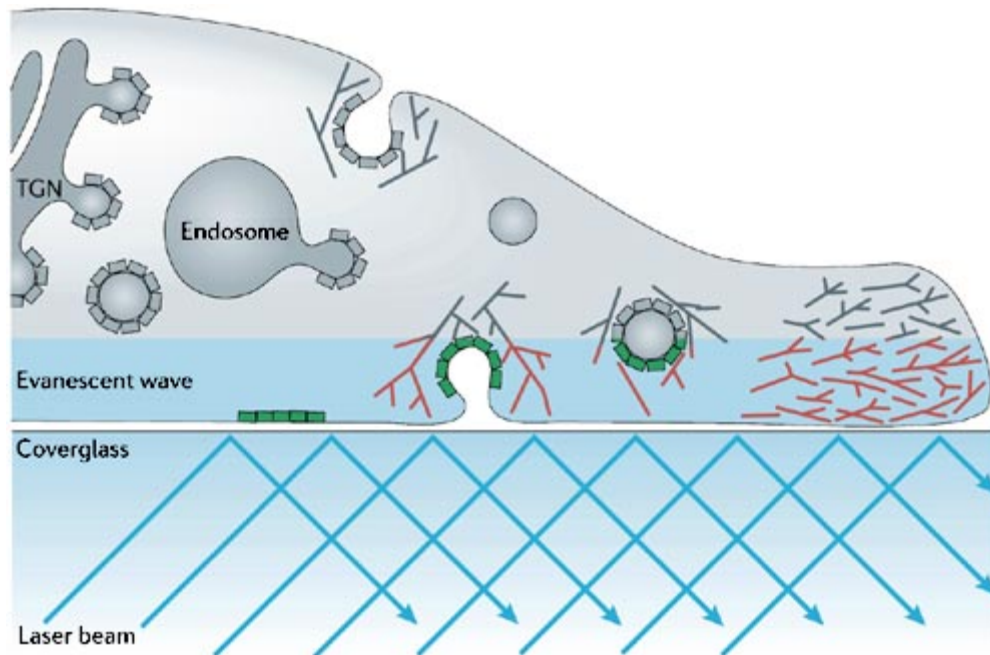


Figure 5.3 TIRF imaging of clathrin mediated endocytosis

One of the common problems in imaging studies of membrane-trafficking events is that it is often difficult to resolve different structures. Typical mammalian cells contain many different kinds of actin structures that are used at various locations in a cell for structural support, motility and trafficking. Similarly, clathrin localises to the plasma membrane and to internal organelles such as endosomes and the Golgi complex. Total internal reflection fluorescence (TIRF) microscopy has been useful in studies of endocytosis because it affords excitation of fluorescent molecules specifically at the interface between the sample and the coverglass. The evanescent wave excites fluorophores that are within ~ 200 nm of the coverglass surface (the structures highlighted in red (actin) and green (clathrin) in the figure, but not those that are further away (the structures with the same shape, but that are coloured grey)). Adapted by permission from Macmillan Publishers Ltd: [Nature Reviews Molecular Cell Biology] [239], Copyright © 2006.

Two general theories exist for the formation of budding CCVs. The first, known as the ‘iterative budding’ model suggests that flat clathrin lattices are present on the cytosolic leaflet of the plasma membrane from which coated vesicles form repeatedly. The second, more elusive theory, describes the apparent production of CCVs from bare membrane initially and subsequently devoid of clathrin. This process is known as ‘*de novo*’ clathrin coated vesicle formation. Ultimately, it is likely that both mechanisms for coated vesicle production occur simultaneously. However, the preference of cargo for a particular pathway has not been adequately investigated. Indeed, although it is logical to assume that receptors which undergo stimulated endocytosis following ligand binding internalise through CCVs formed *de novo*, this has not been observed. For example, the epidermal growth factor receptor and G-protein-coupled receptors seem to cluster at pre-formed clathrin spots following activation [245].

5.3 Materials and methods

5.3.1 Plasmids

The plasmids pEGFP-C1 and pDsRed-N1 were purchased from BD Clontech, France.

5.3.2 Oligonucleotide primers

Non-labelled oligonucleotide primers were synthesised by Sigma-Genosys, UK. All PCR primers used in this study are listed in Table 5.1.

Table 5.1 Oligonucleotide primer sequences for RT-PCR experiments

Primer	Sequence (5' to 3')
Mm Cav-1 EcoRI-For	GCCCGGGAATTCACGGAGG
Mm Cav-1 KpnI-Rev	GCCCGGGTACCTATCTCTTTCTGCGTGC
Mm Clathrin Lca EcoRI-For	GCCCGGGAATTCATGGCCGAGTTGGATCCAT
Mm Clathrin Lca KpnI-Rev	GCCCGGGTACCTCAGTGCACCAGGGGGGCC
pEGFP-C1F	CATGGTCCTGCTGGAGTTCGT
pEGFP-C1R	GTCAGGGGGGAGGTGTG
pDSRED-N1R	GTA CTGGA ACTGGGGGGACAG

5.3.3 Chemical reagents & media

5.3.3.1 General Chemicals

Unless otherwise stated, all chemicals were obtained from Sigma (Poole, UK).

5.3.3.2 Antibiotics

Stock solutions of antibiotics were prepared according to Ausubel et al., (1989), and stored at -20 °C. Ampicillin was used from a 50 mg/ml in 50% (v/v) EtOH stock, tetracycline from 5, 10 or 50 mg/ml in 70 % (v/v) EtOH, kanamycin from 50 mg/ml in dH₂O.

5.3.4 Growth media

Media were prepared using deionised water and autoclaved at 121°C for 20 min at 15 p.s.i.

5.3.4.1 Luria Bertani medium

All bacterial strains were routinely grown in Luria Bertani (LB) broth unless otherwise stated. LB broth was prepared as described by Sambrook et al., (1989) and consisted of 10 g/L tryptone, 5 g/L yeast extract, 10 g/L NaCl and 4 ml/L 1 M NaOH. LB agar was prepared by addition of 0.8 % (w/v) Technical Agar No. 3 (Oxoid, UK) to LB broth, followed by autoclaving.

5.3.5 Growth & storage of bacteria

5.3.5.1 Bacterial growth conditions

Liquid cultures were grown in LB broth in an incubator (Gallenkamp Ltd., UK or New Brunswick Scientific, USA) with agitation at 200 rpm at 37 °C, unless otherwise stated.

5.3.6 DNA manipulation

5.3.6.1 Isolation of mRNA and production of cDNA

Messenger ribonucleic acid (mRNA) and complementary deoxyribonucleic acid (cDNA) was isolated and synthesised respectively from murine fibroblast cells (3T3 cells, ECACC, HPA, UK) using the μ MACS One Step cDNA Kit (Miltenyi Biotec, Surrey, UK) in accordance with the manufacturer's instructions. Cells grown to 90 % confluence in a T75 flask were washed with PBS, then lysed using 1 ml of Lysis/Binding buffer per 10^7 cells and centrifuged (Eppendorf centrifuge 5417R) in a lysate clear column at 13 000 rpm for 3 min to decrease viscosity of sample, followed by addition of Oligo (dT) microbeads. The lysate mixture was then added to a MACS μ column placed within the magnetic field of a thermoMACS separator. The column was then washed, lysate applied, and washed again, leaving mRNA bound to the column. To synthesis cDNA from mRNA, the mRNA was firstly washed followed by addition of a resuspended enzyme mix. The column was sealed and the reaction allowed to proceed for 1 hour at 42 °C. The column was rinsed again and cDNA release solution applied for 10 min at 42 °C. Finally, cDNA was eluted into 30-50 μ l HPLC grade H₂O

(Fisher Scientific, UK). The eluted cDNA was then used as a template for the multiplication of the gene of interest by the polymerase chain reaction (PCR) (Section 5.3.6.3).

5.3.6.2 Isolation of plasmid DNA from electrocompetent *E. coli* cells

Plasmid DNA isolation was performed using the Qiagen Miniprep kit (Qiagen Ltd., Surrey, UK) according to the manufacturer's protocol. Firstly, electrocompetent *E. coli* cells (Top 10 Electropcomp Cells, Invitrogen, UK) were transformed with plasmid DNA (Section 5.3.7). Cells were then pelleted from 1-10 ml of the overnight bacterial culture and subjected to alkaline lysis, they were then neutralised and centrifuged (Eppendorf centrifuge 5417R) at 13,000 rpm for 10 min to remove denatured and precipitated cellular debris. Lysates were then loaded onto a silica-gel filter, washed and plasmid DNA was eluted into 30-50 μ l HPLC grade H₂O (Fisher Scientific, UK). Eluted plasmid DNA was used in all subsequent cloning experiments.

5.3.6.3 Polymerase chain reaction (PCR) amplification

PCR amplifications were performed according to the protocol of Sakai et al., (1988) in a final volume of 50 μ l. The reaction mix consisted of 0.5 μ l Taq (for non-proof reading PCR) or Pfu (for proof reading PCR) polymerase in 1 x buffer (Promega, UK), approximately 1 μ M of each primer, 1.5 mM MgCl₂ (for Taq reactions), 2 mM dNTPs and 1 μ l cDNA or plasmid DNA template. The DNA template used was either from whole cells transferred from a fresh colony or 1 μ l of a chromosomal or plasmid

preparation. Reactions were carried out in a PTC-200 Peltier Thermal Cycler (MJ Research, UK) for a total of 30 cycles. Briefly, the DNA template was denatured at 94 °C for 5 min. This was followed by 30 cycles of denaturation at 94 °C for 30 sec, annealing at 60 °C for 30 sec and extension at 72 °C for 1-2 min. The last cycle finished with an extension at 72 °C for 8 min to ensure completion of all strands. Reaction mixes were then incubated at 4 °C indefinitely to allow PCR reactions to be carried out overnight.

5.3.6.4 DNA agarose gel electrophoresis

DNA loading buffer (6 x stock: 1 ml glycerol; 2 ml 50 x TAE; bromophenol blue 0.002 g; sterile dH₂O to 10 ml) was added to DNA samples and analysed on 0.7, 1.0 or 1.2 % (w/v) agarose gels using a horizontal gel apparatus (Biorad, UK). The gels were prepared using the method described by Sambrook et al., (1989) using analytical grade agarose (Invitrogen, UK) in 0.5 x TBE buffer (Tris Borate EDTA*) with the addition of ethidium bromide to a final concentration of 10 µg/ml. The gels were run in 0.5 x TBE buffer and electrophoresis was performed at 70-120 V. DNA fragments were visualised on a UV transilluminator with GeneSnap software (Syngene, UK).

* 10x TBE: 0.89M Tris base, 0.02M EDTA and 0.89 M boric acid.

5.3.6.5 DNA molecular weight markers

To establish the size of DNA fragments, 1 µg of either 100 bp or 1 kb ladder (Invitrogen, UK) in DNA loading buffer were loaded on agarose gels.

5.3.6.6 DNA restriction enzymes

The restriction enzymes EcoRI and KpnI were purchased from New England Biolabs (UK) and were used according to the manufacturer's instructions. Reactions generally contained 0.05-1 µg DNA, as determined with a nanodrop spectrophotometer, 0.5-1 µl restriction endonuclease and 1 x restriction buffer made to a final volume of 50 µl with dH₂O. The reaction mixture was incubated at 37 °C for a minimum of 1 h or until the digestion was complete. Reactions were analysed on agarose gels and appropriate bands cut out prior to DNA extraction using the Qiagen Gel Extraction Kit (Qiagen, UK).

5.3.6.7 DNA ligation

T4 DNA ligase was purchased from Roche (UK) and was used according to the manufacturer's instructions. Reactions generally contained 0.05-1 µg of digested DNA, 0.5-1 µl T4 DNA ligase and 1 x ligation buffer made to a final volume of 30 µl with dH₂O. The ligation mixture was incubated at 4 °C for 16 h. Ligation reactions were analysed by running a PCR (Section 5.3.6.3) with primers for the ligated gene. A bright band on the agarose gel (Section 5.3.6.4) matching the known size of the ligated gene constituted a successful ligation.

5.3.7 Electroporation of electrocompetent *E. coli* cells

Electroporation was performed in 0.1 cm electrode gap Gene Pulser cuvettes (BioRad, UK) containing 20 µl of competent cells (Top 10 Electropcomp Cells, Invitrogen, UK)

and 1 μ l dialysed DNA. An electroporation pulse of 2.5 kV (25 μ F, 200 Ω) was delivered using the BioRad Gene Pulsar connected to a BioRad pulse controller (BioRad, UK). A 1 ml aliquot of sterile, prewarmed (37 °C) S.O.C. medium (0.5 % Yeast Extract, 2 % Tryptone, 10 mM NaCl, 2.5 mM KCl , 10 mM MgCl₂ , 10 mM MgSO₄ , 20 mM Glucose) was added to the cells and incubated at 37 °C in the absence of antibiotics. After 1 h aliquots of cells were plated onto LB agar plates containing appropriate antibiotics to select for transformants and grown overnight at 37 °C.

5.3.8 DNA sequence analysis

Routine DNA sequencing was conducted by Lark Technologies Inc. (Essex, UK), using the dideoxy chain termination method as described by Sanger et al., (1977).

5.3.9 Transfection

Transfection was performed as described in Chapter 4 (Section 4.3.4). One change from this protocol however was the use of Clathrin-EGFP plasmid in place of the DsRed plasmid.

5.4 Results and discussion

5.4.1 Development of EGFP-clathrin fusion protein

The study of clathrin coated pit dynamics was made considerably easier when it was shown that a green fluorescent protein-clathrin (GFP-clathrin) could function as a reporter for coated pits in live cells [247]. Distinct populations of clathrin coated pits which were either static, disappearing or appearing could be visualised using a combination of the fluorescent protein and a fluorescent microscope. The clathrin molecule is a triskelion-shaped molecule that in higher eukaryotes is composed of three identical heavy chains of molecular weight ~ 192 kDa and three light chains. The light chains either consist of two distinct gene products, denoted light chains a (LCA) and b (LCb), with molecular weights of 36 kDa and 33 kDa respectively [244, 256]. In the following section I will describe the design and development of an EGFP-clathrin light chain a fusion protein, similar to that used by Gaidarov *et al* (1999).

To encode a clathrin gene into the EGFP plasmid, it is first important to understand the makeup of the plasmid to be used. In this case, pEGFP-C1 was obtained from Clontech and had a size of 4.7 Kbp (Fig. 5.4a). This plasmid has a Kanamycin resistance gene and a multiple cloning site (MCS) beginning at position 1330 (Fig. 5.4b). The MCS is where the gene of interest will be inserted and contains a number of restriction sites for this purpose. In this work, the restriction sites digested by the endonucleases *EcoR1* and *Kpn1* were chosen (red circles, Fig. 5.4b) since they were freely available in the lab and more importantly did not cut the clathrin gene or the plasmid outside the MCS.

Figure 5.4c is a schematic illustration demonstrating that the EGFP was coupled to the amino terminus of clathrin LCa and also shows the direction of expression when transfected in living cells.

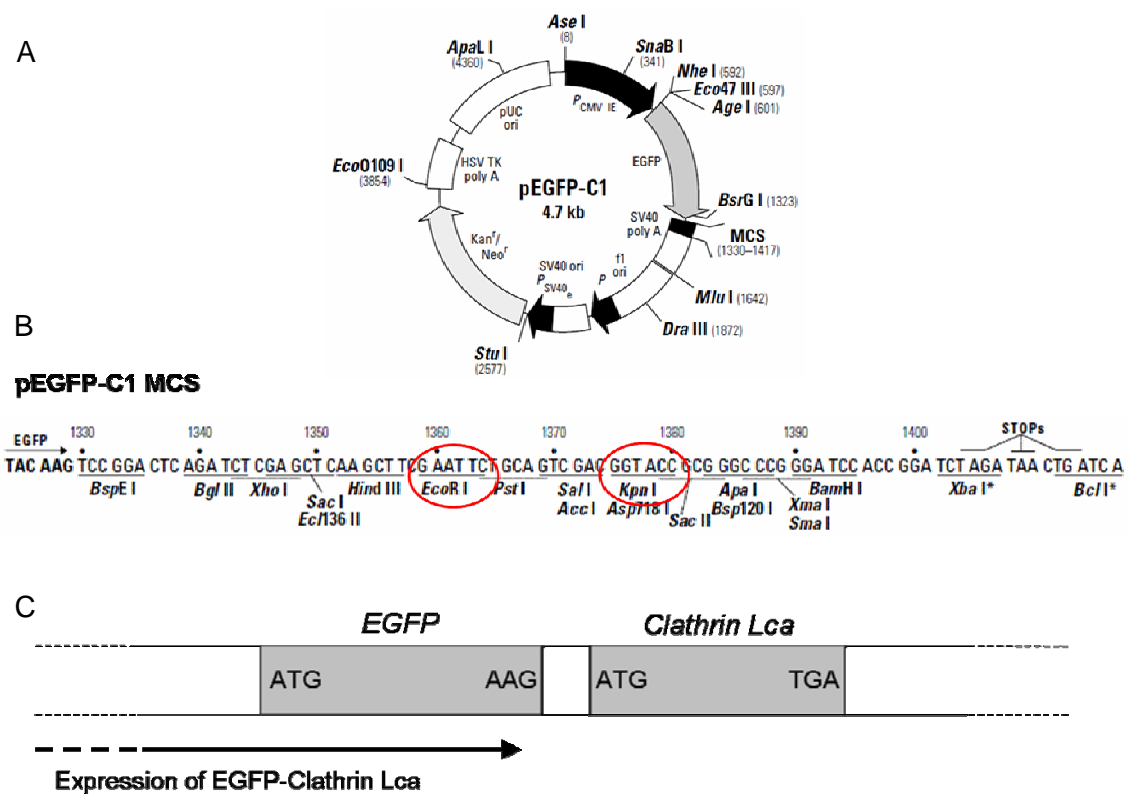


Figure 5.4 Insertion of clathrin LCa into pEGFP-C1

(A) pEGFP-C1 vector information (www.clontech.com). Note the presence of the EGFP gene prior to the MCS. This indicates that we have constructed a plasmid for enhanced GFP coupled to the amino terminus of clathrin light chain a. The plasmid already contains a Kozak consensus translation initiation site and start codon therefore they do not need to be genetically engineered into the amplified insert (B) Multiple cloning site (MCS) of pEGFP-C1. *EcoR*I and *Kpn*I restriction sites are circled in red. After digestion the previously digested clathrin PCR fragments would be ligated into the MCS. (C) Schematic representation of EGFP-Clathrin expression.

The first step in the development of an EGFP-Clathrin fusion protein is to design primers to amplify the clathrin gene from cDNA. The primers used for this purpose are outlined in Table 5.1. Primers for amplifying DNA have three main characteristics. Firstly, they should have a number of GC oligonucleotides needed for attachment and digestion by the restriction enzymes. Secondly, the primer should have suitable restriction sites engineered into it. It is important to check that the restriction enzymes which are being considered do not also cut anywhere within in the DNA fragment to be amplified by PCR. This can be achieved by use of a suitable web program such as Webcutter 2.0 (<http://rna.lundberg.gu.se/cutter2>). Finally, a suitable fragment of the sequence to be amplified should be contained in the primer.

The designed primers can now be used to amplify the clathrin gene from cDNA as shown schematically in Fig. 5.5. This is performed using the polymerase chain reaction (PCR). Developed in 1984 [257], the PCR has become a widely used and indispensable technique in molecular biology labs and further afield. The PCR generally consists of a series of 20 to 40 repeated temperature changes called cycles with each cycle typically consisting of 2-3 discrete temperature steps. The first step, known as the denaturation step, involves heating the reaction to 94-98°C for 20-30 seconds. It causes melting of the DNA template and primers by disrupting the hydrogen bonds between complementary bases of the DNA strands, yielding single strands of DNA. In the annealing step the temperature is lowered to 50-65 °C for 20-40 seconds allowing annealing of the primers to the single-stranded DNA template. Here the DNA polymerase enzyme binds to the primer-template hybrid and begins DNA synthesis. In the extension step the temperature is adjusted according to the DNA polymerase used,

though this value tends to be around 72 °C. At this step the DNA polymerase synthesizes a new DNA strand complementary to the DNA template strand by adding dNTPs that are complementary to the template in 5' to 3' direction, condensing the 5'-phosphate group of the dNTPs with the 3'-hydroxyl group at the end of the nascent (extending) DNA strand. At each extension step, under optimum conditions, the amount of DNA target is doubled, leading to exponential amplification of the specific DNA fragment. Finally, a single elongation step is performed at a temperature of 70-74 °C for 5-15 minutes after the last PCR cycle to ensure that any remaining single-stranded DNA is fully extended. The result of the PCR amplification of clathrin LCa is shown in Fig. 5.6. The band present in rows 2 and 3 represent amplified clathrin LCa.

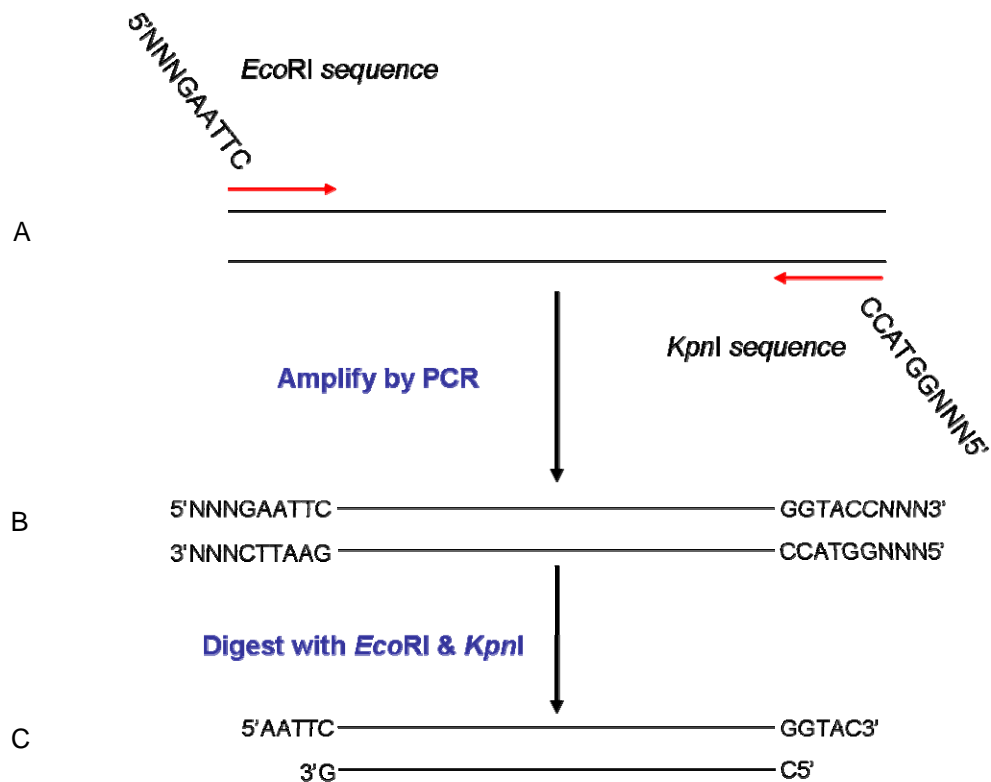


Figure 5.5 Cloning PCR products by addition of restriction sites

Specific PCR primers for Clathrin Lca (represented by red arrows) are designed to amplify a region of interest with the desired recognition sequence for the restriction endonuclease included at the 5' end of the primer. The sense strand primer contains the sense strand of an *EcoRI* restriction site, and the antisense primer contains the complementary sequence of a *KpnI* restriction site. (A) To achieve high efficiency digestion, additional nucleotides must be included on both sides of the restriction endonuclease sequence. (B) Amplification by PCR produces a specific product with an *EcoRI* site at the 5' end and a *KpnI* site at the 3' end. (C) Digestion with *EcoRI* and *KpnI* produces a PCR product that can be controlled directionally.

The next step in the development of EGFP-clathrin is to digest both the amplified clathrin gene (Fig 5.5c) and the EGFP plasmid using restriction endonucleases. These endonucleases (enzymes) cut single or double stranded DNA at specific recognition nucleotide sequences known as restriction sites. The key feature of most restriction sites is that they are palindromic in nature, i.e. they read the same backwards as forwards. In the case of clathrin, the restriction sites have been engineered into the amplified DNA, whereas pEGFP already contains the restriction sites within the MCS. The agarose gel in Fig. 5.7 highlights the difference between restriction enzyme digested (Section 5.3.6.6) and undigested plasmid. The undigested plasmid, i.e. circular DNA (lane 2) forms three distinct bands whereas the digested plasmid only contains two (lanes 3-5). It is important to remember that all these bands represent DNA of the same molecular weight. The reason for this difference highlighted by the gel can be explained by differences in the structure of the DNA in each case. Viewing from top to bottom of the gel in lane 2, the top band contains relaxed DNA (also known as nicked or open circle), next is linearised DNA and finally supercoiled DNA. Supercoiled DNA runs fastest in the gel since it is highly condensed and therefore is able to move through the pores easier. The plasmid DNA becomes linearised after digestion (lanes 3-5) and thus is of the same size as the linear strand in lane 2.

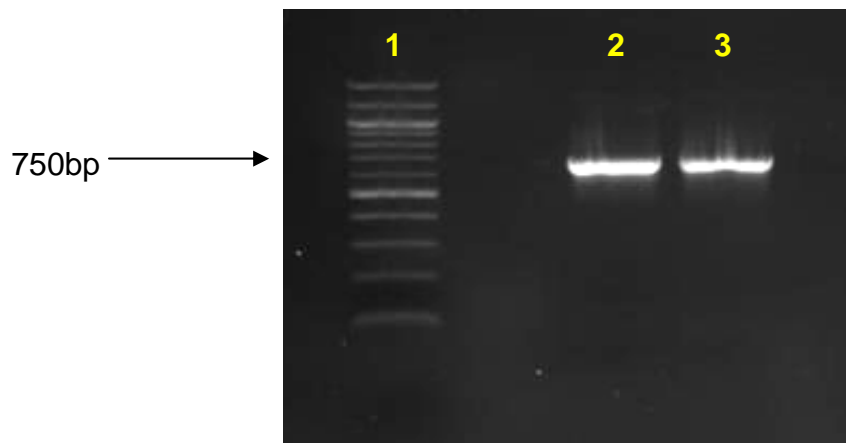


Figure 5.6 Agarose gel showing the PCR amplification of murine clathrin light chain A

Lane 1 – 100 bp DNA step ladder, Lane 2 & 3 – Clathrin Lca. It can be seen that the Clathrin forms a band between 700 and 800 bp as indicated by the DNA step ladder. The murine clathrin light chain a gene is known to be 750 bp in size, therefore this agarose gel indicates that we have successfully amplified the right size of gene.

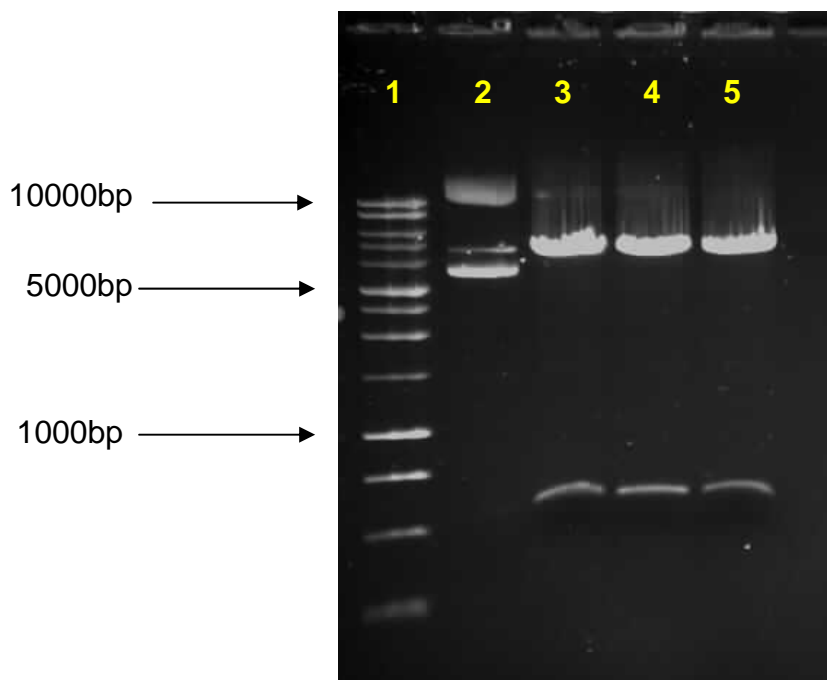


Figure 5.7 Agarose gel showing the digestion of EGFP plasmid

Lane 1 – 1 Kbp DNA step ladder, Lane 2 – undigested EGFP plasmid, Lane 3,4,5 – EcoRI and KpnI digested plasmid. The presence of only 2 bands in lanes 3-5 indicate that this is digested plasmid. The 3 bands in lane 2 indicate the presence of undigested plasmid. The main band of the uncut plasmid occurs at 4.7 Kbp (exact size of circular plasmid DNA).

The next step following digestion of both the plasmid and clathrin DNA is to ligate them together (Fig. 5.8) using DNA ligase. DNA ligase is an enzyme which can link together two DNA strands that have a break in both complementary strands of DNA. In the case of clathrin and EGFP, the breaks have been introduced during digestion (Fig 5.5c). The result of the ligation reaction will be a recombinant plasmid encoding the clathrin gene. It is likely that other products will be formed during ligation known as ‘mismatch’ pairs. These result from the ligation of complementary ends of two plasmid pairs or two insert pairs. Following ligation, the recombinant plasmid is transformed into electrocompetent cells by electroporation and grown overnight on LB-agar plates. After a successful transformation, colonies are screened for plasmids containing the clathrin gene by PCR and then multiplied O/N in LB broth. The recombinant plasmid is harvested and is ready to be used in the next step, which is transfection of the cells.

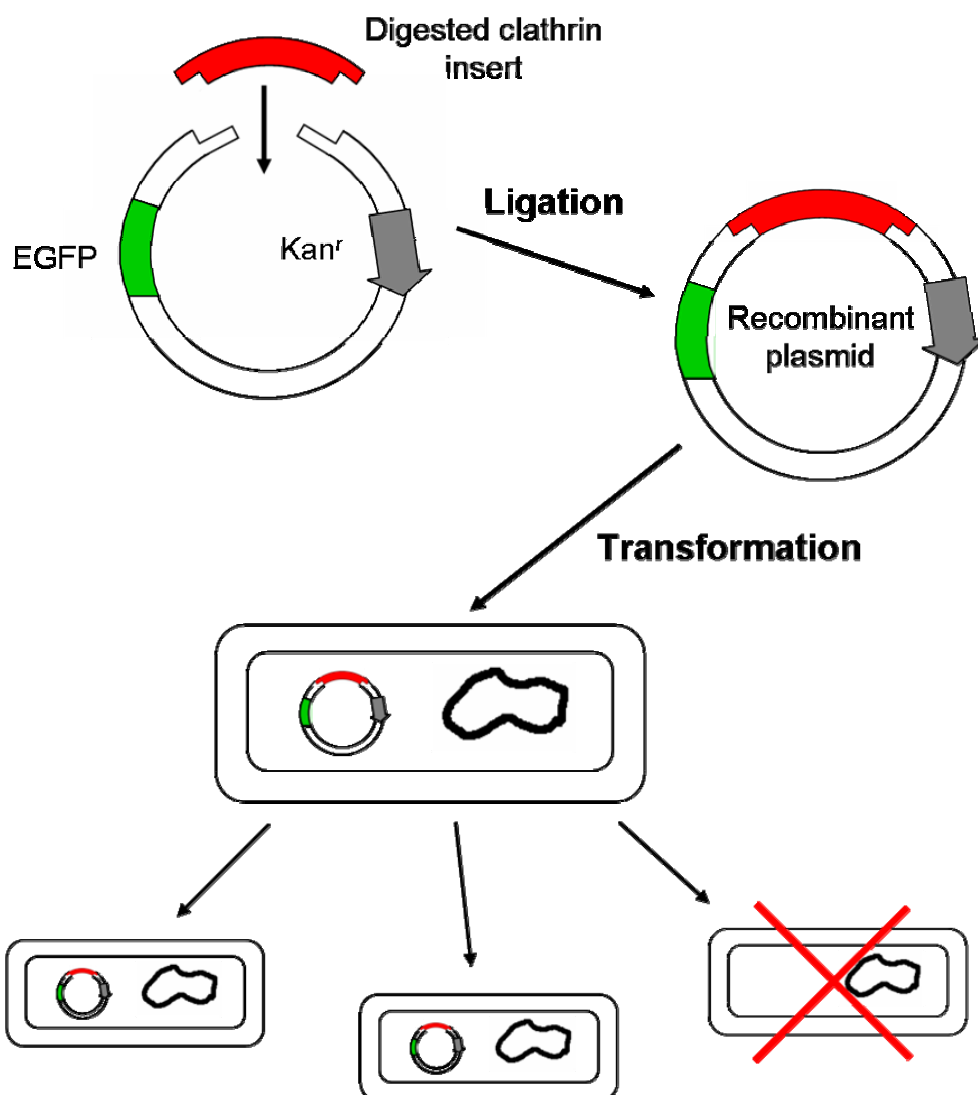


Figure 5.8 Schematic diagram outlining the cloning process

There are a number of steps involved in the cloning process. *EcoRI* and *KpnI* digested *EGFP* and clathrin LCa are firstly ligated using the enzyme T4 DNA ligase. This results in the formation of the recombinant plasmid. Note other mismatch DNA will be produced but for simplicity have not been included. Mismatches form whenever sticky ends from two insert pairs or two plasmid pairs bind together. After ligation, the recombinant plasmid DNA is transformed into electrocompetent *E. coli* cells using electroporation. The transformed cells are subsequently selected using kanamycin on LB-Agar plates for 24 hrs and finally single cultures are grown O/N. Note only cells that have been successfully transformed will multiply since they contain the antibiotic resistance gene for kanamycin.

5.4.2 Clathrin expression in a mouse fibroblast cell line

Gaidarov's seminal work highlighted how a fusion protein consisting of green fluorescent protein and clathrin LCa could be used to visualise the dynamics of endocytic clathrin coated pits and vesicles in mammalian cells [247]. Similar to previous studies, the EGFP-Clathrin developed in this work exhibited a distribution comparable to that of endogenous clathrin. Generally, clathrin is found in an assembled form on the cytoplasmic surface of the plasma membrane in coated pits that are active in endocytosis [258], in the *trans*-golgi network region [259], in a soluble pool in the cytoplasm [260] and in some endosomal structures [261]. A major limitation of this work results from the microscopy technique used to image the EGFP-clathrin. Since the authors used epi-fluorescence microscopy, they were unable to resolve whether the fluorescent spots were actually associated with the plasma membrane or in the cytosol. However, this problem has been reduced by using TIRF microscopy, where only a thin region (50-150 nm) close to the cell coverslip is illuminated. The size of a clathrin coated vesicle (CCV) is approximately 100 nm, therefore it should be possible to observe forming CCVs and clathrin coated pits (CCPs). Indeed, as the vesicles move away from the surface of the cell into the main body, their fluorescence intensity will begin to decrease and eventually disappear due to the evanescent nature of the excitation light [250]. Using TIRF, it can be seen that the EGFP-clathrin is found as discrete puncta in the plasma membrane associated region (Fig. 5.9a). The distribution of discrete clathrin puncta in 3T3 fibroblast cells is similar to that shown by other groups [79]. In epifluorescence microscopy, clathrin is normally observed throughout

the cell, both in puncta (presumably on the plasma membrane) and in a juxtannuclear region (presumably at the Golgi and on Golgi-derived vesicles) [247, 262, 263].

TIRM/TIRF microscopy is an excellent way of studying the dynamics of individually labelled proteins within a living cell whilst simultaneously receiving high resolution topographical information of the basal cell membrane. The TIRF image in Fig. 5.9a shows the distribution of EGFP-clathrin at the plasma membrane of the cell. For a clearer visualisation of discrete fluorescent spots, a low-spatial frequency background due to cytoplasmic EGFP-clathrin has been subtracted from the image. This was achieved by firstly obtaining a Fast Fourier transform (FFT) of the selected TIRF image. Subsequently, a 3 x 3 pixel array was suppressed from the centre of the FFT to remove any low spatial frequencies. Finally, an inverse FFT was performed to give the resultant image, free from fluorescence due to cytoplasmic clathrin. The discrete clathrin puncta seen in this image do not represent individual EGFP-clathrin molecules as these are most likely to be beyond the resolution limit of the microscope. Instead, the puncta represent CCPs which form at the plasma membrane and clathrin coated vesicles which are formed pits that have progressively invaginated, undergone scission and have been released into the cytosol. This image highlights all the advantages associated with TIRF imaging; namely low background fluorescence, high signal-to-noise and high image contrast. The TIRM image (Fig. 5.9b) is similar to those previously described in this thesis. However, unlike other images included here, the image has been overlaid with the EGFP-clathrin distribution image (Fig. 5.9c). This is important because it now illustrates how an event occurring at the basal cell membrane e.g. membrane ruffling or

particle uptake can be imaged non-fluorescently at very high resolution whilst also viewing dynamics of the proteins within the cell.

The direction of migration of the cell is shown in Fig. 5.9d, with the arrow also indicating the leading edge of the cell. The EGFP-clathrin signal appears to be weakest at the lagging edge of the cell and gets progressively stronger towards the leading edge. These results are similar to those seen in Madine Darby Canine Kidney (MDCK) cells [79]. The authors suggest two possible explanations for clathrin polarisation towards the leading edge of the cell. Firstly, the coupling of exocytosis and endocytosis at the leading edge may function to adjust membrane tension to facilitate the generation of motile force by actin polymerisation. Alternatively, it may be important for chemokine, cytokine and growth factor internalisation. One problem with the previous work by Rappoport *et al* (2003) is that they obtained an outline of the cell border by drawing an edge around an epi-fluorescence image of the clathrin signal [79]. This may lead to problems since areas such as the thin lamella may not have any clathrin present, therefore making the cell border region inaccurate. However, using TIRM affords a high resolution view of the whole cell membrane making it extremely easy to visualise the border of the cell. Also, to address the question as to whether the low clathrin signal at the trailing edge of the cell was simply due to the membrane moving out of the evanescent excitation area, the authors added a membrane dye, thus making the experiment more complicated. TIRM shows that the whole cell is present within the evanescent field without the need for an additional fluorescent label and confirms that the low clathrin signal at the trailing edge is not due to the membrane lifting out of the evanescent field.

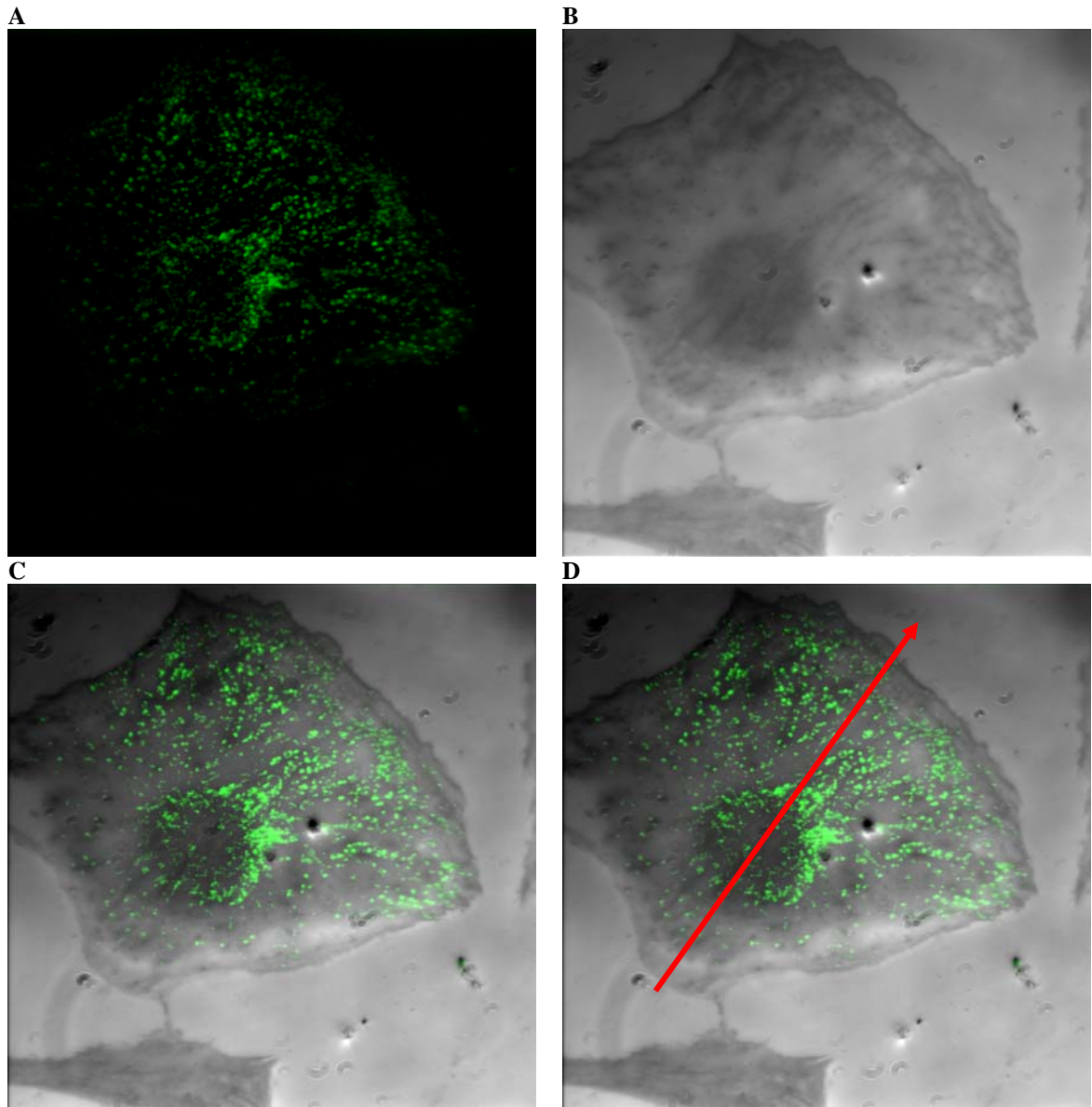


Figure 5.9 TIRM/TIRF analysis of clathrin distribution in a 3T3 fibroblast cell 24 hrs post transfection

A) TIRF image of a 3T3 fibroblast cell transfected with EGFP-clathrin. For a clearer visualisation of discrete fluorescent spots, a low-spatial frequency background due to cytoplasmic EGFP-clathrin has been subtracted from the image. B) TIRM image of the same fibroblast cell captured immediately following the TIRF image. C) Combined TIRM/TIRF image highlighting the distribution of clathrin puncta on the basal cell membrane. Note how the clathrin is distributed in discrete spots. D) Red arrow depicts the apparent migratory direction of this cell. Note the distribution of clathrin towards the leading edge of the cell.

5.4.2.1 Dynamics of clathrin coated pits and vesicles in live cells

In TIRF, the dynamics of the EGFP-clathrin puncta in murine 3T3 cells were similar to those reported previously [79, 247, 253, 264]. The majority of clathrin puncta were relatively stationary throughout the time course of the experiment however, sub-populations of clathrin puncta were seen to move laterally (Fig. 5.10b), appear (Fig. 5.10c) and disappear (Fig. 5.10d) over time. The rate of disappearance of clathrin puncta was as little as 2.4 seconds (Fig. 5.10e). Previous studies were conducted in non-migratory cell lines such as COS-7, MDCK and HeLa cells, however similar observations were made in the migratory 3T3 cell line [264]. In the aforementioned studies the authors found that clathrin dynamics on the upper surface of the cell was only marginally less restricted, therefore this rules out the possibility of cell attachment decreasing the movement. The clathrin spots which increase in intensity over time have been postulated to be coated pits forming on the membrane, whereas those seen to be disappearing are CCPs undergoing internalisation.

There are a number of important criteria which need to be met to verify whether clathrin mediated endocytosis (CME) is indeed being imaged. Fluorescent probes such as GFP are inherently susceptible to photobleaching [265]. Indeed, this property has been put to use in many studies utilising fluorescence recovery after photobleaching (FRAP) [266], including one study using FRAP in combination with GFP-clathrin to examine CCP endocytosis [267]. However, when studying the dynamics of EGFP-Clathrin in living cells using time-lapse TIRF it is important to determine whether events such as disappearance of clathrin puncta (Region 3, Fig. 5.10d) are putative endocytic events or

are simply due to photobleaching of GFP. Luckily, this question can be easily addressed by studying a neighbouring clathrin punctum, for example the spot to the left of the arrow in region 3 (Fig. 5.10d), which does not visibly decrease in intensity over the same time frame. Secondly, disappearance of a CCP should be observed over a number of successive frames and not be the result of lateral spot motility out of the field of view [247, 253]. Thirdly, cargo specific for CME such as transferrin should be co-localised with the clathrin signal [251, 268].

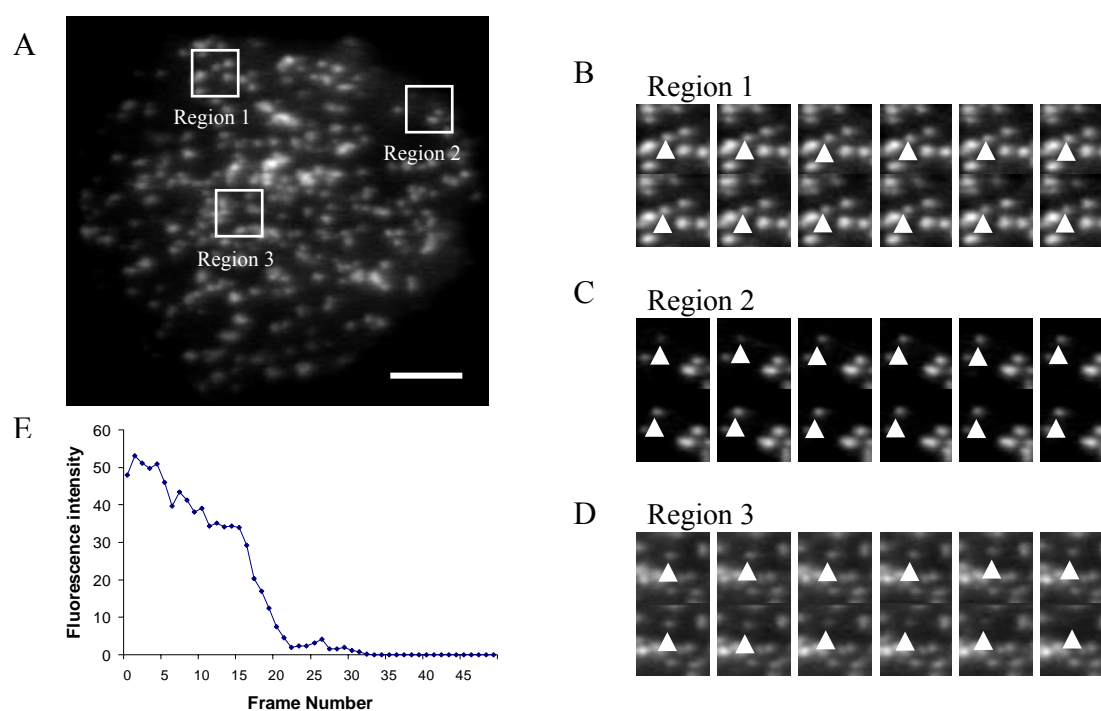


Figure 5.10 TIRF analysis of clathrin coated pit dynamics in 3T3 fibroblast cells

A) TIRF still image (from a sequence taken at 400 milliseconds per frame) demonstrating the presence of numerous EGFP-clathrin puncta. B) 12 sequential images taken from an image sequence of 50, enlarging region 1 from a. The image sequence depicts the lateral movement of the clathrin punctum marked by the arrowhead. C) 12 sequential images enlarging region 2 from a. These images depict the disappearance of the clathrin punctum marked by the arrowhead, presumably by internalisation. D) 12 sequential images enlarging region 3 from a, demonstrating the increasing fluorescence at the spot marked by the arrowhead. E) Quantification of the fluorescence associated with a single EGFP-clathrin punctum. Scale bar equals 10 μm .

5.4.3 Caveolae mediated endocytosis

At the outset of this study, it was planned to image particle uptake in a cell modified to express a GFP-clathrin protein and a Caveolin-1-DsRed protein. This would have greatly benefited the research since it would allow routes of endocytosis to be studied simultaneously, for example a specific size of particle may enter the cell through more than one mechanism even though one mechanism tends to dominate. Unfortunately, the development of the DsRed-Caveolin-1 protein was problematic and could not be expressed in the murine 3T3 cells. Some explanations for this are speculated on below.

The caveolin-1-DsRed protein was made through a fusion of the carboxyl terminus of the caveolin-1 gene into the amino terminus of the DsRed plasmid, i.e. a C-terminally tagged caveolin-1-DsRed. Pelkmans *et al* (2001) showed that even though both N- and C-terminally GFP-tagged caveolin-1 had the same overall distribution in living canine cells, the C-terminally GFP-tagged caveolin-1 allowed normal SV40 viral infection, whereas N-terminally tagged caveolin served as a dominant negative inhibitor, preventing uptake of SV40 into the cell [269]. This confirmed that the N-terminus of caveolin is crucial for caveolae mediated uptake processes. In a C-terminal fusion functional nucleotide sequences such as the Kozak and initiator sequences have to be engineered into the primers, however in an N-terminal fusion they are already contained in the plasmid. Several attempts were made to develop a caveolin-1-DsRed fusion using different primers and cloning strategies, however, each plasmid failed to express the protein in living cells.

5.5 Conclusions

An EGFP-clathrin LCa fusion protein was successfully developed and expressed in murine 3T3 cells. The TIRM/TIRF microscope, introduced in Chapter 4, enabled high resolution tracking of single clathrin punctum on the basal cell membrane. It was found that within a population of clathrin puncta, the majority were seen to be static whereas some were moving laterally and some also appeared and disappeared to and from the membrane. The clathrin coated pit dynamics in murine 3T3 cells visualised using TIRF, were found to be similar to those previously reported. It was found that the dynamics of clathrin could also be followed whilst sequentially imaging the basal cell membrane using the TIRM/TIRF microscope introduced in Chapter 4. This opens the possibility of for instance recording non-fluorescently any dynamic event occurring at the cell membrane (using the TIRM channel) whilst sequentially imaging individually protein dynamics within the cell (using the TIRF channel).

Chapter 6

Clathrin mediated particle endocytosis

6.1 Overview

In Chapter 1 the main mechanisms of endocytosis involved in the uptake of particles in mammalian cells were introduced. Chapter 5 then introduced the most widely studied mechanism, namely clathrin mediated endocytosis. The aim of this chapter is to determine the potential of TIRM for real-time imaging of endocytosis of nanoparticle drug delivery systems in living cells. In addition the use of a combination of TIRM/TIRF microscopy and EGFP-clathrin LCa expressing cells is examined for its potential use in determining whether various sizes of nanoparticles are endocytosed via the clathrin mediated pathway.

6.2 Introduction

So far, the most widely known and best characterised study on particulate endocytosis was performed by Rejman *et al* (2004) [43]. In this work the authors used a combination of pharmacological inhibitors of endocytosis, CLSM and fluorescence activated cell sorting (FACS) to investigate the effect of particle size (latex beads) on the mechanism of entry and subsequent intracellular fate in the non-phagocytic murine melanoma B16-F10 cells. This work revealed that the mechanism by which the beads were internalised and their subsequent intracellular routing, was strongly dependant on particle size. Internalisation of microspheres of diameter <200 nm involved CCPs, whereas with increasing size, a shift to a mechanism which relied on caveolae mediated endocytosis became the predominant pathway of entry for particles of 500 nm in size. This work provides useful insights into the dependence of cellular internalisation mechanisms on particle size, however, it does not provide evidence on the exact routes of endocytosis in these cells. The reasons for this are two-fold. Firstly, it is likely that for each particular particle size, there are a number of different uptake routes available to it [37]. Secondly, the pharmacological inhibitors used in the study suffer from a lack of specificity for the route they are probing [38].

6.3 Materials and methods

6.3.1 Cell labelling for confocal microscopy

A suspension of 3T3 cells was obtained by detaching and removing the cells from tissue culture flasks using 0.25 % trypsin/1 mM EDTA in PBS and placing in 10 ml DMEM. A cell suspension (1.5 ml) with a final concentration of 5×10^4 cells/ml was then added to each chamber of Lab-Tek II slides, and incubated for various lengths of time in a humidified incubator at 37 °C and 5 % CO₂. Cell Tracker Orange (Molecular Probes, Invitrogen, Oregon, USA) was added to the cells, as instructed by the accompanying data sheet, prior to addition of nanoparticles. Briefly, 9 µl DMSO was added to solubilise 50 µg of cell label. This solution was then diluted in serum free DMEM to achieve a final concentration of 10 mM. The cell label was pre-warmed to 37°C, added to the cells and incubated for 45 min. The label solution was then replaced with full cell culture media containing serum and incubated for a further 30 min. Cells were then fluorescently labelled and ready for addition of nanoparticle solutions.

6.3.2 Particle deposition for TIRM/TIRF uptake studies

35 mm glass based dishes (Iwaki, Japan) were coated with a 0.01% PLL solution for 15 minutes at room temperature. Following coating with PLL, the dishes were rinsed three times with distilled water and once with PBS. Particle adhesion to the PLL coated surface was achieved by adding 1 ml of a 0.016% w/v suspension of surfactant-free white carboxyl polystyrene spheres (Interfacial Dynamics Corporation (IDC), Eugene,

OR) to the dish for 30 minutes. The remaining suspension was subsequently removed and the dish was rinsed with PBS and dried O/N at room temperature. 100 nm gold particles were adhered to the PLL coated surface through the addition of a 1 ml suspension of gold nanoparticles (British Biocell International, Cardiff, UK) onto the surface for 1 hr. After this period, the substrate was rinsed three times with PBS and dried O/N at room temperature. 100 nm yellow/green fluospheres carboxylate modified microspheres (Invitrogen, Molecular Probes, Eugene, Oregon, USA) were adhered to the PLL coated surface through the addition of a 1 ml of a 0.002% w/v suspension of fluospheres onto the surface for 15 minutes. After this period, the substrate was rinsed three times with PBS.

6.3.3 Particle uptake for q(RT)²-PCR studies

3T3 cells were plated in a 6-well plate at a density of 2.5×10^5 cells per well in DMEM with FCS and incubated for 24 hrs at 37 °C. For 170 nm yellow-green carboxyl-modified fluospheres (2% w/v solids, Molecular Probes, Invitrogen, Oregon, USA), 5 μ l of suspension was added to 995 μ l of media, resulting in a concentration of 100 μ g / ml. For 2 μ m white carboxyl polystyrene spheres (4% solids, IDC, Eugene, OR), 2.5 μ l of suspension was added to 997.5 μ l of media to achieve a concentration of 100 μ g/ml [270]. After two hours, the cell media and particles were removed and the cells were washed five times with ice-cold PBS. Cells were then lysed using 1 ml of Lysis/Binding buffer per 10^7 cells (Miltenyi Biotec, Surrey, UK), and used for q(RT)²-PCR (Section 6.3.4)

6.3.4 Quantitative real time reverse transcriptase polymerase chain reaction (q(RT)²-PCR)

Forward and reverse PCR primers were created for each of the target genes. PCR reactions were built on ice and performed in a volume of 25 μ L, containing 13 μ L 2x iQ SYBR Green Supermix (Bio-Rad product containing 100 mM KCl, 40 mM Tris-HCl, pH 8.4, 0.4 mM of each dNTP (dATP, dCTP, dGTP and dTTP), iTaq DNA polymerase, 50 units/ml, 6 mM MgCl₂, SYBR Green I, 20 nM fluorescein, and stabilisers), 2 μ M pooled forward and reverse oligonucleotide primers for gene of interest (Table 6.1), 7.5 μ L RNase Free water and 2 μ L cDNA template (see Section 5.3.6.1 for production of cDNA using the lysed material from Section 6.3.3).

Table 6.1 PCR primers for the reference genes HPRT1 and RPL32 and the target gene clathrin used in the qRT²-PCR experiments

Oligonucleotide Name	Sequence (5'-3')
Mm Hprt1 SYBR For	AGTCCCAGCGTCGTGATTAG
Mm Hprt1 SYBR Rev	GGAATAAACACTTTTTCCAAATCCT
Mm Rpl32 SYBR For	GCAAGTTCCTGGTCCACAAT
Mm Rpl32 SYBR Rev	TTGTGAGCAATCTCAGCACA
Mm Cltc SYBR For	CATTCGCTTTCAGGAGCATC
Mm Cltc SYBR Rev	GCAGATGAATTTGTCTGACTCC

Amplification was carried out in a iCycler, Multicolor Real-Time PCR Detection System (Bio-Rad) using the following programme: 15 minutes at 95 °C, followed by 45 cycles of 15 seconds at 95 °C, 20 seconds at 60 °C and 20 seconds at 72 °C. Reactions were then subjected to 1 minute at 95 °C, 1 minute at 55 °C, then 70 cycles of 10 seconds at 58 °C with an increase of 0.5 °C per cycle, enabling melt curve data collection.

Amplification data were plotted for each q(RT)²-PCR reaction and used to calculate cycle threshold (CT) values, from which the difference in threshold cycles for the control and sample known as ΔCT were computed, by use of the Eq. 6.1 below. A negative ΔCT value indicates decreased target gene expression, whereas a positive ΔCT value denotes an increase in target gene expression.

$$\Delta CT_{target} = CT_{control} - CT_{sample} \quad (6.1)$$

To determine the fold change in the target gene the Northern equation (Eq. 6.2) was applied, where efficiency relates to the efficiency of the primer pair used. An Efficiency ΔCT ($E^{\Delta CT}$) >1 indicates a fold increase in the target gene expression, conversely an $E^{\Delta CT}$ <1 signifies the fold decrease in target gene expression.

$$\Delta Expression_{target} = Efficiency^{\Delta CT_{target}} \quad (6.2)$$

The Pfaffl equation (Eq. 6.3) [271] was used to calculate the relative expression ratio of a target gene in relation to an adequate reference gene hypoxanthine phosphoribosyltransferase (Hprt1) and ribosomal protein (Rpl32). A relative expression

ratio >1 indicates a fold increase in the target gene expression after normalisation against a reference gene, conversely a relative expression ratio <1 signifies the fold decrease in target gene expression after normalisation against a reference gene.

$$R = \frac{(\text{Efficiency}_{\text{target}})^{\Delta CT_{\text{target}}}}{(\text{Efficiency}_{\text{reference}})^{\Delta CT_{\text{reference}}}} \quad (6.3)$$

where R is the relative expression ratio.

6.3.5 Microscopy

6.3.5.1 Confocal laser scanning microscopy (CLSM)

A Leica confocal laser scanning microscope (CLSM) (SP2, Leica, Germany) was used for determining the cellular uptake and location of surface modified nanoparticles. A 63 x oil immersion objective lens (1.2 NA) was used during the studies. Yellow-green fluospheres were excited using the 488 nm argon laser line of the confocal microscope and fluorescence detected between 515 and 540 nm. Cell tracker orange was excited using the 543 nm laser line and fluorescence emission collected between 550 and 700 nm. For the purpose of cell localisation studies the microscope was set to image each dye sequentially. A series of optical sections (z-series) was recorded for each image by moving the focal plane step by step through the sample depth. The series of optical sections were examined using the associated software (Leica Confocal Software Version 1.2).

6.3.5.2 Scanning electron microscopy (SEM)

For SEM, samples were fixed in 3% glutaraldehyde in 0.1M sodium cacodylate buffer, pH 7.3, for 2-3 hours. The samples were then washed in 3 X 10 minute changes of 0.1M sodium cacodylate buffer. Specimens were then post-fixed in 1% osmium tetroxide in 0.1M sodium cacodylate buffer for 45 minutes, prior to being washed in three 10 minute changes of 0.1M sodium cacodylate buffer. The samples were then dehydrated in 50%, 70%, 90% and 100% normal grade acetone for 10 minutes each, then for a further two 10 minute changes in analar acetone. Dehydrated samples were then critical point dried, mounted on aluminium stubs and sputter coated with gold palladium.

6.3.6 Image analysis

For overlaying of TIRM and TIRF images, they were first streamed to a kinetic image disc on a PC (Dell, UK). The images from each channel (TIRM and TIRF) were then imported into ImageJ as an image sequence. 16-bit images were converted to RGB images. The RGB images were false coloured using the look-up table (LUT) function on ImageJ. TIRF images were pseudo-coloured green for EGFP-clathrin and TIRM images underwent an inverse LUT prior to a red LUT being applied. The image sequences were overlaid using the image calculator function in ImageJ and adding the images together. The resulting combination image was finally cropped and saved as an Avi file.

6.4 Results and discussion

6.4.1 Particle – cell interactions

The classical experimental model for studying nanoparticle endocytosis involves the addition of a nanoparticle suspension, at a specific concentration, to the cell media for a set length of time, followed by cellular fixation and quantification of uptake (e.g. using fluorescence microscopy, cytometry, spectroscopy etc.) [43]. This model is relatively simple to setup and has been performed in numerous studies [43, 272-275]. However, since most of the particle uptake in such an experimental setup occurs through the apical cell membrane it makes imaging endocytosis events using TIRM/TIRF difficult. TIRM/TIRF is used for imaging the basal cell membrane and hence requires a different way of presenting particles to cells. Sufficiently small particles could be used since they may diffuse underneath the basal membrane and be internalised. For example, Ewers *et al* (2006) studied the internalisation of murine polyoma viral like particles (VLPs) through the basal cell membrane of 3T6 fibroblast cells using TIRF microscopy [276]. In this study the authors found that when a solution of VLPs was added to the cells, after 15 minutes the VLPs drifted into the narrow space between the bottom surface of the cell and the coverslip and could be visualised by TIRF as rapidly moving, blurred fluorescent objects. However, once bound to the basal cell membrane, they appeared as uniform, bright spots that were either stationary or moving laterally. The authors also concluded that VLPs did not begin to be internalised until approximately 45 minutes following addition to the cell culture. Although this approach is very useful for studying smaller particles such as viruses, it precludes the ability for studying larger particles,

due to steric hindrance effects. Ultimately a new experimental design was needed to enable application of TIRM/TIRF to imaging of a range of particle sizes which are undergoing endocytosis via the basal cell membrane.

Polymeric nanoparticles of small size and low density will be in a state of Brownian motion in a liquid medium rather than sediment to the surface. Particles can be easily visualised using TIRM in this state and are seen to move in and out of the evanescent field. In time-lapse TIRM, Brownian motion is represented by the rapid movement of white spots in and out of the image frame, as shown in Fig. 6.1 (yellow arrows). These series of images are taken from a TIRM time-lapse video sequence of 1 μm carboxyl particles added to a PLL coated coverslip. The most likely explanation for the objects appearing white is due to a combination of them reflecting light towards the objective and also due to the fact that they are out of focus. When 1 μm carboxyl modified particles are added to a bare glass coverslip they do not adhere to the surface. However, when added to a PLL coated coverslip they quickly adhere onto the surface, as represented by the yellow and red arrows in Fig. 6.1.

In this study, polystyrene particles were adhered to a PLL coated surface via an electrostatic interaction between the carboxyl groups on the surface of the particle and the amino groups of PLL, as schematically illustrated in Fig. 6.2, and shown experimentally in Fig. 6.1 & 6.3. This approach has also recently been applied by Alberola and Radler (2009) who, seemingly at the same time as our studies, were utilising electrostatic interactions between the particle and the substrate to define the presentation of particles (quantum dots in Alberola's case) to BEAS-2B cells [277]. A key benefit of this approach is that it affords the ability to track the movement of single particles with time.

TIRM has been used to visualise the adherence of 300 nm and 1 μm carboxyl modified white polystyrene particles, as shown in Fig. 6.3a and b respectively. The number of particles attached to the surface and the spacing between them can be controlled by varying the length of time of interaction between the particles and the surface and/or changing the ionic strength of the buffer which causes an increase or decrease of the electrostatic interactions between particles and the substrate [278].

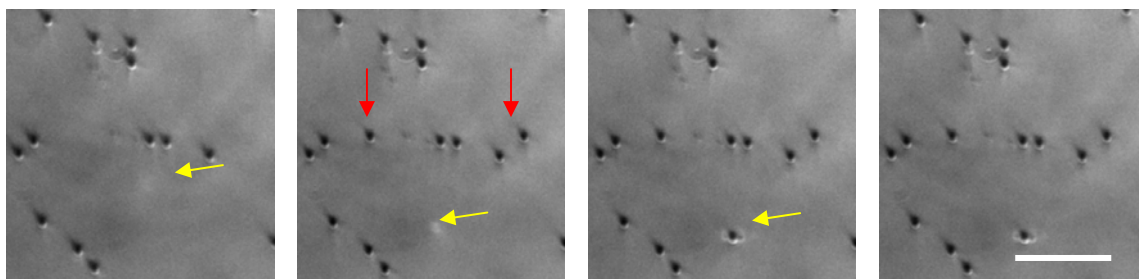


Figure 6.1 TIRM image of polystyrene particles undergoing Brownian motion and adhesion to PLL coated substrate

Each frame represents 1 second. The Brownian motion and subsequent deposition of one particle is highlighted by the yellow arrows. Particle adherence is shown by the red arrows. Scale bar = 10 μm

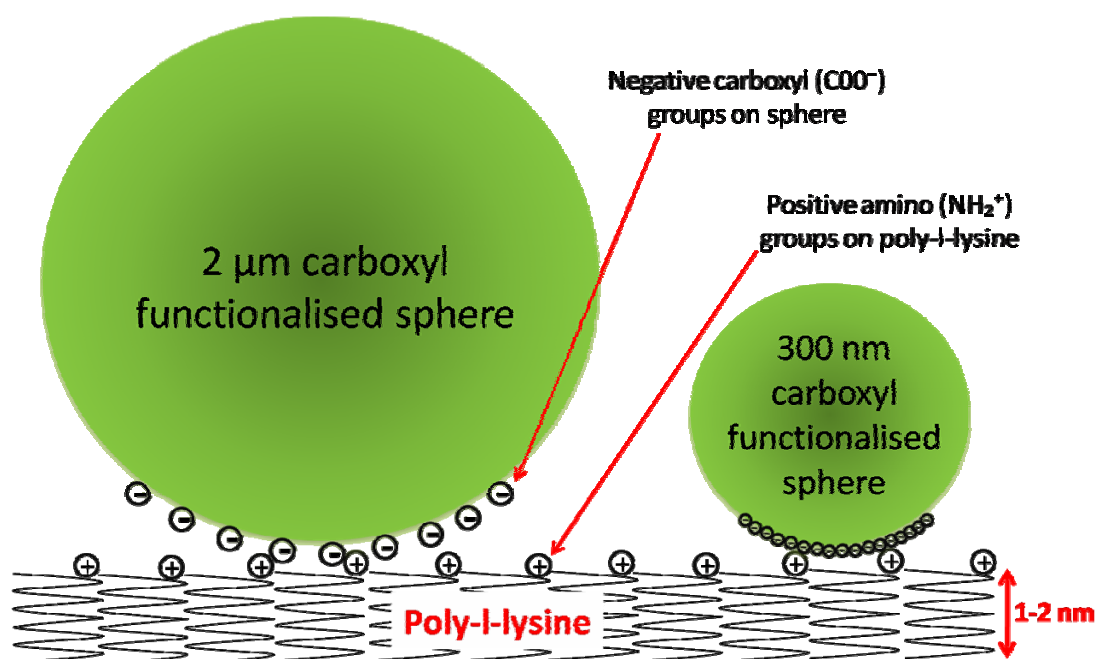


Figure 6.2 Schematic representation of the adherence of white carboxyl polystyrene spheres to a PLL coated coverslip

The PLL solution forms a very thin (1-2 nm) layer on the surface of the coverslip. PLL contains positive amino groups which are available on the surface of (and within) the thin layer for interaction with other molecules. As particles approach the PLL layer either through sedimentation, in the case of 2 μm particles, or through Brownian motion, in the case of 300 nm particles, their surface negatively charged carboxyl groups undergo an electrostatic interaction with the positive amino groups of PLL. This results in the adherence of the particles to the coverslip surface. Note the surface charge of the 300 nm particles is greater (19.5 μEq/g) compared with the 2 μm particles (3.3 μEq/g). This may result in greater adherence to the PLL coated surface for the 300 nm particles. Not drawn to scale.

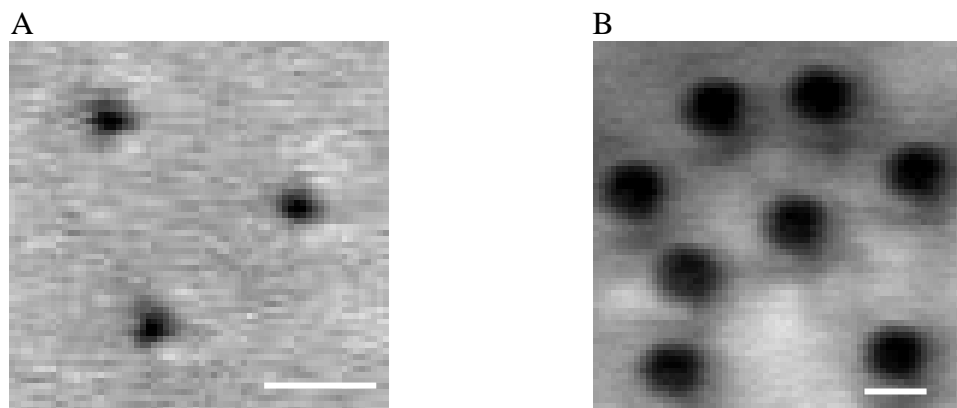


Figure 6.3 TIRM images showing the adherence of white carboxyl polystyrene spheres to a PLL coated coverslip

A) Dark areas represent the adherence of 300 nm and B) 1 μm polystyrene spheres to a PLL coated coverslip. Scale bar represents 1 μm .

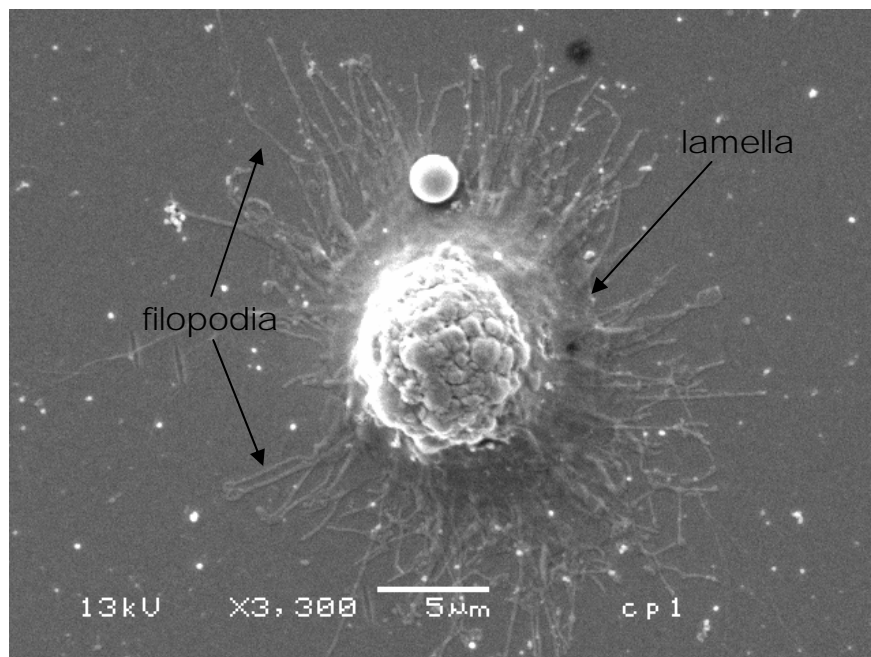
Following successful adhesion of particles onto the surface of the coverslip it was then important to determine whether cells would successfully adhere to the PLL-particle coated surface. The scanning electron micrographs (Fig. 6.4 – 6.5) illustrate the interaction of a 3T3 fibroblast cell with 2 μm polystyrene particles adhered to a PLL-coated surface. The image in Fig. 6.4a shows the interaction of a cell incubated with a 2 μm particle for 30 minutes. It can be seen that the cell is still spherical in nature due to the short length of time it was exposed to the surface and that many protrusions (lamellipodial and filopodia) are present. Some of these protrusions appear in the initial stages of the interaction with the particle. Figure 6.4b shows the interaction between particle and cell at a more advanced stage of the internalisation process. The image shows that the cell membrane is beginning to cover over the two particles, indicating the initial stages of internalisation. At higher magnification (Figure 6.5), membrane invagination around the particles is visible. SEM images demonstrate that not only do

the cells adhere to the PLL coated substrate, but also particles and cells interact in this experimental setup.

A major advantage of presenting the particles to the cells as described here and by the Rädler group is that the particles do not suffer from aggregation, which can occur in many of the more ‘traditional’ studies [213]. Particle aggregation can occur in the medium used to conduct the experiment due to the relatively high (physiological) salt concentration. This aggregation can be problematic since the particles presented to the cells do not accurately reflect the original particle size, shape and surface charge, thus making any conclusions regarding the mechanism of uptake difficult.

An experimental setup, with many similarities to the ‘reverse uptake’ configuration, has been used to control the delivery of DNA from polymer coated substrates into living cells, through substrate mediated delivery [279-284]. In substrate-mediated delivery, also termed ‘reverse transfection’ or solid-phase delivery, plasmid DNA or DNA complexes are immobilised to a surface or biomaterial that supports cell adhesion. Placing the DNA directly in the cellular microenvironment increases its local concentration, which has been shown to enhance gene delivery [284]. Cells subsequently cultured on the substrate can internalise the DNA either directly from the surface, or after release of the DNA from the surface.

A



B

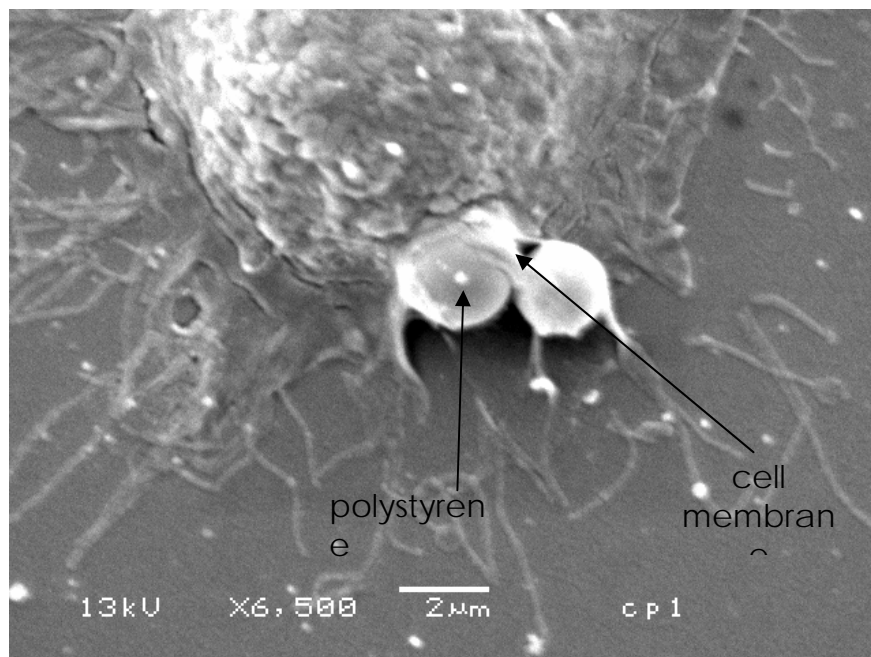


Figure 6.4 SEM images of 2 µm polystyrene beads undergoing internalisation by a 3T3 fibroblast cell

a) Membrane and filopodia of a 3T3 cell at the initial stages of interaction with a 2 µm particle. The cells were incubated with particles for 1 hour followed by fixation. The spherical nature of the cells owes to the short period of time the cells were incubated on the PLL coated surface. b) Two particles at a later stage of internalisation by the cell. It can be seen that the membrane is now beginning to engulf the particles and endocytose them.

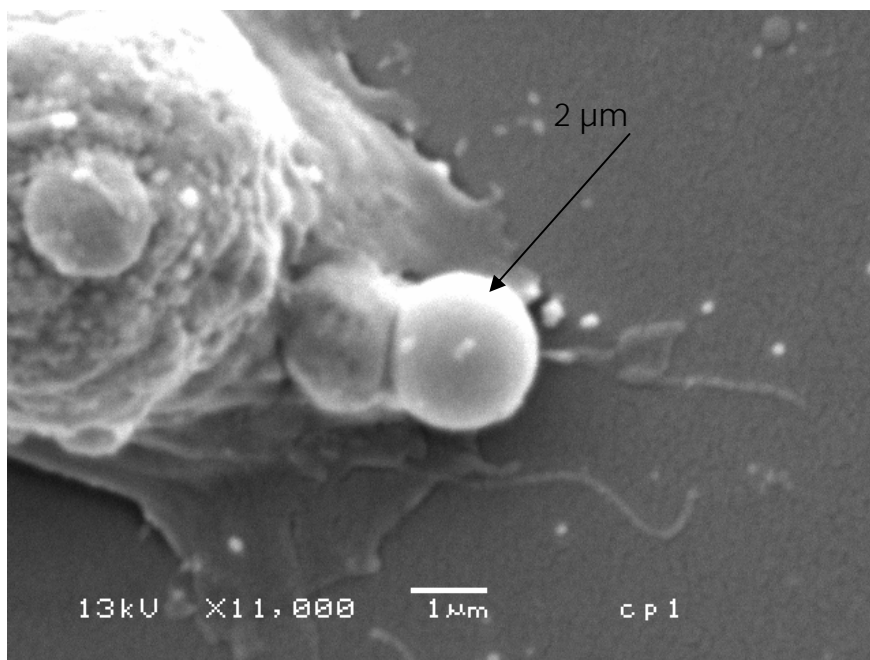


Figure 6.5 SEM images of 2 µm polystyrene beads undergoing internalisation by a 3T3 fibroblast cell

This higher magnification image clearly shows membrane invagination around the particle.

6.4.2 TIRM imaging of particle endocytosis

TIRM is an attractive technique for studying particle uptake by living cells due to its high spatial and temporal resolution, allow for visualisation of single particle uptake. Polymeric particles such as polystyrene and PLGA can be easily visualised down to a size of approximately 300 nm without the need for a fluorescent label, as demonstrated in Fig. 6.3a. Particles with a higher scattering index, such as metallic nanoparticles, can be seen easily viewed, even at a size of approximately 100 nm (this is the case for gold nanoparticles (Fig. 6.6a)). It is noticeable that the 100 nm gold image is almost an inverse image of what is expected in TIRM. Normally, when imaging cell membranes and polystyrene particles for example, dark areas represent the presence of objects in the evanescent field (Fig. 6.1, Fig. 6.3), due to light scattering, as discussed in Chapter 2. For gold, it is clear that there is some other phenomenon being exhibited in the image which predominates the light scattering signal. It is most likely than for TIRM visualisation of metallic nanoparticles such as gold, there is a large reflected light signal being imaged [285]. A TIRM image of 100 nm polystyrene particles is included in Fig.6.6b for comparison to the 100 nm gold image. Three particles are highlighted by the red circles. Clearly, the sensitivity of TIRM for the visualisation of small polymeric nanoparticles is much less than that for metallic nanoparticles such as gold. This is predominately due to the lower scattering power (and reflectivity) of polymeric particles. Indeed, TIRF was performed on the sample, to ensure that the particles were actually present in the field and the black spots were not just artefacts of the imaging process (Fig. 6.6c).

It is important to stress that the major strength of TIRM is that the sample, in this case colloidal drug delivery particles, do not need to be fluorescently labelled to enable them to be imaged. Introducing a label into a nanosystem can be extremely time consuming, costly and may result in phototoxicity due to leaching of the dye. Thus any method which circumvents the need for fluorescent labelling is a major advantage to researchers in this field. It opens the possibility for cell internalisation screening of any type of novel particulate drug delivery device for their endocytosis in living cells. A disadvantage of TIRM arises from the difficulty to image particles from made polymeric materials <100 nm in diameter—due to the low scattering power of these particles—which make up a considerable proportion of the investigated drug and gene delivery systems. However, for the numerous systems above this size range, TIRM can be very useful indeed.

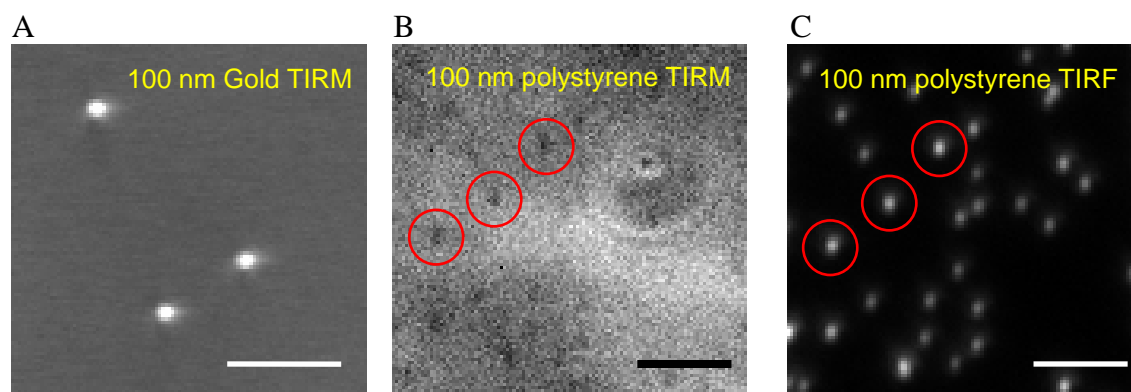


Figure 6.6 TIRM/TIRF images of 100 nm particles.

A) TIRM image of 100 nm colloidal gold attached to a PLL coated coverslip. B) TIRM image of 100 nm carboxyl modified polystyrene particles adhered to a PLL coated coverslip. Three particles are highlighted by the red circles. C) TIRF image of the same sample as that used in B). The same three particles are highlighted by red circles to confirm the presence of the particles in the TIRM image. It can be seen that there are some particles which are clearly visible in the TIRF image are not present in the associated TIRM image. Scale bar represents 1 μm .

The use of TIRM for visualising the cellular internalisation of 500 nm and 2 μm polystyrene particles is shown in Fig. 6.7. In this experiment, the particles have been adhered to the PLL coated substrate as described above (Section 6.3.3), followed by addition of a 3T3 cell suspension. Using TIRM, the process of a cells descent to the substrate and its adherence over a period of approximately 10 minutes from the beginning of the experiment was imaged. The uptake of 2 μm particles by living 3T3 fibroblasts is indicated by the arrows in Fig. 6.7a, and the uptake of 500 nm particles is highlighted by the black arrows in Fig. 6.7b. The images, taken from a typical TIRM series over a period of 10 minutes, have a delay of 10 seconds between each frame. A single particle is seen to disappear between frames one and two, with a further three particles disappearing between frames two and three. There are two possible explanations to explain the disappearance of particles in the TIRM images. Firstly, the cells residing on top of the particles are actively internalising them or secondly, the particles are simply being swept out of evanescent field by movement of the cell membrane.

To test the hypothesis that the particles are being internalised into the cell, identical experimental condition were used, however the particles were fluorescently labelled compared with the standard white non-fluorescent particles used in all other experiments. The optical sectioning capability of the confocal microscope affords the ability to reveal whether particles are inside or outside the cell membrane if the correct fluorescent dyes are used. Cell tracker orange, a chloromethyl derivative that freely diffuses through the membrane of live cells, was excited with the 543 nm laser line and was used to label the cell. Once inside the cell, the dye is believed to undergo a

glutathione *S*-transferase mediated reaction, producing a membrane impermanent glutathione-fluorescent dye adduct. Yellow-Green emitting Fluospheres were used as a model particulate system and illuminated with the 488 nm laser line of the confocal microscope.

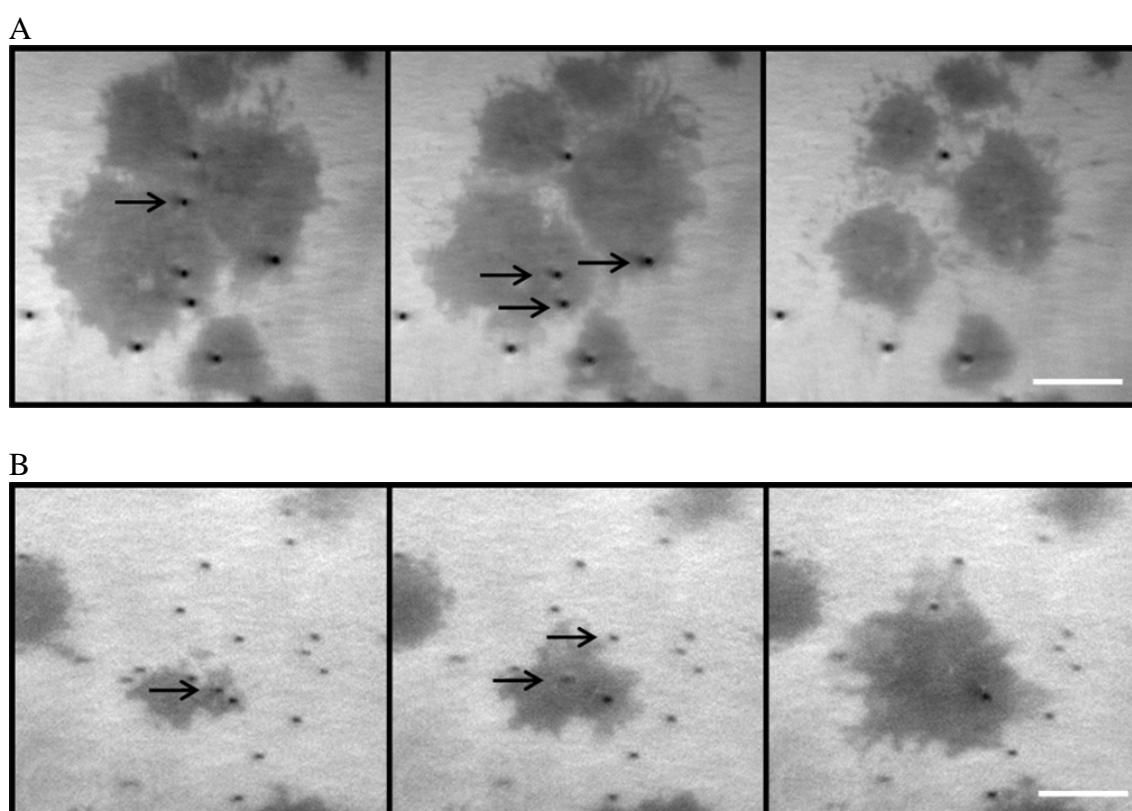


Figure 6.7 TIRM image series depicting the uptake of colloidal particles

Series of images taken from a typical TIRM time-lapse sequence of 3T3 fibroblast cells taking up (a) 2 μm and (b) 500 nm carboxylate modified latex particles by endocytosis. Arrows indicate particles internalised by the cells. There is a 10 second interval between each frame in a) and a 30 second interval between each frame in b). Scale bar represents 20 μm .

Figure 6.8 is a representative z-stack, demonstrating the interaction of fluospheres with living cells in the 'reverse uptake' experimental configuration. The green puncta in the bottom right-hand corner (Fig. 6.8) represent the adhesion profile of 2 μm yellow-green fluospheres to the surface of a PLL coated coverslip. The remaining image in this figure is a z-stack taken 30 minutes following addition of a cell suspension. The maximum projection xy image show that the cells are interacting with a number of particles. Looking at a cross-section through the cell, xz and yz , at the position marked by the arrow, it is possible to see that this particle is indeed present within the cell membrane. This experiment has demonstrated that particles presented to the cell in the 'reverse uptake' configuration are indeed internalised, a finding also made by the Radler group [277]. Therefore it is within reason to conclude that those particles which are seen to disappear in the TIRM image are indeed being internalised by the cell.

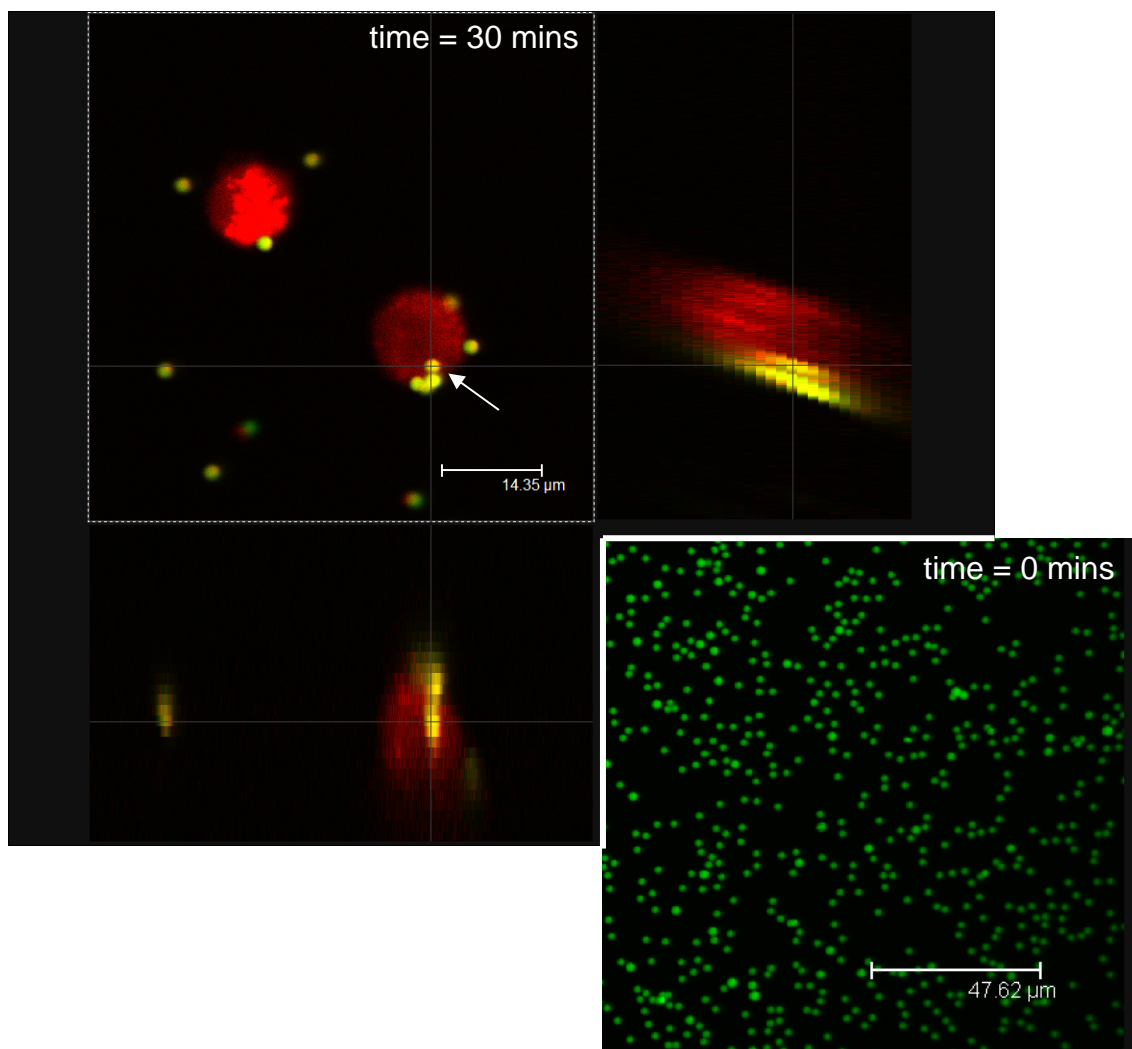


Figure 6.8 Z-stack confocal micrograph illustrating the uptake of 2 μm polystyrene spheres by 3T3 fibroblast cells

Cells are labelled with cell tracker orange solution. Beads used are 2 μm carboxylated yellow-green fluospheres. The green puncta seen in the image in the bottom right hand corner represent 2 μm particles which have adhered to the PLL coated coverslip prior to cell addition. Thirty minutes after addition of living cells, a representative image such as that seen in the top left-hand corner is seen. The 2-dimensional xy image shows that particles are interacting with the cell membrane. The xz and yz images demonstrate that the particle is found inside the cell and is not simply adhered to the cell membrane.

The cost and potential phototoxicity associated with fluorescent labelling makes the method of ‘reverse particle uptake’ in combination with TIRM very appealing for researchers who want to quickly ascertain whether their particulate drug delivery system is internalised by the cell. Indeed, this is the first reported use of optical microscopy for following the dynamics of nanoparticle internalisation in living cells. However, there are a number of questions that the application of this method poses. Firstly, adhering the particle of interest to the PLL-coated surface may impact upon its subsequent extent and mechanism of internalisation. Secondly, the uptake at the basal cell membrane may be different from uptake at the apical membrane, particularly if the technique is applied to study polarised cells where one would need to modify the experimental design. Thirdly, the method offers no insight into the mechanism of endocytosis apart from the determination of whether the particle is internalised or not. It is clear that further work is needed to study the differences between particle uptake at the apical and basal cell membrane. This work, however, is not part of the current study.

To address the issue of elucidating the mechanism of particle endocytosis while using TIRM, it was decided to construct a fluorescence channel onto the existing microscope setup to monitor fluorescently labelled cellular structures while conducting TIRM experiments (Chapter 4 describes development of the TIRM/TIRF microscope, while development of a fluorescently labelled clathrin molecule is described in Chapter 5). It was speculated that by combining these two imaging elements, namely the TIRM/TIRF microscope on non-fluorescent particles and EGFP-clathrin expressing cells, it would be possible to elucidate if indeed particle endocytosis proceeds via a clathrin mediated pathway. Indeed, through the use of other fluorescently tagged endocytic proteins such

as caveolin and flotillin it may be possible to follow other mechanisms of endocytosis, utilising TIRM/TIRF.

It should be noted there are currently many antibodies available which can be used to detect specific endocytic proteins within the cell such as clathrin [286], caveolin-1 [287] and flotillin [288]. These would be considerably easier to use than developing EGFP constructs. However, in this study they have not been utilised for several reasons. Firstly, TIRF imaging is used predominately for imaging living cells, and antibodies are normally applied to fixed cells. It would not be advantageous to apply TIRF to fixed cell imaging, but even if one attempts so, the RI of the fixative is too high to allow generation of the EW in the coverslip. Secondly, in the present work, the focus was to utilise the existing TIRM setup which enables label-free detection of the particulate system, and combine with a fluorescence channel to detect the endocytic marker of interest. There were a few options considered to introduce the fluorescence imaging option into the current TIRM system. Epifluorescence microscopy does not afford great axial resolution [289] and confocal microscopy is technically too difficult to implement at this stage of development. It was hence decided to use TIRF, since it is relatively simple to combine with TIRM (as discussed in Chapter 4) which in turn excludes using antibodies for the reasons outlined above.

6.4.3 Combined TIRM/TIRF microscopy of nanoparticle endocytosis

One of the limitations, mentioned previously, of using the TIR microscope for studying particle uptake is that it does not provide information on the mechanisms of particle uptake. In Chapter 4, it has been shown how a combined TIRM/TIRF microscope can be used to follow events *label-free* at the cell membrane, while at the same time recording a fluorescence image. Chapter 5 introduces a cell line stably expressing an EGFP-tagged clathrin LCa protein which could be successfully visualised using TIRF microscopy. At this stage in the work, by applying TIRM/TIRF microscopy and the EGFP-clathrin LCa expressing cell line to the ‘reverse particle uptake’ experimental design, an entirely new way to gain insight into clathrin mediated particle endocytosis in living cells is achieved.

Figure 6.9a is an image of a 3T3 cell expressing EGFP-clathrin taken using the TIRF channel of the TIRM/TIRF microscope. In Fig. 6.9b, TIRM has been used to image 500 nm particles adhered to a PLL coated coverslip. It is important to note that this image was generated using *label-free* TIRM and has been false-coloured red (as described in section 6.3.6) to aid co-localisation analysis when TIRM and TIRF images are overlaid. An overlay of the TIRM and TIRF images is presented in Fig. 6.9c. A magnified section of this image is shown in Fig. 6.9d. The co-localisation of clathrin with 500 nm particles is denoted by the presence of yellow puncta in the overlaid image (marked by the arrowhead). Image analysis reveals that there are a total of 35 particles

adhered to the PLL coated surface which are presented to the basal cell membrane. Of these, 13 particles (37%) are co-localised with EGFP-clathrin.

One of the benefits of using the TIRM/TIRF system for co-localisation analysis over current techniques stems from the fact that only one fluorescent marker is used to follow two separate events, since the particles can be imaged *label-free*. When two or more fluorescent dyes are used in fluorescent microscopy there is an increased chance that artefacts may arise. For example, given the broad excitation and emission spectra of some fluorophores, each fluorophore can be excited by the same wavelength and exhibit overlapping emission. These overlaps can result in confusing crosstalk or bleed-through between signals associated with different fluorophores in the same sample [290]. Generally, this can be somewhat overcome through the careful use of specialist dichroic mirrors and emission filters. However, even though this reduces the chances of artefact generation, it can never completely abolish them. An additional effect of using these types of mirrors and filters is that it reduces the resulting signal from the fluorophore of interest, which is problematic when imaging dim objects such as EGFP [291].

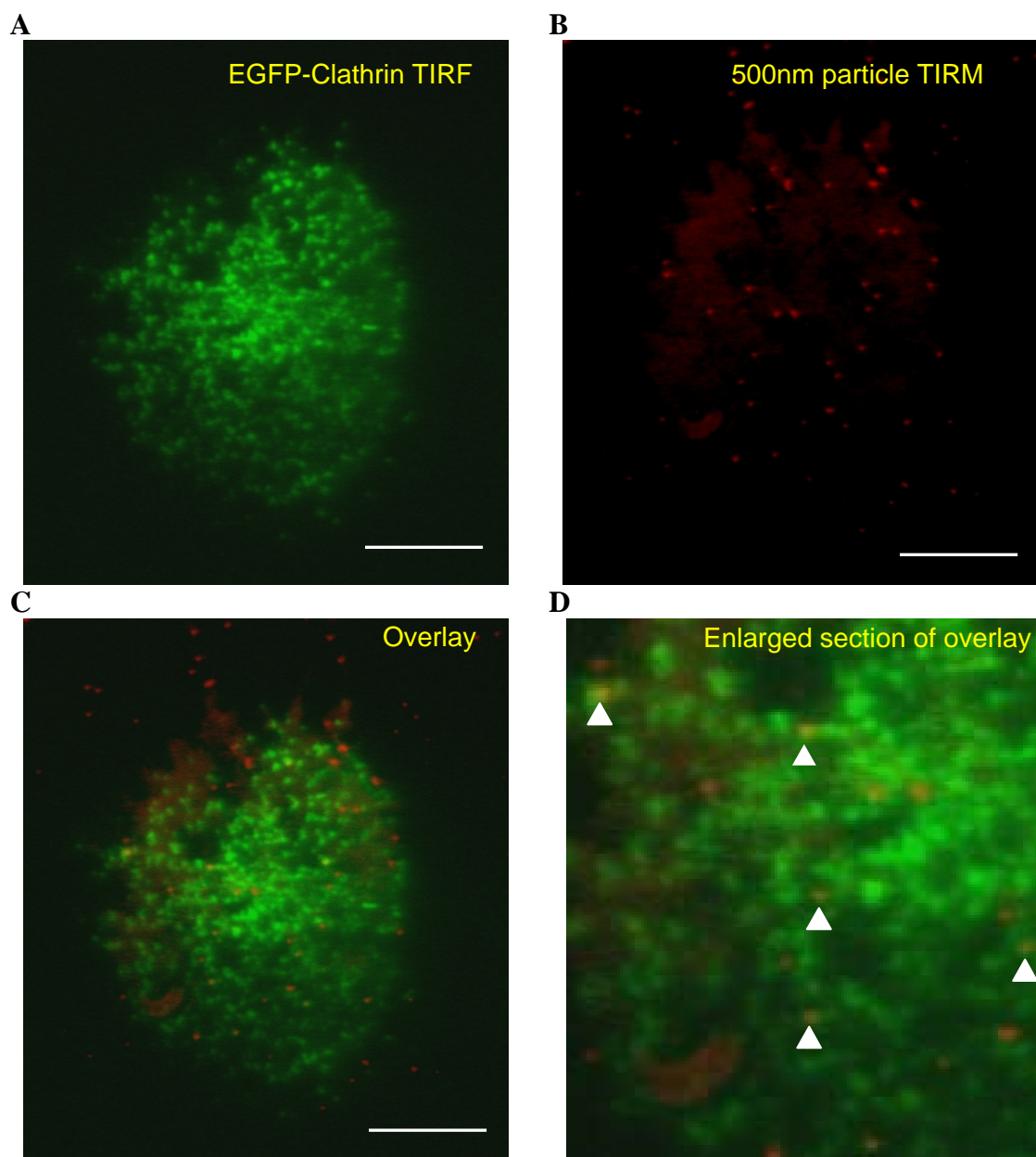


Figure 6.9 Low magnification TIRM/TIRF imaging of 0.5 μm particles undergoing endocytosis by EGFP-clathrin Lca labelled 3T3 cells

A) TIRF image of EGFP-clathrin Lca. B) *Label-free* TIRM image of 500 nm carboxyl modified polystyrene particle adhered to the surface of a PLL coated substrate. Image has had an inverse red LUT applied to aid co-localisation studies. C) Overlay of the TIRF and TIRM images. D) Magnified portion from the overlaid image. Note the presence of yellow puncta (highlighted by the white triangles) which represent the co-localisation of EGFP-clathrin and the 500 nm particle. Scale bar represents 15 μm .

The first studies of particle endocytosis by living cells using TIRM/TIRF microscopy are illustrated in Figure 6.10. In this study, the uptake of 0.5 μm and 1 μm particles was visualised using the TIRM/TIRF microscope and the EGFP-clathrin LCa expressing cell line. Experimental conditions remained the same as before, with particles first adhered to the substrate followed by addition of the cell suspension. The imaging involved capturing of a TIRM image, followed within one second by capture of a TIRF image.

The uptake of 500 nm particles is shown in Fig. 6.10a-c. Figure 6.10a is a series of 12 sequential TIRM images of a 500 nm particle taken from a sequence of 100, at 2 minutes per frame showing the internalisation of the particle. The EGFP-clathrin signal captured at this exact location is shown in Fig. 6.10b. In the centre of the frame a gradual increase in the intensity of an EGFP-clathrin punctum is evident between frames 5 – 7 which is followed by a sudden loss in the fluorescent signal. Figure 6.10c is the result of the TIRM and TIRF images being overlaid. An increase in yellow intensity between frames 5-7 demonstrates the co-localisation of the EGFP-clathrin (TIRF) with the 500 nm particle (TIRM). The green (EGFP), red (particle) and thus yellow (overlay) signal all decrease after frame 8 indicating that the particle has been internalised by the cell.

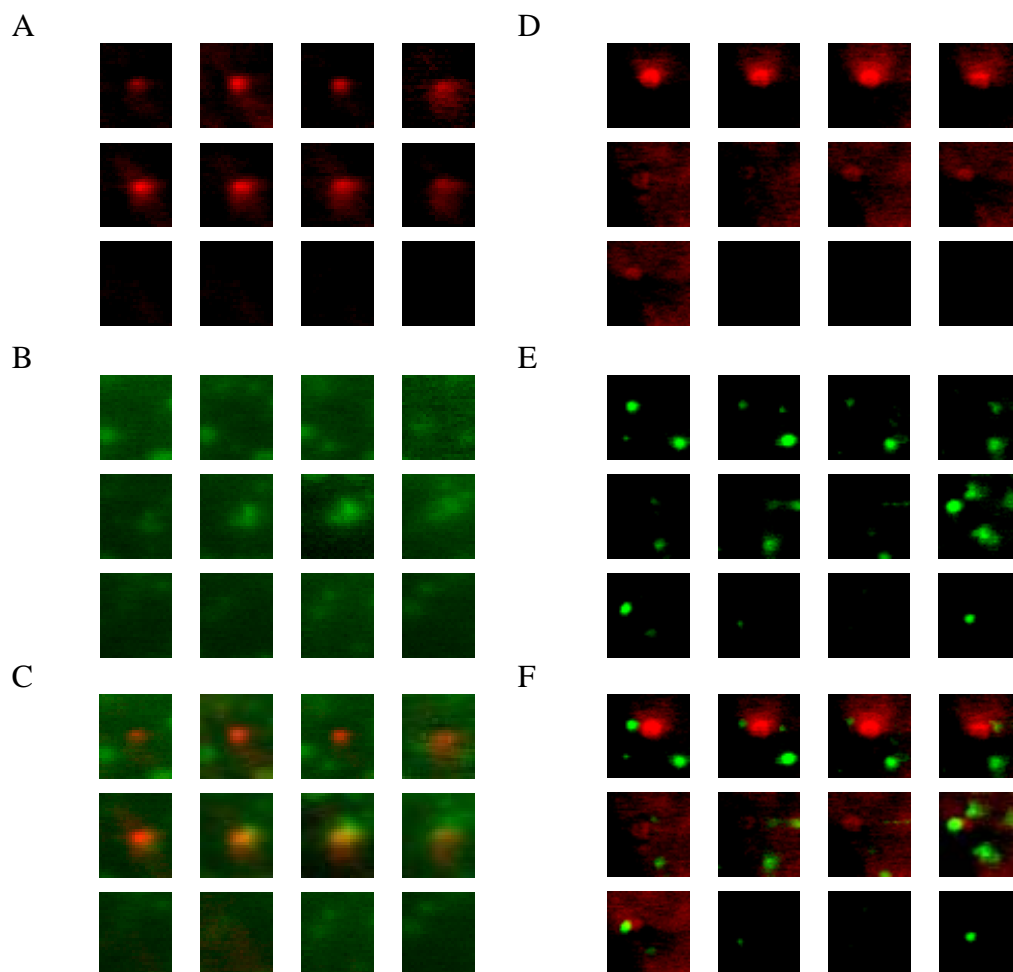


Figure 6.10 TIRM/TIRF images of polystyrene latex endocytosis by 3T3 cells expressing EGFP-Clathrin ($n = 3$)

Cellular Uptake of 500 nm (A-C) and 1 μm polystyrene particles (D-F).

A) 12 sequential TIRM images of a 500 nm particle taken from a sequence of 100, at 2 minutes per frame. The particle is seen to be internalised over the time-course of the experiment which is 24 minutes in total. Images have been pseudo-coloured red and inverted to aid co-localisation analysis. B) 12 sequential TIRF images of EGFP-Clathrin LCa taken from a sequence of 100, at 2 minutes per frame. The clathrin is observed to increase in intensity between frames 5-7, i.e. over a period of 6 minutes. Images are pseudo-coloured green. C) Overlay of TIRM and TIRF images. Frames 5-8 show co-localisation of clathrin and 500 nm particle. D) 12 sequential TIRM images of a 1 μm particle taken from a sequence of 100, at 2 minutes per frame. The particle is seen to be internalised over the time-course of the experiment which is 24 minutes in total. E) 12 sequential TIRF images of EGFP-Clathrin LCa taken from a sequence of 100, at 2 minutes per frame. The image sequence depicts movement of clathrin puncta. F) Overlay of TIRM and TIRF images. Although clathrin can be seen to be in close proximity to the particle there is no co-localisation like that seen with the 500 nm particle.

The gradual increase in EGFP-clathrin intensity followed by a sudden disappearance was also seen in cells not exposed to nanoparticles (Fig. 5.10). Such observations could arise for two reasons. Firstly, in living cells there is a small percentage of clathrin puncta which seemingly form at random sites on the plasma membrane [247]. It is possible that in the present study there has been random localisation of clathrin at the exact site where the particle resides. However, it is unlikely that the clathrin signal randomly initiates where the particle is localised. It is more likely that the clathrin has been recruited here due to the presence of the particle [255, 292]. In the ‘reverse uptake’ configuration the particles cannot ‘actively target’ static CCPs since they are bound to the PLL substrate. In classical uptake studies, where the particle is endocytosed from the bulk solution *via* the apical surface, the particle may ‘surf’ across the surface [43] before actually binding to it and being internalised. In contrast however, our experimental setup substantially restricts any movement and consequently preferential binding of the particle to a specific cell membrane region. In summary, it appears highly likely that the presence of the particle results in recruitment of clathrin to the site.

The correlation of the EGFP-clathrin fluorescent signal with the TIRM signal of the particle suggests that the particle is being internalised *via* CCPs. The time between each sequential frame presented in Fig. 6.10 is 2 minutes, implying that the time taken from the initial recruitment of clathrin to the particle site, up to the internalisation event is approximately 6 minutes. This result represents the first reported direct visualisation using optical microscopy of clathrin mediated endocytosis of 500 nm particles. The most similar work to our which has been reported has looked at the internalisation of the influenza virus by BS-C-1 expressing EYFP-clathrin [293]. This work was performed

using epi-fluorescence microscopy and looked at virus uptake on the apical cell membrane. Similar to the uptake of 500 nm particles seen here, Rust *et al* (2004) unexpectedly found that the majority of virus particles were internalised via *de novo* formation of CCPs and not pre-existing CCPs as originally thought. During virus endocytosis, the clathrin signal persists for approximately 70 seconds prior to internalisation. This is considerably shorter than observed for the internalisation of 500 nm particles (~3-6 minutes) in this work. This period of clathrin persistence represents the time needed for the cell to recruit sufficient clathrin to the site to enable formation of a CCP for particle internalisation. The increasing EGFP-clathrin signal in Fig. 6.10b represents accumulation of clathrin to the endocytic site. Following the recruitment of clathrin to form a CCP, it is likely that the CCP pinches off to form a CCV; represented by the rapid disappearance of the clathrin signal from the TIRF images.

The described clathrin mediated uptake of 500 nm particles is however unexpected, with reports of such an event limited [43]. Moreover, the size of a CCP is approximately 160 nm in mammalian cells [235] which is much smaller than the 500 nm particle believed to be contained within it in this work. Recent work [43] reports that the majority of 500 nm particles were internalised via a caveolae mediated pathway. However, there are a number of differences between that and the present study, primarily including the different cell types used (melanoma B16_F10 vs. 3T3 fibroblast in the present study) and different experimental approaches to study endocytosis. The work by Rejman and colleagues utilises pharmacological inhibitors of endocytosis and confocal co-localisation analysis with caveolin-1 to determine the route of entry of nanoparticles. Previously it has been discussed how the various pharmacological

inhibitors of clathrin such as potassium depletion and hypertonic sucrose [38] can vary in their specificity for blockage of the clathrin-mediated route. Thus, even though the results presented in this chapter differentiate from that reported previously [43], it may be accounted for by the differences in the experimental conditions used.

Another question which these results present is whether or not CCPs can actually internalise a particle of 500 nm diameter. A model proposed by Ehrlich *et al* (2004) [255] suggests that the size of the coated vesicle, and hence the design of its clathrin lattice and the time it takes to achieve its final form, is determined by the size of the cargo, up to a certain limit. Our results have demonstrated that the time of clathrin accumulation for 500 nm particles is larger than in previous studies [255, 293], thus indicating that a larger lattice structure may potentially be being built to enable the particle to be internalised.

The cellular interaction of a 1 μm particle is shown in Figure 6.10d-f. The TIRM images (Fig. 6.10d) show that the particle is internalised between frames 4 – 5. The EGFP-clathrin fluorescence signal can be seen to move laterally (Figure 6.10e), however it is not co-localised with the particle (Fig. 6.10f). Even though a clathrin signal is observed in close proximity to the particle site, it does not completely surround the particle as is the case for internalisation of the 500 nm particle (Fig. 6.10c). The lack of co-localisation of the clathrin fluorescence signal and the 1 μm particle signals thus indicates that these larger particles are potentially being internalised via a clathrin independent mechanism.

Another point which needs addressing from these results is whether it is possible evanescent light scattered by the particle will be transmitted through the cell giving rise to fluorescence outside of the evanescent field, i.e. in the cytosolic regions? This may result in a 'false positive' result. For example, a particle which is present within the EW field may scatter the TIRF illumination, causing it to couple out and excite EGFP-clathrin outside the region of the plasma membrane. When performing image analysis, this could potentially be mistaken for clathrin within the membrane which has associated with the particle, indicating a clathrin mediated route of endocytosis. This potential scattering, which has been discussed in detail in Chapter 2, presents a major problem if occurring, since it would be difficult validating conclusions as to ascertaining whether a particle is undergoing clathrin mediated endocytosis. Careful study of the data, however, leads me to reject this possibility on the following grounds. Temporal analysis of the EGFP-Clathrin LCa signal illustrates that there is no clathrin present at the particle site up until frame 6 of the image sequence (Fig. 6.10b,c). If particle scattering was a major problem, then this temporal analysis of clathrin would show a clathrin signal throughout the timeframe of study and not only at the stage of particle uptake i.e. if scattering was leading to fluorescent excitation of cytosolic clathrin, one would observe this effect over the entire timeframe of the experiment and not just at the moment of particle uptake. This indicates that the EGFP-clathrin signal is indeed coming from the clathrin molecules localised with the particle, and within the evanescent field.

Limitations of the TIRM/TIRF microscope for studying internalisation mechanisms

The major difficulty associated with this work was finding a suitable substrate to perform the ‘reverse uptake’ experiment. There are a number of attributes a substrate should have in order to enable the ‘reverse uptake’ experimental procedure to be performed; 1) the substrate should be sufficiently thin and flat to allow evanescent wave generation (Section 2.4.6), 2) it should adhere to the glass coverslip, 3) it should only ‘stick’ particles gently so that they can be easily internalised by the cells, 4) should be able to adhere a range of particles with different surface characteristics 5) needs to be non-toxic to cells and 6) should ensure gentle adherence of cells to allow cell movement.

In this study, when 300 nm carboxylated polystyrene particles were adhered to PLL coated coverslips and cells subsequently added, there was no particle uptake observed over a period of 4 hours, however uptake of 0.5 and 2 μm particles has been demonstrated (Fig. 6.4). There are potentially two explanations for this. Firstly, the surface charge of the particles is greater for the 300 nm particles (19.5 $\mu\text{Eq/g}$) compared with the 2 μm particles (3.3 $\mu\text{Eq/g}$) [294]. Secondly, the force of interactions between particle and cell, and particle and substrate may be greater for larger particles compared with smaller particles. For example, larger particles may be internalised with an actin regulated system, leading to large driving forces when internalising. Conversely, if smaller particles are internalised via caveolae, which do not use a large degree of actin, then the forces generated by the cell to internalise the particle may not be sufficiently large to overcome the force of adhesion between the particle and the substrate.

However, the mechanisms of force generation that drive endocytosis are not fully understood [295].

6.4.4 Clathrin gene expression after particle exposure

Several papers [250, 296, 297] have discussed the targeting mechanism of an assortment of cargo to clathrin coated pits (CCPs). There are two generally accepted targeting mechanisms, firstly, ligands and bound receptors may target to pre-existing CCPs on the cell surface [248, 252, 268, 298] and secondly, clathrin and its cofactors can be recruited to the site of the bound ligand, leading to *de novo* formation of a CCP at that site [247, 255, 268, 297]. These studies have utilised spinning disc confocal and TIRF microscopy to observe intensity changes associated with CCP formation and movement. This allows one to visualise the entry of cargo, such as G-protein coupled receptors, through targeting of pre-existing clathrin coated pits [263, 299] or whether a new clathrin coated pit is formed at the site of cargo attachment, for example for the entry of the influenza virus into HeLa cells [293, 297].

In Section 6.4.3 it was demonstrated how *de novo* CCP formation in 3T3 cells occurs for the internalisation of 500 nm particles. However, one question that has not been previously addressed in the literature regards the actual ‘origin’ of clathrin; are the *de novo* CCPs formed from a pool of intracellularly present clathrin or does the cell induce the production of clathrin due to the presence of cargo such as a drug delivery device, virus, protein etc. If the later was indeed occurring, then it may be possible to

assess the new clathrin production at the gene expression level, through gene expression analysis methodology.

The aim of the present study is to assess the effects of nanoparticle presentation to 3T3 cells on their clathrin gene expression. There are several methods used to study gene expression, including the 'Invader assay' [300] which combines two signal amplification reactions in series to generate and amplify a fluorescent signal in the presence of the correct target sequence, reverse transcription (RT)-PCR [301] and quantitative real time RT-PCR (qRT²-PCR). qRT²-PCR is the most widely used mRNA quantification methods for research applications such as monitoring transcription *in vivo* [302]. q(RT)²-PCR is the method employed in this study.

6.4.4.1 Method development for q(RT)²-PCR

Normalisation and primer design

The identification of a valid reference for data normalisation remains the most stubborn of problems and none of the solutions proposed are ideal. It is especially difficult when dealing with *in vivo* samples and comparing gene expression patterns between different individuals [302]. Glyceraldehyde 3-phosphate dehydrogenase (GAPDH) is an enzyme that catalyzes the sixth step of glycolysis and thus serves to break down glucose for energy and carbon molecules. It is commonly used as a reference gene in q(RT)²-PCR. A reference gene should have similar mRNA levels in all samples analyzed and they should not be regulated by the experimental treatment or condition used [303]. GAPDH

continues to be used as a reference, despite reports that emphasise problems associated with its use [302].

When selecting reference genes the main inclusion factor in this study was that the mRNA levels were constant when the cell was undergoing endocytosis. As described above, GAPDH is a commonly used reference gene. However in *Mus musculus* there are several GAPDH-like genes of varying sizes arising from different chromosomes. Since the qRT²-PCR experiments performed with the SYBR-green method are extremely dependent on the specificity of the primers and the amplified product, having several different related genes for normalisation may interfere with the results. Therefore, it was decided to investigate the use of other common reference genes which have less chance of unspecific amplification.

Primer3 software (<http://frodo.wi.mit.edu/>) was used to design the oligonucleotide primers (Table 6.1) for this experiment. In this process, it is advisable to initially select two or more reference genes since variability between expression levels may arise when using only one. Therefore, the hypoxanthine phosphoribosyltransferase (Hprt1) and ribosomal protein (RPL32) are chosen here as reference genes since they are not thought to be involved in cellular endocytosis. The specificity of the primers for the Hprt1, RPL32 and clathrin genes is confirmed by performing a melt curve graph (Fig. A.1.1). The presence of only one peak indicates that the primers are specific for the gene of interest only. Two or more peaks would mean that the primers are amplifying other genes in addition to that which is under investigation.

6.4.5 $q(RT)^2$ -PCR results

The PCR standard curve graphs obtained using the SYBR green method for the HPRT1, RPL32 and clathrin primers are shown in Fig. A.1.2. The efficiency of the primers was 97.4%, 80.2% and 96% for the HPRT1, RPL32 and clathrin primers respectively. Following generation of the standard curves, the 3T3 cells which were incubated with either 0.17 μm or 2 μm carboxylated polystyrene particles, for a period of two hours, underwent $q(RT)^2$ -PCR analysis. The resulting CT values were then used along with the primer efficiencies (Fig. A.1.2) in the Pffafl equation (Eq. 6.3) to calculate the relative gene expression of clathrin in 3T3 cells after exposure to 200 nm and 2 μm polystyrene particles for 2 hrs.

Exposure of 3T3 cells to 2 μm particles results in a 30 – 70% reduction in mRNA expression, whereas, exposure to 170 nm particles results in over a 90% reduction in mRNA expression (Table 6.2). A search of the literature has revealed that no other studies of this kind have been performed, excluding any comparisons and arguments however, one can attempt to put forward some tentative arguments for this reduction in gene expression. Initially, it was postulated that exposure of particles to the cells would result in an upregulation of the mRNA expression with the reasoning that this would increase the cells ability of producing more clathrin protein, and thus internalise particles. However, results from this initial experiment show that in fact the opposite may be occurring. This would suggest a mechanism may exist within intracellular communication indicating that there is an overload in the endocytic machinery, which therefore induces a reduction in the production of clathrin, in turn decreasing

internalisation of particles. It is interesting to note that the extent of clathrin down-regulation appears to be inversely proportional to the particle size. A tentative explanation of the phenomenon may be in fact that larger particles (2 μm) are rarely endocytosed via CCPs whereas this is considered to be a principal route for internalisation of smaller particles (100 – 200 nm) [43, 304-307].

Although a tentative link has been shown between particle presentation to cells and a reduction in clathrin gene expression, this study would benefit from further investigation. The number of experiments (n) needs to be increased to verify these initial results. There is also a large difference in clathrin LCa mRNA levels when measured against HPRT1 and RPL32 (Table 6.2). This would benefit from further investigation. It would be useful to study the effect of the particle incubation time (i.e. how long the cells were exposed to particles) on gene expression levels. Indeed this work could be further expanded to look at the effect of additional particle sizes and surface charges.

Table 6.2 Percent decrease in clathrin LCa mRNA expression in 3T3 cells exposed to 2 μm and 0.2 μm particles for 2 hrs (n = 2; mean \pm SD)

Reference gene used in Pffafl equation	% decrease in clathrin LCa mRNA expression following incubation with 0.17 μm particles	% decrease in clathrin LCa mRNA expression following incubation with 2.0 μm particles
HPRT1	92	30
RPL32	94	70

6.5 Conclusions

The work presented in this chapter demonstrates that particles of a size range between 500 nm and 2 microns can be internalised by 3T3 cells in the ‘reverse uptake’ configuration. Application of TIRM to the ‘reverse uptake’ experimental set up affords the real-time imaging of particle endocytosis without prior labelling of either the cell or the particle, providing a novel method for determining cellular entry of drug delivery systems. However, TIRM imaging *per se* does not allow one to elucidate the mechanism of cellular internalisation. The combination of TIRM/TIRF microscopy and EGFP-clathrin expressing cell line has afforded the visualisation of clathrin mediated endocytosis of particles. Analysis has indicated that 500 nm particle have been internalised via a clathrin mediated route, whereas 1 μm particle are internalised via a clathrin independent mechanism. It has also been demonstrated that there is *de novo* clathrin formation at the site of endocytosis prior to internalisation. In essence, the work outlined in this chapter shows that TIRM/TIRF microscopy has the potential to be applied in studies to elucidate the mechanisms of endocytosis pathways without the need to use pharmacological inhibitors, once the appropriately cloned cells are available.

Chapter 7

Summary, Conclusions and Suggestions for Future Work

7.1 Overview of work undertaken in this study

An overview of the work undertaken in this study is shown in Fig. 7.1. The initial aim of the project was develop a label-free microscopy technique to enable the visualisation of nanoparticle endocytosis by living cells. It was hoped this could be achieved through the development of a total internal reflection microscope. A further objective, to elucidate the mechanism of endocytosis through optical imaging, was set midway through the work. Two areas of research were used to achieve this goal namely by development of an EGFP-Clathrin LCa expressing cell line and further modification of the existing TIRM optics to include a fluorescent TIRF channel. It was hoped that a combination of the TIRM/TIRF microscope and the EGFP-Clathrin LCa expressing cell line would allow the visualisation of clathrin mediated endocytosis of nanoparticles in living cells.

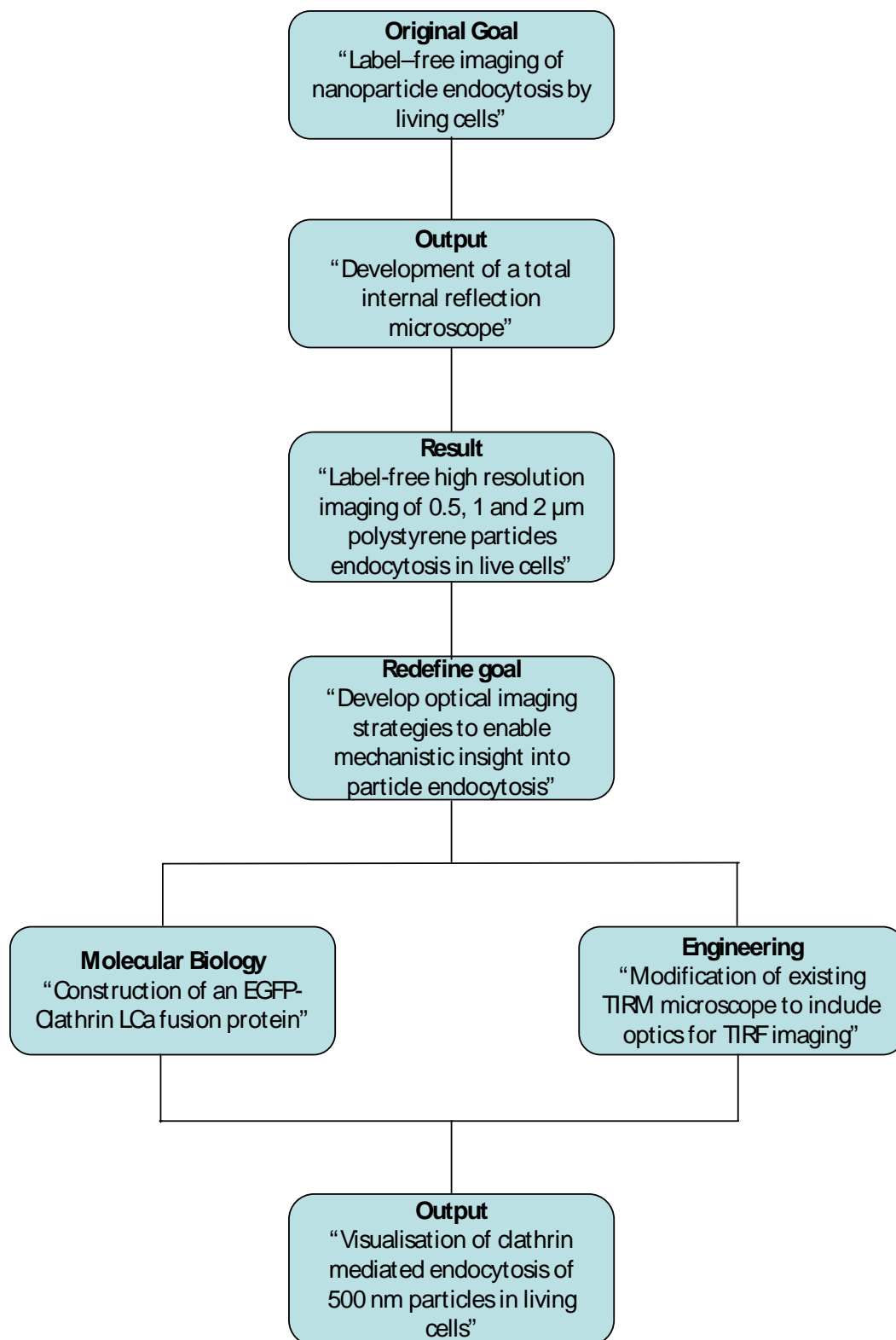


Figure 7.1 Overview of experimental work undertaken in this study.

7.2 Original goal

The work that has been carried out in this project demonstrated that label-free total internal reflection microscopy (TIRM) can be used to generate high resolution images of cell-substrate contacts and can image internalisation of model drug delivery systems without prior labelling of the cell or the delivery system.

7.3 Output

Firstly, a surface plasmon microscope was investigated for the purpose of label free imaging. This system is extremely sensitive, however, as of yet the lateral resolution is lacking. Total Internal Reflection Microscopy was subsequently developed. Similar to SPRM in that it is based upon the notion that evanescent waves are generated at a dielectric interface, the TIRM instrument affords excellent axial resolution and has diffraction limited lateral resolution. A successful TIRM system was built using a LED as the illumination source. This proved extremely useful as it negated all the coherent noise effects associated with using a coherent light source such as a laser.

7.4 Method development

This section reviews the instrumentation and genetically modified cell lines that were developed through the course of the study from an engineering and nanobiotechnology perspective. Given the multidisciplinary nature of this PhD, it is necessary to divide the major elements which have evolved in this work into distinct sections, however a summary will be given at the end to highlight how the two channels of work complemented each other and produced the given outcome.

7.4.1 Optical Engineering

7.4.1.1 TIRM system

In Chapter 2, a novel through the objective total internal reflection microscope (TIRM) was introduced and demonstrated. I have demonstrated that unlike RICM, which works on the principle of interference of light, TIRM is based on the scattering of an evanescent field by objects lying within the field. Several illumination sources were investigated including; a coherent laser source, temporally modulated laser source and light emitting diodes. It was found that a LED gave the best quality images while at the same time proving safe and cost efficient. Being a brightfield technique, the temporal resolution demonstrated is impressive, with frame rates up to 30 frames per second achievable. TIRM can also be combined with other optical techniques such as brightfield microscopy to increase the capability of the system. Maintaining image focus throughout a lengthy time-lapse experiment proved difficult with TIRM due to the

narrow depth of field of the high numerical aperture objective lens. A future modification of the TIRM system should see the implementation of an auto-focus module, such as digital filtering of high frequency information, as discussed in Chapter 2. The evanescent nature of the illumination requires that suitable substrates are used for imaging. For example, if the substrate is too thick or has a high degree of surface roughness, it will result in poor image contrast.

7.4.1.2 TIRM/TIRF system

Further modifications of the TIRM system to include dual-colour TIRF optics were described in Chapter 4. The rationale for inclusion of TIRF optics in the original label-free microscope was to increase its capability for imaging individual proteins within cells. Chapter 4 explains the optical configuration of the TIRM/TIRF microscope in great detail, including description of lenses, lasers, image detector, beamsplitters, dichroics and stages used in the system. Also, methods for construction of the microscope are included. Full automation of image capture was achieved through the iXon software, Andor breakout box and custom built circuitry, making experiments much simpler to perform. Finally, TIRM/TIRF images of 3T3 fibroblast cells expressing the DsRed protein are presented which demonstrate the similarities between the two imaging modalities.

The overall temporal resolution of image capture in the TIRM/TIRF system is currently limited by the need for sequential imaging, i.e. a TIRM image is captured, followed by capture of either one or two TIRF images then repeating this step. This can prove costly

in the temporal sense when one would like to capture dynamic processes at fast frame rates. One possible way of dealing with this problem is to implement an image splitter device such as that produced by Cairn Research (Optosplit III, Cairn Research, UK). This type of image splitter allows simultaneous capture of up to three emission wavelengths on the same camera, thus making image registration simple. The fundamental principle of the splitter is to split the three images based on their emission spectra using a series of mirrors and dichroic beamsplitters, and imaging onto separate areas of the CCD chip which can be subsequently overlaid.

One limitation of the system in its current configuration is that it does not enable imaging of fluorescent processes deeper within the cell, without manual positioning of the TIRF beam. Ideally, the system would allow events occurring at the membrane to be quickly followed if they move into the cell cytoplasm, for example, the disappearance of CCPs seen with TIRF could be followed as it moves deeper into the cell. There are two potential solutions to this which should be considered for future engineering work. The first way is to rapidly switch between TIRF and epi-illumination using mechanical shutters [308, 309]. The second and potentially more powerful approach is through the use of the recently described HILO (highly inclined laminated optical sheet microscopy) technique [310]. In contrast to conventional epifluorescence microscopy, HILO has the ability to optically section through the sample, thus resulting in better signal-to-noise and contrast. One drawback, however, is that the image is only in focus in a small region due to the oblique nature of the incident light [311].

Currently, TIRM images are purely qualitative in nature and offer only a description of the cell adhesion topography, with dark and lighter areas representing regions close and further away from the substrate respectively. One potential improvement to the total internal reflection microscope would be to enable quantitative measurements of cell-substrate distances to be inferred from images, as can be readily made with both TIRF [226-228] and RICM [156]. The principle of quantitative imaging in TIRF is relatively straightforward; firstly images are taken at multiple angles above the critical angle, followed by modeling of the fluorescence intensity, using previously described equations [227, 229], to extrapolate the separation distance and/or concentration of fluorophore. Setting up TIRM to carry out angle scanning is slightly more complex, due to the ring nature of illumination. However, experience within the lab has shown angle scanning TIRM can be achieved using a spatial light modulator (SLM) device. Increasing the illumination angle in TIRM causes the evanescent field penetration depth to decrease. It should be possible to model the intensity distributions from the variable angle TIRM data and subsequently quantify the cell-substrate separation distance. It would then be interesting to measure the correlation between the TIRM and TIRF images. If TIRM proves to be successful for quantifying cell-substrate separation distances, this would be very appealing to researchers in the broad areas of biomaterials and tissue engineering, due to the relative ease and simplicity of TIRM [312].

7.4.2 Molecular biology

The development of an EGFP-clathrin fusion protein was outlined in Chapter 5. After transfection into 3T3 cells this enabled tracking of individual clathrin puncta on the basal membrane using TIRF. TIRF imaging was used to demonstrate three distinct populations of clathrin vesicles; those which appear and disappear, move laterally and those which are static. A DsRed-caveolin-1 fusion was designed but was not successfully expressed in cells. Future work should concentrate on expressing this protein in cells so that it can be co-expressed with EGFP-clathrin and thus allow one to image both proteins simultaneously.

Clathrin mRNA expression in 3T3 cells was investigated using quantitative real time reverse transcriptase PCR after presentation of colloidal particles. It was shown that clathrin expression was reduced after 2 μm polystyrene latex particles were presented to the cells for two hours. Tentative arguments for this are that the cell is down-regulating clathrin production to decrease the particle load within them. Further investigation is required to determine how mRNA levels are affected by incubation time, particle size and charge. This should help to provide a fundamental insight into the molecular basis of particle endocytosis which, to the best of my knowledge has not been performed before. Indeed, primers can be designed to study all of the major endocytic proteins such as actin, caveolin, flotillin and clathrin. This could potentially give an insight into what is happening to the major proteins at the molecular level.

7.5 Outcomes/Results

7.5.1 TIRM imaging of 3T3 and A549 cells

In Chapter 3, application of the TIR microscope to high resolution label-free imaging of the interaction between living cell membranes and a polylysine substrate are shown. Numerous contact points are seen on the surface of 3T3 cells. These are likely to be focal and close contacts. Indeed it is possible to image dynamic events such as membrane ruffling, lamella protrusion and extraction, and filopodia movement. The presence of lamellar bodies in the lung epithelial A549 cell line was easily detectable with TIRM. These can be seen to move laterally, and appear and disappear on the basal cell membrane.

Confirming the nature of the contacts made between 3T3 cells and the PLL substrate, which are shown on the TIRM images in Chapter 3, would be an important future experiment. The best way to do this would be to image fluorescently tagged focal contact proteins, such as vinculin [313] and paxillin [209], using the combined TIRM and TIRF instrument. If there is a correlation between the fluorescently tagged proteins representing focal contacts and the contact areas seen in the TIRM images then this would help to confirm that these contact are readily visible using TIRM, increasing the flexibility of the instrument. Further experiments could examine the tubule-like structures seen in the TIRM images of the A549 cells using fluorescently tagged tubulin [314] and confirm whether they are microtubules. The ability to image microtubules

without the need for fluorescent labelling would greatly simplify experiments where dynamics of these structures are of interest [314].

7.5.2 TIRM/TIRF imaging of clathrin mediated endocytosis

Label free visualisation of 0.5, 1 and 2 μm colloidal particle internalisation by living cells in the ‘reverse uptake’ configuration was achieved using TIRM and confirmed with confocal microscopy. This is the first published description of using the ‘reverse uptake’ configuration for presenting particles to the cell. Although TIRM provides a simple methodology for determining cellular uptake of particulates, it does not provide any mechanistic insight into endocytosis. To achieve this, cells transfected with EGFP-Clathrin LCa, and undergoing internalisation of particles, were imaged using TIRM/TIRF. It was shown that 500 nm particles are seemingly internalised *via* a clathrin mediated pathway whereas 1 μm particles are internalised *via* a clathrin-independent pathway.

The major hurdle which arises when using TIRM/TIRF for imaging of nanoparticle endocytosis is how to control particle adhesion to the substrate. It was discussed in Chapter 6 how the endocytosis of particles < 500 nm could not be achieved, as a potential result of them being too greatly adhered to the surface. Several different surfaces were tested for adhesion properties but none resulted in particle internalisation. It is important that if future internalisation studies are to be carried out using this system then the method of particle presentation to the cell is improved. Some potential methods are discussed below.

Optical tweezers are a method whereby a focussed laser beam (usually near-infrared) is used to provide an attractive or repulsive force to physically move and hold dielectric objects. This makes them excellent tools for transporting particles ranging in size from several micrometres to a few hundred nanometres [315]. There are several ways for achieving optical trapping including using focussed evanescent illumination [316], a single beam, a double beam trap [317] or through counter propagating laser beams which form stable evanescent traps [318]. It is envisioned that optical tweezers could be added to the existing setup through focussing of an infrared beam through the 1.45 NA objective lens. Since force measurements are not required the experimental setup should be more straightforward. Indeed a configuration of epi-fluorescence microscopy and optical tweezers has already been reported [319]. If this is possible to achieve, then it would allow a single particle or multiple particles [320] to be precisely manipulated, meaning that they could be presented to the cell in a controlled manner. For example, one could trap the particle(s) under focused evanescent illumination, add cells and wait for them to come close to the surface before beginning TIRM/TIRF imaging.

Another potential solution is to use a transparent, electrically conducting polymer such as indium tin oxide as a substrate for cell growth [321, 322]. This would allow one to trap particles close to the substrate through electrostatic interactions and subsequently release them at the appropriate time by switching off the electrical field. This allows particles to be presented to the substrate, free from adherent forces. It is currently not known how the electrical potential may affect membrane potentials and endocytic mechanisms, although it has been shown that at an applied current of $20 \mu\text{A}/\text{cm}^2$ has negligible effects on cell morphology and growth [321].

References

- 1 Soppimath, K. S., Aminabhavi, T. M., Kulkarni, A. R. and Rudzinski, W. E. (2001) Biodegradable polymeric nanoparticles as drug delivery devices. *Journal of Controlled Release*. **70**, 1-20
- 2 Müller, R. H., Mäder, K. and Gohla, S. (2000) Solid lipid nanoparticles (SLN) for controlled drug delivery—a review of the state of the art. *European Journal of Pharmaceutics and Biopharmaceutics*. **50**, 161-177
- 3 Kataoka, K., Harada, A. and Nagasaki, Y. (2001) Block copolymer micelles for drug delivery: design, characterization and biological significance. *Advanced Drug Delivery Reviews*. **47**, 113-131
- 4 Duncan, R. (2003) The dawning era of polymer therapeutics. *Nature Reviews Drug Discovery*. **2**, 347-360
- 5 Esfand, R. and Tomalia, D. A. (2001) Poly (amidoamine)(PAMAM) dendrimers: from biomimicry to drug delivery and biomedical applications. *Drug Discovery Today*. **6**, 427-436
- 6 Suh, J., Wirtz, D. and Hanes, J. (2003) Efficient active transport of gene nanocarriers to the cell nucleus. *Proceedings of the National Academy of Sciences*. **100**, 3878-3882
- 7 Henry, S., McAllister, D. V., Allen, M. G. and Prausnitz, M. R. (1998) Microfabricated microneedles: a novel approach to transdermal drug delivery. *Journal of pharmaceutical sciences*. **87**, 922-925

-
- 8 Panyam, J. and Labhasetwar, V. (2003) Biodegradable nanoparticles for drug and gene delivery to cells and tissue. *Advanced Drug Delivery Reviews*. **55**, 329-347
- 9 Zhou, T., Lewis, H., Foster, R. E. and Schwendeman, S. P. (1998) Development of a multiple-drug delivery implant for intraocular management of proliferative vitreoretinopathy. *Journal of Controlled Release*. **55**, 281-295
- 10 Allen, T. M. and Cullis, P. R. (2004) Drug Delivery Systems: Entering the Mainstream. *Science*. **303**, 1818-1822
- 11 Song, C. X., Labhasetwar, V., Murphy, H., Qu, X., Humphrey, W. R., Shebuski, R. J. and Levy, R. J. (1997) Formulation and characterization of biodegradable nanoparticles for intravascular local drug delivery. *Journal of Controlled Release*. **43**, 197-212
- 12 Couvreur, P., Dubernet, C. and Puisieux, F. (1995) Controlled drug delivery with nanoparticles: current possibilities and future trends. *European Journal of Pharmaceutics and Biopharmaceutics*. **41**, 2-13
- 13 Pitaksuteepong, T., Davies, N. M., Tucker, I. G. and Rades, T. (2002) Factors influencing the entrapment of hydrophilic compounds in nanocapsules prepared by interfacial polymerisation of water-in-oil microemulsions. *European Journal of Pharmaceutics and Biopharmaceutics*. **53**, 335-342
- 14 Torchilin, V. P. (2005) Recent advances with liposomes as pharmaceutical carriers. *Nature Reviews Drug Discovery*. **4**, 145-160
- 15 Najlah, M. and D'Emanuele, A. (2006) Crossing cellular barriers using dendrimer nanotechnologies. *Current Opinion in Pharmacology*. **6**, 522-527
- 16 Boswell, G. W., Buell, D. and Bekersky, I. (1998) AmBisome (liposomal amphotericin B): a comparative review. *Journal of Clinical Pharmacology*. **38**, 583-592
- 17 Judson, I., Radford, J. A., Harris, M., Blay, J. Y., van Hoesel, Q., le Cesne, A., van Oosterom, A. T., Clemons, M. J., Kamby, C. and Hermans, C. (2001) Randomised
-

phase II trial of pegylated liposomal doxorubicin (DOXIL®/CAELYX®) versus doxorubicin in the treatment of advanced or metastatic soft tissue sarcoma a study by the EORTC Soft Tissue and Bone Sarcoma Group. *European Journal of Cancer*. **37**, 870-877

18 Micha, J. P., Goldstein, B. H., Birk, C. L., Rettenmaier, M. A. and Brown, J. V. (2006) Abraxane in the treatment of ovarian cancer: The absence of hypersensitivity reactions. *Gynecologic Oncology*. **100**, 437-438

19 Farokhzad, O. C., Cheng, J., Teply, B. A., Sherifi, I., Jon, S., Kantoff, P. W., Richie, J. P. and Langer, R. (2006) Targeted nanoparticle-aptamer bioconjugates for cancer chemotherapy in vivo. *Proceedings of the National Academy of Sciences*. **103**, 6315-6320

20 Ogris, M., Brunner, S., Schuller, S., Kircheis, R. and Wagner, E. (1999) PEGylated DNA/transferrin-PEI complexes: reduced interaction with blood components, extended circulation in blood and potential for systemic gene delivery. *Gene Therapy*. **6**, 595-605

21 Stolnik, S., Dunn, S. E., Garnett, M. C., Davies, M. C., Coombes, A. G. A., Taylor, D. C., Irving, M. P., Purkiss, S. C., Tadros, T. F. and Davis, S. S. (1994) Surface Modification of Poly (lactide-co-glycolide) Nanospheres by Biodegradable Poly (lactide)-Poly (ethylene glycol) Copolymers. *Pharmaceutical Research*. **11**, 1800-1808

22 Medarova, Z., Pham, W., Farrar, C., Petkova, V. and Moore, A. (2007) In vivo imaging of siRNA delivery and silencing in tumors. *Nature Medicine*. **13**, 372-377

23 Derfus, A. M., Chen, A. A., Min, D.-H., Ruoslahti, E. and Bhatia, S. N. (2007) Targeted Quantum Dot Conjugates for siRNA Delivery. *Bioconjugate Chemistry*. **18**, 1391-1396

24 Torchilin, V. P., Rammohan, R., Weissig, V. and Levchenko, T. S. (2001) TAT peptide on the surface of liposomes affords their efficient intracellular delivery even at low temperature and in the presence of metabolic inhibitors. *Proceedings of the National Academy of Sciences*. **98**, 8786-8791

-
- 25 Nakase, I., Niwa, M., Takeuchi, T., Sonomura, K., Kawabata, N., Koike, Y., Takehashi, M., Tanaka, S., Ueda, K., Simpson, J. C., Jones, A. T., Sugiura, Y. and Futaki, S. (2004) Cellular Uptake of Arginine-Rich Peptides: Roles for Macropinocytosis and Actin Rearrangement. *Molecular Therapy*. **10**, 1011-1022
- 26 Sanvicens, N. and Marco, M. P. (2008) Multifunctional nanoparticles - properties and prospects for their use in human medicine. *Trends in Biotechnology*. **26**, 425-433
- 27 ESF-EMBO Symposium. (2007) Probing Interactions between Nanoparticles/Biomaterials and Biological Systems. In European Science Foundation (ESF) Research Conference on Probing Interactions between Nanoparticles/Biomaterials and Biological Systems. November 3 - 8th. Sant Feliu de Guixols, Spain
- 28 Na, K., Seong Lee, E. and Bae, Y. H. (2003) Adriamycin loaded pullulan acetate/sulfonamide conjugate nanoparticles responding to tumor pH: pH-dependent cell interaction, internalization and cytotoxicity in vitro. *Journal of Controlled Release*. **87**, 3-13
- 29 Hong, S., Bielinska, A. U., Mecke, A., Keszler, B., Beals, J. L., Shi, X., Balogh, L., Orr, B. G., Baker, J. R. and Banaszak Holl, M. M. (2004) Interaction of Poly(amidoamine) Dendrimers with Supported Lipid Bilayers and Cells: Hole Formation and the Relation to Transport. *Bioconjugate Chemistry*. **15**, 774-782
- 30 Luo, Y., Bernshaw, N. J., Lu, Z. R., Kopecek, J. and Prestwich, G. D. (2002) Targeted delivery of doxorubicin by HPMA copolymer-hyaluronan bioconjugates. *Pharmaceutical Research*. **19**, 396-402
- 31 Coombes, A. G. A., Tasker, S., Lindblad, M., Holmgren, J., Hoste, K., Toncheva, V., Schacht, E., Davies, M. C., Illum, L. and Davis, S. S. (1997) Biodegradable polymeric microparticles for drug delivery and vaccine formulation: the surface attachment of hydrophilic species using the concept of poly(ethylene glycol) anchoring segments. *Biomaterials*. **18**, 1153-1161
-

- 32 Miller, C. R., Bondurant, B., McLean, S. D., McGovern, K. A. and O'Brien, D. F. (1998) Liposome-Cell Interactions in Vitro: Effect of Liposome Surface Charge on the Binding and Endocytosis of Conventional and Sterically Stabilized Liposomes. *Biochemistry*. **37**, 12875-12883
- 33 Bartlett, D. W., Su, H., Hildebrandt, I. J., Weber, W. A. and Davis, M. E. (2007) Impact of tumor-specific targeting on the biodistribution and efficacy of siRNA nanoparticles measured by multimodality in vivo imaging. *Proceedings of the National Academy of Sciences*. **104**, 15549-15554
- 34 Li, W. and Szoka, F. C. (2007) Lipid-based Nanoparticles for Nucleic Acid Delivery. *Pharmaceutical Research*. **24**, 438-449
- 35 Luten, J., van Nostrum, C. F., De Smedt, S. C. and Hennink, W. E. (2008) Biodegradable polymers as non-viral carriers for plasmid DNA delivery. *Journal of Controlled Release*. **126**, 97-110
- 36 Limbach, L. K., Li, Y., Grass, R. N., Brunner, T. J., Hintermann, M. A., Muller, M., Gunther, D. and Stark, W. J. (2005) Oxide nanoparticle uptake in human lung fibroblasts: Effects of particle size, agglomeration, and diffusion at low concentrations. *Environmental Science & Technology*. **39**, 9370-9376
- 37 Jones, A. T. (2008) Gateways and tools for drug delivery: Endocytic pathways and the cellular dynamics of cell penetrating peptides. *International Journal of Pharmaceutics*. **354**, 34-38
- 38 Ivanov, A. I. (2008) Exocytosis and Endocytosis. *Methods in Molecular Biology*. **440**. Springer, London
- 39 Xia, T., Kovichich, M., Liong, M., Zink, J. I. and Nel, A. E. (2008) Cationic Polystyrene Nanosphere Toxicity Depends on Cell-Specific Endocytic and Mitochondrial Injury Pathways. *American Chemical Society Nano*. **2**, 85-96
- 40 Mellman, I. (1996) Endocytosis and molecular sorting. *Annual Review of Cell and Developmental Biology*. **12**, 575-625

- 41 D'Souza, V. M., Bareford, L. M., Ray, A. and Swaan, P. W. (2006) Cytoskeletal scaffolds regulate riboflavin endocytosis and recycling in placental trophoblasts. *The Journal of Nutritional Biochemistry*. **17**, 821-829
- 42 Gratton, S. E. A., Ropp, P. A., Pohlhaus, P. D., Luft, J. C., Madden, V. J., Napier, M. E. and DeSimone, J. M. (2008) The effect of particle design on cellular internalization pathways. *Proceedings of the National Academy of Sciences*. **105**, 11613-11618
- 43 Rejman, J., Oberle, V., Zuhorn, I. S. and Hoekstra, D. (2004) Size-dependent internalization of particles via the pathways of clathrin- and caveolae-mediated endocytosis. *Biochemical Journal*. **377**, 159-169
- 44 Harush-Frenkel, O., Rozentur, E., Benita, S. and Altschuler, Y. (2008) Surface Charge of Nanoparticles Determines Their Endocytic and Transcytotic Pathway in Polarized MDCK Cells. *Biomacromolecules*. **9**, 435-443
- 45 Wagner, E., Zenke, M., Cotten, M., Beug, H. and Birnstiel, M. L. (1990) Transferrin-Polycation Conjugates as Carriers for DNA Uptake into Cells. *Proceedings of the National Academy of Sciences*. **87**, 3410-3414
- 46 Lee, R. J. and Huang, L. (1996) Folate-targeted, Anionic Liposome-entrapped Polylysine-condensed DNA for Tumor Cell-specific Gene Transfer. *Journal of Biological Chemistry*. **271**, 8481-8487
- 47 Sudimack, J. and Lee, R. J. (2000) Targeted drug delivery via the folate receptor. *Advanced Drug Delivery Reviews*. **41**, 147-162
- 48 Barry, M. A., Dower, W. J. and Johnston, S. A. (1996) Toward cell-targeting gene therapy vectors: Selection of cell-binding peptides from random peptide-presenting phage libraries. *Nature Medicine*. **2**, 299-305
- 49 Heintzmann, R. and Ficz, G. (2006) Breaking the resolution limit in light microscopy. *Briefings in Functional Genomics and Proteomics*. **5**, 289-301

- 50 Stephens, D. J. and Allan, V. J. (2003) Light Microscopy Techniques for Live Cell Imaging. *Science*. **300**, 82-86
- 51 Zernike, F. (1955) How I Discovered Phase Contrast. *Science*. **121**, 345-349
- 52 Nomarski, G. (1957) From phase contrast to contrast by interference. *Reviews Haematology*. **12**, 439-442
- 53 Cohen, H., Levy, R. J., Gao, J., Fishbein, I., Kousaev, V., Sosnowski, S., Slomkowski, S. and Golomb, G. (2000) Sustained delivery and expression of DNA encapsulated in polymeric nanoparticles. *Gene Therapy*. **7**, 1896-1905
- 54 Jain, T. K., Morales, M. A., Sahoo, S. K., Leslie-Pelecky, D. L. and Labhasetwar, V. (2005) Iron oxide nanoparticles for sustained delivery of anticancer agents. *Molecular Pharmaceutics*. **2**, 194-205
- 55 Roy, I., Ohulchansky, T. Y., Bharali, D. J., Pudavar, H. E., Mistretta, R. A., Kaur, N. and Prasad, P. N. (2005) Optical tracking of organically modified silica nanoparticles as DNA carriers: A nonviral, nanomedicine approach for gene delivery. *Proceedings of the National Academy of Sciences*. **102**, 279-284
- 56 Fattal, E., Vauthier, C., Aynie, I., Nakada, Y., Lambert, G., Malvy, C. and Couvreur, P. (1998) Biodegradable polyalkylcyanoacrylate nanoparticles for the delivery of oligonucleotides. *Journal of Controlled Release*. **53**, 137-143
- 57 Janes, K. A., Fresneau, M. P., Marazuela, A., Fabra, A. and Alonso, M. J. (2001) Chitosan nanoparticles as delivery systems for doxorubicin. *Journal of Controlled Release*. **73**, 255-267
- 58 Schenke-Layland, K., Riemann, I., Damour, O., Stock, U. A. and König, K. (2006) Two-photon microscopes and in vivo multiphoton tomographs -- Powerful diagnostic tools for tissue engineering and drug delivery. *Advanced Drug Delivery Reviews*. **58**, 878-896

- 59 Stabler, G., Somekh, M. G. and See, C. W. (2004) High-resolution wide-field surface plasmon microscopy. *Journal of Microscopy*. **214**, 328-333
- 60 Somekh, M. G., See, C. W. and Goh, J. (2000) Wide field amplitude and phase confocal microscope with speckle illumination. *Optics Communications*. **174**, 75-80
- 61 Yeatman, E. and Ash, E. A. (1987) Surface plasmon microscopy. *Electronics Letters*. **23**, 1091-1092
- 62 Raether, H. (1988) *Surface Plasmons on Smooth and Rough Surfaces and on Gratings*. Springer Tracts in Modern Physics. **111**. Springer, Toronto
- 63 Rothenhaeusler, B. and Knoll, W. (1988) Surface-plasmon microscopy. *Nature*. **332**, 615-617
- 64 Giebel, K. F., Bechinger, C., Herminghaus, S., Riedel, M., Leiderer, P., Weiland, U. and Bastmeyer, M. (1999) Imaging of Cell/Substrate Contacts of Living Cells with Surface Plasmon Resonance Microscopy. *Biophysical Journal*. **76**, 509-516
- 65 Kano, H. and Knoll, W. (1998) Locally excited surface-plasmon-polaritons for thickness measurement of LBK films. *Optics Communications*. **153**, 235-239
- 66 Kano, H. and Knoll, W. (2000) A scanning microscope employing localized surface-plasmon-polaritons as a sensing probe. *Optics Communications*. **182**, 11-15
- 67 Toyama, S., Aoki, K. and Kato, S. (2005) SPR observation of adsorption and desorption of water-soluble polymers on an Au surface. *Sensors & Actuators: B. Chemical*. **108**, 903-909
- 68 Steiner, G., Sablinskas, V., Hübner, A., Kuhne, C. and Salzer, R. (1999) Surface plasmon resonance imaging of microstructured monolayers. *Journal of Molecular Structure*. **509**, 265-273
- 69 Nelson, B. P., Grimsrud, T. E., Liles, M. R., Goodman, R. M. and Corn, R. M. (2000) Surface plasmon resonance imaging measurements of DNA and RNA

hybridization adsorption onto DNA microarrays. *Journal of the American Chemical Society*. **122**, 4177-4184

70 Lee, H. J., Goodrich, T. T. and Corn, R. M. (2001) SPR imaging measurements of 1-D and 2-D DNA microarrays created from microfluidic channels on gold thin films. *Analytical Chemistry*. **73**, 5525-5531

71 Smith, E. A., Kyo, M., Kumasawa, H., Nakatani, K., Saito, I. and Corn, R. M. (2002) Chemically induced hairpin formation in DNA monolayers. *Journal of the American Chemical Society*. **124**, 6810-6811

72 Wegner, G. J., Lee, H. J., Marriott, G. and Corn, R. M. (2003) Fabrication of histidine-tagged fusion protein arrays for surface plasmon resonance imaging studies of protein-protein and protein-DNA interactions. *Analytical Chemistry*. **75**, 4740-4746

73 Kyo, M., Yamamoto, T., Motohashi, H., Kamiya, T., Kuroita, T., Tanaka, T., Engel, J. D., Kawakami, B. and Yamamoto, M. (2004) Evaluation of MafG interaction with Maf recognition element arrays by surface plasmon resonance imaging technique. *Genes to Cells*. **9**, 153-164

74 Kanda, V., Kariuki, J. K., Harrison, D. J. and McDermott, M. T. (2004) Label-free reading of microarray-based immunoassays with surface plasmon resonance imaging. *Analytical Chemistry*. **76**, 7257-7262

75 Wolf, L. K., Fullenkamp, D. E. and Georgiadis, R. M. (2005) Quantitative Angle-Resolved SPR Imaging of DNA-DNA and DNA-Drug Kinetics. *Journal of the American Chemical Society*. **127**, 17453-17459

76 Yildiz, A., Forkey, J. N., McKinney, S. A., Ha, T., Goldman, Y. E. and Selvin, P. R. (2003) Myosin V Walks Hand-Over-Hand: Single Fluorophore Imaging with 1.5 nm Localization. *Science*. **300**, 2061-2065

77 Douglass, A. D. and Vale, R. D. (2005) Single-Molecule Microscopy Reveals Plasma Membrane Microdomains Created by Protein-Protein Networks that Exclude or Trap Signaling Molecules in T Cells. *Cell*. **121**, 937-950

- 78 Reck-Peterson, S. L., Yildiz, A., Carter, A. P., Gennerich, A., Zhang, N. and Vale, R. D. (2006) Single-Molecule Analysis of Dynein Processivity and Stepping Behavior. *Cell*. **126**, 335-348
- 79 Rappoport, J. Z. and Simon, S. M. (2003) Real-time analysis of clathrin-mediated endocytosis during cell migration. *Journal of Cell Science*. **116**, 847-855
- 80 Axelrod, D. (1981) Cell-substrate contacts illuminated by total internal reflection fluorescence. *The Journal of Cell Biology*. **89**, 141-145
- 81 Burmeister, J. S., Truskey, G. A. and Reicher, W. M. (1994) Quantitative analysis of variable-angle total internal reflection fluorescence microscopy (VA-TIRFM) of cell/substrate contacts. *Journal of microscopy*. **173**, 39-51
- 82 Binnig, G., Quate, C. F. and Gerber, C. (1986) Atomic force microscope. *Physical Review Letters*. **56**, 930-933
- 83 Turner, Y. T. A., Roberts, C. J. and Davies, M. C. (2007) Scanning probe microscopy in the field of drug delivery. *Advanced Drug Delivery Reviews*. **59**, 1453-1473
- 84 Radmacher, M., Tillmann, R. W., Fritz, M. and Gaub, H. E. (1992) From molecules to cells: imaging soft samples with the atomic force microscope. *Science*. **257**, 1900-1905
- 85 Henderson, E., Haydon, P. G. and Sakaguchi, D. S. (1992) Actin filament dynamics in living glial cells imaged by atomic force microscopy. *Science*. **257**, 1944
- 86 Häberle, W., Hörber, J. K., Ohnesorge, F., Smith, D. P. and Binnig, G. (1992) In situ investigations of single living cells infected by viruses. *Ultramicroscopy*. **42**, 1161
- 87 Shen, Y., Sun, J. L., Zhang, A., Hu, J. and Xu, L. X. (2007) A new image correction method for live cell atomic force microscopy. *Physics in Medicine and Biology*. **52**, 2185-2196

-
- 88 Rotsch, C., Braet, F., Wisse, E. and Radmacher, M. (1997) AFM imaging and elasticity measurements on living rat liver macrophages. *Cell Biology International*. **21**, 685-696
- 89 Müller, D. J., Engel, A., Matthey, U., Meier, T., Dimroth, P. and Suda, K. (2003) Observing membrane protein diffusion at subnanometer resolution. *Journal of molecular biology*. **327**, 925-930
- 90 Hansma, P. K., Drake, B., Marti, O., Gould, S. A. and Prater, C. B. (1989) The scanning ion-conductance microscope. *Science*. **243**, 641-643
- 91 Korchev, Y. E., Milovanovic, M., Bashford, C. L., Bennett, D. C., Sviderskaya, E. V., Vodyanoy, I. and Lab, M. J. (1997) Specialized scanning ion-conductance microscope for imaging of living cells. *Journal of Microscopy*. **188**, 17-23
- 92 Gorelik, J., Shevchuk, A. I., Frolenkov, G. I., Diakonov, I. A., Lab, M. J., Kros, C. J., Richardson, G. P., Vodyanoy, I., Edwards, C. R. W. and Klenerman, D. (2003) Dynamic assembly of surface structures in living cells. *Proceedings of the National Academy of Sciences*. **100**, 5819-5822
- 93 Korchev, Y. E., Gorelik, J., Lab, M. J., Sviderskaya, E. V., Johnston, C. L., Coombes, C. R., Vodyanoy, I. and Edwards, C. R. W. (2000) Cell Volume Measurement Using Scanning Ion Conductance Microscopy. *Biophysical Journal*. **78**, 451-457
- 94 Dutta, A. K., Korchev, Y. E., Shevchuk, A. I., Hayashi, S., Okada, Y. and Sabirov, R. Z. (2008) Spatial Distribution of Maxi-Anion Channel on Cardiomyocytes Detected by Smart-Patch Technique. *Biophysical Journal*. **94**, 1646-1655
- 95 Shin, W. and Gillis, K. D. (2006) Measurement of changes in membrane surface morphology associated with exocytosis using scanning ion conductance microscopy. *Biophysical Journal*. **91**, 63-65
- 96 Shevchuk, A. I., Hobson, P., Lab, M. J., Klenerman, D., Krauzewicz, N. and Korchev, Y. E. (2008) Endocytic pathways: combined scanning ion conductance and
-

surface confocal microscopy study. *Pflügers Archiv European Journal of Physiology*. **456**, 227-235

97 Frankel, D. J., Pfeiffer, J. R., Surviladze, Z., Johnson, A. E., Oliver, J. M., Wilson, B. S. and Burns, A. R. (2006) Revealing the Topography of Cellular Membrane Domains by Combined Atomic Force Microscopy/Fluorescence Imaging. *Biophysical Journal*. **90**, 2404-2413

98 Korchev, Y. E., Bashford, C. L., Milovanovic, M., Vodyanoy, I. and Lab, M. J. (1997) Scanning ion conductance microscopy of living cells. *Biophysical Journal*. **73**, 653-658

99 Kemp, S. J., Thorley, A. J., Gorelik, J., Seckl, M. J., O'Hare, M. J., Arcaro, A., Korchev, Y., Goldstraw, P. and Tetley, T. D. (2008) Immortalisation of Human Alveolar Epithelial Cells to Investigate Nanoparticle Uptake. *American Journal of Respiratory Cell and Molecular Biology*. **39**, 591-597

100 Gorelik, J., Shevchuk, A., Ramalho, M., Elliott, M., Lei, C., Higgins, C. F., Lab, M. J., Klenerman, D., Krauzewicz, N. and Korchev, Y. (2002) Scanning surface confocal microscopy for simultaneous topographical and fluorescence imaging: Application to single virus-like particle entry into a cell. *Proceedings of the National Academy of Sciences*. **99**, 16018-16023

101 Syngé, E. H. (1928) A suggested method for extending microscopic resolution into the ultramicroscopic region. *Philosophical Magazine*. **6**, 356

102 Ash, E. A. and Nicholls, G. (1972) Super-resolution aperture scanning microscope. *Nature*. **237**, 510-512

103 Pohl, D. W., Denk, W. and Lanz, M. (1984) Optical stethoscopy: Image recording with resolution $\lambda/20$. *Applied Physics Letters*. **44**, 651-653

104 Lewis, A., Isaacson, M., Harootunian, A. and Muray, A. (1984) Development of a 500 Å spatial resolution light microscope: I. light is efficiently transmitted through $[\lambda/16]$ diameter apertures. *Ultramicroscopy*. **13**, 227-231

-
- 105 de Bakker, B. I., Bodnar, A., van Dijk, E., Vamosi, G., Damjanovich, S., Waldmann, T. A., van Hulst, N. F., Jenei, A. and Garcia-Parajo, M. F. (2008) Nanometer-scale organization of the alpha subunits of the receptors for IL2 and IL15 in human T lymphoma cells. *Journal of Cell Science*. **121**, 627-633
- 106 de Lange, F., Cambi, A., Huijbens, R., de Bakker, B., Rensen, W., Garcia-Parajo, M., van Hulst, N. and Figdor, C. G. (2001) Cell biology beyond the diffraction limit: near-field scanning optical microscopy. *Journal of Cell Science*. **114**, 4153-4160
- 107 Hell, S. W. and Wichmann, J. (1994) Breaking the diffraction resolution limit by stimulated emission: stimulated-emission-depletion fluorescence microscopy. *Optics Letters*. **19**, 780-780
- 108 Hell, S. W. and Kroug, M. (1995) Ground-state-depletion fluorescence microscopy: A concept for breaking the diffraction resolution limit. *Applied Physics B: Lasers and Optics*. **60**, 495-497
- 109 Gustafsson, M. G. L. (2005) Nonlinear structured-illumination microscopy: Wide-field fluorescence imaging with theoretically unlimited resolution. *Proceedings of the National Academy of Sciences*. **102**, 13081-13086
- 110 Heintzmann, R., Jovin, T. M. and Cremer, C. (2002) Saturated patterned excitation microscopy—a concept for optical resolution improvement. *Journal of the Optical Society of America A*. **19**, 1599-1609
- 111 Schermelleh, L., Carlton, P. M., Haase, S., Shao, L., Winoto, L., Kner, P., Burke, B., Cardoso, M. C., Agard, D. A. and Gustafsson, M. G. L. (2008) Subdiffraction Multicolor Imaging of the Nuclear Periphery with 3D Structured Illumination Microscopy. *Science*. **320**, 1332-1336
- 112 Shao, L., Isaac, B., Uzawa, S., Agard, D. A., Sedat, J. W. and Gustafsson, M. G. L. (2008) I5S: Wide-Field Light Microscopy with 100-nm-Scale Resolution in Three Dimensions. *Biophysical Journal*. **94**, 4971-4983
-

- 113 Thompson, R. E., Larson, D. R. and Webb, W. W. (2002) Precise Nanometer Localization Analysis for Individual Fluorescent Probes. *Biophysical Journal*. **82**, 2775-2783
- 114 Betzig, E., Patterson, G. H., Sougrat, R., Lindwasser, O. W., Olenych, S., Bonifacino, J. S., Davidson, M. W., Lippincott-Schwartz, J. and Hess, H. F. (2006) Imaging Intracellular Fluorescent Proteins at Nanometer Resolution. *Science*. **313**, 1642-1645
- 115 Hess, S. T., Girirajan, T. P. K. and Mason, M. D. (2006) Ultra-High Resolution Imaging by Fluorescence Photoactivation Localization Microscopy. *Biophysical Journal*. **91**, 4258-4272
- 116 Rust, M. J., Bates, M. and Zhuang, X. (2006) Sub-diffraction-limit imaging by stochastic optical reconstruction microscopy (STORM). *Nature Methods*. **3**, 793-796
- 117 Klar, T. A., Jakobs, S., Dyba, M., Egnér, A. and Hell, S. W. (2000) Fluorescence microscopy with diffraction resolution barrier broken by stimulated emission. *Proceedings of the National Academy of Sciences*. **97**, 8206-8210
- 118 Donnert, G., Keller, J., Medda, R., Andrei, M. A., Rizzoli, S. O., Luhrmann, R., Jahn, R., Eggeling, C. and Hell, S. W. (2006) Macromolecular-scale resolution in biological fluorescence microscopy. *Proceedings of the National Academy of Sciences*. **103**, 11440-11445
- 119 Schmidt, R., Wurm, C. A., Jakobs, S., Engelhardt, J., Egnér, A. and Hell, S. W. (2008) Spherical nanosized focal spot unravels the interior of cells. *Nature Methods*. **5**, 539-544
- 120 Willig, K. I., Rizzoli, S. O., Westphal, V., Jahn, R. and Hell, S. W. (2006) STED microscopy reveals that synaptotagmin remains clustered after synaptic vesicle exocytosis. *Nature*. **440**, 935-939

- 121 Sieber, J. J., Willig, K. I., Kutzner, C., Gerding-Reimers, C., Harke, B., Donnert, G., Rammner, B., Eggeling, C., Hell, S. W. and Grubmuller, H. (2007) Anatomy and Dynamics of a Supramolecular Membrane Protein Cluster. *Science*. **317**, 1072-1076
- 122 Kellner, R. R., Baier, C. J., Willig, K. I., Hell, S. W. and Barrantes, F. J. (2007) Nanoscale organization of nicotinic acetylcholine receptors revealed by stimulated emission depletion microscopy. *Neuroscience*. **144**, 135-143
- 123 Donnert, G., Keller, J., Wurm, C. A., Rizzoli, S. O., Westphal, V., Schonle, A., Jahn, R., Jakobs, S., Eggeling, C. and Hell, S. W. (2007) Two-Color Far-Field Fluorescence Nanoscopy. *Biophysical Journal*. **92**, 161-165
- 124 Hein, B., Willig, K. I. and Hell, S. W. (2008) Stimulated emission depletion (STED) nanoscopy of a fluorescent protein-labeled organelle inside a living cell. *Proceedings of the National Academy of Sciences*. **105**, 14271-14276
- 125 Willig, K. I., Harke, B., Medda, R. and Hell, S. W. (2007) STED microscopy with continuous wave beams. *Nature Methods*. **4**, 915-918
- 126 Chi, K. R. (2009) Super-resolution microscopy: breaking the limits. *Nature Methods*. **6**, 15-18
- 127 Scherer, N. F. (2006) Imaging: Pointillist microscopy. *Nature Nanotechnology*. **1**, 19-20
- 128 Fernandez-Suarez, M. and Ting, A. Y. (2008) Fluorescent probes for super-resolution imaging in living cells. *Nature Reviews Molecular Cell Biology*. **9**, 929-943
- 129 Shroff, H., Galbraith, C. G., Galbraith, J. A. and Betzig, E. (2008) Live-cell photoactivated localization microscopy of nanoscale adhesion dynamics. *Nature Methods*. **5**, 417-423
- 130 Shroff, H., Galbraith, C. G., Galbraith, J. A., White, H., Gillette, J., Olenych, S., Davidson, M. W. and Betzig, E. (2007) Dual-color superresolution imaging of

genetically expressed probes within individual adhesion complexes. *Proceedings of the National Academy of Sciences*. **104**, 20308-20313

131 Juette, M. F., Gould, T. J., Lessard, M. D., Mlodzianoski, M. J., Nagpure, B. S., Bennett, B. T., Hess, S. T. and Bewersdorf, J. (2008) Three-dimensional sub-100 nm resolution fluorescence microscopy of thick samples. *Nature Methods*. **5**, 527-529

132 Vaziri, A., Tang, J., Shroff, H. and Shank, C. V. (2008) Multilayer three-dimensional super resolution imaging of thick biological samples. *Proceedings of the National Academy of Sciences*. **105**, 20221-20226

133 Hess, S. T., Gould, T. J., Gudheti, M. V., Maas, S. A., Mills, K. D. and Zimmerberg, J. (2007) Dynamic clustered distribution of hemagglutinin resolved at 40 nm in living cell membranes discriminates between raft theories. *Proceedings of the National Academy of Sciences*. **104**, 17370-17375

134 Manley, S., Gillette, J. M., Patterson, G. H., Shroff, H., Hess, H. F., Betzig, E. and Lippincott-Schwartz, J. (2008) High-density mapping of single-molecule trajectories with photoactivated localization microscopy. *Nature Methods*. **5**, 155-157

135 Gustafsson, M. G. L. (2008) Super-resolution light microscopy goes live. *Nature Methods*. **5**, 385-387

136 Bates, M., Huang, B., Dempsey, G. T. and Zhuang, X. (2007) Multicolor Super-Resolution Imaging with Photo-Switchable Fluorescent Probes. *Science*. **317**, 1749-1753

137 Huang, B., Wang, W., Bates, M. and Zhuang, X. (2008) Three-Dimensional Super-Resolution Imaging by Stochastic Optical Reconstruction Microscopy. *Science*. **319**, 810-813

138 Huang, B., Jones, S. A., Brandenburg, B. and Zhuang, X. (2008) Whole-cell 3D STORM reveals interactions between cellular structures with nanometer-scale resolution. *Nature Methods*. **5**, 1047-1052

-
- 139 Gustafsson, M. G. L. (2000) Surpassing the lateral resolution limit by a factor of two using structured illumination microscopy. *Journal of Microscopy*. **198**, 82-87
- 140 Gustafsson, M. G. L., Shao, L., Carlton, P. M., Wang, C. J., Golubovskaya, I. N., Cande, W. Z., Agard, D. A. and Sedat, J. W. (2008) Three-Dimensional Resolution Doubling in Wide-Field Fluorescence Microscopy by Structured Illumination. *Biophysical Journal*. **94**, 4957-4970
- 141 Gustafsson, M. G. L., Agard, D. A. and Sedat, J. W. (1996) 3D widefield microscopy with two objective lenses: experimental verification of improved axial resolution. In *Three-Dimensional Microscopy: Image Acquisition and Processing III* (Cogswell, C. J., Kino, G. S. and Wilson, T., ed.). 62-66, SPIE, San Jose, CA, USA
- 142 Gustafsson, M. G. L., Agard, D. A. and Sedat, J. W. (1999) I 5 M: 3D widefield light microscopy with better than 100nm axial resolution. *Journal of Microscopy*. **195**, 10-16
- 143 Gustafsson, M. G. L., Agard, D. A. and Sedat, J. W. (1995) Sevenfold improvement of axial resolution in 3D wide-field microscopy using two objective lenses. In *Three-Dimensional Microscopy: Image Acquisition and Processing II* (Wilson, T. and Cogswell, C. J., ed.). 147-148, SPIE, San Jose, CA, USA
- 144 Schrader, M. and Hell, S. W. (1996) 4Pi-confocal images with axial superresolution. *Journal of Microscopy*. **183**, 110-115
- 145 Bahlmann, K., Jakobs, S. and Hell, S. W. (2001) 4Pi-confocal microscopy of live cells. *Ultramicroscopy*. **87**, 155-164
- 146 Nagorni, M. and Hell, S. W. (1998) 4Pi-Confocal Microscopy Provides Three-Dimensional Images of the Microtubule Network with 100 to 150 nm Resolution. *Journal of Structural Biology*. **123**, 236-247
- 147 Egner, A., Verrier, S., Goroshkov, A., Söling, H. D. and Hell, S. W. (2004) 4Pi-microscopy of the Golgi apparatus in live mammalian cells. *Journal of Structural Biology*. **147**, 70-76
-

- 148 Hell, S. W., Lindek, S. and Stelzer, E. H. K. (1994) Enhancing the Axial Resolution in Far-field Light Microscopy: Two-photon 4Pi Confocal Fluorescence Microscopy. *Journal of Modern Optics*. **41**, 675-681
- 149 Hell, S. and Stelzer, E. H. K. (1992) Fundamental improvement of resolution with a 4 Pi-confocal fluorescence microscope using two-photon excitation. *Optics Communications*. **93**, 277-282
- 150 Hell, S. and Stelzer, E. H. K. (1992) Properties of a 4Pi confocal fluorescence microscope. *Journal of the Optical Society of America A*. **9**, 2159-2159
- 151 Somekh, M. G., Hsu, K. and Pitter, M. C. (2008) Resolution in structured illumination microscopy: a probabilistic approach. *Journal of the Optical Society of America A*. **25**, 1319-1329
- 152 Lipson, S. G. (2003) Why is super-resolution so inefficient? *Micron*. **34**, 309-312
- 153 Byrne, G. D., Pitter, M. C., Zhang, J., Falcone, F. H., Stolnik, S. and Somekh, M. G. (2008) Total internal reflection microscopy for live imaging of cellular uptake of sub-micron non-fluorescent particles. *Journal of Microscopy*. **231**, 168-179
- 154 Ambrose, E. J. (1956) A surface contact microscope for the study of cell movements. *Nature*. **178**, 1194
- 155 Ambrose, E. J. (1961) The movements of fibrocytes. *Experimental Cell Research*. **8**, 54-73
- 156 Abercrombie, M. and Dunn, G. A. (1975) Adhesions of fibroblasts to substratum during contact inhibition observed by interference reflection microscopy. *Experimental Cell Research*. **92**, 57-62
- 157 Curtis, A. S. G. (1964) The mechanism of adhesion of cells to glass: A Study by Interference Reflection Microscopy. *The Journal of Cell Biology*. **20**, 199-215

- 158 Ploem, J. S. (1975) Reflection-contrast microscopy as a tool in investigations of the attachment of living cells to a glass surface. In: R. Van Furth, Ed. Mononuclear phagocytes in immunity, infection and pathology. Blackwell Scientific Publications, Oxford, London. 405-421
- 159 Lochner, L. and Izzard, C. S. (1973) Dynamic aspects of cell-substrate contact in fibroblast motility. *Journal of Cell Biology*. **59**, 199
- 160 Bereiter-Hahn, J. (1979) Quantitative reflection contrast microscopy of living cells. *The Journal of Cell Biology*. **82**, 767-779
- 161 Wazawa, T. and Ueda, M. (2005) Total internal reflection fluorescence microscopy in single molecule nanobioscience. *Advances in Biochemical Engineering Biotechnology*. **95**, 77-106
- 162 Axelrod, D. (2001) Total Internal Reflection Fluorescence Microscopy in Cell Biology. *Traffic*. **2**, 764-774
- 163 Axelrod, D., Burghardt, T. P. and Thompson, N. L. (1984) Total Internal Reflection Fluorescence. *Annual Reviews in Biophysics and Bioengineering*. **13**, 247-268
- 164 Axelrod, D. (2001) Selective imaging of surface fluorescence with very high aperture microscope objectives. *Journal of Biomedical Optics*. **6**, 6-13
- 165 Axelrod, D. (2003) Total internal reflection fluorescence microscopy in cell biology. *Biophotonics, Pt B*. **361**, 1-33
- 166 Azzam, R. M. A. (1979) Optical detection of cell-surface changes associated with malignant transformations in vitro. *Microscopica Acta*. **81**, 313-316
- 167 Prieve, D. C., Luo, F. and Lanni, F. (1987) Brownian motion of a hydrosol particle in a colloidal force field. *Faraday Discussions of the Chemical Society*. **83**, 297-307

- 168 Braun, D. and Fromherz, P. (1997) Fluorescence interference-contrast microscopy of cell adhesion on oxidized silicon. *Applied Physics A: Materials Science & Processing*. **65**, 341-348
- 169 Braun, D. and Fromherz, P. (1998) Fluorescence Interferometry of Neuronal Cell Adhesion on Microstructured Silicon. *Physical Review Letters*. **81**, 5241-5244
- 170 Betzig, E., Lewis, A., Harootunian, A., Isaacson, M. and Kratschmer, E. (1986) Near Field Scanning Optical Microscopy (NSOM): Development and Biophysical Applications. *Biophysical Journal*. **49**, 269-279
- 171 Prieve, D. C. (1999) Measurement of colloidal forces with TIRM. *Advances in Colloid and Interface Science*. **82**, 93-125
- 172 Kleshchanok, D. and Lang, P. R. (2007) Steric Repulsion by Adsorbed Polymer Layers Studied with Total Internal Reflection Microscopy. *Langmuir*. **23**, 4332-4339
- 173 Bevan, M. A. and Scales, P. J. (2002) Solvent Quality Dependent Interactions and Phase Behavior of Polystyrene Particles with Physisorbed PEO-PPO-PEO. *Langmuir*. **18**, 1474-1484
- 174 Kleshchanok, D., Tuinier, R. and Lang, P. R. (2006) Depletion Interaction Mediated by a Polydisperse Polymer Studied with Total Internal Reflection Microscopy. *Langmuir*. **22**, 9121-9128
- 175 Helden, L., Koenderink, G. H., Leiderer, P. and Bechinger, C. (2004) Depletion Potentials Induced by Charged Colloidal Rods. *Langmuir*. **20**, 5662-5665
- 176 Blickle, V., Speck, T., Helden, L., Seifert, U. and Bechinger, C. (2006) Thermodynamics of a Colloidal Particle in a Time-Dependent Nonharmonic Potential. *Physical Review Letters*. **96**, 70603-70607
- 177 Prieve, D. C. and Walz, J. Y. (1993) Scattering of an evanescent surface wave by a microscopic dielectric sphere. *Applied Optics*. **32**, 1629-1641

- 178 Robertson, S. K. and Bike, S. G. (1998) Quantifying Cell-Surface Interactions Using Model Cells and Total Internal Reflection Microscopy. *Langmuir*. **14**, 928-934
- 179 Cappello, G., Badoual, M., Ott, A., Prost, J. and Busoni, L. (2003) Kinesin motion in the absence of external forces characterized by interference total internal reflection microscopy. *Physical Review E*. **68**, 21907-21907
- 180 Abney, J. R., Scalettar, B. A. and Thompson, N. L. (1992) Evanescent interference patterns for fluorescence microscopy. *Biophysical Journal*. **61**, 542-552
- 181 Molloy, J. E., Dholakia, K. and Padgett, M. J. (2003) Preface: Optical tweezers in a new light. *Journal of Modern Optics*. **50**, 1501-1507
- 182 Molloy, J. E. and Padgett, M. J. (2002) Lights, action: optical tweezers. *Contemporary Physics*. **43**, 241-258
- 183 Arimoto, R. and Murray, J. M. (1996) Orientation-dependent visibility of long thin objects in polarization-based microscopy. *Biophysical Journal*. **70**, 2969-2980
- 184 McCutchen, C. W. (1964) Optical Systems for Observing Surface Topography by Frustrated Total Internal Reflection and by Interference. *Review of Scientific Instruments*. **35**, 1340-1345
- 185 Murray, J. M. and Eshel, D. (1992) Evanescent-wave microscopy: a simple optical configuration. *Journal of microscopy*. **167**, 49-62
- 186 Verschueren, H. (1985) Interference reflection microscopy in cell biology: methodology and applications. *Journal of Cell Science*. **75**, 279-301
- 187 Gingell, D. (1981) The interpretation of interference-reflection images of spread cells: significant contributions from thin peripheral cytoplasm. *Journal of Cell Science*. **49**, 237-247
- 188 Stout, A. L. and Axelrod, D. (1989) Evanescent field excitation of fluorescence by epi-illumination microscopy. *Applied Optics*. **28**, 5237-5242

- 189 Harris, A. (1973) Location of Cellular Adhesions to Solid Substrata. *Developmental Biology*. **35**, 97-114
- 190 Weber, I. (1995) Motility and substratum adhesion of Dictyostelium wild-type and cytoskeletal mutant cells: a study by RICM/bright-field double-view image analysis. *Journal of Cell Science*. **108**, 1519-1530
- 191 Bravo-Zanoguera, M., Massenbach, B., Kellner, A. L. and Price, J. H. (1998) High-performance autofocus circuit for biological microscopy. *Review of Scientific Instruments*. **69**, 3966-3977
- 192 Shen, F., Hodgson, L. and Hahn, K. (2006) Digital autofocus methods for automated microscopy. *Methods in Enzymology*. **414**, 620-632
- 193 Shen, F., Hodgson, L., Price, J. H. and Hahn, K. M. (2008) Digital differential interference contrast autofocus for high-resolution oil-immersion microscopy. *Cytometry. Part A: the journal of the International Society for Analytical Cytology*. **73A**, 658-666
- 194 Picart, C., Lavallo, P., Hubert, P., Cuisinier, F. J. G., Decher, G., Schaaf, P. and Voegel, J. C. (2001) Buildup Mechanism for Poly(L-lysine)/Hyaluronic Acid Films onto a Solid Surface. *Langmuir*. **17**, 7414-7424
- 195 Zhu, A. P., Fang, N., Chan-Park, M. B. and Chan, V. (2006) Adhesion contact dynamics of 3T3 fibroblasts on poly (lactide-co-glycolide acid) surface modified by photochemical immobilization of biomacromolecules. *Biomaterials*. **27**, 2566-2576
- 196 Langer, R. and Vacanti, J. P. (1993) Tissue engineering. *Science*. **260**, 920-926
- 197 Stevens, M. M. and George, J. H. (2005) Exploring and Engineering the Cell Surface Interface. *Science*. **310**, 1135-1138
- 198 Khademhosseini, A., Suh, K. Y., Yang, J. M., Eng, G., Yeh, J., Levenberg, S. and Langer, R. (2004) Layer-by-layer deposition of hyaluronic acid and poly-l-lysine for patterned cell co-cultures. *Biomaterials*. **25**, 3583-3592

- 199 Lee, J. H., Khang, G., Lee, J. W. and Lee, H. B. (1998) Interaction of Different Types of Cells on Polymer Surfaces with Wettability Gradient. *Journal of Colloid and Interface Science*. **205**, 323-330
- 200 Petronis, S., Gretzer, C., Kasemo, B. and Gold, J. (2003) Model porous surfaces for systematic studies of material-cell interactions. *Journal of Biomedical Materials Research Part A*. **66**, 707-721
- 201 Khademhosseini, A., Langer, R., Borenstein, J. and Vacanti, J. P. (2006) Microscale technologies for tissue engineering and biology. *Proceedings of the National Academy of Sciences*. **103**, 2480-2487
- 202 Ruardy, T. G., Schakenraad, J. M., van der Mei, H. C. and Busscher, H. J. (1997) Preparation and characterization of chemical gradient surfaces and their application for the study of cellular interaction phenomena. *Surface Science Reports*. **29**, 3-30
- 203 Kam, Z., Zamir, E. and Geiger, B. (2001) Probing molecular processes in live cells by quantitative multidimensional microscopy. *Trends in Cell Biology*. **11**, 329-334
- 204 Jamil, M. M. A., Denyer, M. C. T., Youseffi, M., Britland, S. T., Liu, S., See, C. W., Somekh, M. G. and Zhang, J. (2008) Imaging of the cell surface interface using objective coupled widefield surface plasmon microscopy. *Journal of Structural Biology*. **164**, 75-80
- 205 Raucher, D. and Sheetz, M. P. (2000) Cell Spreading and Lamellipodial Extension Rate Is Regulated by Membrane Tension. *The Journal of Cell Biology*. **148**, 127-136
- 206 Pollanen, J., Hedman, K., Nielsen, L. S., Dano, K. and Vaheri, A. (1988) Ultrastructural Localization of Plasma Membrane-Associated Urokinase-Type Plasminogen Activator at Focal Contacts. *The Journal of Cell Biology*. **106**, 87-95

- 207 Tawil, N., Wilson, P. and Carbonetto, S. (1993) Integrins in point contacts mediate cell spreading: factors that regulate integrin accumulation in point contacts vs. focal contacts. *The Journal of Cell Biology*. **120**, 261-271
- 208 Leyton, L., Schneider, P., Labra, C. V., Rüegg, C., Hetz, C. A., Quest, A. F. G. and Bron, C. (2001) Thy-1 binds to integrin beta3 on astrocytes and triggers formation of focal contact sites. *Current Biology*. **11**, 1028-1038
- 209 Rivelino, D., Zamir, E., Balaban, N. Q., Schwarz, U. S., Ishizaki, T., Narumiya, S., Kam, Z., Geiger, B. and Bershadsky, A. D. (2001) Focal Contacts as Mechanosensors: Externally Applied Local Mechanical Force Induces Growth of Focal Contacts by an mDia1-dependent and ROCK-independent Mechanism. *The Journal of Cell Biology*. **153**, 1175-1186
- 210 Piscevic, D., Knoll, W. and Tarlov, M. J. (1995) Surface plasmon microscopy of biotin-streptavidin binding reactions on UV-photopatterned alkanethiol self-assembled monolayers. *Supramolecular Science*. **2**, 99-106
- 211 Yamaji, S., Suzuki, A., Sugiyama, Y., Koide, Y., Yoshida, M., Kanamori, H., Mohri, H., Ohno, S. and Ishigatsubo, Y. (2001) A Novel Integrin-linked Kinase-binding Protein, Affixin, Is Involved in the Early Stage of Cell-Substrate Interaction. *The Journal of Cell Biology*. **153**, 1251-1264
- 212 Aaronson, S. A. and Todaro, G. J. (1968) Development of 3T3-like lines from Balb-c mouse embryo cultures: transformation susceptibility to SV40. *Journal of Cellular Physiology*. **72**, 141-148
- 213 Stearns, R. C., Paulauskis, J. D. and Godleski, J. J. (2001) Endocytosis of Ultrafine Particles by A549 Cells. *American Journal of Respiratory Cell and Molecular Biology*. **24**, 108-115
- 214 Mason, R. J. and Williams, M. C. (1977) Type II alveolar cell. Defender of the alveolus. *The American review of respiratory disease*. **115**, 81-91

- 215 Hornung, J. and Fuhr, G. (1997) Influence of polylysine on adhesion of fibroblasts to glass substrates visualized by total internal reflection microscopy. *Experimental Biology Online*. **1**, 1-11
- 216 Gingell, D. (1985) Topography of cell-glass apposition revealed by total internal reflection fluorescence of volume markers. *Journal of Cell Biology*. **100**, 1334-1338
- 217 Fehrenbach, H. (2001) Alveolar epithelial type II cell: defender of the alveolus revisited. *Respiratory Research*. **2**, 33-46
- 218 Haagsman, H. P. and Van Golde, L. M. G. (1991) Synthesis and Assembly of Lung Surfactant. *Annual Review of Physiology*. **53**, 441-464
- 219 Stokes, G. G. (1852) On the Change of Refrangibility of Light. *Philosophical Transactions of the Royal Society of London*. **142**, 463-562
- 220 Steyer, J. A. and Almers, W. (2001) A real-time view of life within 100 nm of the plasma membrane. *Nature Reviews Molecular Cell Biology*. **2**, 268-275
- 221 Thompson, N. L. and Axelrod, D. (1983) Immunoglobulin surface-binding kinetics studied by total internal reflection with fluorescence correlation spectroscopy. *Biophysical Journal*. **43**, 103-114
- 222 Sarkar, A., Robertson, R. B. and Fernandez, J. M. (2004) Simultaneous atomic force microscope and fluorescence measurements of protein unfolding using a calibrated evanescent wave. *Proceedings of the National Academy of Sciences*. **101**, 12882-12886
- 223 Blandin, P., Lévêque-Fort, S., Lécart, S., Zeller, P., Lenkei, Z., Druon, F. and Georges, P. (2007) Development of a TIRF-FLIM microscope for biomedical applications. In *Confocal, Multiphoton, and Nonlinear Microscopic Imaging III* (Wilson, T. and Periasamy, A., ed.). 66300B, SPIE, Munich, Germany

- 224 Thompson, N. L., Burghardt, T. P. and Axelrod, D. (1981) Measuring surface dynamics of biomolecules by total internal reflection fluorescence with photobleaching recovery or correlation spectroscopy. *Biophysical Journal*. **33**, 435-454
- 225 Hashido, M., Hayashi, K., Hirose, K. and Iino, M. (2006) Ca²⁺ lightning conveys cell–cell contact information inside the cells. *EMBO Reports*. **7**, 1117-1123
- 226 Stock, K., Sailer, R., Strauss, W. S. L., Lyttek, M., Steiner, R. and Schneckenburger, H. (2003) Variable-angle total internal reflection fluorescence microscopy (VA-TIRFM): realization and application of a compact illumination device. *Journal of Microscopy*. **211**, 19-29
- 227 Reichert, W. M. and Truskey, G. A. (1990) Total internal reflection fluorescence (TIRF) microscopy. I. Modelling cell contact region fluorescence. *Journal of Cell Science*. **96**, 219-230
- 228 Truskey, G. A., Burmeister, J. S., Grapa, E. and Reichert, W. M. (1992) Total internal reflection fluorescence microscopy (TIRFM). II. Topographical mapping of relative cell/substratum separation distances. *Journal of Cell Science*. **103**, 491-499
- 229 Gingell, D. (1987) General electromagnetic theory of total internal reflection fluorescence: the quantitative basis for mapping cell-substratum topography. *Journal of Cell Science*. **87**, 677-693
- 230 Burmeister, J. S., Olivier, L. A., Reichert, W. M. and Truskey, G. A. (1998) Application of total internal reflection fluorescence microscopy to study cell adhesion to biomaterials. *Biomaterials*. **19**, 307-325
- 231 Bradbury, S. (1984) *An Introduction to the Optical Microscope*. Royal Microscopical Society Microscopy Handbooks. Oxford University Press for Royal Microscopical Society, USA
- 232 Giannone, G., Dubin-Thaler, B. J., Rossier, O., Cai, Y., Chaga, O., Jiang, G., Beaver, W., Döbereiner, H.-G., Freund, Y., Borisy, G. and Sheetz, M. P. (2007)

Lamellipodial Actin Mechanically Links Myosin Activity with Adhesion-Site Formation. *Cell*. **128**, 561-575

233 Protein, M. F. (2008) BD Living Colors™ DsRed-Monomer Fluorescent Protein. Clontech, 2

234 Mayor, S. and Pagano, R. E. (2007) Pathways of clathrin-independent endocytosis. *Nature Reviews Molecular Cell Biology*. **8**, 603-612

235 Conner, S. D. and Schmid, S. L. (2003) Regulated portals of entry into the cell. *Nature*. **422**, 37-44

236 Hans, M. L. and Lowman, A. M. (2002) Biodegradable nanoparticles for drug delivery and targeting. *Current Opinion in Solid State and Materials Science*. **6**, 319-327

237 Parton, R. G. and Simons, K. (2007) The multiple faces of caveolae. *Nature Reviews Molecular Cell Biology*. **8**, 185-194

238 Tagawa, A., Mezzacasa, A., Hayer, A., Longatti, A., Pelkmans, L. and Helenius, A. (2005) Assembly and Trafficking of Caveolar Domains in the Cell: Caveolae as Stable, Cargo-Triggered, Vesicular Transporters. *The Journal of Cell Biology*. **170**, 769-779

239 Kaksonen, M., Toret, C. P. and Drubin, D. G. (2006) Harnessing actin dynamics for clathrin-mediated endocytosis. *Nature Reviews Molecular Cell Biology*. **7**, 404-414

240 Moskowitz, H. S., Yokoyama, C. T. and Ryan, T. A. (2005) Highly Cooperative Control of Endocytosis by Clathrin. *Molecular Biology of the Cell*. **16**, 1769-1776

241 Ungewickell, E. J. and Hinrichsen, L. (2007) Endocytosis: clathrin-mediated membrane budding. *Current Opinion in Cell Biology*. **19**, 417-425

242 Bretscher, M. S. (1982) Surface uptake by fibroblasts and its consequences. In *Cold Spring Harbor Symposium on Quantitative Biology*. 707-712, CSH, Cold Spring Harbor, NY

- 243 Heuser, J. (1980) Three-dimensional visualization of coated vesicle formation in fibroblasts. *The Journal of Cell Biology*. **84**, 560-583
- 244 Kirchhausen, T. (2000) Clathrin. *Annual Review of Biochemistry*. **69**, 699-727
- 245 Rappoport, J. Z. (2008) Focusing on clathrin-mediated endocytosis. *Biochemical Journal*. **412**, 415-423
- 246 Takei, K., McPherson, P. S., Schmid, S. L. and De Camilli, P. (2002) Tubular membrane invaginations coated by dynamin rings are induced by GTP-big gamma S in nerve terminals. *Nature*. **374**, 186-190
- 247 Gaidarov, I., Santini, F., Warren, R. A. and Keen, J. H. (1999) Spatial control of coated-pit dynamics in living cells. *Nature Cell Biology*. **1**, 1-7
- 248 Bellve, K. D., Leonard, D., Standley, C., Lifshitz, L. M., Tuft, R. A., Hayakawa, A., Corvera, S. and Fogarty, K. E. (2006) Plasma membrane domains specialized for clathrin-mediated endocytosis in primary cells. *Journal of Biological Chemistry*. **281**, 16139-16146
- 249 Rappoport, J. Z., Kemal, S., Benmerah, A. and Simon, S. M. (2006) Dynamics of clathrin and adaptor proteins during endocytosis. *American Journal of Physiology-Cell Physiology*. **291**, C1072-C1081
- 250 Rappoport, J., Simon, S. M. and Benmerah, A. (2004) Understanding Living Clathrin-Coated Pits. *Traffic*. **5**, 327-337
- 251 Rappoport, J. Z., Benmerah, A. and Simon, S. M. (2005) Analysis of the AP-2 adaptor complex and cargo during clathrin-mediated endocytosis. *Traffic*. **6**, 539-547
- 252 Rappoport, J. Z., Taha, B. W., Lemeer, S., Benmerah, A. and Simon, S. M. (2003) The AP-2 Complex Is Excluded from the Dynamic Population of Plasma Membrane-associated Clathrin. *Journal of Biological Chemistry*. **278**, 47357-47360

- 253 Rappoport, J. Z., Taha, B. W. and Simon, S. M. (2003) Movement of Plasma-Membrane-Associated Clathrin Spots Along the Microtubule Cytoskeleton. *Traffic*. **4**, 460-467
- 254 Keyel, P. A., Watkins, S. C. and Traub, L. M. (2004) Endocytic Adaptor Molecules Reveal an Endosomal Population of Clathrin by Total Internal Reflection Fluorescence Microscopy. *Journal of Biological Chemistry*. **279**, 13190-13204
- 255 Ehrlich, M., Boll, W., van Oijen, A., Hariharan, R., Chandran, K., Nibert, M. L. and Kirchhausen, T. (2004) Endocytosis by Random Initiation and Stabilization of Clathrin-Coated Pits. *Cell*. **118**, 591-605
- 256 Young, A. (2007) Structural insights into the clathrin coat. *Seminars in Cell and Developmental Biology*. **18**, 448-458
- 257 Saiki, R. K., Scharf, S., Faloona, F., Mullis, K. B., Horn, G. T., Erlich, H. A. and Arnheim, N. (1985) Enzymatic amplification of beta-globin genomic sequences and restriction site analysis for diagnosis of sickle cell anemia. *Science*. **230**, 1350-1354
- 258 Anderson, R. G., Vasile, E., Mello, R. J., Brown, M. S. and Goldstein, J. L. (1978) Immunocytochemical visualization of coated pits and vesicles in human fibroblasts: relation to low density lipoprotein receptor distribution. *Cell*. **15**, 919-933
- 259 Keen, J. H., Willingham, M. C. and Pastan, I. (1981) Clathrin and coated vesicle proteins Immunological characterization. *Journal of Biological Chemistry*. **256**, 2538-2544
- 260 Goud, B., Huet, C. and Louvard, D. (1985) Assembled and unassembled pools of clathrin: a quantitative study using an enzyme immunoassay. *Journal of Cell Biology*. **100**, 521-527
- 261 Stoorvogel, W., Oorschot, V. and Geuze, H. J. (1996) A novel class of clathrin-coated vesicles budding from endosomes. *Journal of Cell Biology*. **132**, 21-33

-
- 262 Engqvist-Goldstein, A. E. Y., Warren, R. A., Kessels, M. M., Keen, J. H., Heuser, J. and Drubin, D. G. (2001) The actin-binding protein Hip1R associates with clathrin during early stages of endocytosis and promotes clathrin assembly in vitro. *Journal of Cell Biology*. **154**, 1209-1224
- 263 Santini, F., Gaidarov, I. and Keen, J. H. (2002) G protein-coupled receptor/arrestin3 modulation of the endocytic machinery. *Journal of Cell Biology*. **156**, 665-676
- 264 Merrifield, C. J., Feldman, M. E., Wan, L. and Almers, W. (2002) Imaging actin and dynamin recruitment during invagination of single clathrin-coated pits. *Nature Cell Biology*. **4**, 691-698
- 265 Swaminathan, R., Hoang, C. P. and Verkman, A. S. (1997) Photobleaching recovery and anisotropy decay of green fluorescent protein GFP-S65T in solution and cells: cytoplasmic viscosity probed by green fluorescent protein translational and rotational diffusion. *Biophysical Journal*. **72**, 1900-1907
- 266 White, J. and Stelzer, E. (1999) Photobleaching GFP reveals protein dynamics inside live cells. *Trends in Cell Biology*. **9**, 61-65
- 267 Wu, X., Zhao, X., Baylor, L., Kaushal, S., Eisenberg, E. and Greene, L. E. (2001) Clathrin exchange during clathrin-mediated endocytosis. *Journal of Cell Biology*. **155**, 291-300
- 268 Merrifield, C. J., Perrais, D. and Zenisek, D. (2005) Coupling between Clathrin-Coated-Pit Invagination, Cortactin Recruitment, and Membrane Scission Observed in Live Cells. *Cell*. **121**, 593-606
- 269 Pelkmans, L., Kartenbeck, J. and Helenius, A. (2001) Caveolar endocytosis of simian virus 40 reveals a new two-step vesicular-transport pathway to the ER. *Nature Cell Biology*. **3**, 473-483
- 270 Pietzonka, P., Rothen-Rutishauser, B., Langguth, P., Wunderli-Allenspach, H., Walter, E. and Merkle, H. P. (2002) Transfer of lipophilic markers from PLGA and
-

polystyrene nanoparticles to Caco-2 monolayers mimics particle uptake. *Pharmaceutical Research*. **19**, 595-601

271 Pfaffl, M. W. (2001) A new mathematical model for relative quantification in real-time RT-PCR. *Nucleic Acids Research*. **29**, 45-50

272 Deshpande, M. C., Davies, M. C., Garnett, M. C., Williams, P. M., Armitage, D., Bailey, L., Vamvakaki, M., Armes, S. P. and Stolnik, S. (2004) The effect of poly(ethylene glycol) molecular architecture on cellular interaction and uptake of DNA complexes. *Journal of Controlled Release*. **97**, 143-156

273 Panyam, J. and Labhasetwar, V. (2003) Dynamics of Endocytosis and Exocytosis of Poly (D, L-Lactide-co-Glycolide) Nanoparticles in Vascular Smooth Muscle Cells. *Pharmaceutical Research*. **20**, 212-220

274 Harush-Frenkel, O., Debotton, N., Benita, S. and Altschuler, Y. (2007) Targeting of nanoparticles to the clathrin-mediated endocytic pathway. *Biochemical and Biophysical Research Communications*. **353**, 26-32

275 Chavanpatil, M. D., Khdair, A. and Panyam, J. (2007) Surfactant-polymer Nanoparticles: A Novel Platform for Sustained and Enhanced Cellular Delivery of Water-soluble Molecules. *Pharmaceutical Research*. **24**, 803-810

276 Ewers, H., Smith, A. E., Sbalzarini, I. F., Lilie, H., Koumoutsakos, P. and Helenius, A. (2005) Single-particle tracking of murine polyoma virus-like particles on live cells and artificial membranes. *Proceedings of the National Academy of Sciences*. **102**, 15110-15115

277 Alberola, A. P. and Rädler, J. O. (2009) The defined presentation of nanoparticles to cells and their surface controlled uptake. *Biomaterials*. **30**, 3766-3770

278 Hanarp, P., Sutherland, D. S., Gold, J. and Kasemo, B. (2003) Control of nanoparticle film structure for colloidal lithography. *Colloids and Surfaces A: Physicochemical and Engineering Aspects*. **214**, 23-36

- 279 Pannier, A. K., Anderson, B. C. and Shea, L. D. (2005) Substrate-mediated delivery from self-assembled monolayers: Effect of surface ionization, hydrophilicity, and patterning. *Acta Biomaterialia*. **1**, 511-522
- 280 Levy, R. J., Song, C., Tallapragada, S., DeFelice, S., Hinson, J. T., Vyavahare, N., Connolly, J., Ryan, K. and Li, Q. (2001) Localized adenovirus gene delivery using antiviral IgG complexation. *Gene Therapy*. **8**, 659-667
- 281 Segura, T., Volk, M. J. and Shea, L. D. (2003) Substrate-mediated DNA delivery: role of the cationic polymer structure and extent of modification. *Journal of Controlled Release*. **93**, 69-84
- 282 Segura, T., Chung, P. H. and Shea, L. D. (2005) DNA delivery from hyaluronic acid-collagen hydrogels via a substrate-mediated approach. *Biomaterials*. **26**, 1575-1584
- 283 Shen, H., Tan, J. and Saltzman, W. M. (2004) Surface-mediated gene transfer from nanocomposites of controlled texture. *Nature Materials*. **3**, 569-574
- 284 Luo, D. and Saltzman, W. M. (2000) Enhancement of transfection by physical concentration of DNA at the cell surface. *Nature Biotechnology*. **18**, 893-895
- 285 Sokolov, K., Follen, M., Aaron, J., Pavlova, I., Malpica, A., Lotan, R. and Richards-Kortum, R. (2003) Real-Time Vital Optical Imaging of Precancer Using Anti-Epidermal Growth Factor Receptor Antibodies Conjugated to Gold Nanoparticles. *Cancer Research*. **63**, 1999-2004
- 286 Brodsky, F. M. (1985) Clathrin structure characterized with monoclonal antibodies. I. Analysis of multiple antigenic sites. *Journal of Cell Biology*. **101**, 2047-2054
- 287 Galbiati, F., Volonté, D., Engelman, J. A., Watanabe, G., Burk, R., Pestell, R. G. and Lisanti, M. P. (1998) Targeted downregulation of caveolin-1 is sufficient to drive cell transformation and hyperactivate the p42/44 MAP kinase cascade. *The EMBO Journal*. **17**, 6633-6648

- 288 Bickel, P. E., Scherer, P. E., Schnitzer, J. E., Oh, P., Lisanti, M. P. and Lodish, H. F. (1997) Flotillin and Epidermal Surface Antigen Define a New Family of Caveolae-associated Integral Membrane Proteins. *Journal of Biological Chemistry*. **272**, 13793-13802
- 289 Egner, A. and Hell, S. W. (2005) Fluorescence microscopy with super-resolved optical sections. *Trends in Cell Biology*. **15**, 207-215
- 290 Lichtman, J. W. and Conchello, J. A. (2005) Fluorescence microscopy. *Nature Methods*. **2**, 910-919
- 291 Shaner, N. C., Steinbach, P. A. and Tsien, R. Y. (2005) A guide to choosing fluorescent proteins. *Nature Methods*. **2**, 905-909
- 292 Puthenveedu, M. A. and von Zastrow, M. (2006) Cargo Regulates Clathrin-Coated Pit Dynamics. *Cell*. **127**, 113-124
- 293 Rust, M. J., Lakadamyali, M., Zhang, F. and Zhuang, X. (2004) Assembly of endocytic machinery around individual influenza viruses during viral entry. *Nature Structural and Molecular Biology*. **11**, 567-573
- 294 Nunnally, M. H. (2003) Certificate of Analysis for 300 nm and 2 μ m carboxyl modified spheres. Invitrogen, Oregon.
- 295 Merrifield, C. J. (2004) Seeing is believing: imaging actin dynamics at single sites of endocytosis. *Trends in Cell Biology*. **14**, 352-358
- 296 Perrais, D. and Merrifield, C. J. (2005) Dynamics of Endocytic Vesicle Creation. *Developmental Cell*. **9**, 581-592
- 297 Lakadamyali, M., Rust, M. J. and Zhuang, X. (2004) Endocytosis of influenza viruses. *Microbes and Infection*. **6**, 929-936
- 298 Blanpied, T. A., Scott, D. B. and Ehlers, M. D. (2002) Dynamics and Regulation of Clathrin Coats at Specialized Endocytic Zones of Dendrites and Spines. *Neuron*. **36**, 435-449

- 299 Scott, M. G. H., Benmerah, A., Muntaner, O. and Marullo, S. (2002) Recruitment of Activated G Protein-coupled Receptors to Pre-existing Clathrin-coated Pits in Living Cells. *Journal of Biological Chemistry*. **277**, 3552-3559
- 300 Kwiatkowski, R. W., Lyamichev, V., de Arruda, M. and Neri, B. (1999) Clinical, genetic, and pharmacogenetic applications of the invader assay. *Molecular Diagnosis*. **4**, 353-364
- 301 Becker-Andre, M. and Hahlbrock, K. (1989) Absolute mRNA quantification using the polymerase chain reaction (PCR). A novel approach by a PCR aided transcript titration assay (PATY). *Nucleic Acids Research*. **17**, 9437-9446
- 302 Bustin, S. A. (2002) Quantification of mRNA using real-time reverse transcription PCR (RT-PCR): trends and problems. *Journal of Molecular Endocrinology*. **29**, 23-39
- 303 Willems, E., Mateizel, I., Kemp, C., Cauffman, G., Sermon, K. and Leyns, L. (2006) Selection of reference genes in mouse embryos and in differentiating human and mouse ES cells. *International Journal of Developmental Biology*. **50**, 627-635
- 304 Huang, M., Ma, Z., Khor, E. and Lim, L. Y. (2002) Uptake of FITC-Chitosan Nanoparticles by A549 Cells. *Pharmaceutical Research*. **19**, 1488-1494
- 305 Qaddoumi, M. G., Gukasyan, H. J., Davda, J., Labhasetwar, V., Kim, K. J. and Lee, V. H. (2003) Clathrin and caveolin-1 expression in primary pigmented rabbit conjunctival epithelial cells: role in PLGA nanoparticle endocytosis. *Molecular Vision*. **9**, 559-568
- 306 Huang, D. M., Hung, Y., Ko, B. S., Hsu, S. C., Chen, W. H., Chien, C. L., Tsai, C. P., Kuo, C. T., Kang, J. C. and Yang, C. S. (2005) Highly efficient cellular labeling of mesoporous nanoparticles in human mesenchymal stem cells: implication for stem cell tracking. *The FASEB Journal*. **19**, 2014-2016

-
- 307 Chung, T.-H., Wu, S.-H., Yao, M., Lu, C.-W., Lin, Y.-S., Hung, Y., Mou, C.-Y., Chen, Y.-C. and Huang, D.-M. (2007) The effect of surface charge on the uptake and biological function of mesoporous silica nanoparticles in 3T3-L1 cells and human mesenchymal stem cells. *Biomaterials*. **28**, 2959-2966
- 308 Merrifield, C. J., Feldman, M. E., Wan, L. and Almers, W. (2002) Imaging actin and dynamin recruitment during invagination of single clathrin-coated pits. *Nature Cell Biology*. **4**, 691-698
- 309 Weisswange, I., Bretschneider, T. and Anderson, K. I. (2005) The leading edge is a lipid diffusion barrier. *Journal of Cell Science*. **118**, 4375-4380
- 310 Tokunaga, M., Imamoto, N. and Sakata-Sogawa, K. (2008) Highly inclined thin illumination enables clear single-molecule imaging in cells. *Nature Methods*. **5**, 159-161
- 311 Dunsby, C. (2008) Optically sectioned imaging by oblique plane microscopy. *Optics Express*. **16**, 20306-20316
- 312 Lauffenburger, D. A. and Horwitz, A. F. (1996) Cell Migration: A Physically Integrated Molecular Process. *Cell*. **84**, 359-369
- 313 Iwanaga, Y., Braun, D. and Fromherz, P. (2001) No correlation of focal contacts and close adhesion by comparing GFP-vinculin and fluorescence interference of DiI. *European Biophysics Journal*. **30**, 17-26
- 314 Rusan, N. M., Fagerstrom, C. J., Yvon, A.-M. C. and Wadsworth, P. (2001) Cell Cycle-Dependent Changes in Microtubule Dynamics in Living Cells Expressing Green Fluorescent Protein- α Tubulin. *Molecular Biology of the Cell*. **12**, 971-980
- 315 Moffitt, J. R., Chemla, Y. R., Smith, S. B. and Bustamante, C. (2008) Recent Advances in Optical Tweezers. *Annual Review of Biochemistry*. **77**, 205-228
- 316 Gu, M., Haumonte, J. B., Micheau, Y., Chon, J. W. M. and Gan, X. (2004) Laser trapping and manipulation under focused evanescent wave illumination. *Applied Physics Letters*. **84**, 4236-4238
-

- 317 Guck, J., Ananthakrishnan, R., Moon, T. J., Cunningham, C. C. and Käs, J. (2000) Optical Deformability of Soft Biological Dielectrics. *Physical Review Letters*. **84**, 5451-5454
- 318 Christopher D. Mellor, C. D. B. (2006) Array Formation in Evanescent Waves. *Chemical Physics and Physical Chemistry*. **7**, 329-332
- 319 Mameren, J. v., Modesti, M., Kanaar, R., Wyman, C., Wuite, G. J. L. and Peterman, E. J. G. (2006) Dissecting Elastic Heterogeneity along DNA Molecules Coated Partly with Rad51 Using Concurrent Fluorescence Microscopy and Optical Tweezers. *Biophysical Journal*. **91**, L78-L80
- 320 Dame, R. T., Noom, M. C. and Wuite, G. J. L. (2006) Bacterial chromatin organization by H-NS protein unravelled using dual DNA manipulation. *Nature*. **444**, 387-390
- 321 Wong, J. Y., Langer, R. and Ingber, D. E. (1994) Electrically Conducting Polymers can Noninvasively Control the Shape and Growth of Mammalian Cells. *Proceedings of the National Academy of Sciences*. **91**, 3201-3204
- 322 Parce, J. W., Owicki, J. C., Kercso, K. M., Sigal, G. B., Wada, H. G., Muir, V. C., Bousse, L. J., Ross, K. L., Sikic, B. I. and McConnell, H. M. (1989) Detection of cell-affecting agents with a silicon biosensor. *Science*. **246**, 243-247

Appendix - Results from qRT²-PCR experiments

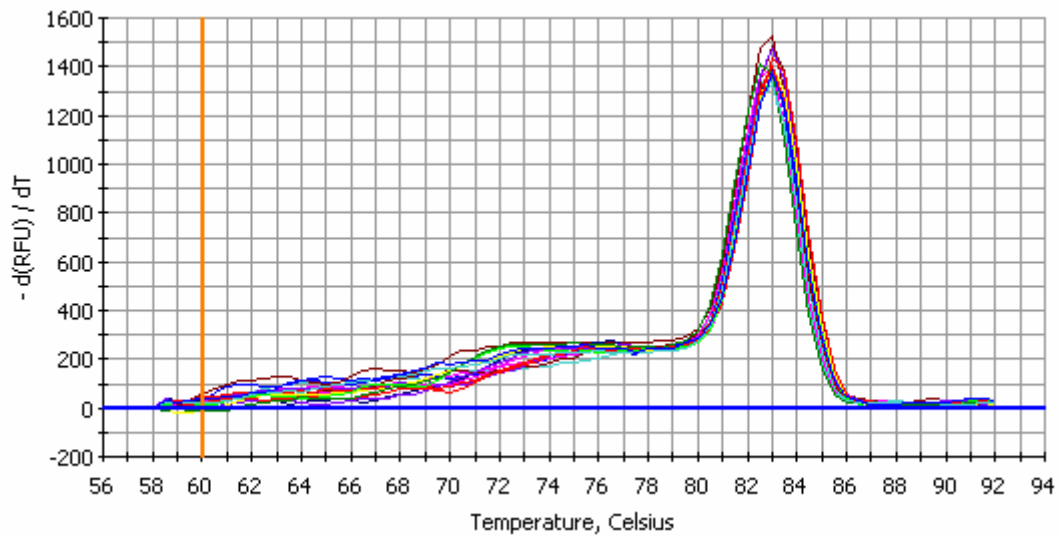


Figure A.1.1 Melt curve graph for SYBR-490 and HPRT1, RPL32 and Clathrin genes.

Only one peak can be seen indicating that the primers are specific for each individual gene.

A

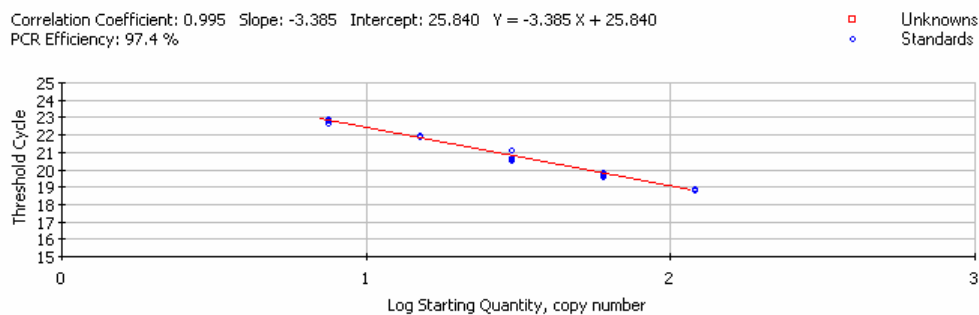
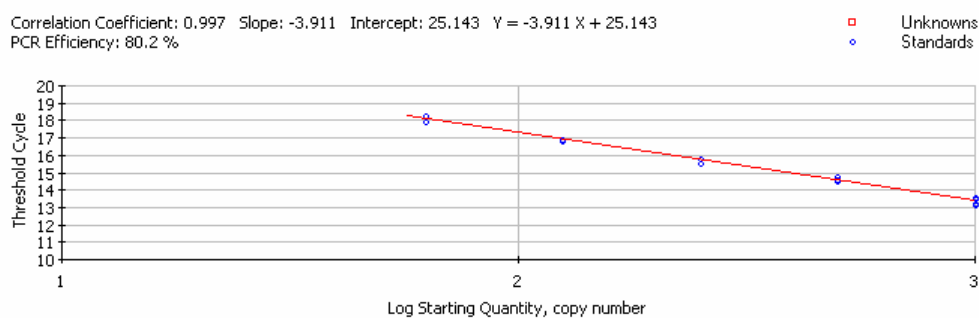
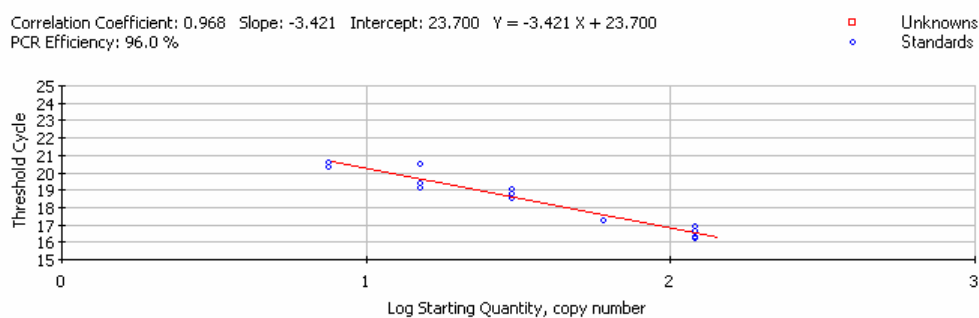
**B****C**

Figure A.1.2 $q(RT)^2$ -PCR standard curve graphs obtained using the SYBR green method

A) HPRT1 efficiency is 97.4 % and the correlation coefficient is 0.995. B) RPL32 efficiency is 80.2 % and the correlation coefficient is 0.997. C) Clathrin LCa efficiency is 96.0 % and the correlation coefficient is 0.968. These results indicate that the results are accurate for the experimental conditions used.